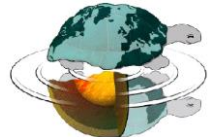




UNIVERSITÀ DEGLI STUDI DI MILANO

Dottorato di Ricerca in Scienze della Terra

Cycle n° XXX



Melt-rock interaction at the mantle-crust transition zone in the oceanic spreading lithosphere: an experimental study

Ph.D. Thesis

Justine E. Francomme
ID n° R11071

Tutor

Prof. Patrizia Fumagalli

Coordinator

Prof. Elisabetta Erba

Academic Year

Co- Tutor

2016-2017

Dr. Giulio Borghini

Acknowledgments

The research leading to these results has received funding from the People Programme (Marie Curie Actions) of the European Union's Seventh Framework Programme FP7/2007-2013/under REA grant agreement n°608001.

Further, thank you to my supervisors for their support: Prof. Dr. Patrizia Fumagalli and Dr. Giulio Borghini.

Also, thank you to the reviewers of this dissertation: Prof. Dr. Costanza Bonadiman and Prof. Dr. Ricardo Tribuzio.

I especially want to thank Andrea Risplendente for his help and expertise at the Milan Electron Microprobe. As well, as the work with our Piston Cylinders can at times be challenging, I greatly benefited from the knowledge and teamwork in the experimental petrology lab. Thank you: Prof. Dr. Stefano Poli and Luca S. Capizzi.

Grateful thanks to Prof. Dr. Benoit Ildefonse and Dr. Fabrice Barou for their expertise during EBSD analysis performed at Géosciences Montpellier.

Thank you Prof. Dr. Giancarlo Capitani for his help for sample preparation at the University of Milano Bicocca and his expertise for TEM analysis at the University of Sienna.

Thank you Prof. Dr. Jürgen Koepke, Prof. Dr. Elizabetha Rampone and Dr. Renat Almeev, who were open during ABYSS-ITN meetings for helpful discussions. Furthermore, thank you to the ABYSS students team who constituted a great working and supporting team along those last 3 years: Adriana Currin, Valentin Basch, Dr. Carlotta Ferrando, Sofia Escario, Dr. Katarina Loss, Dr. Kristina Dunkel, Rachael Moore, Zeudia Pastore, Barbara Zielman, Emmanouil Giampouras, Manuel Menzel, Dr. Aurélien Beaumais, Dr. Thomas Grant and Pavel Smal.

Finally, for the personal support I received, I want to address a big thank you to my parents Cathy and Jean Luc, and my sister Audrey, who always supported me on the way to the doctorate degree. Great support also came from my friends and especially Antoine who has been constantly present these last months.

It was a pleasure to share everyday work with many friends and colleagues. A special thank you to Davide Comboni and Gianluca Sessa, who were patient, friendly and helpful office colleagues.

Table of content

Table of tables	6
Table of figures	7
Research aim	11
Chapter 1. Objectives and Background	13
1.1. The role of melt-rock reactions in the origin of troctolites at mantle-crust transition at oceanic lithosphere extensional settings.....	13
1.2. State of the art of experimental strategies to investigate melt-rock interactions	15
1.3. Aims	16
Chapter 2. Experimental and analytical techniques	19
2.1. Starting Material	20
2.2. Experimental procedure	24
2.2.1. Pre-sintered dunite – Basalt dissolution experiments.....	24
2.2.2. Powder to powder reactive dissolution-crystallization	24
2.3. Sample Preparation	24
2.4. Analytical techniques	25
2.4.1. Microprobe analysis.....	25
2.4.2. Image analysis.....	25
2.4.3. EBSD analysis.....	25
2.4.4. Transmission Electron Microscopy analysis.....	27
Chapter 3. Olivine reactive dissolution as a function of run duration and melt composition.	29
3.1. Experimental procedure	29
3.2. Results	30
3.2.1. Textures and phase abundances.....	32
3.2.2. Mineral chemistry.....	41
3.3. Effect of time on olivine dissolution	50
3.3.1. Phase assemblage variations as a function of time.....	50
3.3.2. Olivine-rich layer texture evolution as a function of time.....	51

3.3.3. Effect of time on reacted melt and olivine compositions	53
3.4. Effect of time on olivine dissolution	57
Chapter 4. Step-cooled experiments: reactive dissolution-crystallization	61
4.1. Experimental methods	61
4.2. Textures and phase abundances of experimental results.....	63
4.2.1. Phase assemblage and textures	63
4.2.2. Phase assemblage of olivine-rich layer by image analysis	66
4.2.3. EBSD analysis: phases abundance and microstructural aspects.....	67
4.3. Mineral chemistry of reactive dissolution crystallization	75
4.3.1. Olivine composition	75
4.3.2. Plagioclase chemistry.....	77
4.3.3. Clinopyroxene chemistry	79
4.4. Discussion	82
4.4.1. Role of Pressure on textures and mineral chemistry.....	82
4.4.2. The role of melt composition on textures and mineral chemistry.....	89
4.4.3. Comparison with natural occurrences.....	90
Chapter 5. Future perspectives: Melt infiltration in pre-sintered dunite.....	95
5.1. Experimental strategy.....	95
5.2. Results	97
5.2.1. Lithologies and textures	97
5.2.2. Mineral chemistry	99
5.2.3. Transmission Electron Microscopy investigations.....	102
5.3. Discussion	106
Chapter 6. Conclusion.....	107
Appendix and References.....	111
A1. Appendix	111
A1.1. Figures	111

A1.2. Tables	115
A2. References	175

Table of tables

Table 2-1. Representative major element compositions of starting material.....	22
Table 3-1: Experimental run conditions and phase assemblages of selected runs.....	31
Table 3-2: Representative major element compositions of olivine in isothermal experiments.....	115
Table 3-3: Representative major element compositions of glass in isothermal experiments.....	133
Table 4-1: Experimental run conditions and phase assemblages of selected runs.....	62
Table 4.2: Representative major element compositions of olivine from ol-rich layer from step-cooled experiments	148
Table 4-4: Representative major element compositions of plagioclase from ol-rich layer from step-cooled experiments.....	161
Table 4-4: Representative major element compositions of clinopyroxene from ol-rich layer from step-cooled experiments.....	169
Table 5-1: Experimental run conditions and phase assemblages of dunite reactive dissolution experiments using melt AH6 and AH3.....	97

Table of figures

Figure 2-1: Experimental strategies and setups for dunite infiltrations and powder to powder experiments	21
Figure 2-2: Comparison between compositions of starting synthetic basalt powders (AH3, AH6 and HDRBC) and Atlantic and Pacific MORBs	22
Figure 2-3: Pictures of San Carlos olivine used as starting material	23
Figure 2-4: MDI-01 and OM01 thin sections prepared for TEM investigation	28
Figure 3-1: Temperature vs time diagrams showing the phase assemblages in the olivine-rich layer	31
Figure 3-2: Representative Electron Backscattered images from short duration isothermal experiments	33
Figure 3-3: Representative Electron Backscattered images from the olivine-rich layer of eight isothermal experiments conducted at 1250 °C	34
Figure 3-4: Representative Electron Backscattered images from the olivine-rich layer of experiment OM07	35
Figure 3-5: Representative Electron Backscattered images from the olivine-rich layer of experiments OM24 and OM15.....	36
Figure 3-6: Misorientation maps of isothermal experiment samples	38
Figure 3-7: KAM maps of isothermal experiment samples	39
Figure 3-8: Variations of Mean Grain area (blue), Shape Factor (pink) and GOS (green) for each step cooled experiment investigated with EBSD	40
Figure 3-9: EBSD maps of olivine single subhedral and euhedral grains	41
Figure 3-10: Grain Orientation Spread (GOS) versus Shape Factor (grain tortuosity).....	42
Figure 3-11: Plots of measured X_{Mg} in olivine as a function of distance in millimeter.....	44
Figure 3-12: Plots of measured XMg in olivine as function of NiO (in wt%).....	45
Figure 3-13: Rim-to-core X_{Mg} profiles across four olivines.....	46
Figure 3-14: Plots of measured X_{Ca} and X_{Mg} in glass as a function of distance.....	48
Figure 3-15: Plots of measured SiO_2 and CaO in glass as a function of distance	49
Figure 3-16: Plots of measured Al_2O_3 and TiO_2 in glass as a function of distance	49
Figure 3-17: Microstructural sketch for the olivine reactive dissolution and crystallization, and olivine-rich troctolite formation along our experiments	53

Figure 3-18: Part of the total alkalis versus silica diagram for glasses from the olivine rich layer	58
Figure 3-19: Fe-Mg partitioning between melt and olivine for selected experiments conducted with melt AH6	59
Figure 3-20: Fe-Mg partitioning between melt and olivine for selected experiments as a chemical vs. textural focused study	60
Figure 4-1: Temperature and time history of the three dissolution experiments reported in this study	62
Figure 4-2: Representative BSE images illustrating the textures of the olivine-rich layer with different starting melts.....	64
Figure 4-3: Phase repartition within the olivine-rich layer of experimental charges from selected runs.	65
Figure 4-4: EBSD maps of the olivine-rich layer of OM02 and OM20.....	70-71
Figure 4-5: Misorientation maps and Kernel average misorientations maps for olivine single grains from OM02 and OM20	72
Figure 4-6: Shape factor versus Grain orientation spread for 60 selected grains (euhedral and subhedral) from OM02 and OM20 experiments	72
Figure 4-7: TEM micrographs from OM02 thin section	74
Figure 4-8: Plots of measured X_{Mg} and nickel abundance in olivine as a function of distance	77
Figure 4-9: Composition of plagioclase from the olivine-rich layer.....	79
Figure 4-10: Composition of clinopyroxene from the olivine-rich layer	81
Figure 4-11: Variations of X_{An} vs. Al_2O_3 in plagioclase	84
Figure 4-12: Variations of a) TiO_2 and b) Jadeite (Jd) vs X_{Mg} in clinopyroxene from the olivine-rich layer of each step-cooled experiment	87
Figure 4-13: Variation of a) X_{Mg} versus NiO content in olivine and b) X_{Mg} in olivine vs anorthite content in plagioclase	88
Figure 5-1: EBS and EBSD images of sintered dunite used as starting material for dunite infiltrations experiments	96
Figure 5-2: Representative BSE images illustrating the geometry and texture of three experiments	100
Figure 5-3: Representative BSE image from MDI-02 melt layer	101
Figure 5-4: Representative BSE image from MDI-02 interface	101
Figure 5-5: Representative X-ray chemical maps of porous melt flow in MDI-01.....	101
Figure 5-6: Olivine and melt X_{Mg} variation as function of distance within experiments MDI-01 and MDI-	

03	102
Figure 5-7: TEM micrographs from MDI-01 thin section at 10k to 12k X magnification in three different zones around hole.....	104	
Figure 5-8: TEM micrographs from MDI-01	105	
Figure 5-9: Olivine crystal compositional transect	105	
Appendix 3-1: OM26 sample observed at microscope under reflected light	111	
Appendix 3-2: Color combination chemical map of OM26 sample	111	
Appendix 3-3: EBS image of OM10.....	112	
Appendix 4-1: Clinopyroxene and plagioclase misorientation maps for OM02 and OM20	113	

Research Aim

Studies on oceanic lithosphere suggest that melt-rock reactions play a key role in the origin of olivine-rich troctolites. We performed reactive dissolution and crystallization experiments in a piston-cylinder in order to provide experimental constraints on the formation of olivine-rich troctolites at the mantle-crust transition zone through melt-rock reaction. Experimental charges consist of three-layers samples made by: (1) basalt glass powder, (2) powder of San Carlos olivine (Fo_{90}) mixed with 9% of basalt, and (3) melt trap. We used 3 synthetic MORB-type glasses ($X_{\text{Mg}} = \text{Mg}/(\text{Mg}+\text{Fe}) = 0.74, 0.62 \text{ and } 0.58$). Experiments have been conducted at 0.5 and 0.7 GPa, following an isobaric step-cooled temperature path from 1300 to 1150 °C, to induce reactive dissolution of olivine and in-situ crystallization of interstitial phases from the reacted melt. Time-solved isothermal time-solved experiments have also been performed at 0.5 and 0.7 GPa and 1200 to 1300 °C for various durations from 20 minutes to 60 hrs. The effect of pressure, melt composition and time on melt-rock reaction have been evaluated by textural observations, phase abundance and mineral chemistry. Moreover, dunite infiltration experiments with a dissolution couple made of sintered dunite rod and basalt powder at 0.7 GPa and 1150 to 1250 °C have been also performed, with the aim of evaluating melt transport properties within dunite matrix.

Step-cooled experiments show a layered lithological sequence from olivine-gabbro, to olivine-rich troctolite or dunite. In troctolite and dunite, plagioclase and clinopyroxene poikiloblasts include small rounded olivines but also euhedral to subhedral embayed olivines: evidences of disequilibrium and dissolution. Vermicular glass remains as interstitial phases within the troctolite. Isothermal experiments consist of olivine and glass with olivine habits similar to those observed in step-cooled runs. A textural homogenization is observed as function of run duration, driven by a more regular repartition of grain size and shape testified by recrystallized “smooth” and large subhedral olivine with curvilinear to euhedral grain boundaries.

Mineral chemistry significantly varies within the olivine-rich layer along the experimental charge. Olivine ranges from Fo_{82} at the olivine-gabbro/troctolite interface to Fo_{90} in the troctolite layer. Clinopyroxene X_{Mg} increases from 0.63 to 0.90. Plagioclase composition varies from An_{50} to An_{75} , and it tends to increase going far from the interface. As expected, large anorthite variations are coupled with rather constant forsterite values, deviating from fractional crystallization paths. In isothermal experiments, olivine ranges from Fo_{86} to Fo_{90} along the olivine-rich layer. Melt compositions vary as function of starting material and run duration. Run duration favors the extent of melt-rock reaction, leading to a chemical homogenization of reacted melts and olivine compositions. Only slow diffuser elements, such as Al and Ti still remain highly heterogeneous in the reacted melt.

In the troctolite, higher abundances of interstitial phases are observed at lower pressure suggesting higher extent of olivine dissolution. At higher pressure, early crystallization of

interstitial reacted melts, due to stability of clinopyroxene and plagioclase at higher temperature, inhibits the reaction.

TEM and EPMA investigations on dunite infiltrations highlighted that melt percolation occurs by the dissolution of olivine at grain boundaries. Melt percolates along planar crystalline surfaces with straight contacts such as “layers”, dissolves olivine creating lobate rims. Olivine dissolution and recrystallization by the reactive melt is localized at the dunite-melt reservoir boundary where olivine varies from Fo₇₅ to Fo₉₀.

Experiments are texturally and chemically comparable with olivine-rich troctolites from natural study cases, supporting their origin by melt-olivine reaction.

Chapter 1. Objectives and Background

1.1. The role of melt-rock reactions in the origin of troctolites at mantle-crust transition at oceanic lithosphere extensional settings

Olivine-rich troctolites are diffuse in oceanic ridge environments (e.g. Lissenberg and Dick, 2008; Godard et al., 2009; Drouin et al., 2009; 2010; Sanfilippo et al., 2013, 2015, and references therein), and in ophiolitic sequences (e.g. Borghini et al., 2007; Sanfilippo and Tribuzio, 2013; Sanfilippo et al., 2014). Textural, microstructural and geochemical characteristics of some olivine-rich troctolites are consistent with melt-rock reaction processes at the mantle-crust transition zone (MTZ, Coleman, 1977; Kelemen 1991), rather than originated by fractional crystallization from a primitive MORB (Drouin et al., 2009, 2010; Sanfilippo and Tribuzio, 2013a,b; Sanfilippo et al., 2015; Rampone et al., 2016). They are indeed interpreted as the result of reactive MORB-type melt percolation by dissolution and reactive crystallization within an olivine-rich matrix (Drouin et al., 2009, 2010; Sanfilippo et al., 2015). Olivine chadacrysts with rounded to subhedral habit and curviplanar boundaries embedded into large poikilitic crystals of clinopyroxene and plagioclase constitute a textural evidence of disequilibrium between olivine matrix and crystallizing melts, during solidification of the olivine-rich troctolites (Borghini et al., 2007; Drouin et al., 2009; Sanfilippo and Tribuzio, 2013a,b; Sanfilippo et al., 2013; Dygert et al., 2016). They are thought to result from partial corrosion of preexistent subhedral olivine and simultaneous crystallization of plagioclase and clinopyroxene from a reacted melt (Drouin et al., 2009). High X_{Mg} ($X_{Mg} = Mg/(Mg+Fe)$) and Cr_2O_3

content in clinopyroxene oikocrysts, the correlation of X_{Mg} in clinopyroxene with X_{An} in plagioclase (from 0.69 to 0.82) suggest that interstitial phases crystallized from a MORB-type melt buffered by the surrounding olivine (Borghini et al., 2007; Borghini and Rampone 2007; Drouin et al., 2009). As well, trace element compositions in clinopyroxene exhibit negative Eu anomalies when plagioclase displays strong positive Eu anomalies suggesting that plagioclase and clinopyroxene could have precipitated concomitantly from a chemically buffered reservoir (Drouin et al., 2009). Furthermore, trace element concentrations in olivine from Atlantis Massif suggest that olivine is not in equilibrium with MORB but with a highly fractionated depleted melt, and this has been used to infer its mantle origin (Drouin et al., 2009).

At a microstructural scale, olivines from troctolites of the Atlantis Massif show dislocation creep and a preferred orientation unusual in mantle peridotites, interpreted as the result of melt impregnation (Drouin et al., 2010). Melt-rock origin implies a multi stage process (e.g. Drouin et al., 2010; Sanfilippo et al., 2013). The first stage involves the genesis of the dunite. Mantle dunite is inferred to have formed by melt-rock interaction between olivine-saturated melts and mantle peridotite (harzburgite/lherzolite). In this context, the origin of “replacive” dunites is driven by pyroxene preferential dissolution and new olivine recrystallization from reacted melts (Dick, 1977; Quick, 1981; Kelemen et al., 1990; 1995; Suhr, 1999, Daines and Kohlstedt, 1994; Morgan and Liang, 2003, 2005; Drouin et al., 2010; Sanfilippo and Tribuzio, 2013a). A second stage involves the impregnation of dunite by percolating MORB-type melt leading to olivine dissolution and plagioclase and clinopyroxene crystallization (Drouin et al., 2009, 2010; Sanfilippo and Tribuzio, 2013). A third stage concerns the enrichment in incompatible lithophile elements related to the progressive closure of the melt percolation system within a crystalline matrix. This process has been well described in layered intrusions (see Barnes, 1986; Meyer et al., 1989; Ross and Elthon, 1997; Chalokwu and Grant, 1990; Bedard, 1994; Cawthorn, 1996; Gillis and Meyer, 2001; Charlier et al., 2005 and Bernstein, 2006) and ophiolitic cumulates (Tribuzio et al., 1999, 2000; Borghini and Rampone, 2007), and usually called “trapped melt effect”.

1.2. State of the art of experimental strategies to investigate melt-rock interactions

Several experimental studies have been carried out on melt-peridotite reaction processes inferred to act at the upper mantle-crust transition zone. Pilot experimental works by Daines and Kohlstedt (1994) and Morgan and Liang (2003, 2005) contributed to the understanding of dunite formation by reactive dissolution-reprecipitation processes. They performed layered experiments using sintered peridotite and melt layer and obtained porous melt flow and finger-like infiltration of basalt within peridotite driven by orthopyroxene and clinopyroxene dissolution and olivine crystallization. Following studies by Lambert et al. (2008) and Van den Bleeken et al. (2010, 2011) focused on melt transport in the upper mantle. Lambert et al. (2008) carried out adiabatic decompression experiments on focused magma transport into highly permeable channels showing a genetic relationship between focused magma transport, dunite bodies of the upper mantle and the generation of primitive MORBs. Van den Bleeken et al. (2010, 2011) performed melt percolation and crystallization experiments, with a primitive melt overlain by a powdered peridotite layer and a layer of vitreous carbon spheres under isothermal and isobaric conditions. Experiments resulted in partial melting of the peridotite and melt fractionation. Using compositional and textural evidences they demonstrated that reaction between peridotite and the percolating melt occurs by a combination of dissolution-reprecipitation and solid state diffusion that lead to the formation of well equilibrated phases. More recently, Tursack and Liang (2012) and Saper and Liang (2014) performed basalt-peridotite interaction experiments focusing on reactive dissolution and in-situ recrystallization leading to the formation of plagioclase-bearing ultramafics. General outcomes of these studies concern the dependence of melt-rock reaction processes on intensive parameters like pressure, temperature, composition of the reacting melt and the starting composition of dissolving peridotite.

Dissolution by silicate melts of single crystals of olivine has been also studied experimentally and theoretically (Zhang et al., 1989; Chen and Zhang, 2008; Soulié et al., 2017). These studies show that olivine resorption in molten silicates is a very fast process. Chen and Zhang (2008) calculated a dissolution rate of olivine of $0.87 \text{ } \mu\text{m/min}$ (Fo_{90} olivine dissolved by a basaltic melt with 6 wt% MgO at $1250 \text{ } ^\circ\text{C}$ and 0.1 MPa). Pure forsterite dissolution by chondrule-like melts experiments at high-temperature (1450-1540 $^\circ\text{C}$) by Soulié

et al. (2017) gave dissolution rates from ~6 µm/min to ~22 µm/min. The extent of olivine dissolution and reacted melt composition depends on temperature, pressure, time, melt composition and viscosity and olivine grain size (Chen and Zhang, 2008). On this purpose we propose to evaluate the role of time, temperature and reactive melt composition through dunite-dissolution experiments.

1.3. Aims

Although melt-rock reaction processes have been invoked to explain peculiar textures and mineral chemistry in natural olivine-rich troctolites, reactive dunite dissolution and in-situ crystallization have not been yet experimentally investigated. By performing dunite reactive dissolution experiment we focus on the understanding of the two final stages of olivine-rich troctolite formation: (1) dunite impregnation by percolating MORB-type melt leading to olivine dissolution, plagioclase and clinopyroxene crystallization and (2) the trapped melt effect observed at the closure of the melt percolation system leading to enrichment in incompatible lithophile elements. We provide experimental constraints to the origin of olivine-rich troctolites by reactive dunite dissolution and in-situ crystallization experiments. We propose to evaluate the role of pressure, temperature, melt-composition and time on the origin of olivine-rich troctolites.

As non-intensive parameters, like grain size and interconnected porosity have been determined as critical factors for melt-rock reaction processes in the upper mantle (Daines and Kohlstedt, 1994), we used a melt-bearing dunite (with controlled grain size) as starting dunite juxtaposed to a melt layer following previously adopted experimental setups (Van den Bleeken et al., 2010, 2011; Tursack and Liang, 2012; Saper and Liang., 2014). Our experiments serve to examine melt-rock interaction that potentially occurs in oceanic spreading lithosphere at the MTZ, simulating reactive melt transport in dunite of the upper mantle and crystallization of reacted melt. Through three distinct experimental approaches, this dissertation aims to evaluate the role of pressure, time and basaltic melt composition on the lithologies resulting from dunite reactive dissolution and reactive crystallization processes, as well as, the development of textures and the evolution of the mineral chemistry.

The work is composed of four main parts:

Chapter 2 carefully reports all the details of experimental setups and analytical techniques used in this study.

Chapter 3 displays and discusses the results of isothermal, time-solved dunite dissolution recrystallization experiments. This chapter investigates the role of time (run duration) and reactive melt composition in the kinetics of dunite reactive dissolution, chemistry of reacted melt and development olivine dissolution textures.

Chapter 4 exposes results and discussion of dissolution and in-situ crystallization experiments. Specific aim is to provide constraints on the role of pressure and basaltic melt composition in the lithologies resulting from dissolution and reactive crystallization processes, as well as, the development of textures and the evolution of the mineral chemistry. The results are finally compared with natural occurrences.

Chapter 5 presents a project on dunite infiltrations experiments. Experiments consist in dunite reactive dissolution by using a sintered dunite-basalt layer dissolution couple. This part represents a future perspective aimed to combine the chemistry of melt-rock interactions to the physics of melt migration by reactive dissolution, exploring at the grain-scale the melt distribution and the wetting behavior at low melt fractions.

Chapter6 summarizes the most relevant conclusions of this study.

Chapter 2. Experimental and analytical techniques

We performed several olivine-MORB reactive dissolution experiments adopting two different setups taking inspiration by previous experimental studies dedicated to melt-rock interaction processes. The first one was the dunite infiltration setup, where a basalt layer is juxtaposed to a sintered dunite and overlain by carbon spheres in a graphite-lined molybdenum capsule (Fig. 2-1). The second experimental setup was the powder to powder (P2P) strategy: synthetic basaltic melt powder is overlain by a fine olivine powder layer (mixed with basalt powder) and a layer of vitreous carbon spheres (Fig. 2-2). This setup is mainly based on previous similar studies on peridotite dissolution and crystallization experiments (e.g. Tursack and Liang, 2012; Saper and Liang, 2014; Van den Bleeken et al., 2010; 2011). In order to improve melt migration through the olivine layer we used olivine mixed to the starting basaltic melt powder (9%), to simulate melt impregnated dunite (as Saper and Liang, 2014) and also to place vitreous carbon spheres (as Van den Bleeken et al. 2010). The three-layers experimental charge is contained in a graphite-lined platinum capsule (Fig. 2-1). Experiments were carried out at P-T conditions appropriate for the MTZ (i.e. 1150 °C to 1300 °C and 0.5 GPa and 0.7 GPa) in a single stage piston-cylinder apparatus at the Dipartimento di Scienze della Terra, University of Milano. In order to evaluate the importance of the melt trap, one experiment was conducted without the carbon spheres layer.

2.1. Starting Material

In order to investigate the role of melt composition, we used in the experiments three MORB-type synthetic glasses well known in terms of phase equilibria: two tholeiitic basalts AH6 ($X_{Mg} = 0.62$) and AH3 ($X_{Mg} = 58$) from Husen et al., (2016), and a primitive one HDRBC ($X_{Mg} = 0.74$) defined by Gillis et al. (2014) (Tab. 2-1 and Fig. 2-2). All the basaltic glasses were provided by the Institut für Mineralogie at Leibniz Universität of Hannover. The synthesis procedure of basaltic glasses AH6 and AH3 has been described by Husen et al. (2016). HDRBC basaltic glass powder has been prepared following this same procedure.

Starting melt compositions are reported in Table 2-1 and plotted together with Atlantic and Pacific Mid Oceanic Ridge Basalts (MORB) from the Pet Data Base in Figure 2-2.

Melts AH6 and AH3 represent glasses from Shatsky Rise (IODP expedition 324). AH6 represents the average composition of 15 olivine-hosted melt inclusions from phric basalts and AH3 is an analogue of the most MgO-rich natural glass recovered in the Ori Massif (Husen et al., 2016). They represent differently evolved basaltic melts, not in equilibrium with mantle olivine and therefore expected to react with San Carlos olivine. HDRBC is the Hess Deep Rift Bulk Composition (Gillis et al., 2014); its composition is closer to a MORB and is expected to be less reactive with San Carlos olivine. Indeed, consistently with a Kd_{Fe-Mg} of 0.31 (Toplis, 2005), San Carlos olivine (Fo_{90}) would be in equilibrium with a melt of $X_{Mg}=0.75$. All melt used in our experiments does not contain NiO (Tab. 2-1) and basalts AH3 and HDRBC are Cr-free. Main differences between the three basalts are in terms of X_{Mg} which increases from the most evolved melt to the most primitive, but also TiO_2 which is significantly higher in AH3 (Tab. 2.1), and Al_2O_3 lower in AH3.

Olivine-rich layer consists of fine olivine powder, obtained from hand-picked San Carlos olivine natural grains. San Carlos olivine (Fo_{90}) is from mantle xenoliths from Arizona (Dohmen et al., 2007, Spandler and O'Neil, 2009). Purest grains were selected under binocular and then crushed two times 20 minutes under ethanol in an agate mortar, dried and sieved to grain sizes of 36-64 μm . The powder was dried at 600 °C for 1h in the horizontal oven and kept at 110 °C under vacuum in order to avoid any trace of water in the olivine. Selected and sieved starting olivine grains are represented in Figure 2-3 a, b, c, and their average composition is reported in Table 1. To prepare the basalt-olivine mixture, olivine

powder has been mixed with 9% of basaltic melt powder in an agate mortar and then stored at 110 °C under vacuum. Observations by Electron Microprobe (EMP) and Electron Back Scattered Diffusion (EBSD) (Figure 2-3 a, b, c) highlighted that starting San Carlos olivine is chemically homogeneous and does not present many misorientations.

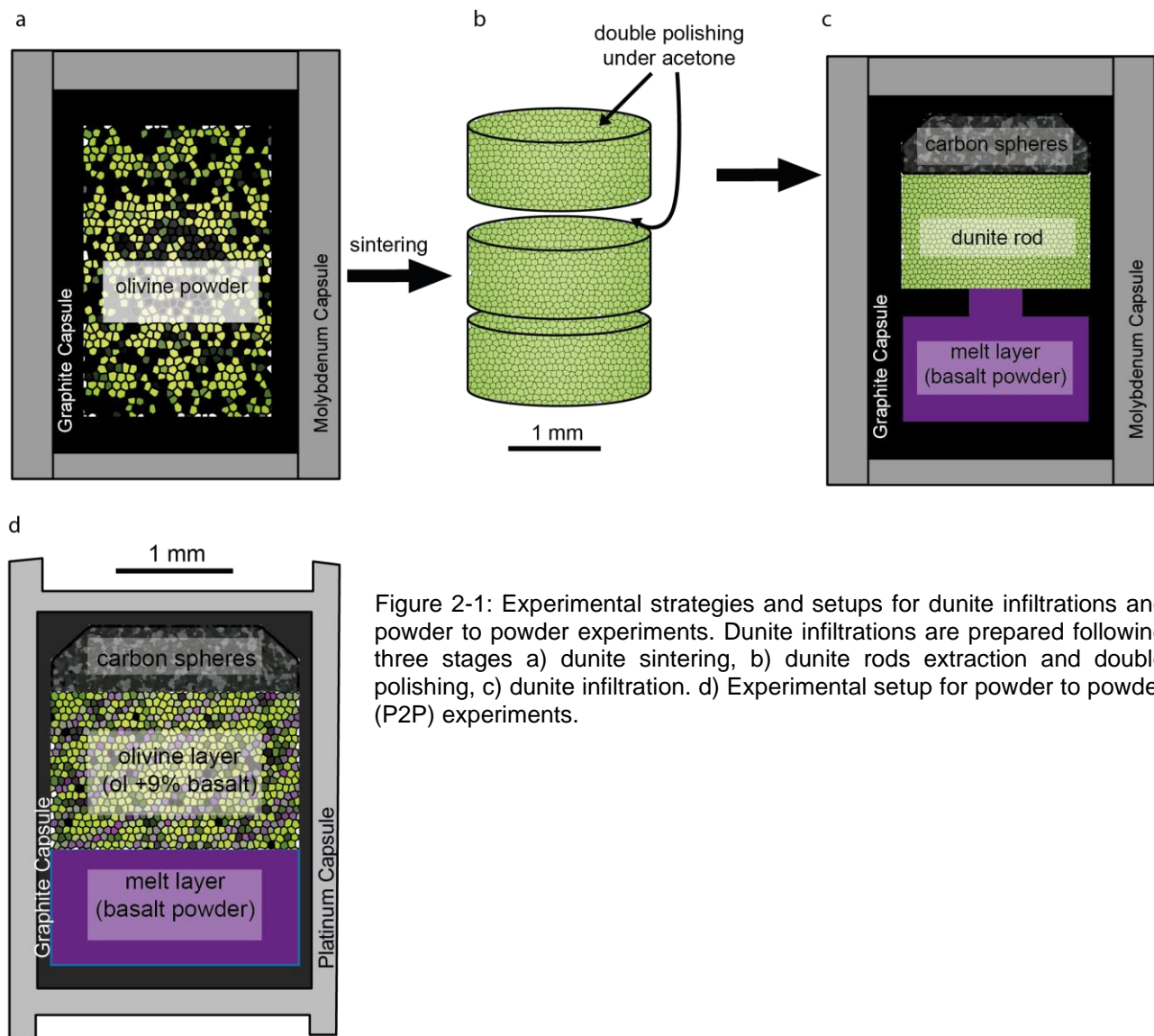


Figure 2-1: Experimental strategies and setups for dunite infiltrations and powder to powder experiments. Dunite infiltrations are prepared following three stages a) dunite sintering, b) dunite rods extraction and double polishing, c) dunite infiltration. d) Experimental setup for powder to powder (P2P) experiments.

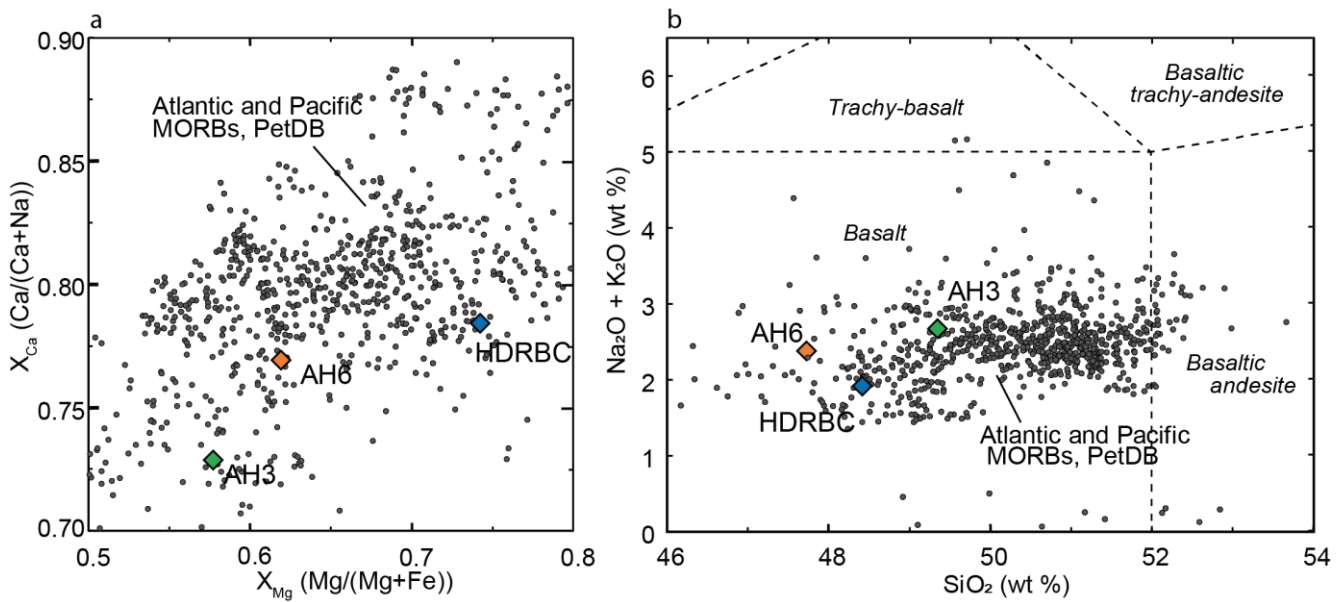


Figure 2-2: Comparison between compositions of starting synthetic basalt powders (AH3, AH6 and HDRBC) and Atlantic and Pacific MORBs from the Pet Data Base in (a) $X_{\text{Mg}} = \text{Mg}/(\text{Mg}+\text{Fe})$ vs $X_{\text{Ca}} = \text{Ca}/(\text{Ca}+\text{Na})$, and (b) TAS (Total alkaline vs Silica) diagrams.

Table 2-1: Representative major element compositions of experimental starting material

Sample	San Carlos Olivine		AH6 ¹	AH3 ¹	HDRBC ²
	(n=17) ³	Average	SD ⁴		
SiO_2	40.54	0.72	47.70	49.33	48.25
TiO_2	0.00	0.00	0.89	1.45	0.83
Al_2O_3	0.01	0.02	16.76	15.67	16.57
Cr_2O_3	0.04	0.06	0.09	0.00	0.00
FeO	8.85	0.62	9.51	10.49	7.68
MnO	0.12	0.08	0.19	0.17	0.14
NiO	0.37	0.09	0.00	0.00	0.00
MgO	49.16	0.75	8.62	8.00	12.37
CaO	0.07	0.04	13.80	12.18	11.90
Na_2O	0.01	0.03	2.28	2.49	1.80
K_2O	0.00	0.01	0.10	0.18	0.11
Total	99.16	1.09	99.94	100.20	99.65
X_{Mg}^5	0.90	-	0.62	0.58	0.74
X_{Ca}^6	-	-	0.77	0.73	0.79

¹from Husen et al. (2016), ²from Gillis et al. (2014), ³n: number of analysis,

⁴SD: Standard deviation ($1(\sigma)$), ⁵ $X_{\text{Mg}} = \text{Mg}/(\text{Mg}+\text{Fe})$, ⁶ $X_{\text{Ca}} = \text{Ca}/(\text{Ca}+\text{Na})$

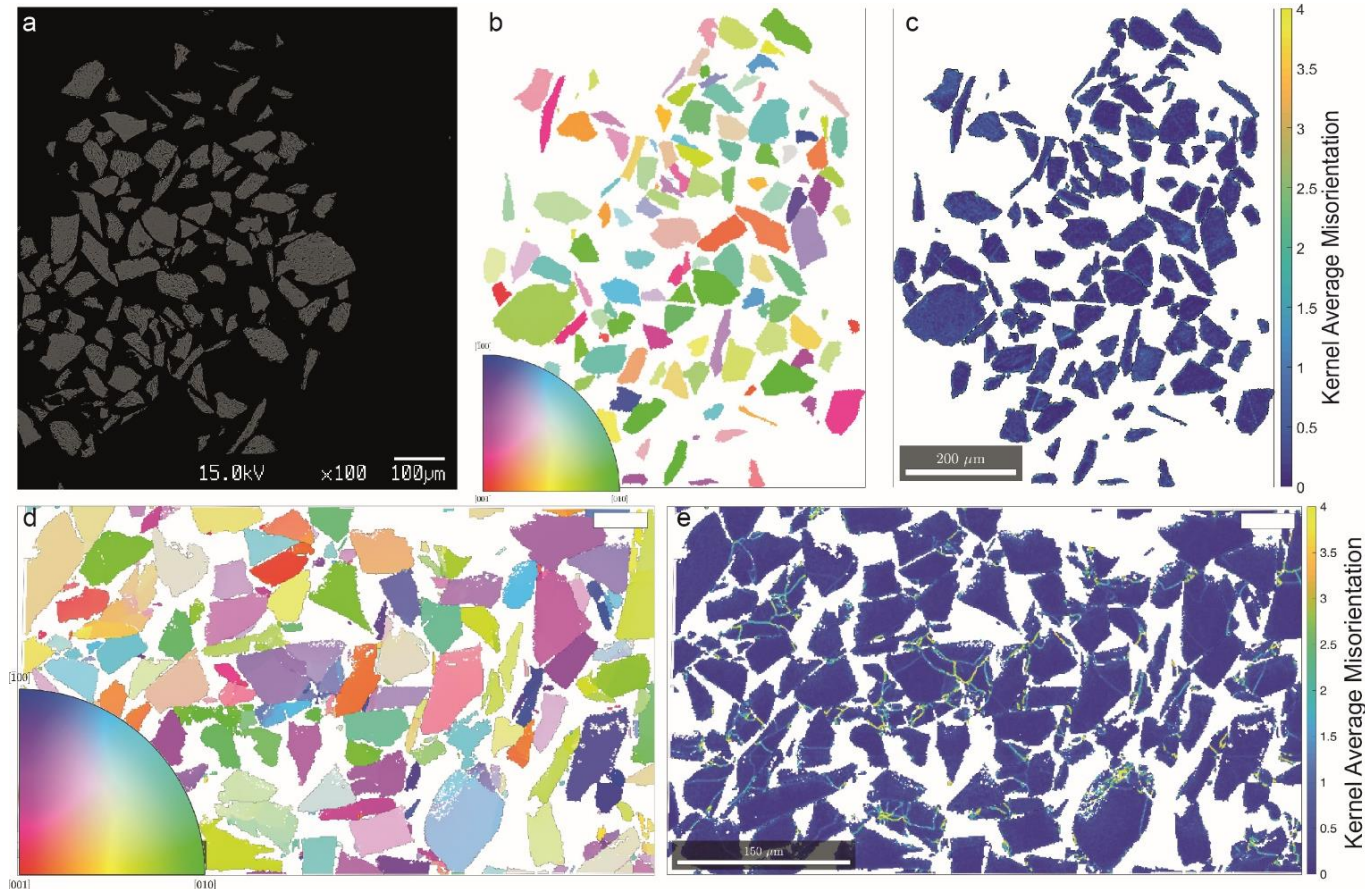


Figure 2-3: Pictures of San Carlos olivine used as starting material. First we illustrated the grinded and sieves San Carlos olivine, chosen as starting material, by a) Backscattered electron (BSE) image, b) Orientation map with an inverse pole figure (IPF) colored scale and c) Crystal Average Misorientations (KAM) map, highlighting subgrain boundaries within the grains. San Carlos olivine grains which experimented 0,5 GPa (400 °C) for 10 minutes (OM26) represented in d) IPF orientation map and e) KAM map.

2.2. Experimental procedure

2.2.1. Pre-sintered dunite – Basalt dissolution experiments

We model dunite reactive dissolution by using a sintered dunite-basalt layer dissolution couple. Five dunite infiltration experiments were performed at 0.7 GPa, 1150 °C–1250 °C. Five dunite-infiltration experiments have been performed in a single stage piston cylinder at 0.7GPa, with a progressively evolving experimental strategy in order to enhance the melt percolation through the pre-sintered dunite rods. Three experiments have been conducted at temperatures of 1250 °C and 1200 °C at 0.7 and 0.5 GPa, for different run durations (from 48 to 120 hrs.). Only one experiment was conducted following step-cooled procedure described thereafter. Full experimental procedure is presented in Chapter 5.

2.2.2. Powder to powder reactive dissolution-crystallization

Layers of i) basaltic powder, ii) olivine (+ 9% melt) powder and iii) carbon spheres were loaded into a graphite container (2.7mm OD, 2mm ID) that was closed with a graphite lid (Fig. 2-1c). The amount of glass powder added to the olivine layer is similar to that adopted by Saper and Liang (2014) (12%), and it enhanced the porosity of olivine matrix during the first high-t step of experiments. A rock/melt ratio of 0.7 was kept fixed, assumed to be reasonable to maintain an endless melt reservoir. The graphite container was placed in a Pt capsule (3 mm OD, 2.8 mm ID) that was welded (Fig. 2-1d). Salt-Pyrex-MgO assemblies were employed and stored in an oven at 110 °C for 24 hours before being placed in the piston-cylinder apparatus. Temperature was measured with Pt-PtRh thermocouple (S-type) and monitored using a Eurotherm controller, thermocouples with estimated accuracy of ±1.5 °C. With this setup we performed two series of experiments, isothermal time-solved vs. step cooled, which will be described in the following Chapters 3 and 4, respectively.

2.3. Sample Preparation

Capsules have been cut longitudinally with diamond saw, the two half of capsules impregnated with a drop of Epoxy resin and placed under vacuum for some seconds in order to induce sample impregnation by the resin. Resulting samples have been finally embedded in Epoxy. After solidification of the resin, the samples are hand-polished using silicon carbide grinding paper from P600 to P4000 and then ¼ µm diamond paste.

2.4. Analytical techniques

2.4.1. Microprobe analysis

Chemical analysis, backscattered electron (BSE) images and X-ray chemical maps were obtained using JEOL 8200 Super Probe at Dipartimento di Scienze della Terra, University of Milano (Italy). Accelerating voltage of 15 kV was applied for all analysis. All phases were measured with a beam current of 20 nA and 1 µm beam size. As glass portions are often smaller than 5 µm, most of glass analysis have been performed with 1 µm beam to avoid any contamination; where it was possible some 5 and 10 µm beam analysis were performed and compared with 1 µm ones. Compositions of core and rims of selected mineral grains were analyzed, either mineral grains profiles.

2.4.2. Image analysis

We performed image analysis on X-ray chemical maps obtained with the electron microprobe in EDS and WDS to quantify phase abundances and, therefore, determine lithologies observed across run products. Chemical maps were combined in multispectral RGB images constituted of Calcium, Magnesium and Aluminum maps with IMAGEJ®. Then we proceeded to image supervised classification based on region of interested pre-selection with the software ENVI®. We defined 2 to 5 classes per sample, depending on the phases in presence: olivine, clinopyroxene, plagioclase, glass and graphite. The classification was based on the area selected (regions of interest) as representative of those classes. After classification, we generated a new image files with one color per class and calculated phase abundance statistics. Usually we run the classification procedure on selected zones of study, in order to avoid zones like the melt layer-olivine layer interface where phase proportions are different. Generally, the classification obtained critically depends on the choice of the pixels for the region of interest; therefore, we always compare the final classification image with original maps and EBS images in order to minimize errors.

2.4.3. EBSD analysis

We performed Electron Back Scattered Diffraction analysis on 10 samples, including 3 of starting material (Fig. 2-3), using the CamScan X500FE Crystal Probe facility at Géosciences Montpellier. We mapped olivine-rich zones of those samples with a step size of 0.6 or 1 µm. Precise phase abundances and crystal orientation maps were obtained. MTEX

(version 4.2.1), a free MatLab[©] toolbox (Hielscher and Schaeben, 2008; Bachmann et al., 2011; Mainprice et al., 2014; <http://mTEX-toolbox.github.io/>), and used for analysis and observation of crystallographic features (e.g. orientation maps, CPO, crystal shape and size analysis, misorientations and subgrain identification). Olivine and other phases (clinopyroxene and plagioclase) CPO, shape factor, area, tortuosity and crystallographic and textural parameters were measured by indexation of electron backscattered diffraction (EBSD) pattern using the CamScan X500FE Crystal Probe facility at Géosciences Montpellier on Olivine-rich layer of 8 samples. EBSD pattern are generated by interaction of a vertical incident electron beam with a high-quality polished samples in a CamScan CrystalProbe X500FE, SEM developed for EBSD analysis, with an electronic column tilted at 70 °C. The Crystal Probe was used at an accelerating voltage of 15 kV and step sizes of 0.6 and 1 µm. EBSD patterns were indexed automatically using the AZtec software from Oxford Instruments. Qualitative Energy Dispersive spectroscopy (EDS) element maps were acquired simultaneously to the EBSD maps using the X-MaxN 20-mm² EDS detector of the Crystal Probe. Non-indexed areas remain on EBSD maps; therefore post-acquisition data treatment was done using the Tango software of the Channel 5 suite (HKL Technology). Isolated non-indexed pixels as well as indexed pixels surrounded by pixels assigned to a different phase were removed. Non-indexed pixels that have a minimum of six neighboring pixels with almost equal orientations were given the average of those orientations. Crystallographic orientations and grain characteristics were analyzed and visualized using the MATLAB toolbox MTEX (version 4.3.1; <http://mTEX-toolbox.github.io>). Misorientation thresholds for specific angle from 2 to 15° were used during olivine subgrain and grain identification, respectively. Grains and subgrains smaller than 10 pixels were excluded.

Several parameters helpful for the understanding of olivine texture and phase abundance evolution as a function of time, were extracted from EBSD analysis. We provide some definitions of main observed parameters used in chapter 3 and 4. For more precisions, refer to Maitland and Sitzman (2007) and Mainprice et al. (2004). The tortuosity of each grain is given by the Shape Factor, SF= P/EP where P is the perimeter of a grain and EP is the equivalent perimeter. A higher shape factor is corresponding to a greater grain tortuosity. Crystal misorientations are given by Mis2Mean colored maps, where each pixel is colored as a function of the degree of its rotation with respect to the mean orientation of the grain. It enable to visualize inner grain dislocations, forming subcells. Subgrain boundaries can be

identified thanks to Kernel Average Misorientation (KAM) colored maps, where each pixel is colored as a function of the degree of orientation change with respect to his four neighbors, and concretely represent subgrain boundaries. The degree of misorientation of each crystal is given by the Grain Orientation Spread (GOS), which is a numerical parameter calculated from the mean misorientation inside single grain. Nine samples from isothermal time-solved experiments were analyzed with EBSD, three of starting material and six from time solved isothermal experiments.

2.4.4. Transmission Electron Microscopy analysis

As melt-rock interaction is expected to involve grain boundaries, subgrains distribution and diffusion an explorative Transmission Electron Microscope study has been carried out on selected experiments. A powder to powder experiment performed following a step-cooled procedure (OM02, 0.5 GPa, AH6 melt composition against impregnated dunite) and a dunite-melt infiltration experiment (MDI-01, 0.7 GPa, 1250 °C, AH6 melt composition against pre-sintered dunite) have been carefully prepared. A 300 µm slice has been obtained out of the epoxy impregnated experimental capsules using a fine circular diamond saw. TEM samples have been double-polished down to ~30 µm thickness at the Department of Earth and Environmental Sciences (DISAT) of Milano Bicocca University. In order to get an electron transparent region the samples were ion milled using a precision Ion Polishing system GATAN Model 691 at the Dipartimento di Scienze della Terra “Ardito Desio”, University of Milano. TEM analysis were performed using a JEOL 2010 at DSFTA, University of Siena (Italy). Both thin sections obtained from the experimental capsules are illustrated in Figure 2-4.

—

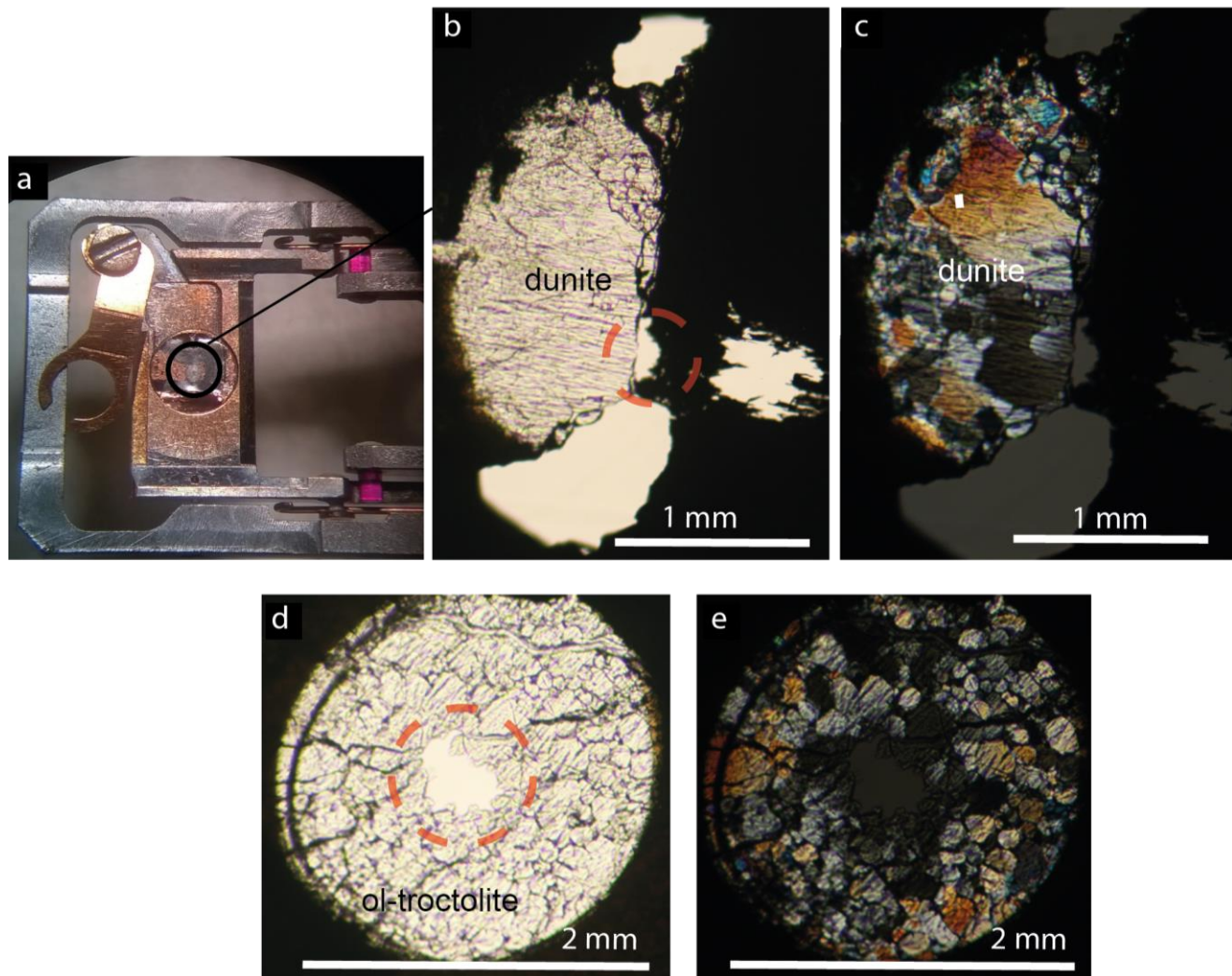


Figure 2-4: MDI-01 thin section prepared for TEM investigation. a: Thin section in the sample holder; b and c: Thin section PPL and XPL images of MDI-01; d and e: Thin section PPL and XPL images of OM02. The sample is thinner on the zone circled in red, TEM investigation can only be performed in this restrained zone.

Chapter 3. Olivine reactive dissolution as a function of run duration and melt composition

3.1. Experimental procedure

In order to evaluate the extent and kinetics of olivine dissolution by reaction with the melt and the evolution of reacted melt composition, we performed isothermal experiments at different pressures, temperatures and using three starting melts (HDRBC, AH6 and AH3). For isothermal experiments the powder to powder (P2P) setup has been used (see Chapter 2). The charge was firstly heated to 400 °C, then pressurized to 0.5 or 0.7 GPa before to reach to run temperature (1300 °C, 1250 or 1200 °C; see Tab. 3-1). In order to investigate the kinetics of olivine reactive dissolution-recrystallization, we performed isothermal experiments by varying run duration, from 20 minutes to 60 hours. At the end of the experiment, charge was quenched by shutting off the power supply. All experimental conditions of isothermal experiments are reported Table 3-1.

Most P2P experiments have been performed with a starting melt-rock ratio in the dunite matrix of 9% (see Chapter 2 for more details). Attempts to evaluate the effect of different melt-rock ratio have been also addressed performing experiments with a ratio of 0 and 15%. The experiment OM10 was performed with an initial melt-rock ratio of 0% (Tab. 3-1), but the initial geometry has been lost after experiments. In experiment OM19, 15% melt-

rock ratio in olivine-bearing starting layer has been adopted.

3.2. Results

Run conditions and results are reported in Table 3-1 and Figure 3-1. All the isothermal time solved experiments maintained the initial geometry of the experimental charge. Run results will be then described referring to the run products observed in the basalt layer and those in the impregnated San Carlos olivine layer.

At 1300 °C and 1250 °C the basalt layer results in a glass, while the impregnated olivine layer is composed of olivine + glass. The carbon spheres succeed to act as melt trap and indeed some melt has been recognized among them (Fig. 3-2 and Fig. 3-3). At temperature < 1250 °C the basalt layer at the bottom of charge is partially crystallized (see Tab. 3-1) while in the impregnated olivine clinopyroxene and plagioclase occur (Fig. 3-4). In the next section, we trace the evolution of melt composition as a result of interaction with the olivine matrix, by comparing the phase assemblages observed within the impregnated dunite layer with results of equilibrium crystallization experiments reported by Husen et al. (2016).

Table 3- 1: Experimental conditions and phase assemblages of isothermal time-solved experiments

Name	Pressure (GPa)	Starting Melt	Temperature (°C)	Time (hrs)	m/r ratio (%)	Run products*
						olivine-rich layer melt layer
<u>At 0.5 GPa</u>						
OM23	0.5	AH6	1300	0.5	9	ol(89)-gl(11) gl
OM24	0.5	AH6	1300	0.3	9	ol-gl gl
OM26	0.5	AH6	400	0.1	9	ol-gl gl
<u>At 0.7 GPa, AH6</u>						
OM07	0.7	AH6	1200	24	9	ol-gl-cpx-plag ol-gl-cpx-plag
OM12	0.7	AH6	1250	12	9	ol(95)-gl(5)-(cpx) gl
OM15	0.7	AH6	1250	24	9	ol(94)-gl(6) ol-gl
OM18	0.7	AH6	1250	60	9	ol(91)-gl(9) gl
OM19	0.7	AH6	1250	60	15	ol(90)-gl(10) gl
<u>At 0.7 GPa, AH3</u>						
OM08	0.7	AH3	1200	24	9	ol(91)-gl(4)-cpx(5) gl-cpx
OM09	0.7	AH3	1200	48	9	ol(92)-gl-cpx-plag ol-gl-cpx-plag
OM10	0.7	AH3	1200	48	0	ol-gl-cpx-plag ol-gl-cpx-plag
OM11	0.7	AH3	1250	12	9	ol(95)-gl(5)-(cpx) gl-plg-cpx
OM14	0.7	AH3	1250	24	9	ol(95)-gl-cpx-plag gl-plg-cpx
OM17	0.7	AH3	1250	60	9	ol-gl ol-gl
<u>At 0.7 GPa, HDRBC</u>						
OM13	0.7	HDRBC	1250	12	9	ol-gl-(cpx) gl-cpx
OM16	0.7	HDRBC	1250	24	9	ol(90)-gl-cpx(6)-plag(3) ol-gl-cpx-plag

ol: olivine; gl: glass; cpx: clinopyroxene; plag: plagioclase; melt/rock ratio refers to the starting basalt powder proportion inside the olivine layer. Starting melts AH6 and AH3 are from Husen et al. (2016) and HDRBC from Gillis et al. (2014). In parenthesis the phase abundances retrieved by image analysis are reported.

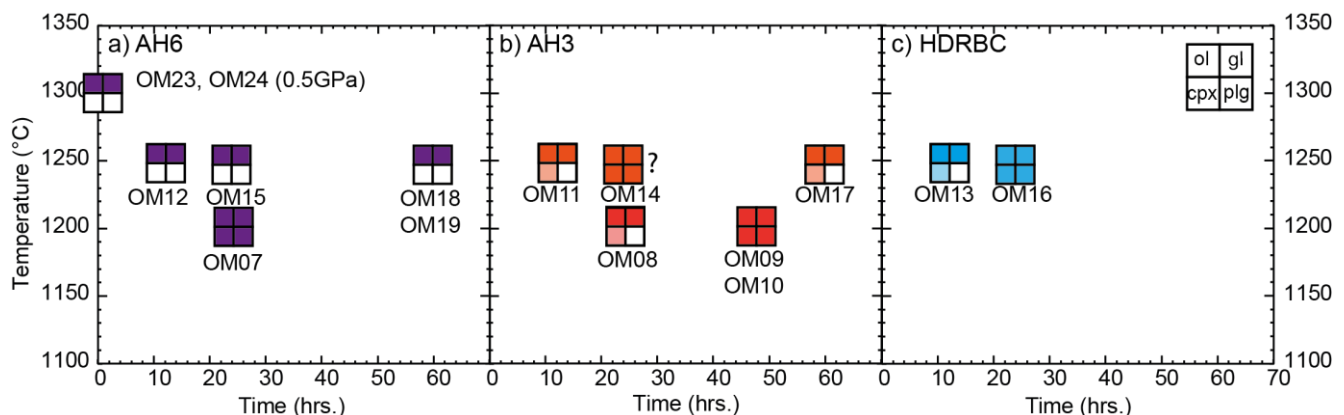


Figure 3-1: Temperature vs. experimental run duration diagrams showing the phase assemblages in the olivine-rich layer for the three starting basaltic melts (AH6 $X_{\text{Mg}}=0.62$, AH3 $X_{\text{Mg}}=0.58$ and HDRBC $X_{\text{Mg}}=0.74$). All experiments have been performed at 0.7 GPa except for the shortest run (20 minutes – OM24, 30 minutes – OM23) carried out at 0.5 GPa. Lighter colors mark the presence of the mineral phase as skeletal crystals assumed to be quenched phases.

3.2.1. Textures and phase abundances

A selection of BSE images illustrating the most representative texture in isothermal experiments are shown in Figures 3-2 and 3-3. All the experiments present similar textural features. Olivine occurs irregularly shaped, with lobate rims as evidence of resorbed grains. Rounded olivines and subhedral crystals also occur. Such textures suggest that olivine has been partially dissolved by reacting melt and recrystallized from reacted melt (Fig. 3-5).

Remarkably a time dependent textural evolution is observed. Figure 3-3 displays BSE images of experiments lasted 12, 24 and 60 hours, performed at 0.7 GPa and 1250 °C with the three starting melt compositions. In 12 and 24 hours experiments, olivine occurs both as coarse (~50-125 µm) and small crystals (~10 µm). Coarse olivines are irregularly shaped (polygonal to elongated) with crenulated to curvilinear grain boundaries. Cusped rims mark corrosion by the melt. Small olivines occur as small aggregates and some isolated grains, generally showing rounded to subhedral habit, resulting from larger grain disruption or recrystallization.

In 60 hours experiments, olivine crystal size is rather homogeneous; crystals are subhedral with smooth curvilinear and polygonal grain boundaries (Fig. 3-5). Therefore, the texture of the dunite matrix varies as a function of time, showing a development toward more homogeneous olivine grain size distribution and in crystal shape.

At lower pressure, in short duration experiments, the incipient first stage of olivine reactive dissolution is well observable (Fig. 3-2). Channels of melt of less than 1 µm of size are observed within large crystals that result to be split into smaller rounded or euhedral portion of grains (Fig. 3-5a, white arrows). Within large olivine grains, dissolution is initiated by penetrating melt following straight directions. An overgrowth facetting is visible on detached grains (Fig. 3-5a), as described by Boudier (1991) and Erdmann et al. (2014). By comparing Figure 3-2 b and c, we can observe an increase of the amount of small rounded grains as result of olivine disruption.

3.2.1.1. Phase abundances

Olivine-melt proportions within the impregnated dunite layer were evaluated by image analysis on X-ray chemical maps with ImageJ and ENVI software as described in Chapter 2.

(2.4.2.). Phase proportions calculated are reported in Table 3-1. Olivine-glass proportions are dependent on time. In experiments performed at 0.7 GPa, at 1250 °C using melt composition AH6 the glass abundance increases from 5 to 11% as run duration increases from 12 to 60 hours respectively. Similar results have been obtained using melt composition AH3, resulting in melt proportion of 5 and 11% at the same pressure, temperature and time conditions, suggesting that the melt compositions does not influence phase abundances. Proportions of melt versus olivine has been evaluated by both image analysis on X-Ray chemical maps and EBSD. The results provided by the two techniques are rather in agreement and display a difference of 1 to 2%.

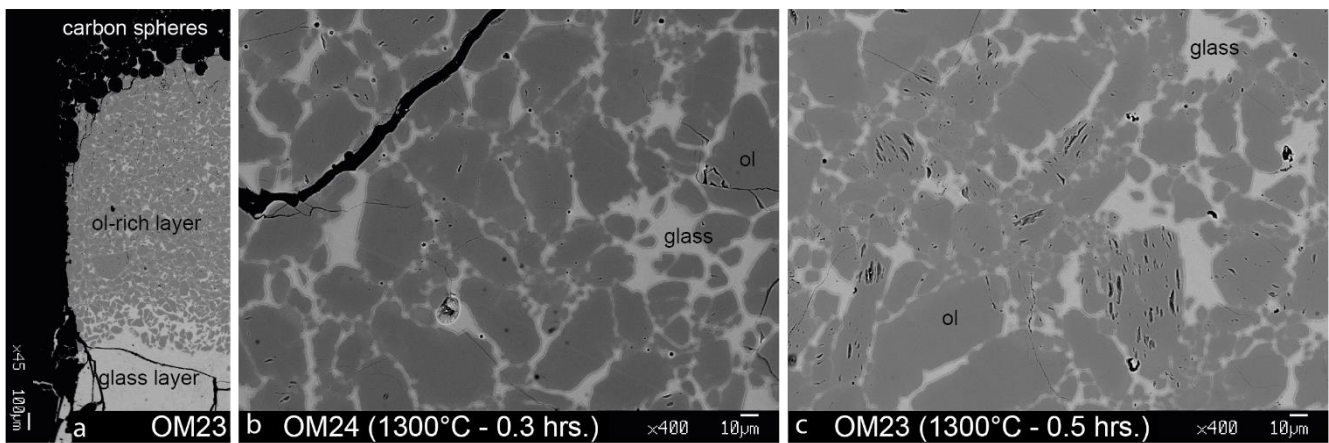


Figure 3-2: Representative Back-Scattered Electron (BSE) images from short duration isotermal experiments. a: Representation of the full capsule with the three layers: 1- the basal glass layer, 2-the olivine-rich layer and 3- the carbon spheres layer. b: Representative image of the olivine-rich layer from experiment OM24. c: Representative image of the olivine-rich layer from experiment OM23

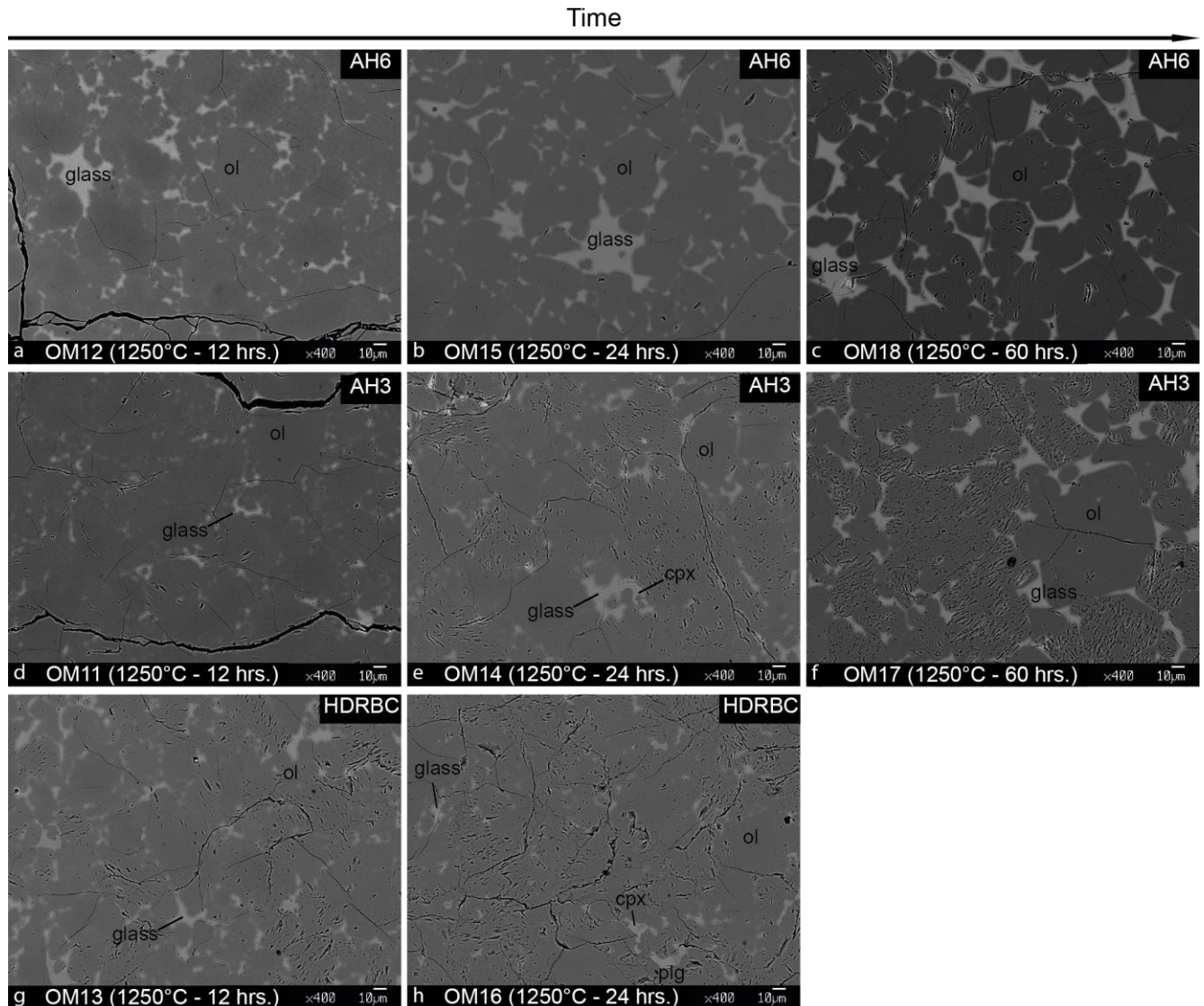


Figure 3.3: Representative BSE images from the olivine-rich layer of eight isothermal experiments conducted at 1250 °C with all three different starting melts AH6 ($X_{\text{Mg}}=0.62$), AH3 ($X_{\text{Mg}}=0.57$) and HDRBC ($X_{\text{Mg}}=0.74$) for three different durations: 12 hours (a, d, g), 24 hours (b, e, h) and 60 hours (c, f).

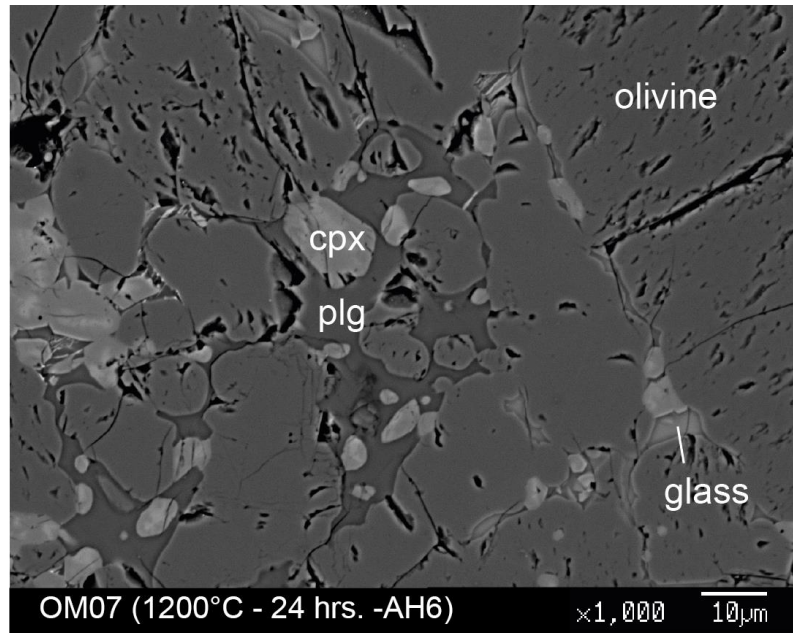


Figure 3-4: Representative BSE images from the olivine-rich layer of experiment OM07 conducted at 1200 °C for 24 hours with melt AH6. Olivine and clinopyroxene crystals are included in larger poikilitic plagioclase.

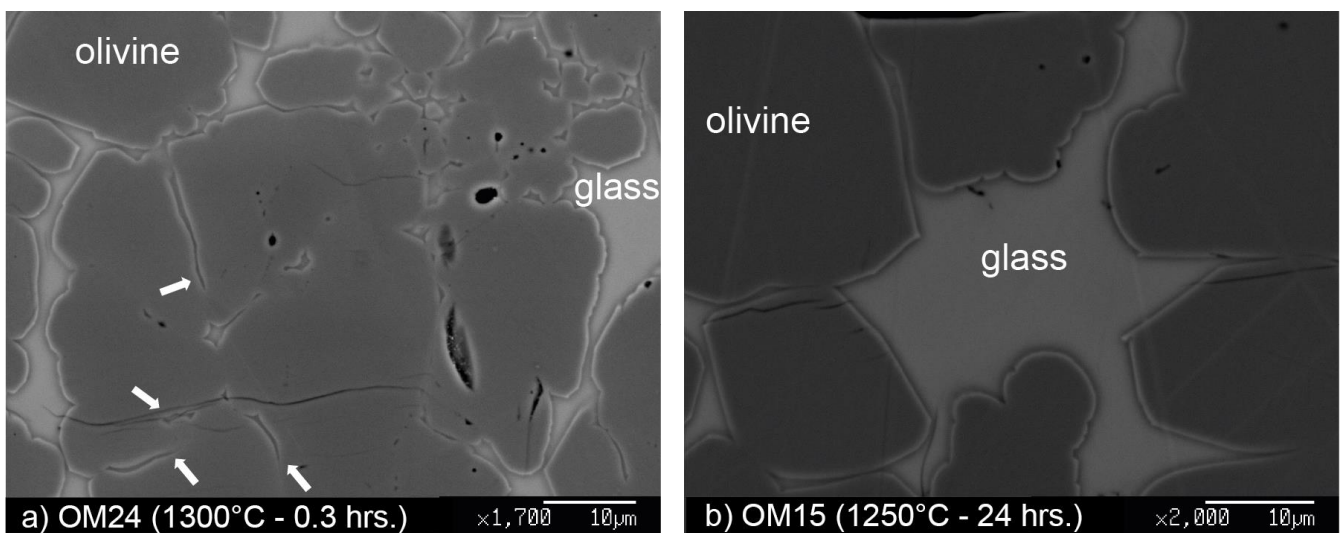


Figure 3-5: Representative BSE images from the olivine-rich layer of experiments OM24 and OM15. a) Channels of melt of less than 1 μm of size are observed within large crystals. b) Curvilinear to straight polygonal grain boundaries in olivine.

3.2.1.2. Results of EBSD analysis

Microstructures resulting from reactive dissolution-recrystallization process have been evaluated by Electron backscattered diffraction (EBSD) analysis at Géosciences Montpellier, with the acquisition parameters and data post treatments presented in Chapter 2 (section -IV-3). Both Figures 3-6 and 3-5 shows that shortest experiments OM23 (1300 °C-0.5 hrs-AH6), OM11 (1250 °C-12 hrs.-AH3) and OM12 (1250 °C-12 hrs.-AH6) have greater grain-size, and higher grain size heterogeneity than longer experiments OM18 (1250 °C-60 hrs.-AH6) and OM19 (1250 °C-60 hrs.-AH6(15%)).

The olivine-rich layer from 12 hours experiments OM11 (1250 °C-12 hrs-AH3) and OM12 (1250 °C-12 hrs-AH3) and the 24 hours experiment OM15 (1250 °C-24 hrs-AH6), can be assimilated as a porphyroclastic texture, with larger olivine crystals up to ~150 µm associated with aggregates of smaller olivine grains (<10 µm) (Fig. 3-6b and c). Coarse olivine grains are irregularly shaped, polygonal to elongated with crenulated to curvilinear grain boundaries (Fig. 3-9). The identification of separated olivine with EBSD analysis provides a better observation of olivine crystal shape. Indeed, observation by electron microprobe, previously presented, did not provide detailed information on crystal shapes because of the high density of olivine. Grains present evidences of resorption highlighted by cuspatate-shapes (Fig. 3-9). Small olivine grains occur as small aggregates and some isolated grains, generally rounded. These aggregates of olivine small grains generate a decrease of olivine average grain area from 30 minutes to 12 hours experiments (Fig. 3-6a and b). On another hand, in experiments of 60 hours OM18 (1250 °C-60 hrs-AH6) and OM19 (1250 °C-60 hrs-AH6(15 %)) olivine grains are more homogeneously shaped. Larger grains (100-150 µm) are subhedral with euhedral to cusped smooth grain boundaries (Fig. 3-6 d and f) and small grains rounded to euhedral.

Olivine grain size increases from 12 hours experiments to 60 hours one, as represented on Figure 3-8. OM12 (12hrs.) displays average grains size of 150 µm when OM18 (60 hrs.) is 890. This histogram (Figure 3-8) represents average grain area, grain orientation spread and grain tortuosity (per experiment) calculated with Matlab software. Therefore, from 0.5 to 60 hours experiments a constant decrease of olivine crystal misorientation GOS is observed (Fig. 3-8, in green), from 2 in OM23 (0.5 hrs.) to 0.6 in OM18 (60 hrs). The grain tortuosity, showed by the shape factor (Fig. 3-8, in pink) does not display

major differences. Internal orientations of olivine crystals also vary as a function of time. Figure 3-6 represents misorientation maps as a function of run duration and shows a decrease of the amount of misorientated crystals as time increases. In KAM maps (Fig. 3-7 a, b, c and d) a decrease of the amount of subgrains as run duration increases is observed. Intragranular misorientation and subgrain boundaries are generally present and abundant in subhedral crystals.

As observed by Boudier (1991), olivine grains present corrosion by the melt occurring in zone of higher subgrain boundaries density or along subgrain boundaries (Fig. 3-9). Figure 3-9a and b highlight that in general, numerous subgrain boundaries are observed in olivine subhedral porphyroclasts. Inversely, olivine euhedral porphyroclasts have less subgrain boundaries. Smaller grains do not present subgrain and seem to be the result of larger olivine grain disruption by reaction with the melt.

As we observed euhedral to subhedral grains, we also proceeded to a grain per grain study selecting 15 of the most euhedral olivine grains per sample and 15 of the most tortuous on which all previously mentioned crystallographic parameters were extracted from EBSD maps and presented in Figure 3-10. By studying selected grains (Fig. 3-9 and 3-10), we observed euhedral olivine crystals with a GOS value below 4 and euhedral olivine with a GOS value under 2 (OM23 excluded). Figure 3-10 displays grain tortuosity (shape factor) against grain orientation spread (GOS) for these selected olivine grains. The two populations euhedral and subhedral are strictly distinct and split in two clusters. Euhedral olivine crystals have a low tortuosity and a low GOS whereas subhedral olivine crystals present a high tortuosity coupled with a high GOS, as highlighted by the EBSD maps in Figure 3-7. An exception is visible for OM23, experiment of 30 minutes, where no real euhedral olivine has been found and selected “euhedral” olivines are less tortuous than subhedral one.

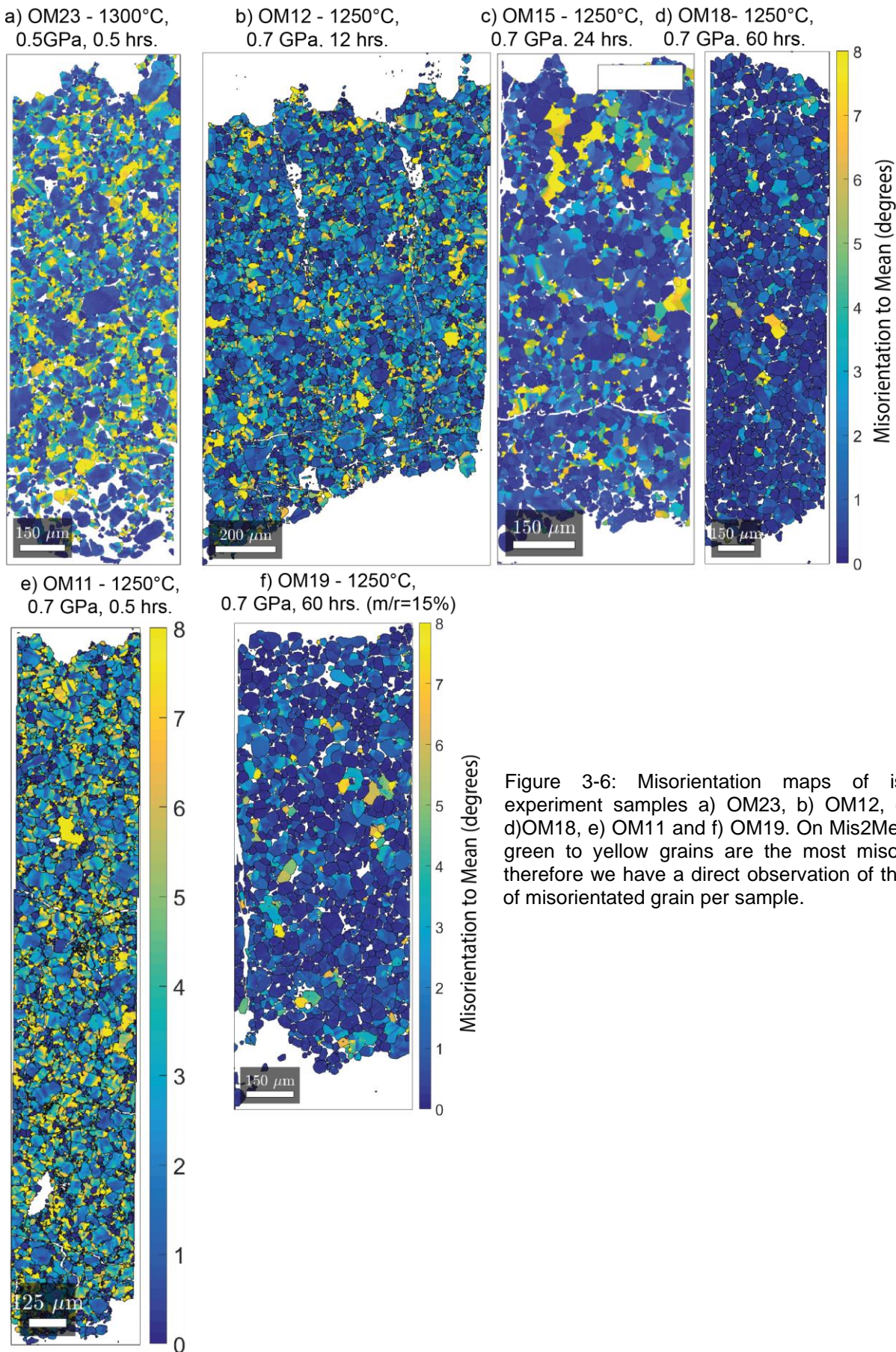


Figure 3-6: Misorientation maps of isothermal experiment samples a) OM23, b) OM12, c) OM15, d) OM18, e) OM11 and f) OM19. On Mis2Mean maps, green to yellow grains are the most misorientated, therefore we have a direct observation of the amount of misorientated grain per sample.

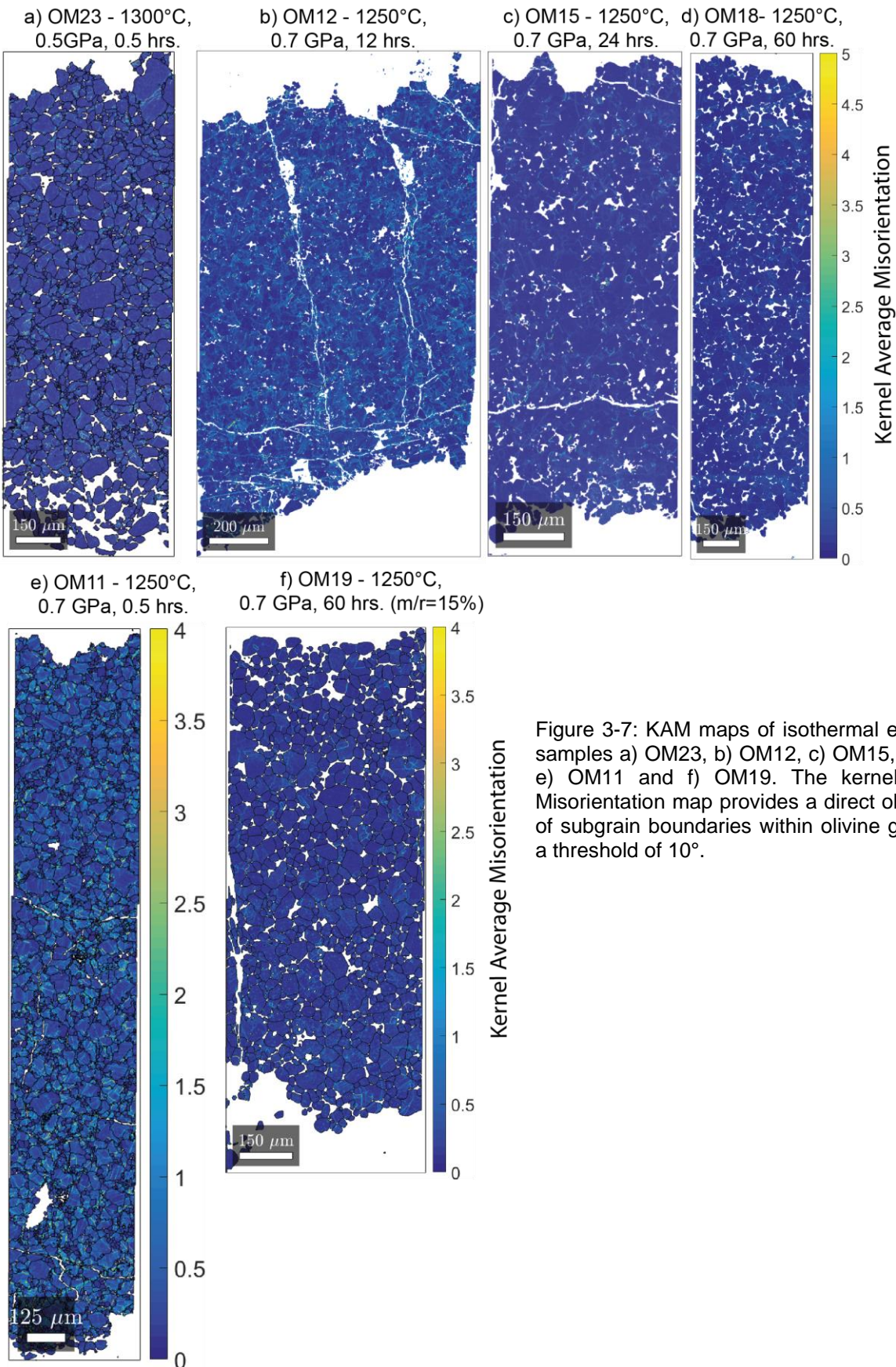


Figure 3-7: KAM maps of isothermal experiment samples a) OM23, b) OM12, c) OM15, d) OM18, e) OM11 and f) OM19. The kernel Average Misorientation map provides a direct observation of subgrain boundaries within olivine grains with a threshold of 10°.

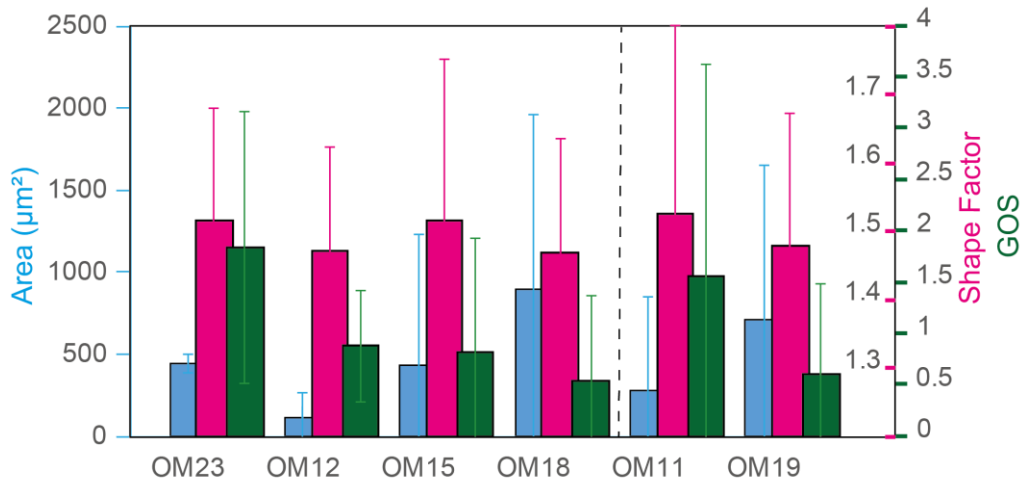


Figure 3-8: Variations of Mean Grain area (blue), Shape Factor (pink) and GOS (green) in olivines from step-cooled experiments studied by EBSD. The average is calculated with the Matlab software on all olivine grains of the olivine-rich layer. Error bars represent standard deviation. OM23, OM12, OM15 and OM18 are experiments performed with AH6 starting melt composition at increasing run duration from left to the right. OM11 has been carried out at the same conditions of OM18 (0.7 GPa, 1250 °C, 60 hours) but with a starting melt-olivine ratio of 15%. OM19 has been carried out at the same conditions of OM12 (0.7 GPa, 1200 °C, 12 hours) but using AH3 starting melt composition.

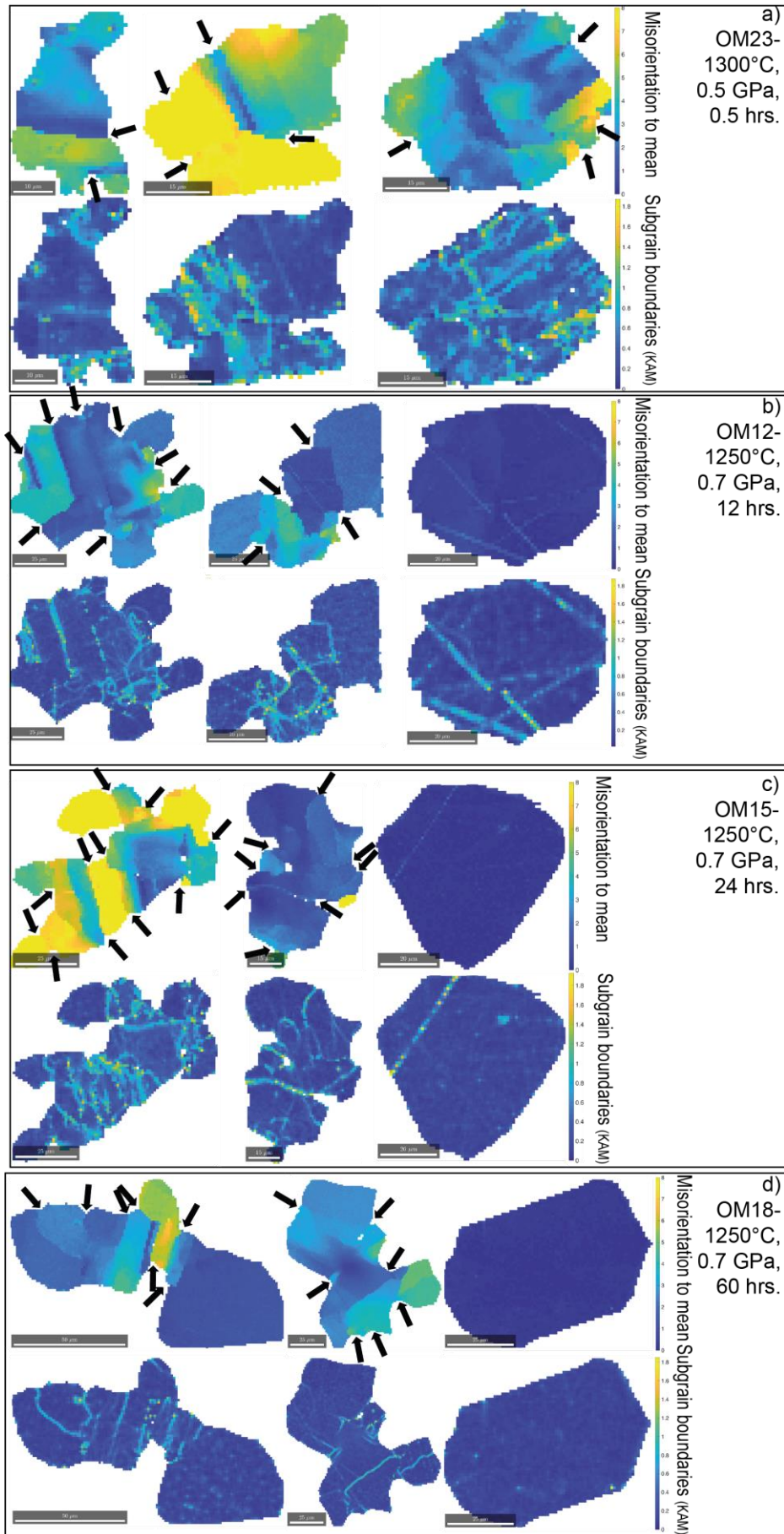


Figure 3-9: EBSD maps of olivine single subhedral and euhedral grains from experiments a) OM23, b) OM12, c) OM15 and d) OM18. Selected grain is represented by misorientation map (Mis2Mean) and KAM maps, highlighting subgrain boundaries with a threshold of 12°. Figures of resorption, large or pitch angles, are highlighted with black arrows on Mis2Mean maps. Resorptions follow subgrain boundaries, or occur in zones of high subgrains abundance. On euhedral grains represented (right) for b, c, and d, high values of KAM follow straight lines which are not corresponding to any orientation differences, highlighting an artefact due to polishing.

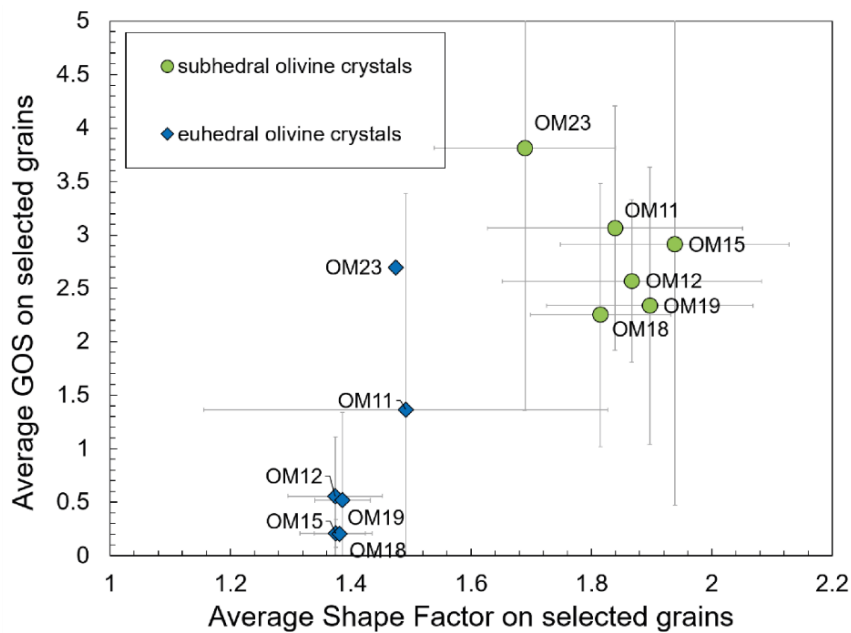


Figure 3-10: Grain Orientation Spread (GOS) versus Shape Factor (grain tortuosity) for 15 euhedral and 15 subhedral olivine crystals per sample for experiments OM23, OM11, OM12, OM15, OM18 and OM19. Error bars represent the standard deviation for the average calculated on 15 grains of olivine. The perfect split between the two clusters, euhedral and subhedral crystals is mainly due to the fact that each crystal is selected for its high regularity and irregularity respectively.

3.2.2. Mineral chemistry

Table 3-2 (in Appendix) reports the composition of olivine and glass analyzed in isothermal experiments. Composition of phases varies along the experimental charge, therefore, in the following diagrams we plotted chemical composition as function of distance d (in mm) is defined by $X_{\text{analysys}} - X_{\text{reference}}$, where X_{analysys} is the coordinate of a given analysis and $X_{\text{reference}}$ the coordinate of a reference analysis in the interface zone (generally the first olivine analyzed within the interface). X, Y, Z coordinates of each analysis are provided by the microprobe data output.

3.2.2.1. Olivine chemistry

Figure 3-11 displays compositional variations in olivine along the olivine-rich layer of 10 samples. Olivine compositions are spatially heterogeneous going from the interface (0 mm) to the top of the experimental charge (1.5 to 2 mm, depending on the sample). Closer to the interface, lowest X_{Mg} (~ 0.85) in olivine is observed. Along the olivine-rich layer, X_{Mg} in olivine increases and approaches original San Carlos composition (0.90). The largest

compositional variation is observed in OM15 (Fig. 3-11 b, pink squares), from 0.86 to 0.90. OM17, OM18 and OM19 (Fig. 3-11c) present only slighter variations from 0.87~0.89 to 0.90. Core to rim variations are observed mainly in experiments OM11, 12 and 13 and can be attributed to a run duration effect being these experiments the shortest ones at 0.7 GPa (12 hours). NiO in olivine also varies as a function of distance from 500 ppm to 3500 ppm (Fig. 3-12 a, b, c) with a maximum value in the center of the olivine-rich layer. We represented NiO versus X_{Mg} in olivine in Figure 3-12 d, e and f. Core to rim variations are present, with lower NiO in olivine rims. Lower NiO content is found in OM17, 18 and 19 and does not overpass 2500 ppm.

Figure 3-13 displays core-rim profiles across four olivine grains of comparable size (~60 μm), from two experiments performed with melt AH6 lasted 12 and 60 hours at the same PT conditions (OM12 and OM18). We analyzed olivines from the melt-olivine-rich layer interface and the olivine-rich layer. Both grains show Fe enrichment along their rims compared to their cores. The X_{Mg} rim-core zoning is more pronounced in the shortest experiment (OM12, 12 hrs) than in the longest one (OM18, 60 hrs). Additionally, in OM12, the X_{Mg} core-rim zoning is higher at the interface than in the olivine-rich layer. In OM18, profiles are almost flat, reflecting low core-rim compositional variation as observed in Figure 3-11 c.

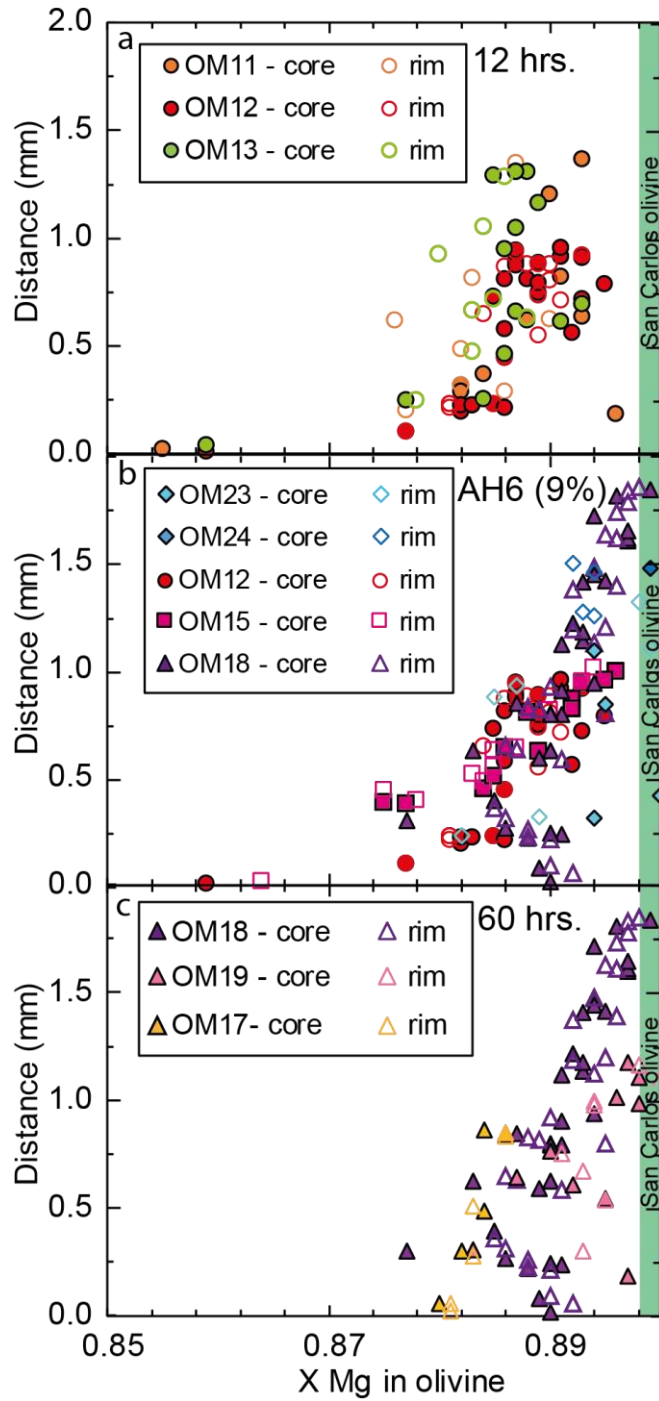


Figure 3-11: X_{Mg} in olivine as a function of distance (mm). Distance = 0 marks the approximate location of interface between glass layer and olivine-rich layer; a) olivine from experiments conducted for 12 hours at 0.7 GPa with AH3 (orange), AH6 (red), and HDRBC (green), b) olivine in all experiments conducted with melt AH6 at 0.5GPa (OM23 and OM24) and 0.7 GPa (OM12, OM15 and OM18) for various run durations, c) olivine in 60 hours experiments. Empty symbols are rim, full symbols are cores. The green line marks the composition of San Carlos olivine.

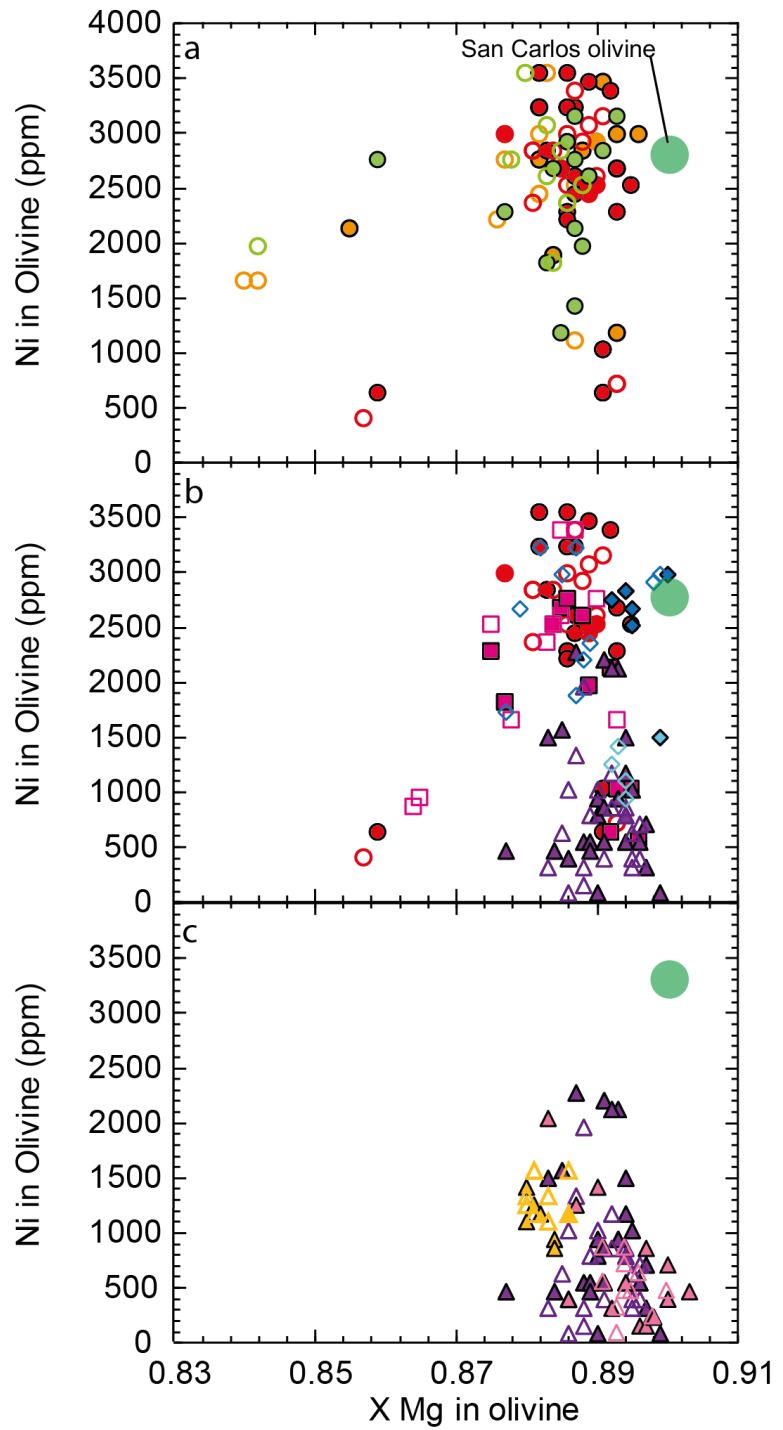


Figure 3-12: X_{Mg} versus NiO (in wt%) in olivine. Distance = 0 marks the approximate location of interface between glass layer and olivine-rich layer. for symbols and legend see figure 3-11.

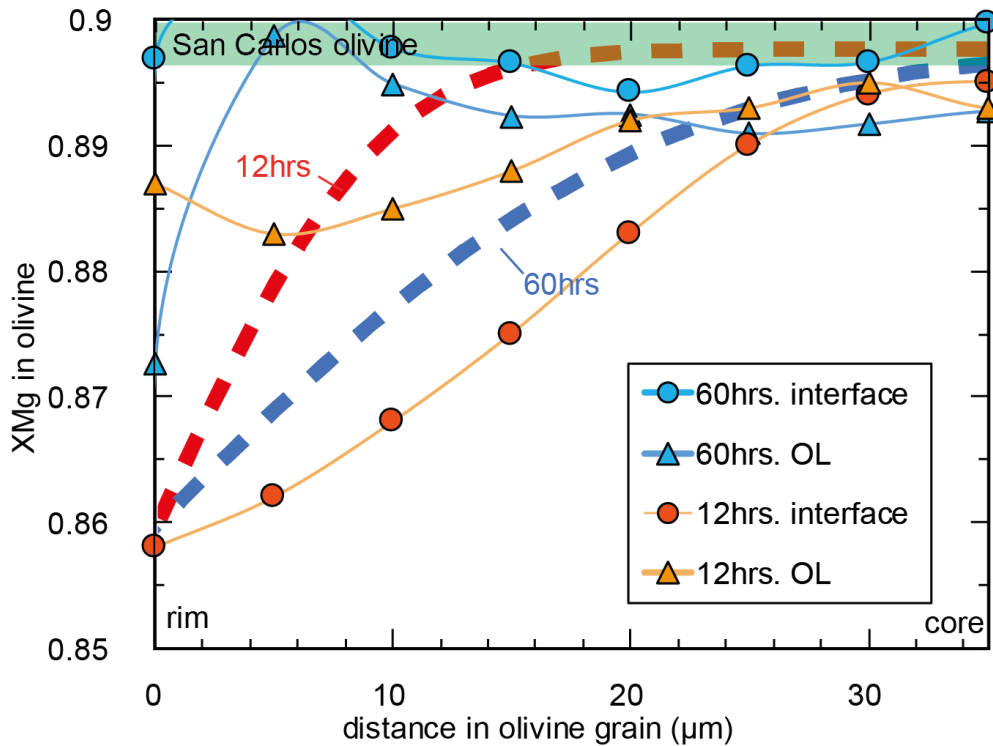


Figure 3-13: Rim-to-core X_{Mg} profiles across four olivines from two experiments OM12 (12 hours) and OM18 (60 hours). Circles represent olivine profile from the interface zone whereas triangles mark olivines from the olivine-rich layer. Analyses were realized with a step size of 5 μm . The green line marks original San Carlos olivine composition. Two dashed lines were plot as a model of Fe-Mg diffusion between olivine and melt. Calculation is done following diffusion equation Eq (3-1) and diffusion coefficient given by Spandler and O'Neill (2010). The orange and blue dashed lines model Fe-Mg diffusion for 12 hours and 60 hours respectively.

3.2.2.2. Melt compositions

Figure 3-14, Figure 3-15 and Figure 3-16 display melt compositional variations measured in glass along the olivine-rich layer from 10 samples (a: from 12 hours experiments with three different starting melts, b: from 60 hours experiments, and c: from all experiments conducted with the starting melt AH6). Analyses were performed with 1 μm beam, but where melt pockets were large enough we performed 5 μm beam size.

No significant variations were observed between analysis performed with 5 and 1 μm beams (see Table 4-2 analysis from OM23 and OM24). In diagrams of Figures 3-14, 3-15 and 3-16, we also reported starting melts (AH6, AH3 and HDRBC) compositions together with the composition of melt from equilibrium crystallization experiments performed at 0.7 GPa and 1225 °C with melts AH6 and AH3 by Husen et al. (2016). As observed for olivine

composition, from the interface (0 mm) to the top of the experimental charge (1.5 to 2.2 mm, depending on the sample), melt compositions are heterogeneous both along the capsule and at the same distance x . X_{Ca} in experiments with AH6 melt (Fig. 3-14 c) displays composition between AH6 compositions and equilibrium melt composition. In runs with AH3 melt, X_{Ca} value is close or lower than equilibrium melt (Fig. 3-14 a, b). in experiments with HDRBC, X_{Ca} of the melt is far lower from the starting value. X_{Mg} content of the reacted melt is significantly higher than X_{Mg} of starting melt, and higher than the equilibrium melt value for melts AH6 and AH3 but not for melt HDRBC (Fig. 3-14 d, e, f). SiO_2 content of reacted melts is close to those of starting melt and equilibrium melt compositions and presents an increase from the interface to the spheres layer (Fig. 3-15 a, b, c). Ca content in the reacted melt ranges between the starting melt and the equilibrium melt compositions for experiment with melt AH6 (Fig. 3-15 d, e, f). Al_2O_3 content of reacted melt, for all experiments, is extremely variable but in general it increases in the olivine rich layer (Fig. 3-16 a, b, c). Finally, TiO_2 content of the melt is mainly different between experiments run with melt AH3 and the two others (AH6 and HDRBC), following the starting melt composition.

Along the olivine-rich layer, X_{Mg} in melt increases as function of distance until 0.74~0.75 in experiments conducted with AH6, ~0.70 with HDRBC and AH3 (Fig. 3-14). The weaker spatial trend is observed in OM17 with melt X_{Mg} composition between 0.55 and 0.63. In experiments performed with melt AH6, X_{An} and Ca and Al_2O_3 decreases as a function of distance along the olivine-rich layer, whereas SiO_2 and X_{Mg} increases. Beside the compositional variations as a function of distance along the sample, a large heterogeneity of melt composition is observed at the same distance in single experiments. For example in OM15, around 0.5 mm distance, a melt pocket of ~0.60 X_{Mg} and one of ~0.75 were analyzed. In many experiments large variations in reacted melt composition occur (Fig. 3-14, Fig. 3-15 and Fig. 3.16).

In olivine reactive dissolution experiments performed with AH6 melt, we observed textural and chemical variations in olivine and melt as a function of experimental run duration (or time) and melt composition. The role of these two parameters on melt-rock reaction has been evaluated. Both parameters are firstly discussed from the textural point of view and then with chemical compositions.

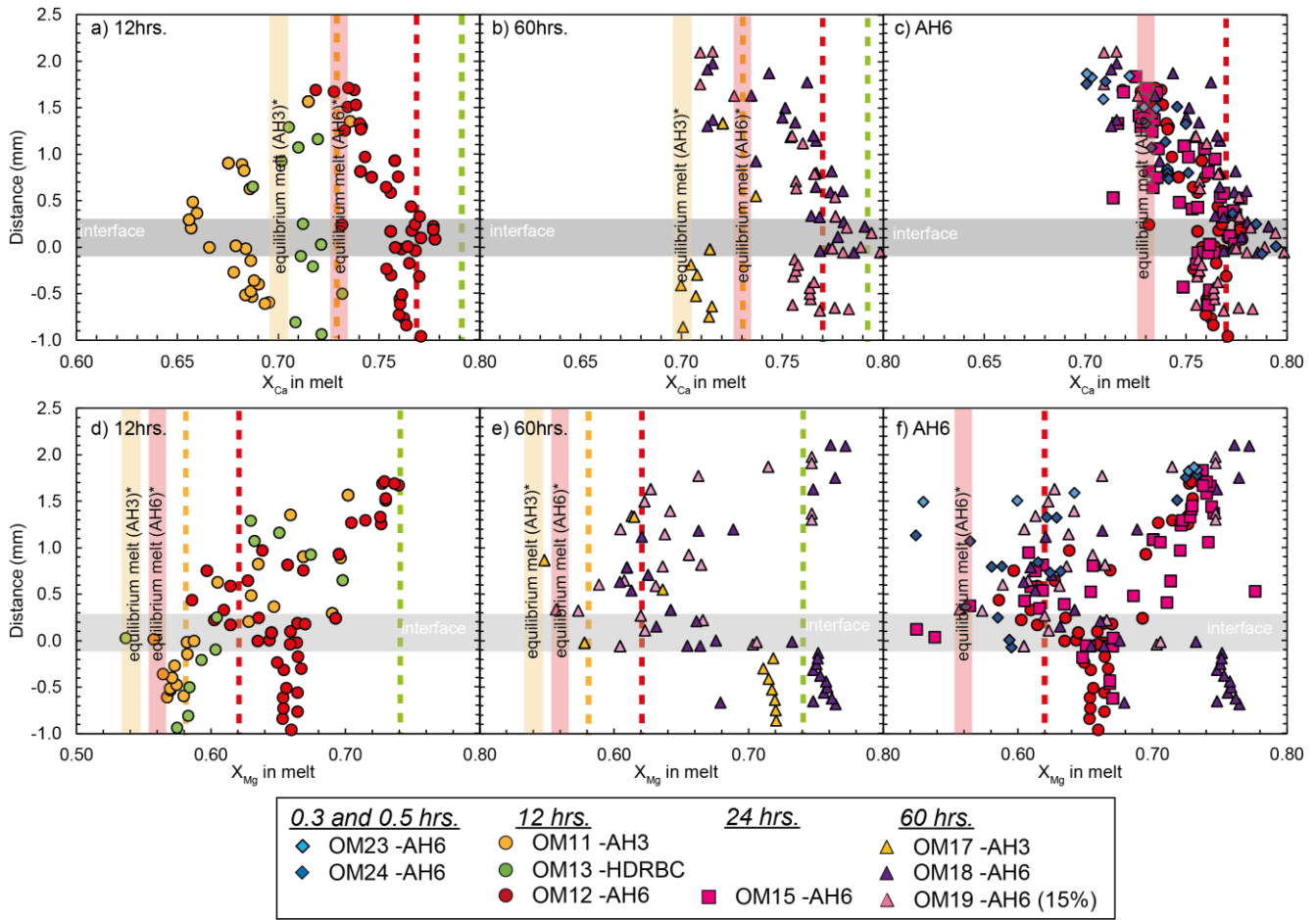


Figure 3-14: X_{Ca} and X_{Mg} contents in glass as a function of distance (mm) along the olivine-rich layer and carbon spheres layer. Distance = 0 marks the approximate location of glass layer-olivine-rich layer interface at the end of the experiment. a) glass compositions from experiments conducted for 12 hours at 0.7 GPa with three different melts AH3, AH6 and HDRBC, b) glass analysis in 60 hours experiments, c) glass in all experiments conducted with melt AH6 at 0.5GPa (OM23 and OM24) and 0.7 GPa (OM12, OM15 and OM18) for various run durations. Yellow, red vertical lines mark the composition of melt at equilibrium during equilibrium crystallization of melts AH3 and AH6 respectively, from Husen et al. (2016). Dashed lines represent starting melt compositions: red for AH6, yellow for AH3 and green for HDRBC (from Husen et al., 2016; Gillis et al., 2014).

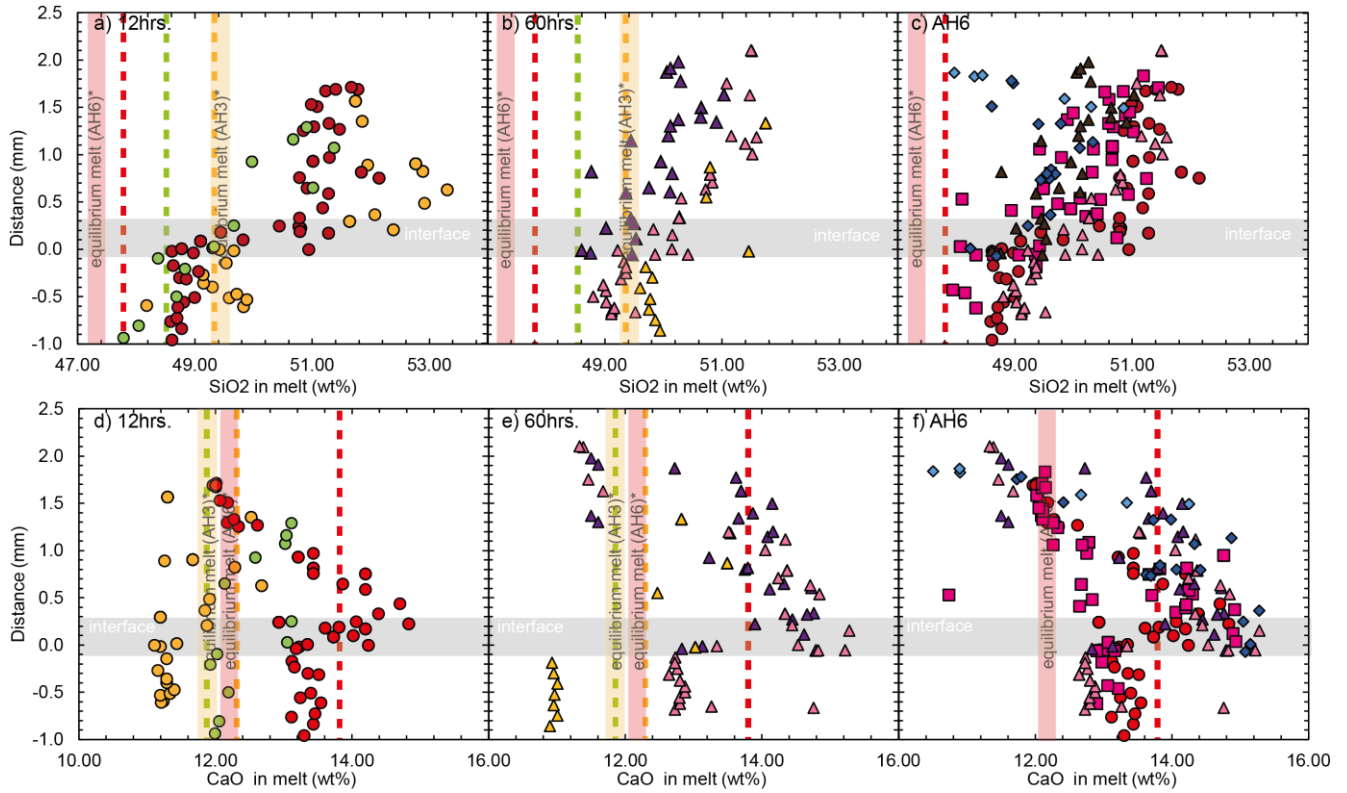


Figure 3-15: SiO_2 and CaO content in glass as a function of distance (mm) along the olivine-rich layer and carbon spheres layer (legend in figure 3-14).

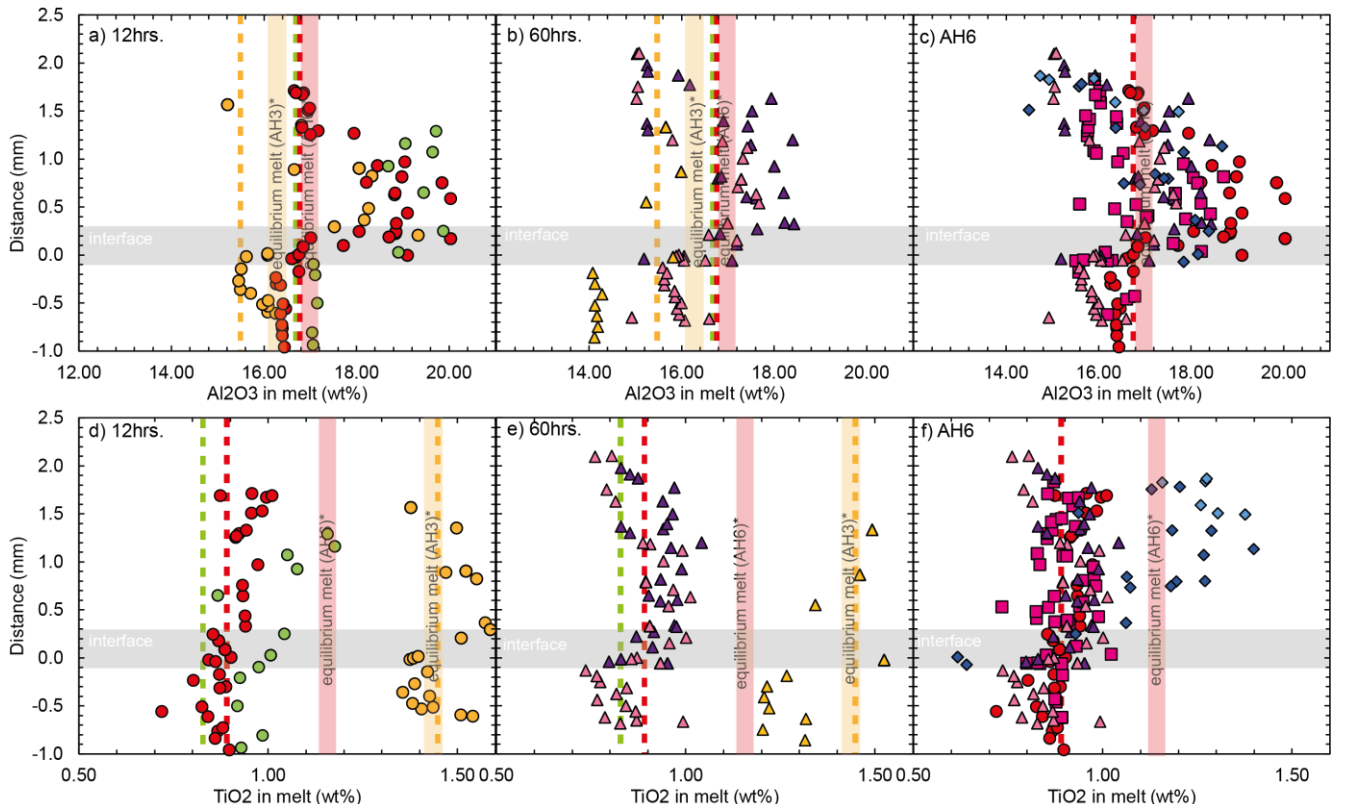


Figure 3-16: Al_2O_3 and TiO_2 contents in glass as a function of distance (mm) along the olivine-rich layer and carbon spheres layer (legend in previous figure 3-14).

3.3. Effect of time on olivine dissolution

3.3.1. Phase assemblage variations as a function of time

As observed in Figures 3-1, Figure 3-3 and Figure 3-4, phase assemblage in experiments varies as a function of time. In experiments performed using melt AH6 (Fig. 3-1a), at $T \geq 1250$ °C (0.7 GPa), the olivine-rich layer is composed of olivine and glass in various proportions as a function of time, whereas at $T = 1200$ °C clinopyroxene and plagioclase crystallize and coexist with olivine and glass. This is in agreement with equilibrium experiments on melt AH6 (Husen et al., 2016) that report clinopyroxene-in and olivine+plagioclase-in reactions between 1250 and 1225 °C (at 0.7 GPa), respectively.

Remarkably, when clinopyroxene and plagioclase occur (at 1200 °C, run lasted 24 hours), clinopyroxene is included in plagioclase (Fig. 3-4) confirming the order of crystallization of equilibrium experiments at 0.7 GPa, i.e. clinopyroxene before plagioclase. Therefore, for melt composition AH6 the melt-dunite interaction is not modifying phase assemblages.

AH3 behaves differently. In experiments performed with melt AH3, olivine and glass coexist at 1250 °C in runs lasted 12 and 60 hours (Fig. 3-3 d, e, f). In 24 hours experiments the phase assemblage is constituted by olivine-glass-clinopyroxene and plagioclase. The olivine + glass assemblage persists at 1200 °C in the 24 hours experiment (OM14; Fig. 3-3 e), whereas in the 48 hours runs clinopyroxene and plagioclase occur together with olivine and traces of glass with no influence of different melt-rock ratio (OM09, 9% melt-rock ratio; OM10, without pre-impregnation of the dunite matrix).

Similar results are obtained in the experiments performed with HDRBC melt compositions: at 1250 °C, 0.7 GPa, olivine + glass occur in run lasted 12 hours, whereas olivine-glass-clinopyroxene-plagioclase in longer experiment (24 hrs) (Fig. 3-3 g and h).

These results can be explained as a time dependent evolution of the melt-dunite interaction. At 1250 °C, in run lasted 12 hours, clinopyroxene crystallizes from the melt and it occurs together with olivine and glass. This is consistent with equilibrium crystallization of melt AH3 (Husen et al., 2016). As time increases to 24 hours, a more abundant crystallization occurs and plagioclase appears together with clinopyroxene and glass (OM14). These results

are not consistent with the order of crystallization found in equilibrium experiments performed on bulk AH3. Indeed, as shown in Figure 2 of Husen et al. (2016), at 0.7 GPa clinopyroxene starts crystallizing from AH3 between 1225 and 1250 °C, followed by plagioclase between 1200 and 1225 °C. Olivine-in reaction, presenting a negative slope, is reported at lower temperature (1175-1200 °C).

Furthermore, it is remarkable that phase distribution along the olivine-rich layer in experiments OM14 (AH3, 24hrs, 1250 °C) and OM16 (HDRBC, 24 hrs, 1250 °C) is not homogenous: clinopyroxene and plagioclase are more abundant close to the melt interface, and progressively decrease toward the upper portion of the olivine rich layer, coupled with an increase in glass proportion. This could reflect a compositional change in melt composition due to progressive assimilation of olivine in the melt. Indeed, the resulted enrichment of MgO content in the reacted melt is expected to modify phase equilibria, shifting the plagioclase-clinopyroxene cross over toward higher pressure and increasing the liquidus temperatures (Fig. 2 of Husen et al., 2016). This effect is expected to be more effective close to the melt sink rather than the upper portion of the dunite matrix.

As time further proceeds, after 60 hrs (Fig. 3-3 c and f), the interaction involves also clinopyroxene and plagioclase dissolution in the melt. The heterogeneous phases distribution along the capsule is removed and only olivine and glass remain. At 1200 °C, a similar evolution of phase assemblages is observed. It is worthy to mention that the melt layer follows a coupled evolution, being almost completely molten in 12 hours experiment, partially crystallized with clinopyroxene + plagioclase symplectites in the 24 hours experiment, and again almost completely molten in 60 hours run.

3.3.2. Olivine-rich layer texture evolution as a function of time

By running time-solved experiments (12, 24, 60 hrs.) at fixed pressure and temperature (0.7GPa, 1250 °C) and using identical starting material (San Carlos olivine + AH6 melt)), we managed to observe a textural evolution of the melt-olivine couple as a function of time by EMPA and EBSD investigations.

On a first hand, by comparing experiments OM12 (12 hrs.), OM15 (24 hrs.) and OM18 (60 hrs.)(Figure 3-3a, b, c), we can observe an homogenization of the grain size and shape, coupled to a decrease of the abundance of small grains. Olivine crystals progressively

evolve from tortuous shapes (crenulated to curvilinear grain boundaries) to smooth rounded and euhedral ones. A larger amount cusped crystals is found in shorter experiments OM12 and OM15 the result of intense corrosion following subgrains boundaries. Such observations are consistent with previous studies (Boudier, 1991; Levine et al., 2016). Aggregates of small olivine ($<10 \mu\text{m}$), also more abundant in OM12 and OM15, are assumed to be formed by intense corrosion of large olivine crystals along subgrain boundaries. This process creates clusters of small olivine crystals preserving the orientation of the “parental” crystal. It should be noted that EBSD observation did not confirm this hypothesis systematically, mainly because of grain rotation (Boudier, 1991), evidence of melt percolation. By increasing run duration, olivine dissolution and recrystallization leads to the formation of crystals with euhedral to curved boundaries. The creation of euhedral boundaries is known as the result of a double process of corrosion and overgrowth (Boudier, 1991). We can infer than the extent of olivine dissolution-recrystallization by a reactive melt increases as a function of time, leading to a homogenization of grain shapes and sized.

On the other hand, all misorientations observed at the first stages (12-24 hours) disappeared at 60 hours (Fig. 3-6d). By comparing EBSD maps of the starting San Carlos olivine before and after the input of a pressure of 0.5 GPa (Fig. 2-2), we showed that misorientations observed in several short duration experiments are due to the confining pressure. These misorientations are still visible after 12 and 24 hours of experiment, but are largely erased after 60 hours. We can infer that all olivine crystals present in OM18 are the result of intense dissolution recrystallization. Boudier (1991) describes recrystallized olivine as bounded to the same kind of crystallographic planes. No textural distinction can be done between original San Carlos olivine and recrystallized rims. But the weakly misorientated crystal should be the result of recrystallization around dissolved grains.

Small crystal aggregates are completely dissolved in 60 hours (Fig. 3-3c and Fig. 3-6d) and melt percolation increases as crystallinity decreases. Indeed, we observe an increase of the melt-rock-ratio from 6 to 11%, implying a homogenization of reacting melt composition as a function of time that we are going to discuss. In shorter duration experiments, we can expect highly variable reacted melt compositions as an effect lower melt-rock ratio (Hersum et al. 2005). By selecting images from EMPA and EBSD analysis we reconstructed the process of olivine dissolution-recrystallization (Fig. 3-17).

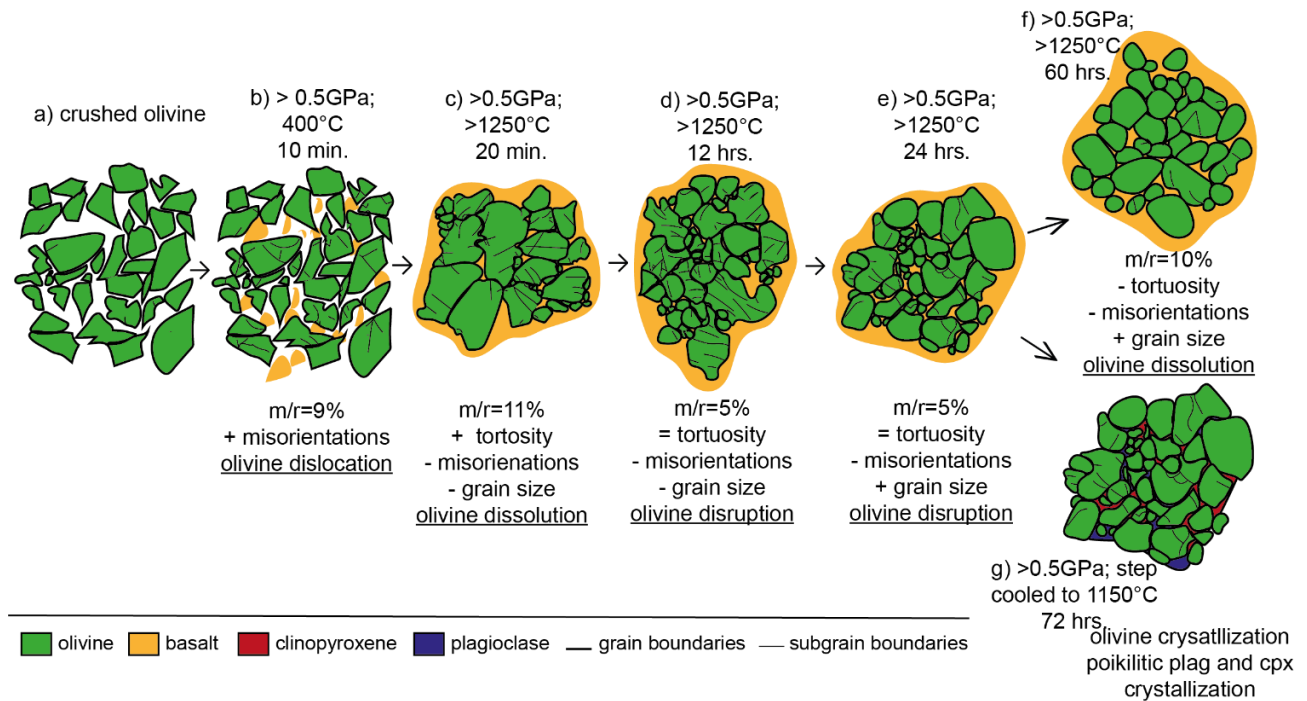


Figure 3-17: Microstructural sketch for the olivine reactive dissolution and crystallization, and olivine-rich troctolite formation along our experiments with both experimental strategies based on EBSD and EMP observations. For a discussion, see the text. m/r = melt/rock. a) Weakly deformed olivine is placed with basalt powder in a capsule for experimentation. b) Dislocations are generated in olivine by pressurizing up to 0.5 or 0.7 GPa. c) Basalt dissolves olivine following grain boundaries and subgrains formed under pressure, increasing grain tortuosity and generating small rounded to euhedral grains. d) Increase of the amount of small rounded grains generating a pseudo-porphyroclastic texture as large olivine is corroded along grain boundaries and generate small olivine grain aggregates and reducing porosity. e) Olivine dissolution-recrystallization process starts to erase misorientations and homogenize olivine textures. Some small grain aggregates remains. f) Olivine grain tortuosity, size heterogeneity decreases, major misorientations and dislocations are erased. Grain size increases by dissolution of small olivine aggregates and recrystallization on larger grains. g) If the experiment is step-cooled to 1150 °C, deformed plagioclases and clinopyroxenes crystallized from reacted melt as poikilitic and interstitial grains (→Chapter 4).

3.3.3. Effect of time on reacted melt and olivine compositions

We can observe an effect of time on three different features: the composition of olivine, the composition of the reacted melt and the melt-olivine equilibrium.

In Figure 3-11 and Figure 3-12 (b and e) we compare olivine composition after 12, 24 and 60 hours experiment. The variation of X_{Mg} in olivine decreases as a function of time (see OM12 (AH6-12 hrs.), OM15 (AH6-24 hrs.) and OM18 (AH6-60 hrs.) in Fig. 3-11), displaying narrower X_{Mg} trends. Additionally we observe a global increase of X_{Mg} in olivine as a function of time especially close to the interface. We can infer that longer run duration led to a greater extent of melt-rock reaction and a chemical homogenization of olivine composition as

observed by Saper and Liang (2014). This homogenization effect is also proved by NiO content in olivine. X_{Mg} versus NiO covariation (Fig. 3-12 c) shows large compositional variations in NiO content in OM12 (AH6-12 hrs.) and OM15 (AH6-24 hrs.), from 500 ppm to 3500 ppm. On the contrary olivine of OM18 (AH6-60 hrs.) have a lower NiO content (0 ppm to ~2400 ppm) and a smaller compositional variability. Regarding the absence of NiO in the starting basalt powders (Tab. 2-1), olivine with lower NiO than San Carlos olivine might be re-equilibrated with the melt by diffusion, dissolution and recrystallization. The fact that olivine present in 60 hours experiments has almost no inner-deformations and a low NiO content supports a re-crystallization origin. We observed a high X_{Mg} in olivine in all experiments, and no olivine has a composition coherent with the equilibrium crystallization of the melt AH6 ($X_{\text{Mg}} < 0.82$; Husen et al., 2016). This shows a buffering effect of the reacting melt by the host dunite similar to observations of (Tursack and Liang, 2012; Saper and Liang, 2014; Van den Bleeken et al., 2010). Low NiO and constant X_{Mg} for longer experiments attest of an effect of time on olivine composition. Dissolution and recrystallization of olivine extent increases with time leading to a massive replacement of original San Carlos olivine.

Additionally, as described in the results, core-rim variations decrease as function of time (Fig. 3-13). The comparison of obtained core-rim profiles with theoretical ones is done following Spandler and O'Neill (2010). We chose to reduce the model to the case of one-dimensional diffusion into a semi-infinite slab with constant composition maintained in the melt at the interface described by the Eq 3-1 given by Darken and Gurry (1953) and Crank (1975).

$$\frac{c_i - c(x)}{c_i - c_0} = \operatorname{erf}\left(\frac{x}{2(D_m t)^{\frac{1}{2}}}\right) \quad \text{Eq 3.1}$$

D_m is the chemical diffusion coefficient given by Spandler and O'Neill (2010), ($D_m = 6.17 \times 10^{-16}$ for Fe and Mg), $c(x)$ the concentration at distance x , c_i the concentration at the interface crystal-glass ($x = 0$), c_0 the initial concentration and t is the duration of the experiment. The flattening of profiles follows the expected trend for Fe-Mg diffusion as function of time, but the profiles we obtained are not consistent with diffusion profiles models given by the diffusion equation. We can affirm that diffusion is not the solely leading process during melt-rock interaction and that core-rim profiles observed in olivine are the result of dissolution-recrystallization at olivine grain boundaries coupled with diffusion.

Reacted melt compositions also varies with time. In Figures 3-14, 3-15 and 3-16, we represented glass compositions from the olivine-rich layer only. Indeed, the composition of the melt is highly variable along experimental charge. Here, we only compare glass for the olivine-rich layer. Figure 3-18c displays SiO_2 versus $\text{Na}_2\text{O}+\text{K}_2\text{O}$ in the glass, and show that no important time effect is observed between experiments conducted at 1250 °C and 0.7 GPa. However OM12 (12 hrs.) have glasses slightly richer in SiO_2 (up to 52%). SiO_2 content in reacted melt depends on time and presents a lower variability for longer experiments (Fig. 3-15c). X_{Mg} , X_{Ca} , TiO_2 and Al_2O_3 variations follow the global behavior of a decrease of the compositional heterogeneities as a function of time (Fig. 3-14c, 3-15c and 3-16c). Indeed, experiment OM18 (60 hrs.) displays more homogeneous glass compositions for all major elements observed, consistently with observations done on textures and olivine composition. TiO_2 and Al_2O_3 compositional variations (Fig. 3-16c) as a function of time are the largest compared with other oxides. It is consistent with the fact that they are slow diffuser elements and with results from previous studies by Van den Bleeken et al. (2010). Reversely, Na_2O , FeO and MgO , fast diffusers does not display large heterogeneities as function of time, only OM18 (60 hrs.) present a smaller heterogeneity. From 12 to 24 hours compositional heterogeneity of various phases increases. We can suppose that between 24 hours and 60 hours, enough olivine is dissolved to induce a more efficient percolation of melt within the olivine matrix. In our experiments the melt-rock ratio is about 10, which corresponds to a maximum permeability of the olivine-rich layer of 10^{-11} cm^2 (see Fig. 12 in Hersum et al., 2005; Liang et al., 2001). For such permeability, a large degree of melt flow channelization (i.e. preferential circulations of melt along channels) occurs, inducing the spatial distribution of compatible and incompatible elements highly heterogeneous. The increase of the melt-rock ratio for longer experiments lead to a reduction of chemical heterogeneities in melt and olivine consistently with Daines and Kohlstedt, (1994) and Hersum et al., 2005. We would expect reacted melt such as those obtained in experiments of 12 hours or 24 hours to crystallize highly heterogeneous plagioclase and clinopyroxene in the case of a cooling (see Chapter 4). Indeed, Hersum et al. (2005) model predicts that neighboring crystals might have completely different element concentrations.

In our experiments the average Fe-Mg exchange distribution coefficients $Kd_{\text{Mg-Fe}}^{\text{olivine-melt}} = \frac{X_{\text{Fe}}^{\text{ol}} * X_{\text{Fe}}^{\text{melt}}}{X_{\text{Mg}}^{\text{ol}} * X_{\text{Mg}}^{\text{melt}}}$ are 0.20 to 0.29, for an expected equilibrium of 0.31 (Toplis 2005). Figure 3-19 displays X_{Mg} in olivine, versus X_{Mg} in the melt and highlight that the equilibrium is

not reached for al olivine but we tend to approach it of experiments OM12 (AH6-12 hrs.), OM15 (AH6-24 hrs.) and OM18 (AH6-60 hrs.). It is at the interface that olivine and melt approaches equilibrium. Considering that Fe-Mg partitioning at the interface shows conditions close to olivine-melt equilibrium (Fig. 3-19) and that we observed the lowest Ni content in that zone, we can assume that all the olivine from the interface is recrystallized from reacted melt in that zone. The two experiments OM23 and OM24 conducted for 30 and 20 minutes respectively, display olivine-melt couple far from equilibrium, which is consistent with the short duration of the experiment. In order to better understand situations of melt-olivine equilibrium, we performed a focused textural study, by comparing analysis from cusped to resorbed rims and euhedral ones. Data are shown in Figure 3-20. As a result we did not observe any compositional difference between resorbed and euhedral rims; even small rounded olivines are identical and not in equilibrium with the melt. Some cases of good melt-olivine equilibrium were observed (overlined with pink) in experiment OM18 (60 hrs.-AH6) within the olivine-rich layer and at the interface olivine-rich layer-melt layer. Resorbed, euhedral and rounded olivines are in equilibrium with the surrounding melt. This observation is consistent with the greater extent of melt-rock reaction as function of time also observed by Saper and Liang (2014), leading, in our case, to local cases of equilibrium.

3.4. Effect of melt composition on olivine dissolution

No effect of melt composition has been observed on textures. By comparing BSE images and EBSD maps from OM11 and OM12, conducted with AH3 and AH6 respectively, no differences have been noticed.

Hersum et al. (2005) inferred that reactive melt to have an effect on textural and chemical evolution of the igneous microstructures during porous melt flow. In the three experiments of 12 hours, performed starting melts AH3, AH6 and HDRBC olivine compositions does not vary as a function of starting melt composition (Fig. 3-12 a). In 60 hours experiments, olivine of OM17 is slightly more evolved, which is consistent with the nature of the reacted melt AH3 ($X_{Mg} = 0.57$) employed. Reacted melts from experiment conducted with the melt AH3 (OM11-12 hrs. and OM17 - 60hrs) are the most evolved and reach the composition of basaltic andesite (Fig. 3-18) for the shortest one. All reacted melts remain in the field of Atlantic and Pacific MORB documented in Pet Data Base (Fig. 3-18). In experiments of 12 hours (Fig. 3-14, 3-15, 3-16), we observe an increase of X_{Mg} compared with starting composition attesting that initial X_{Mg} is completely erased by olivine buffering effect. FeO and MgO contents, fast diffusers, are erased by olivine assimilation (Fig. 3-14). Whereas CaO, TiO₂ and Al₂O₃, remain close to initial or equilibrium melt compositions. Al₂O₃ variations seem to display more heterogeneous variations at 12 hours, but are erased at 60 hours (Fig. 3-16).

Experiment performed with HDRBC-melt led to a global decrease of X_{Mg} , highlighting olivine crystallization. San Carlos olivine is in equilibrium with a melt with $X_{Mg} = 0.75$, close to HDRBC composition (0.74). Therefore, we can assume that saturation is reached and that olivine crystallizes at a greater extent than it is dissolved. For X_{Ca}, TiO₂ and Al₂O₃ (Figure 3-15 and 3-16) the reacted melt keeps a composition close to the starting melt, melt-rock interaction generates only an increase of compositional heterogeneities for all elements observed.

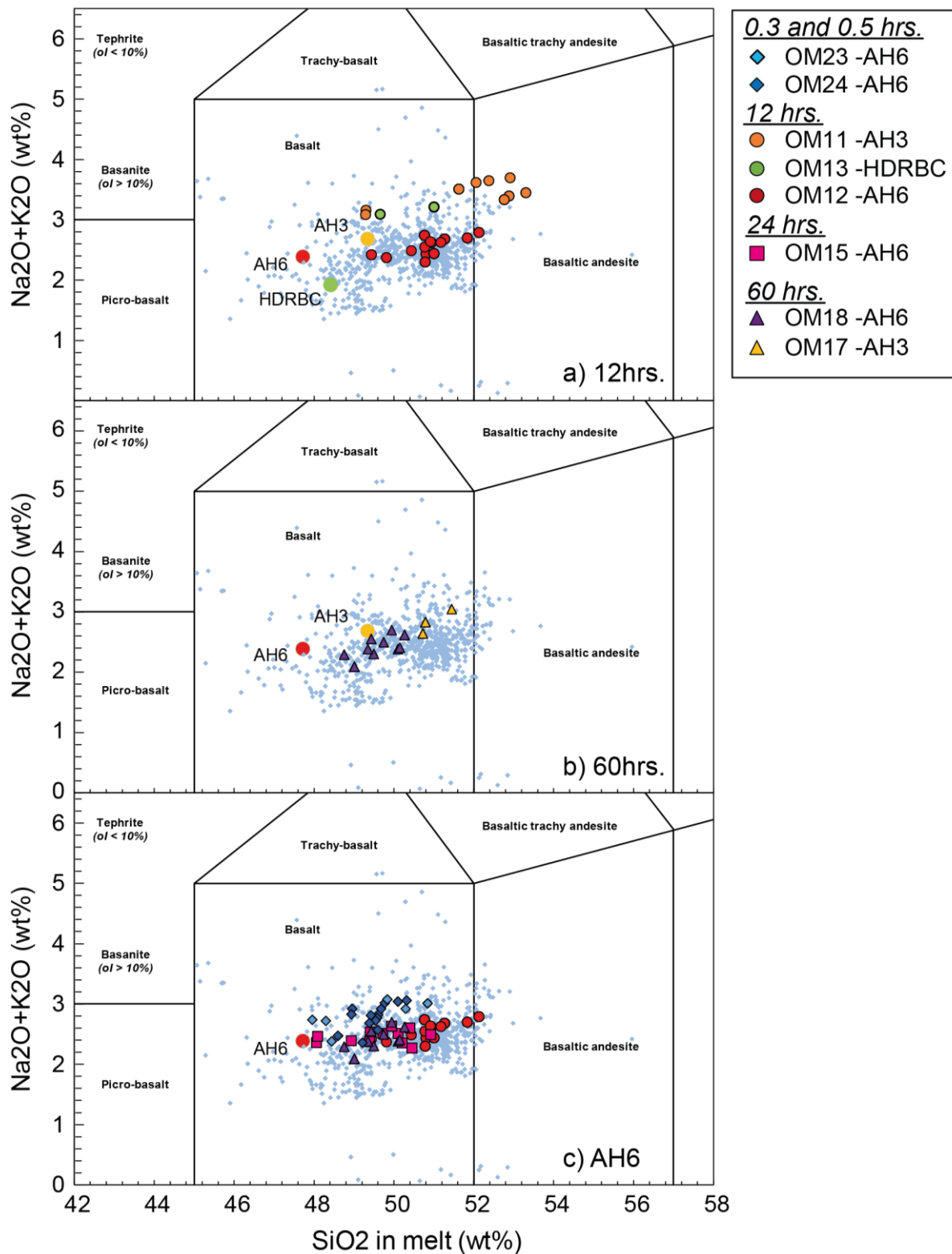


Figure 3-18: Part of the total alkalis ($\text{Na}_2\text{O}+\text{K}_2\text{O}$; wt%) versus silica (SiO_2 ; wt%) diagram for glasses from the olivine rich layer on selected runs conducted at $1250\text{ }^{\circ}\text{C}-0.7\text{ GPa}$ and $1300\text{ }^{\circ}\text{C}-0.5\text{ GPa}$ employing AH3 and AH6 from Husen et al. (2016) and HDRBC Gillis et al. (2014). In gray we reported Atlantic and Pacific MORBs from Pet Data base. We separated experiments conducted for 12 hours (a), 60 hours (b). and in c those conducted with AH6-melt for all run durations from 0.3 hours to 60 hours.

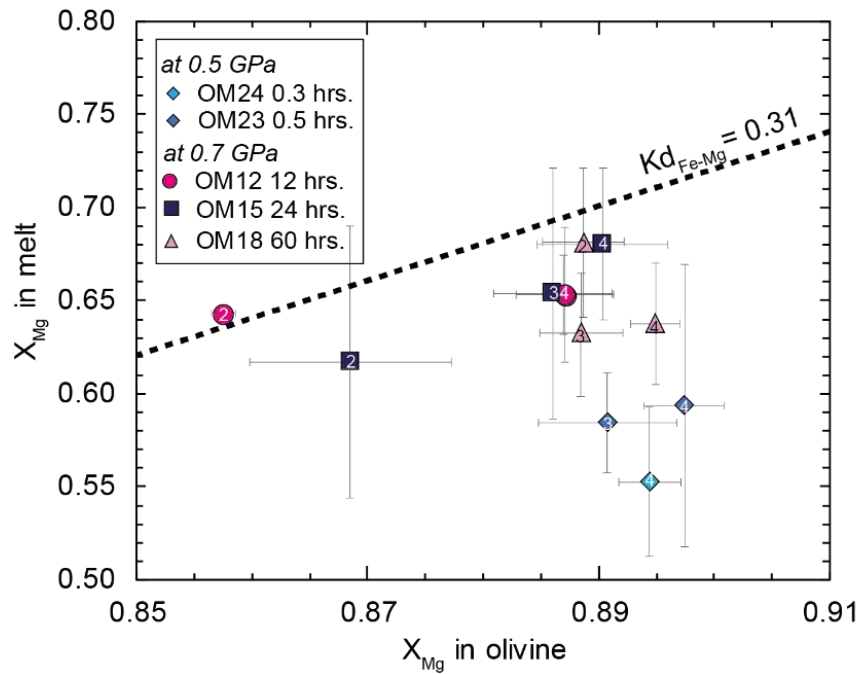


Figure 3-19: Fe-Mg partitioning between melt and olivine for selected experiments conducted with melt AH6. Each point correspond to the average olivine composition of a zone per sample: 2: the interface, 3: the bottom of the olivine-rich layer, 4: the upper part of the olivine-rich layer.

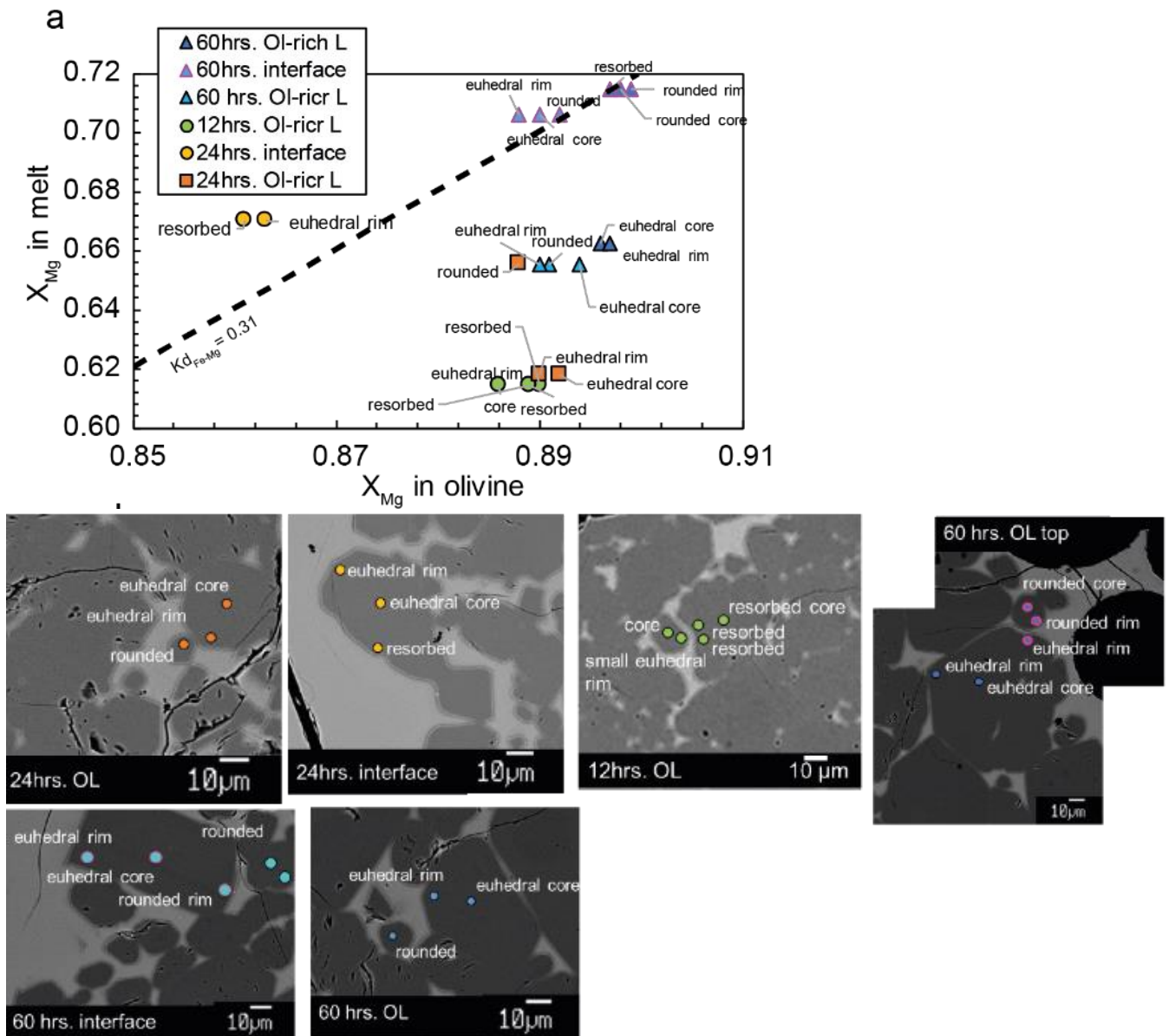


Figure 3-20: Fe-Mg partitioning between melt and olivine for selected experiments as a chemical vs. textural focused study. Each point corresponds to an analysis represented on the BSE image below.

Chapter 4. Step-cooled experiments: reactive dissolution-crystallization

4.1. Experimental methods

Step-cooled experiments were performed following the powder to powder (P2P) setup described in Chapter 2. In order to investigate in-situ crystallization of reacted melt in the dunite matrix, we performed four step-cooled experiments. The charge was first pressurized to 0.5 or 0.7 GPa at 400 °C and then temperature was raised to 1300 °C. For step-cooled experiments, temperature was maintained at 1300 °C for 24 hours; the charge was then step-cooled to 1150 °C at a rate of 10°/min following the temperature path of Figure 4-1. During cooling, pressure has been maintained fixed. Experiments were quenched by shutting off the power supply. Experimental conditions are reported in Table 4-1. In order to evaluate the role of pressure in reactive dissolution and in-situ crystallization of reacted melts, we performed experiments at 0.5 and 0.7 GPa. The role of starting melt composition has also been studied, performing experiments on three different starting basalts previously described (Tab. 2-1).

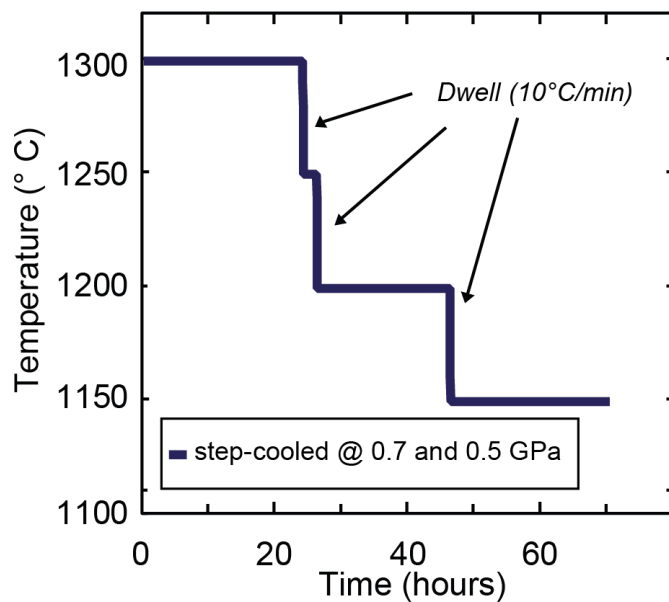


Figure 4-1: Temperature versus time path of dissolution experiments. Time = 0 marks the beginning of the experiment, when the target temperature of 1300 °C was reached

Table 4-1: Experimental run conditions and run products.

	Temperature (°C)		Cooling Process	Starting Melt	Total duration (h)	Lithology of the olivine-rich layer
	Initial	Final				
<u>Runs at 0.5 GPa</u>						
OM02	1300	1150	Step	AH6	72	ol-Troctolite
OM03	1300	1150	Step	HDRBC	72	ol-Troctolite – dunite
<u>Runs at 0.7 Gpa</u>						
OM01*	1300	1150	Step	AH6	72	ol-Troctolite – wehrlite-dunite
OM20	1300	1150	Step	AH6	72	pl- and cpx- bearing dunite
OM21 (no melt trap)	1300	1150	Step	AH6	72	pl- and cpx- bearing dunite
OM22	1300	1150	Step	AH3	72	pl- and cpx- bearing dunite
OM15	1250	1250	None	AH6	24	olivine + glass

ol= olivine; pl=plagioclase; cpx=clinopyroxene; Step: step-cooled temperature path with a dwell of 10 °C/minute. Melt-rock ratio in the charge was 0.7. (*) in OM01 the geometry during the experiment has been only partially maintained and some of the starting material escaped from the graphite capsule; ol-Troctolite: olivine-rich troctolite

4.2. Textures and phase abundances of experimental results

4.2.1. Phase assemblage and textures

Run products consist in two layer samples following the initial geometry (Fig. 2-4 d and Fig. 4-3): i) glass-bearing olivine-gabbro replacing the initial melt layer, ii) olivine-rich layer replacing the starting impregnated dunite. This latter is composed of olivine-rich troctolite (ol-troctolite) or plagioclase- and clinopyroxene-bearing dunite (Fig. 4-2 and 2), depending on pressure and starting basalt composition. Most of the analytical efforts have been focused on olivine-rich layer in order to study olivine dissolution and re-crystallization and the mineral chemistry of interstitial phases from the reacted melt. Figure 4-2 contains BSE images showing the most representative textures in olivine-rich layer in experimental samples. Within the carbon spheres, some olivine, clinopyroxene and plagioclase crystallized. Few amounts of glass have been observed; they are usually smaller than 10 μm , and are generally interstitial to mineral phases (Fig. 4-1).

Textures of the olivine-rich layer are similar in all the step-cooled experiments. Olivine-rich layer is composed by olivine, plagioclase, clinopyroxene and very few amounts of glass (Fig. 4-2a). Olivine is the most abundant phase showing large subhedral crystals (~30 to about 150 μm), with straight euhedral to smooth curvilinear grain boundaries (Fig. 4-2a, b, d). Generally, olivines also present cusped grain boundaries and embayed rims evidence of olivine resorption as showed by arrows on Figure 4-2. Large poikilitic plagioclase and clinopyroxene (Fig. 4-2a) include small rounded olivine. Generally, contacts between plagioclase and clinopyroxene are rather sharp and straight (Fig. 4-2b, d), suggesting their coprecipitation from reacted interstitial melt.

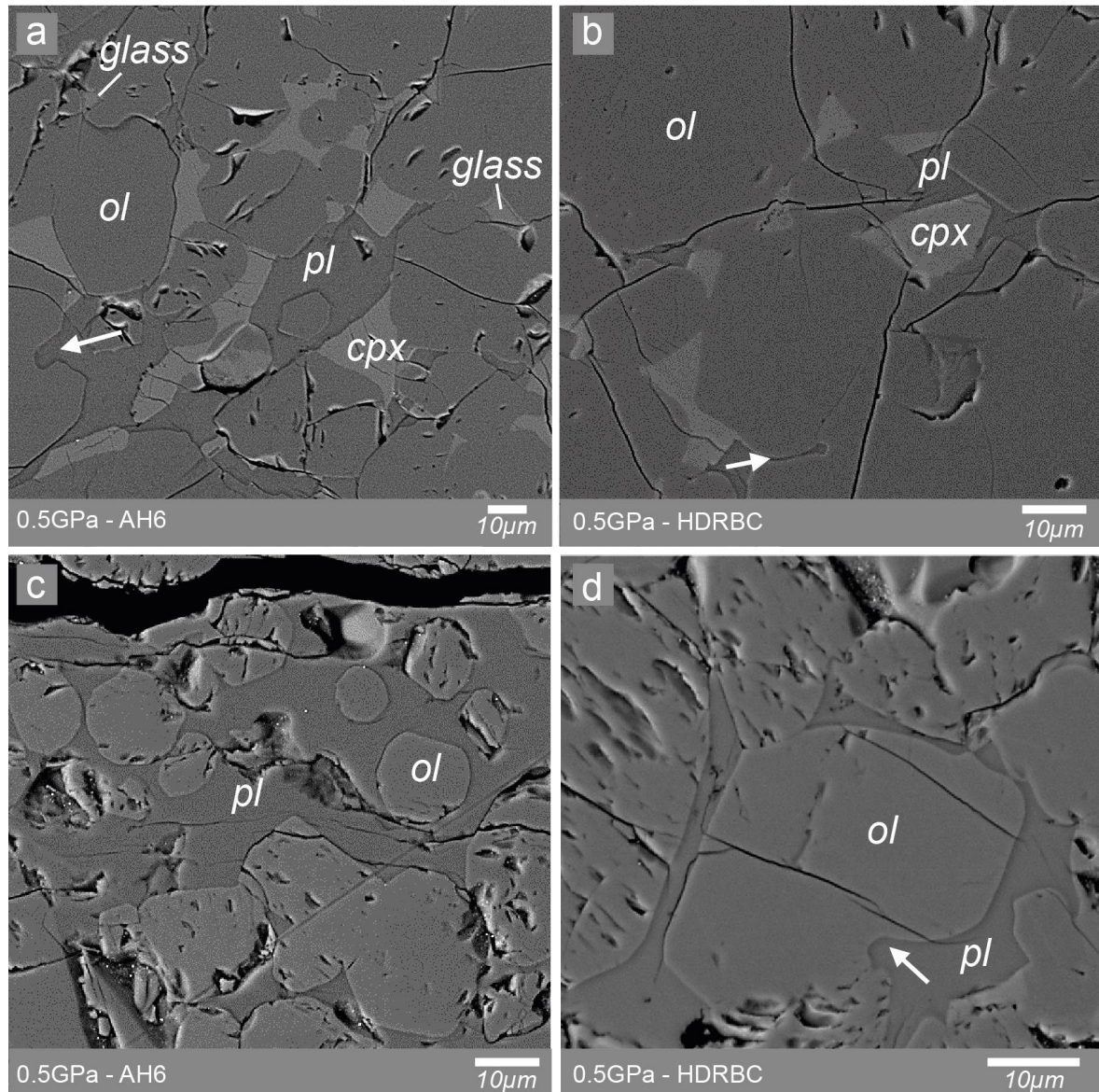


Figure 4-2: Representative BSE images illustrating the textures of the olivine-rich layer with different starting melts. a) olivine-rich troctolite from experiment OM02 with large subhedral olivine and small rounded crystals included plagioclase and clinopyroxene poikilitic crystals. Glass occurs as small interstitial portions. b) Olivine rich troctolite from experiment OM03 with olivine showing figures of resorption (arrow). Contacts between interstitial plagioclase and clinopyroxene are sharp. c) Globular olivines included in a large poikilitic plagioclase. d) Embayed subhedral olivine included in a poikilitic plagioclase.

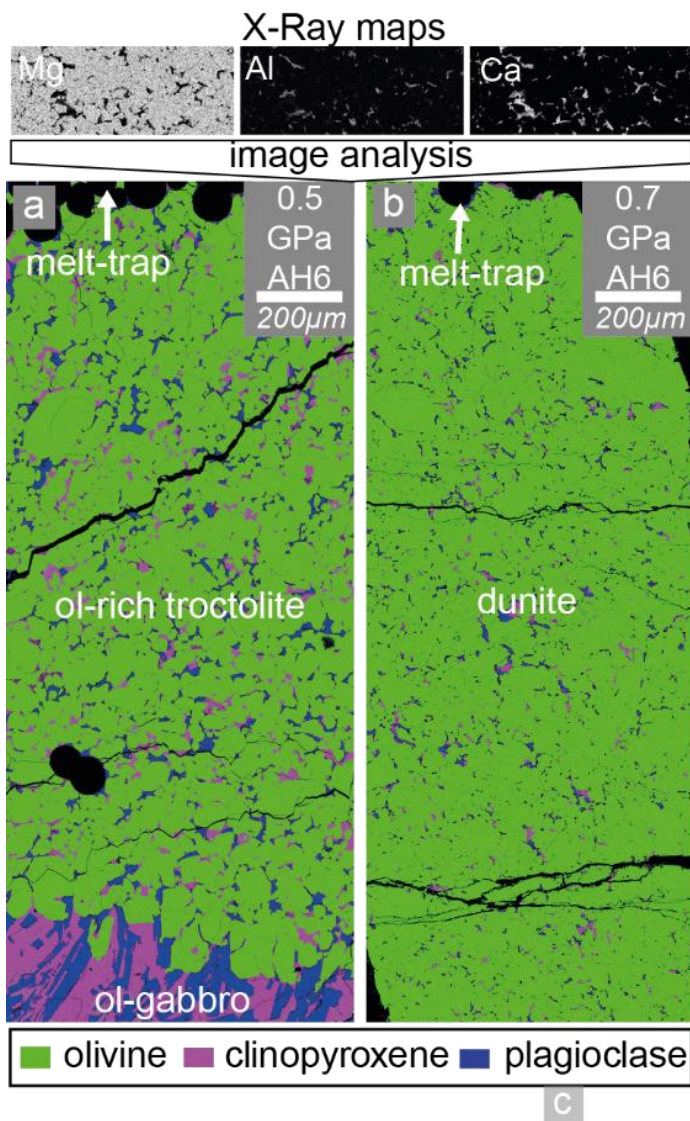
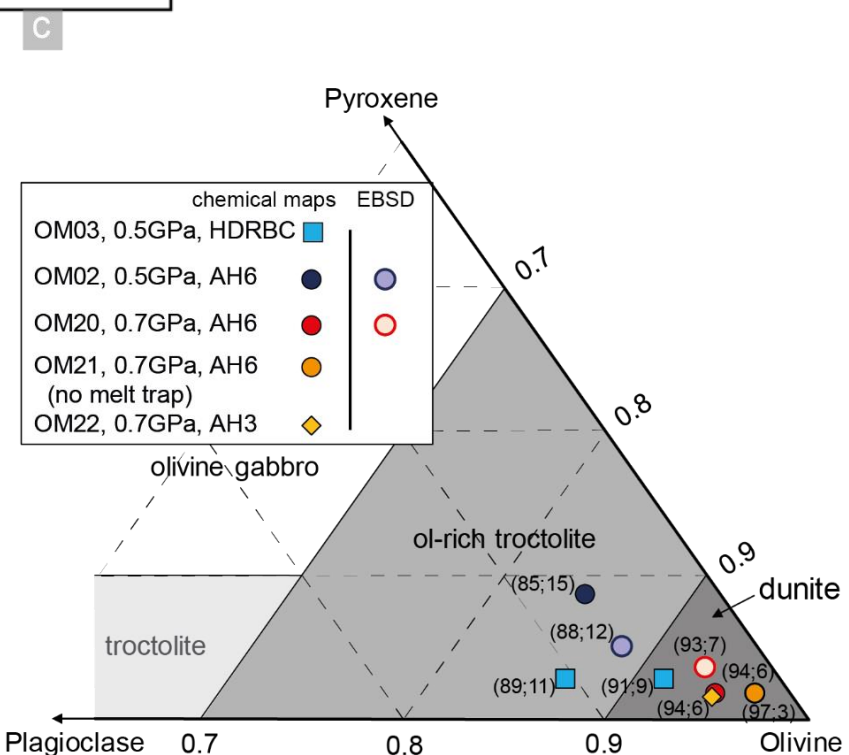


Figure 4-3: Phase distribution within the olivine-rich layer. Phase maps of experiments (a) OM20 and (b) OM02, step cooled experiments conducted with the starting melt AH6, at 0.7 and 0.5 GPa respectively are shown. False color images are obtained by performing a supervised classification based on the selection of regions of interest (olivine-cpx-plagioclase-graphite) with the software ENVI® on RGB images made of Ca, Mg and Al X-ray chemical maps. Olivine is in green, clinopyroxene in purple and plagioclase in blue. (c) Phase abundances for selected areas represented on the diagram Olivine-Plagioclase-Pyroxene. EBSD analysis provides phases abundance, represented with lighter colors for two experiments.



4.2.2. Phase assemblage of olivine-rich layer by image analysis

Phase abundances within the olivine-rich layer were calculated by image analysis performed on X-ray chemical maps (Fig. 4-3a and b) for all step-cooled experiments and the isothermal experiment OM15 (1250 °C, 0.7 GPa). Results are reported in a triangular diagram olivine-pyroxene-plagioclase of Figure 4-3c. The olivine-rich layer from experiments performed at 0.5 GPa (OM02 and OM03) has lower olivine modal abundance compared with experiments at 0.7 GPa (OM20, OM21 and OM22, Table 4-1). Such difference in olivine abundance likely reflects the porosity of olivine matrix at the high-temperature step of the experiment and is illustrated by phase maps of Figure 4-3a and b. It should be noted that here and in the following paragraphs we intend as porosity the abundance of interstitial phases such as clinopyroxene, plagioclase and melt without considering new olivine that could additionally crystallized from the reacted melt. The step-cooled experiment OM02 (0.5 GPa, AH6) consists of a rather homogeneous olivine-rich troctolite made by 85% olivine and 15% plagioclase + clinopyroxene (Fig. 4-3 a and c). However, experiments OM20 (0.7 GPa, AH6) and OM22 (0.7 GPa, AH3) resulted in a plagioclase- and clinopyroxene-bearing dunite (94% olivine and 6% plagioclase + clinopyroxene) with similar plagioclase/clinopyroxene modal ratio (Fig. 4-3 b and c). Experiment OM21 (0.7 GPa, AH6), performed without the carbon spheres trap, resulted in dunite with higher olivine content (97% olivine and 3% plagioclase + clinopyroxene). As the starting olivine content was 91%, olivine amount increased during this experiment, suggesting crystallization of this mineral phase.

A slight variation in phases abundance is observed within the olivine-rich layer in the experiment OM03 (0.5 GPa, melt HDRBC). This concerns a sensible difference in ratio between olivine and interstitial phases amounts, 89% and 11% in the lower part, 91% and 9% in the upper part (Fig. 4-2c).

The isothermal experiment OM15 (1250 °C, 0.7 GPa, AH6) carried out for 24 hours provided us the snapshot of the dissolution at the first high-temperature step before the cooling of experiments (see Chapter 3). Although, it has been run at lower temperature (1250 °C instead of 1300 °C), it still can give information on olivine–melt relation because starting melt AH6 is expected to be above the liquidus, as documented by Husen et al. (2016). Indeed, this experiment resulted in two layers, a glass layer overlaid by a glass-bearing olivine-rich layer.

Olivine texture and proportions (94 % olivine – 6 % melt) are close to those resulting from step-cooled experiment.

4.2.3. EBSD analysis: phases abundance and microstructural aspects

In order to evaluate olivine-melt relation, it is important to detect grain boundaries and any geometrical aspects (crystal size distribution, shape) of the solid matrix. Our samples contain very high modal olivine (up to 94%). As a result, BSE images at the Electron microprobe do not allow to distinguish grain boundaries. Therefore, EBSD analyses were carried out. EBSD technique provides grain boundaries definition, allow to evaluate phases abundance, and furthermore it gives numerical outputs on crystal shape and size and crystal misorientations. In particular Olivine and interstitial phases (clinopyroxene and plagioclase) orientation, Crystal Preferred Orientation (CPO), shape factor, area, tortuosity and crystallographic and textural parameters were measured by indexation of electron backscattered diffraction (EBSD) pattern using the CamScan X500FE Crystal Probe facility at Géosciences Montpellier on the olivine-rich layer of 2 samples OM02 (0.5 GPa, AH6) and OM20 (0.7 GPa, AH6) (Fig. 4-4). EBSD acquisition is described in Chapter 2 (2.4.3).

OM02 (0.5 GPa, AH6) and OM20 (0.7 GPa, AH6) (Fig. 4-4), olivine occurs as large subhedral to euhedral olivine crystals (Fig. 4-5 and Fig. 4-6 c), with respectively straight and smooth curvilinear grain boundaries, and small rounded ones. Sample OM20 (Fig. 4-4 and Fig. 4-5 (e, f, g)) contains smaller and more tortuous olivines with crenulated grain boundaries. Statistics obtained by EBSD maps treatment give average olivine crystal size of ~23 µm for OM02 and ~10 µm for OM20, with maximum size of 113 and 165 µm, respectively. OM20 sample has higher olivine content with smaller olivine crystal size, in agreement with abundances obtained from X-Ray chemical maps. Concerning tortuosity and elongation of olivine crystals, shape factor (~1.5 for OM02 and ~1.6 for OM20) and aspect ratio (~1.5 for both) are quite similar. Whereas tortuosity is similar at both pressures (0.5 and 0.7 GPa), Grain Orientation Spread (GOS) varies. Indeed, OM02 olivine crystals have an average GOS value of 0.45 and a maximum of 6.6, whereas OM20 olivine crystals have respectively 0.52 and 7.7. More misorientations are recorded by olivine crystals in OM20 sample at 0.7 GPa compared with OM02 sample at 0.5 GPa. Figure 4-4 and 4-4 display maps of GOS for olivine crystals

from the olivine-rich layers. Olivine crystals from the sample OM20 show more misorientation than those from sample OM02. The most misoriented crystals (in green and yellow) are mainly subhedral tortuous ones. By comparing maps of Misorientation to Mean (Mis2Mean) and Grain Orientation Spread (GOS) between OM02 and OM20 (Fig. 4-4), we observe that misorientations and subgrain boundaries are more abundant in OM20 sample. Misoriented crystals are in both cases randomly spread along the olivine-rich layer with no special spatial repartition.

Figure 4-4 also displays olivine, plagioclase and clinopyroxene crystals orientations in OM02 and OM20 samples. Olivine is randomly oriented. As olivine crystals were randomly oriented at the initial state of the experiment (cf. OM26 in Fig. 2-2 d), no deformation has been induced during piston cylinder runs. Maps of plagioclase crystals orientations are able to observe polysynthetic twin crystals, visible by straight color change within plagioclase crystals (Fig. 4-4). Observation of twin crystals highlights that plagioclases are large poikilitic crystals including olivine crystals. These, interstitial plagioclase crystals can reach ~200 µm in OM02 and ~150 µm in OM20 (Fig.4-4 c and i). In OM20 sample, the abundance of interstitial phases (plagioclase and clinopyroxene) is smaller and porosity within the olivine matrix is lower than in OM02 sample. Large poikilitic crystals of clinopyroxene are observed in crystal orientation maps where large zones (100 to 300µm) show uniform crystal orientation. EBSD observation confirmed that plagioclase and clinopyroxene occur as large poikilitic crystals in olivine-rich troctolite and plagioclase-bearing dunite. Appendix 4-1 displays misorientation maps of plagioclase and clinopyroxene for experiment OM02 and OM20, highlighting that both phases present misorientation. We can assume that misorientations in all phases are due to the confining pressure during experiments

We selected 15 euhedral and 15 subhedral olivine crystals in runs OM02 (0.5 GPa, AH6) and OM20 (0.7 GPa, AH6). Figure 4-5 displays Mis2Mean and KAM maps of euhedral and subhedral olivine crystals from samples OM02 and OM20. Mis2Mean maps highlight misorientation within olivine crystal and KAM maps shows subgrain boundaries (or artefacts as rays on the sample). Subhedral grains from the two samples are tortuous with curvilinear grain boundaries, evidences of grain resorption. A huge amount of misorientations are visible in subhedral crystals compared with euhedral crystals. We highlighted with black arrows all the figures of crystal corrosion by the melt and observed (as in isothermal experiments) that it follows subgrain boundaries or zones highly misoriented. Figure 4-6 displays Shape factor

versus Grain orientation spread in selected crystals and highlight that grain tortuosity increases as function of increasing misorientations. Two clusters made of euhedral and subhedral olivine crystals are separated. Euhedral crystals present lower tortuosity and less misorientation, according to the maps previously presented. On the contrary, subhedral crystals are logically more tortuous and are less misorientated.

The EBSD observation of OM02 (0.5 GPa, AH6) and OM20 (0.7 GPa, AH6) highlighted that olivine dissolution preferentially starts at the subgrains boundaries, inducing the formation of tortuous olivine crystals. We also observed that pressure influences the texture. At higher pressure olivine crystals present more misorientations, more subgrains are more tortuous and present larger grain size variability.

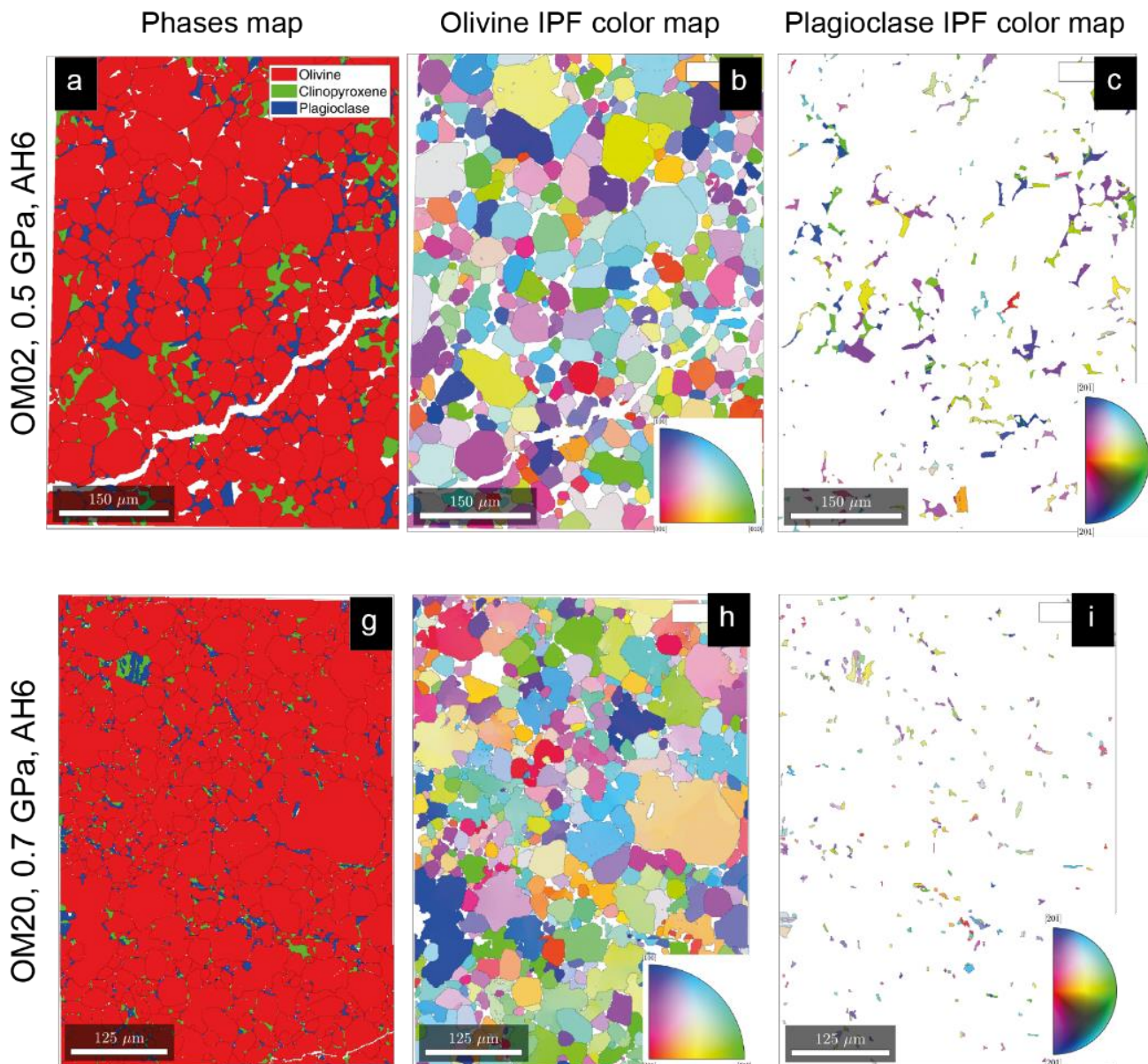
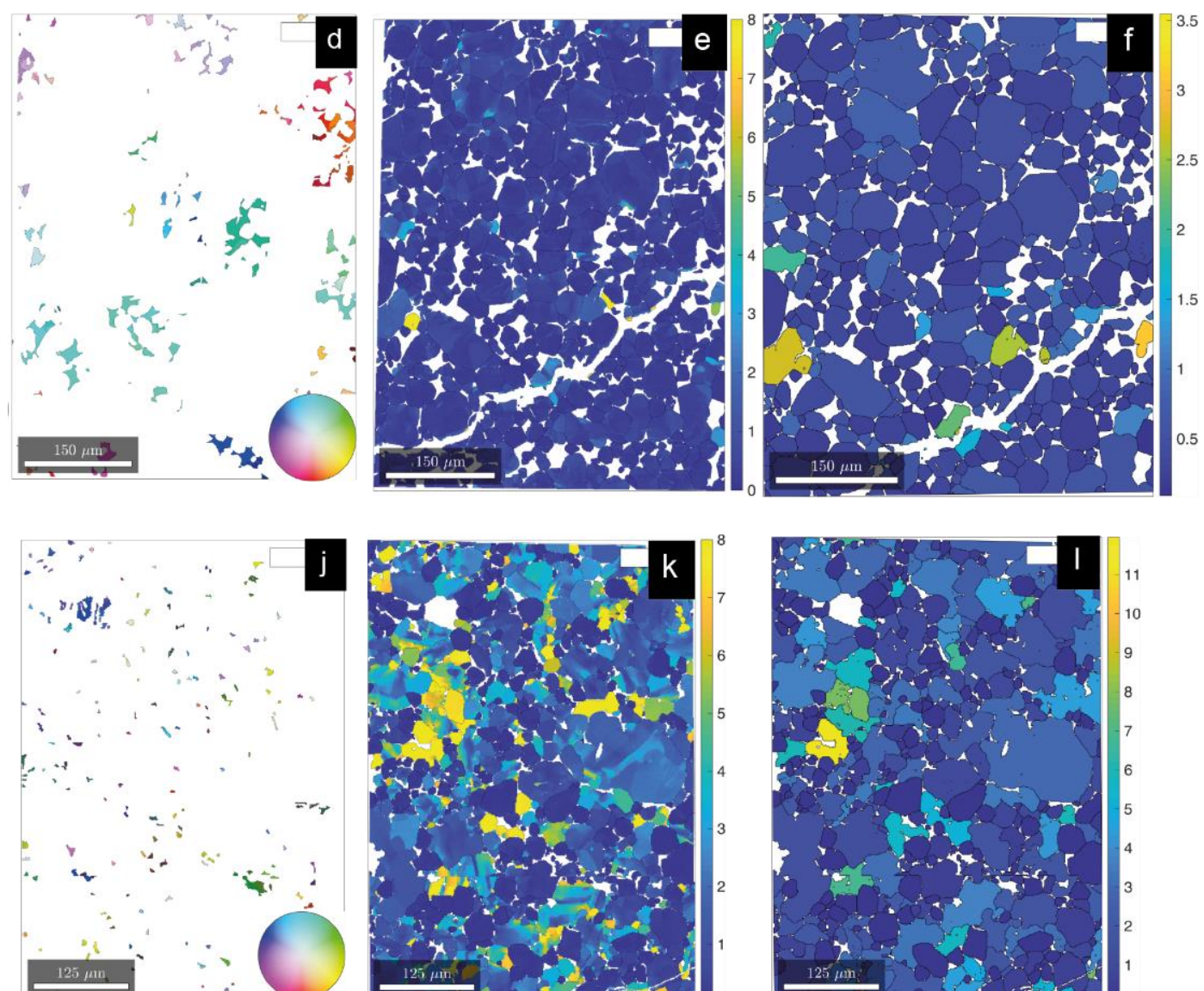


Figure 4-4: EBSD maps of the olivine-rich layer of OM02 and OM20. a and g: Phases distribution maps, b and h: olivine crystals orientation maps with IPF(inverse pole figure) colors, c and i: plagioclase crystals orientation maps, d and j: cpx crystals orientation maps, e and k: Olivine misorientation maps, f and l: Grain orientation spread maps. For IPF color maps of olivine, plagioclase and clinopyroxene we placed as legend corresponding colored inverse pole figures for orthorhombic, monoclinic and triclinic systems.

Clinopyroxene IPF color map **Olivine misorientation (degree)** **GOS in olivine**

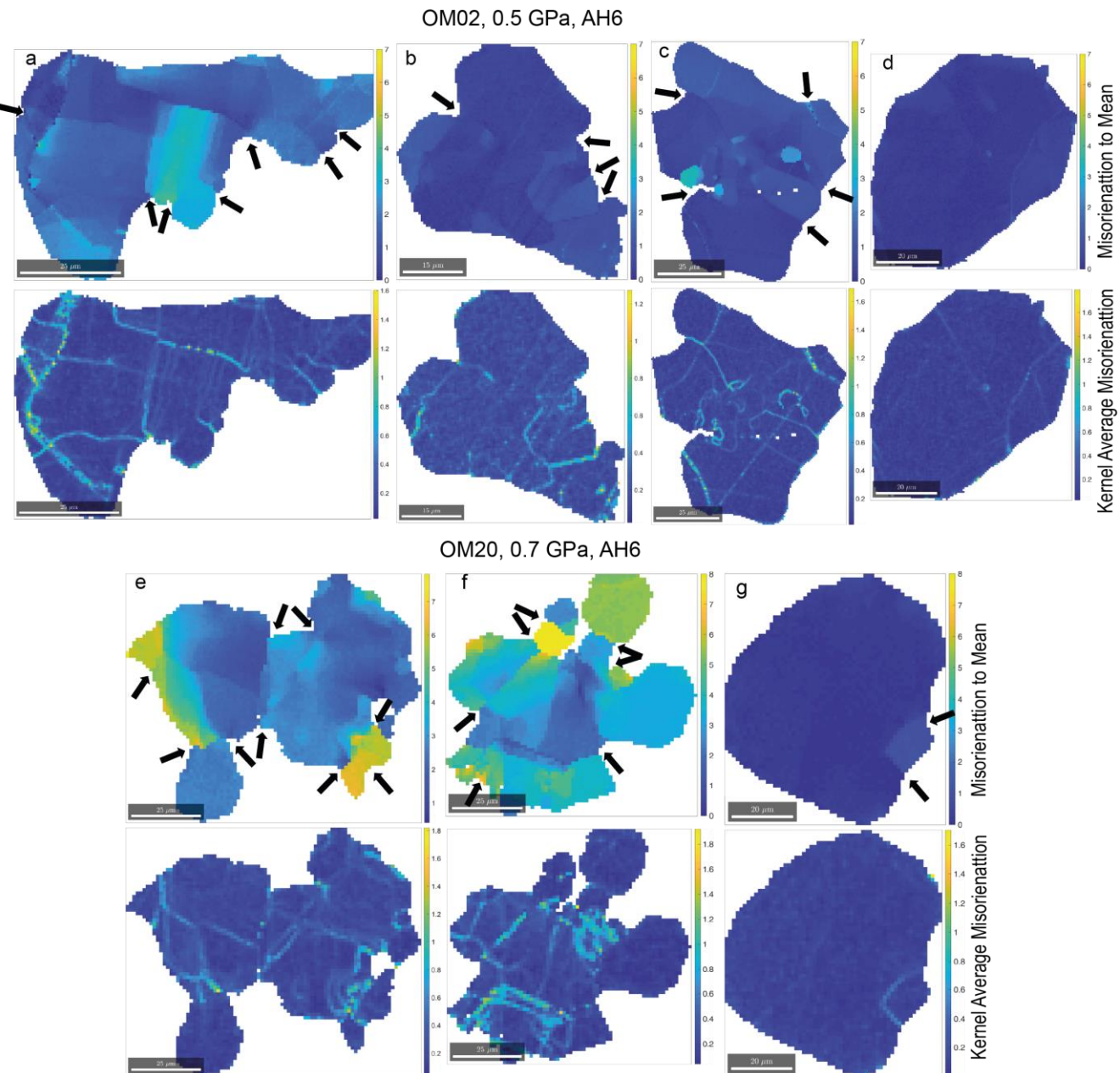


Figure 4-5: Misorientation maps and Kernel average misorientations maps for olivine single grains from OM02 and OM20. a, b, c, d represent Mis2Mean and KAM maps of grains from OM02 olivine crystals, and e, f, g represent olivine crystals from OM20. Black arrows mark olivine corrosion.

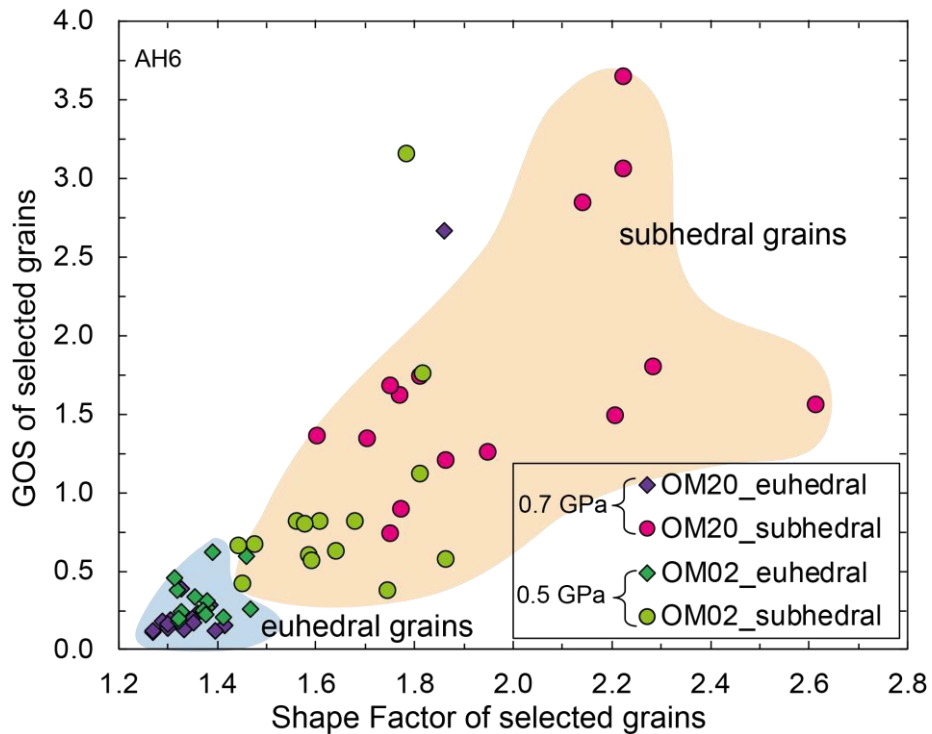


Figure 4-6: Shape factor versus Grain orientation spread for 60 selected grains (euhedral and subhedral) from OM02 and OM20 experiments. Diamonds represent euhedral olivines, whereas circles represent subhedral ones.

As a preliminary and explorative study we performed TEM observations in OM02 sample. The sample was prepared following the procedure of Chapter 2 (2.4.4). The final polishing procedure was performed attempting to include in the TEM sample all the phases, i.e. olivine, clinopyroxene, plagioclase and glass.

Investigations of the geometrical relation between olivine and glass at the nano-scale confirm that the preferential on-set of olivine dissolution are grain boundaries (Fig. 4-7a).

Figure 4-7c presents dislocations observed under 12 kX magnification. All dislocations are straight and parallel, following a unique direction. San Carlos olivine is known to be divided into several subgrains (50 to 200 μm large), with a dislocation density lower than $10^5/\text{cm}^2$ (or $10^{-3}/\mu\text{m}^2$) (Kohlshted and Goetze, 1974). Therefore a high density of dislocations in run charges (Fig. 4-7c) is an experimental result.

As piston cylinder experiments are expected to distribute pressure homogeneously to the sample, further work and more detailed analysis, including a profound comparison with San Carlos unreacted starting materials, are required in order to verify whether the occurrence of dislocations can be related to a slightly uneven distribution of pressure in experimental procedure or can be associated to melt-olivine reaction and olivine dissolution.

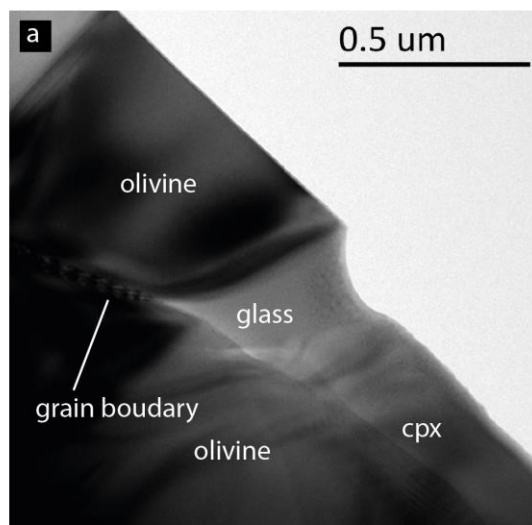
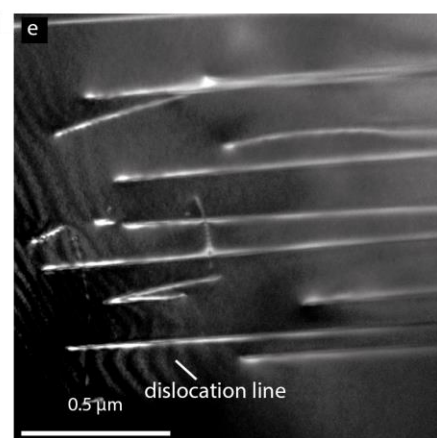
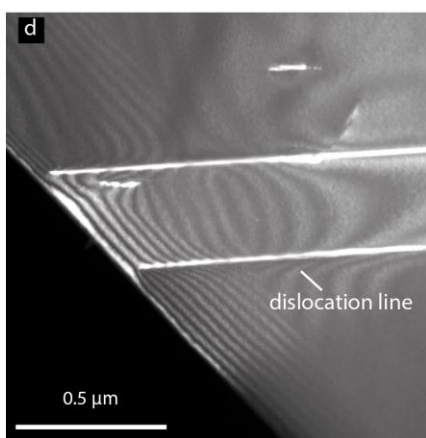
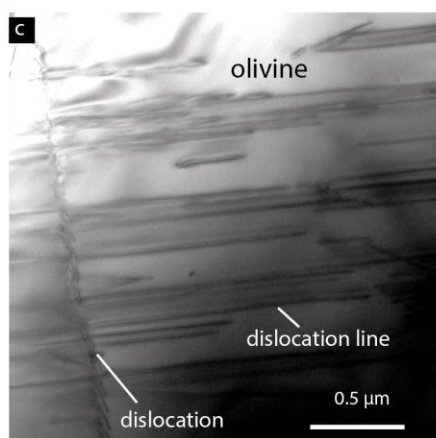
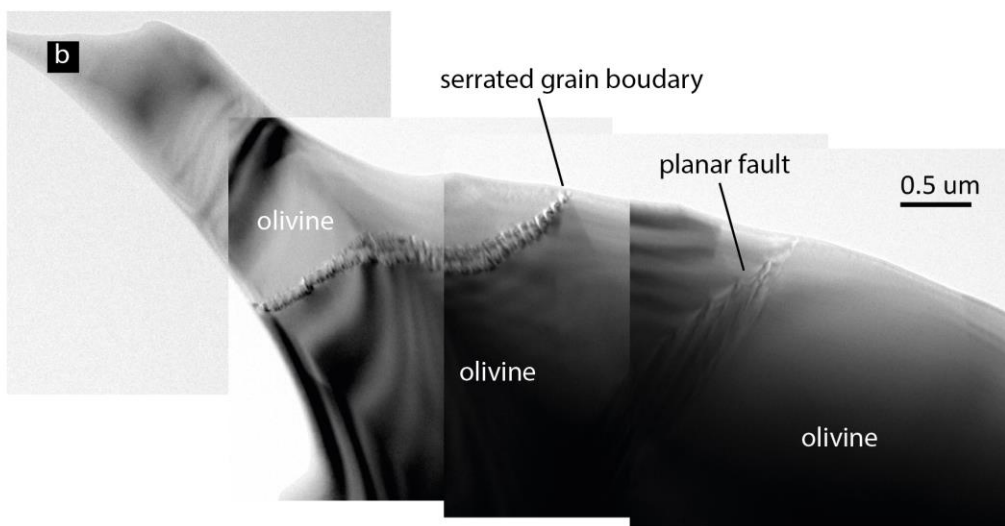


Figure 4-7: TEM micrographs from OM02 thin section at a) 20k X magnification b) 10k X magnification, c) 12 k X magnification and d) and e) 20k X magnification. The three images show the presence of dislocations within olivine grains. a) present a contact between olivine and corrosive melt. d) and e) are diffraction images from dislocations observed in c).



4.3. Mineral chemistry of reactive dissolution crystallization

Olivine, clinopyroxene and plagioclase compositions from olivine-rich layer of five step-cooled experiments were measured by microprobe analysis and are reported in Table 4-1, Table 4-2 and Table 4-3 (in Appendix).

4.3.1. Olivine composition

Olivine displays a large compositional variability along the olivine-rich layer. X_{Mg} and Ni content variations in olivine versus distance (from the interface between gabbro layer and olivine-rich layer to the top of capsule) are represented in Figure 4-8. In all step-cooled experiments, X_{Mg} in olivine systematically displays an increase from the interface (bottom) to the carbon spheres layer (top). At the interface, a zone of ~0.25 mm within the interface between olivine-gabbro and the olivine-rich layer, olivine chemical compositions display a large heterogeneity (Fig. 4-7),

A higher heterogeneity in olivine X_{Mg} composition observed at 0.7 GPa highlights an effect of pressure on olivine compositions. Along the olivine-rich layer, OM20 (0.7 GPa, AH6) displays an increase of X_{Mg} from 0.83 at the interface to 0.89 at the top, whereas OM02 (0.5 GPa, AH6) displays variations of X_{Mg} from 0.87 to 0.90 (Fig. 4-7a and c). On the contrary, larger core to rim composition variations in olivine are observed at lower pressure, with systematical lower X_{Mg} in olivine rims. Olivine grains displays core to rim variations from 0.89 to 0.88 in OM02, and no significant one in OM20 (Fig. 4-7). No significant correlation between olivine composition and starting melt composition has been found in the olivine-rich layer. At 0.5 GPa, OM03 (HDRBC) olivine X_{Mg} varies from 0.88 to 0.90 (Fig. 4-7), similarly to OM02. Additionally, in Figure 4-8a and c, shaded grey area represent the X_{Mg} of olivine in equilibrium crystallization experiments using melt AH6 from 1150 °C (lower values) to 1225 °C (higher values) at 0.7 and 0.4 GPa, (Husen et al., 2016). Olivines from the olivine-rich layer in our reaction experiments never match the values resulting from simple equilibrium crystallization (Fig. 4-7).

Olivines retaining the composition of San Carlos olivine were almost never found in step-cooled experiment, indicating that the starting olivine composition is totally erased by melt-olivine reaction. We compared the step-cooled experiment OM20 (0.7 GPa, AH6) and the

isothermal experiment OM15 (0.7GPa, AH6, 1250 °C). Despite the difference of capsule length between OM15 and other experiments run at 0.7 GPa, the trend of X_{Mg} against distance of olivine is comparable to the one of OM20 (Fig. 4-7c). In OM15, San Carlos olivine composition has been only retained at the top of the experimental charge (Fig. 4-7c), whereas OM20 systematically presents olivines with $X_{\text{Mg}} < 0.90$ (Fig. 4-7c). Such result indicates that olivine composition is affected by the reaction with starting melt, already during the first high-temperature step, although olivine composition further evolves during the step-cooled procedure.

Variations of Ni content in olivine with distance (Figure 4-8b and d) define a bell-shaped trend for all experiments at 0.5 GPa and 0.7 GPa. Indeed, Ni content in olivine displays maximum value at about the middle of olivine-rich layer and decreases at the contact with the carbon spheres and the olivine-gabbro. The maximum value is about 2600 ppm at 0.5 GPa and 3400 ppm at 0.7 GPa (Fig. 4-7b and d). Minimum Ni contents are below the limit of detection of the microprobe analysis, reflecting the equilibration with starting melts, which are Ni-free (Table 2-1). Remarkably, olivine Ni content across the olivine-rich layer is systematically lower than the San Carlos olivine values (~2800 ppm), except for few olivines in OM20 (0.7 GPa, AH6) with Ni content up to 3400 ppm (Fig. 4-7d). As for X_{Mg} , cores of olivine have slightly higher Ni content than rims, for example from 629 to 1886 ppm in OM02 and from 2957 to 3112 ppm in OM20 (Fig. 4-7 and Tab. 4-2 → analysis OM02-88 and 89 and OM20-08OC and OR). Again, the core-rim variability is larger at 0.5 GPa than at 0.7 GPa (Fig. 4-7).

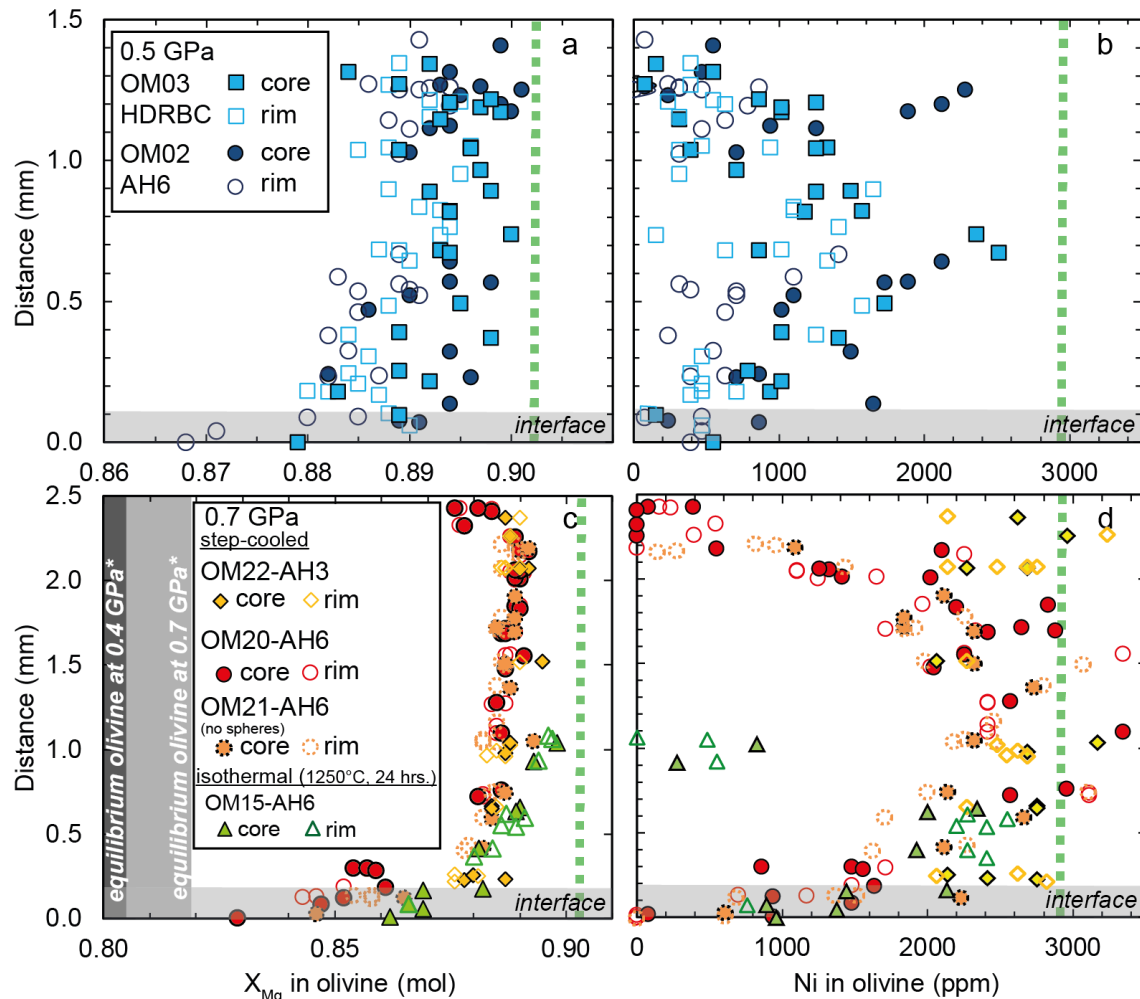


Figure 4-8: X_{Mg} (a, c) and nickel abundance (b, d) in olivine as a function of distance (in mm) for each experiment. Distance = 0 mm marks the ol-gabbro/olivine-rich layer boundary. For a better readability we separated data from experiments at 0.5 GPa on the top and 0.7 GPa on the bottom. Empty symbols represents data from rim analysis and full symbols represents cores. Composition of San Carlos olivine is represented by green dashed line. As well, we represented field of composition of olivine crystallized at equilibrium from the melt AH6 at 0.7 GPa from 1250 °C to 1200 °C and 0.4 GPa from 1225 °C to 1150 °C (Husen et al., 2016), in gray.

4.3.2. Plagioclase chemistry

Figure 4-9a displays Anorthite content (X_{An}) variations in plagioclase versus distance, along the olivine-rich layer, in OM02, OM03, OM20, OM21 and OM22. For experiments conducted with melt AH6 (OM02 and OM20), the maximum variability of X_{An} in plagioclase is observed within the interface zone of 0.25 mm previously described.

In the olivine-rich layer (interface excluded), the maximum X_{An} heterogeneity observed ranges from 0.61 to 0.68 in OM02 (0.5 GPa, AH6) and 0.59 to 0.68 in OM20 (0.7 GPa, AH6) (Fig. 4-8a). At 0.7 GPa, plagioclase varies towards lower X_{An} . Moreover, at 0.7 GPa, in

experiments OM20 (0.7 GPa, AH6) and OM21 (0.7 GPa, AH6, no carbon spheres), plagioclases present a bell-shaped profile of X_{An} along the olivine-rich layer.

At 0.5 GPa, plagioclases analyzed in experiments OM02 (0.5 GPa, AH6) and OM03 (0.5 GPa, HDRBC) do not show significant difference in X_{An} that decreases from bottom to top along the olivine-rich layer, from 0.72 at the interface in both runs, to 0.61 in OM02 and 0.62 in OM03 (Fig. 4-8) olivine-rich. Plagioclase analyzed within the carbon spheres of OM02 has the lowest X_{An} (0.52). On contrary, significantly lower X_{An} values have been found in plagioclases from OM22 (AH3, 0.7 GPa), from 0.53 to 0.62, and it likely reflect different X_{Ca} of starting melt (Tab. 2-1).

In Figure 4-9a, we also reported compositions of plagioclase from equilibrium crystallization experiments with AH6 at 0.4 and 0.7 GPa and temperature from 1225 to 1150 °C (Husen et al., 2016). Plagioclases resulting from crystallization of reacted melt at 0.5 GPa plots well far from composition of plagioclase in equilibrium crystallization experiments except for few plagioclases at the interface. At 0.7 GPa, equilibrium composition is reached only in the middle of the olivine-rich layer around 1.25 mm from the interface. However, plagioclases from reacted experiments systematically vary towards lower X_{An} values (Fig. 8-8a), both for melt AH6 and AH3.

In order to further investigate the heterogeneity of plagioclase composition, we realized a focused study on single plagioclase interstitial grains from experiment OM20 (0.7 GPa, AH6), illustrated by Figure 4-9b and c. In Figure 4-9b we reported Al_2O_3 over X_{An} for three single plagioclases, whilst Figure 4-9c represents EBS images of the analyzed single plagioclases. We also reported compositions of plagioclase crystallized at equilibrium from AH6 from Husen et al. (2016); several analyses give X_{An} lower than equilibrium plagioclase. The three studied plagioclases present a high variation of X_{An} , one from 0.62 to 0.69 being the largest within the plagioclase represented in yellow. Consistently, the highest X_{An} value corresponds to the highest Al_2O_3 content. The plagioclase represented in orange highlights core-rim variation (from $X_{An} = 0.67$ in the core, to 0.61 and 0.65 in the rims).

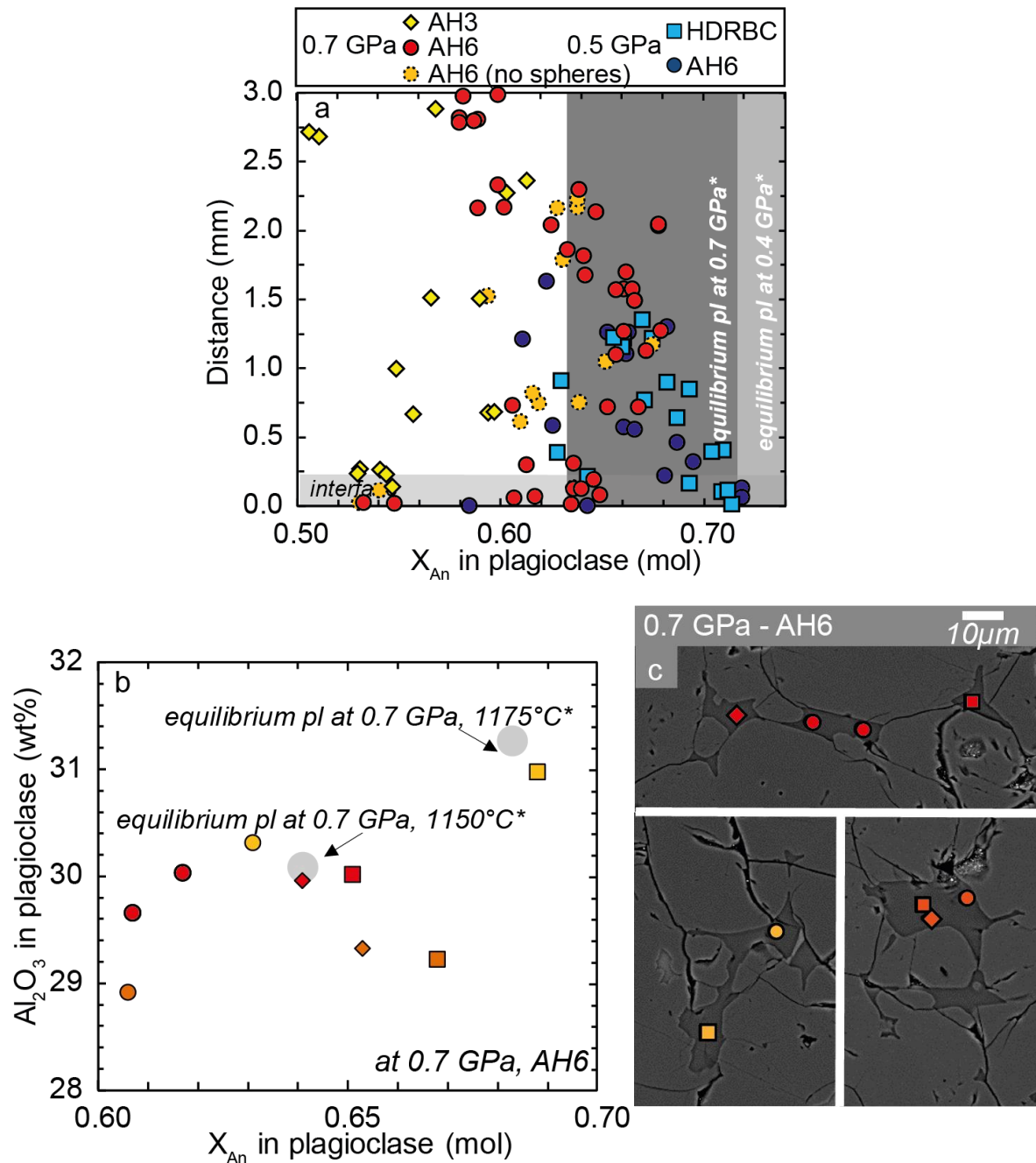


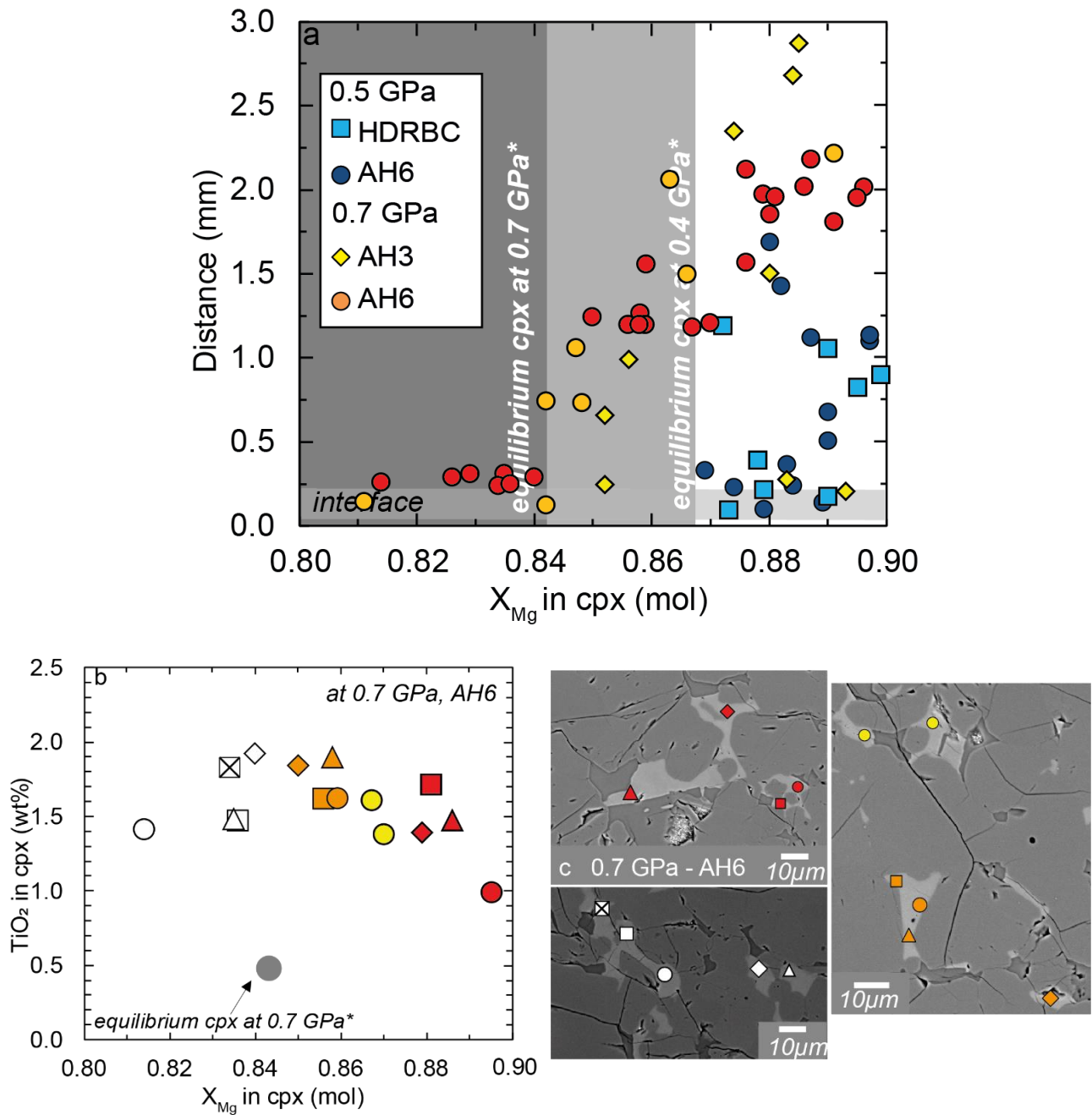
Figure 4-9: Composition of plagioclase from the olivine-rich layer. (a) Anorthite content in plagioclase as a function of distance (in mm) for each experiment. Distance = 0 mm marks the ol-gabbro/olivine-rich layer boundary. We represented compositions of plagioclase crystallized at equilibrium from the melt AH6 at 0.7 GPa and 1150 °C and 1175 °C (Husen et al., 2016), in gray. (b) X_{An} vs Al_2O_3 in selected plagioclases from the experiment OM20, each symbol corresponding to the one used in (c) BSE images illustrating large poikilitic plagioclase.

4.3.3. Clinopyroxene chemistry

Clinopyroxene from the olivine-rich layer displays a large variability. Figure 4-10a shows $X_{\text{Mg}} = (\text{Mg}/(\text{Mg}+\text{Fe}_{\text{tot}}))$ values of clinopyroxene vs. distance. X_{Mg} variability in

clinopyroxene is higher at 0.7 GPa than at 0.5 GPa. At 0.5 GPa, X_{Mg} varies from ~0.87 at the interface to ~0.90 in the upper part of the olivine-rich layer (Fig. 4-9a). At 0.7 GPa, in experiments with melt AH6 (OM21 and OM20), similar profiles along the capsule present a progressive increase of X_{Mg} with distance, from 0.81-0.84 at the interface to 0.89 on the top of the olivine-rich layer in OM21 and 0.83 to 0.90 in OM20. In Figure 4-10a, the equilibrium compositions reported by Husen et al. 2016 are indicated as reference (shaded grey area, lower values correspond to lower temperatures). Equilibrium composition is reached only in the first 0.75 mm of the olivine-rich layer at 0.7 GPa. Few clinopyroxenes have been analyzed in OM22 (0.7 GPa, AH3) sample but a general increase of X_{Mg} with distance similar to OM20 (0.7 GPa, AH6) one is observable. X_{Mg} is slightly higher in OM22. As observed for plagioclase the highest heterogeneity is observed at the interface, along the first 2.50 mm of the olivine-rich troctolite.

In order to check any compositional zonation in interstitial crystals, we performed a focused study on single clinopyroxenes from experiment OM20 (0.7 GPa, AH6). Figure 4-10b illustrates variations of X_{Mg} against TiO_2 content in analyses pointed in various colors on Figure 4-10c. The highest variability observed is from 0.81 to 0.84 in the clinopyroxene pointed with white symbols. Clinopyroxene presents high intracrystalline chemical variability.



4.4. Discussion

The three-layers setup was employed to favor melt percolation through dunite at experimental conditions. We used carbon spheres at the top of the olivine-layer to induce advection melt percolation upward in the capsule (e.g. van den Bleeken et al., 2010), and possibly enhance the extent of melt-olivine reaction. Our experiments indicated that pre-impregnation of the dunite by the starting melt improved the melt percolation at the first stage of the step cooling procedure. Indeed, the liquidus temperatures of starting melts, i.e. 1225 °C at 0.5 GPa and 1250 °C at 0.7 GPa for starting melt AH6 and ~1210 °C for AH3 (Husen et al., 2016), are far below the San Carlos olivine solidus (around 1800 °C; Bowen and Schairer, 1932). Thus, the presence of liquid within the olivine matrix imposed a preexistent pathway for the melt advection driven by the spheres, simulating reactive porous melt flow as previously documented by Saper and Liang (2014). As the layer of carbon spheres has a limited in volume capacity, once the trap has been filled by melt in the early stage of the experiment, the system can be considered as closed, and melt percolation in the charge drastically inhibited. Additional experiments performed at 1300 °C and 0.5 GPa for short durations, highlight that after 20 minutes at experimental conditions the melt trap is already filled, closing the system.

4.4.1. Role of Pressure on textures and mineral chemistry

4.4.1.1. The role of pressure on textures

Estimates of modal abundances of olivine and interstitial phases (plagioclase and clinopyroxene) in olivine-rich troctolite show significant differences as a function of pressure. In runs OM02 (0.5 GPa) and OM20 (0.7 GPa), the average abundance of olivine in the olivine-rich layer is 84 and 91%, respectively (Fig.4-3). At 0.5 GPa the olivine-rich layer obtained is olivine rich-troctolite while it is plagioclase- and clinopyroxene-bearing dunite at 0.7 GPa. At lower pressure, the final lower abundance of olivine likely resulted from higher porosity within the olivine matrix at the first high-temperature stage of experiment. Therefore, pressure influences the extent of olivine dissolution, as well as, the final abundances of olivine and interstitial phases.

At 1300 °C, above the liquidus (i.e. > 1245 °C at 0.7 GPa, and > 1225 °C at 0.5 GPa),

olivine reacted in some extent with interstitial melt, because melt (AH6; $X_{\text{Mg}}61$), and San Carlos olivine (Fo_{90}) are in disequilibrium. This leads to reactive dissolution of olivine that, in turn, results in higher porosity within the dunite. At 0.5 GPa, as the experiment stays for a longer duration over the liquidus temperature, the olivine dissolution by the melt is enhanced.

During the cooling, once the liquidus of the reacted melt is crossed, clinopyroxene plagioclase and olivine can crystallize from the reacted melt. This step leads to the reduction of porosity by recrystallization of olivine and crystallization of clinopyroxene and plagioclase as interstitial phases. As a consequence, the local melt flow is progressively precluded. Crystallization begins at higher temperature at 0.7 GPa than at 0.5 GPa (Husen et al., 2016). As the extent of crystallization is higher at higher pressure the final porosity is therefore lower and explains the inability to produce olivine rich-troctolite at 0.7 GPa with an initial dunite impregnation rate of 9%. Olivine-rich troctolite formed at 0.5 GPa starting from a dunite impregnation rate of 9%.

EBSD results indicated that misorientations and subgrain abundance increases as a function of increasing experimental pressure (Fig. 4-3 e and k). Therefore, a more massive disruption of olivine along subgrain boundaries (Boudier 1991, Erdmann et al. 2014) occurs at higher pressure and generate a large amount of olivine small crystals as observed in phase abundance maps (Fig. 4-2 and Fig. 4-3 a and g).

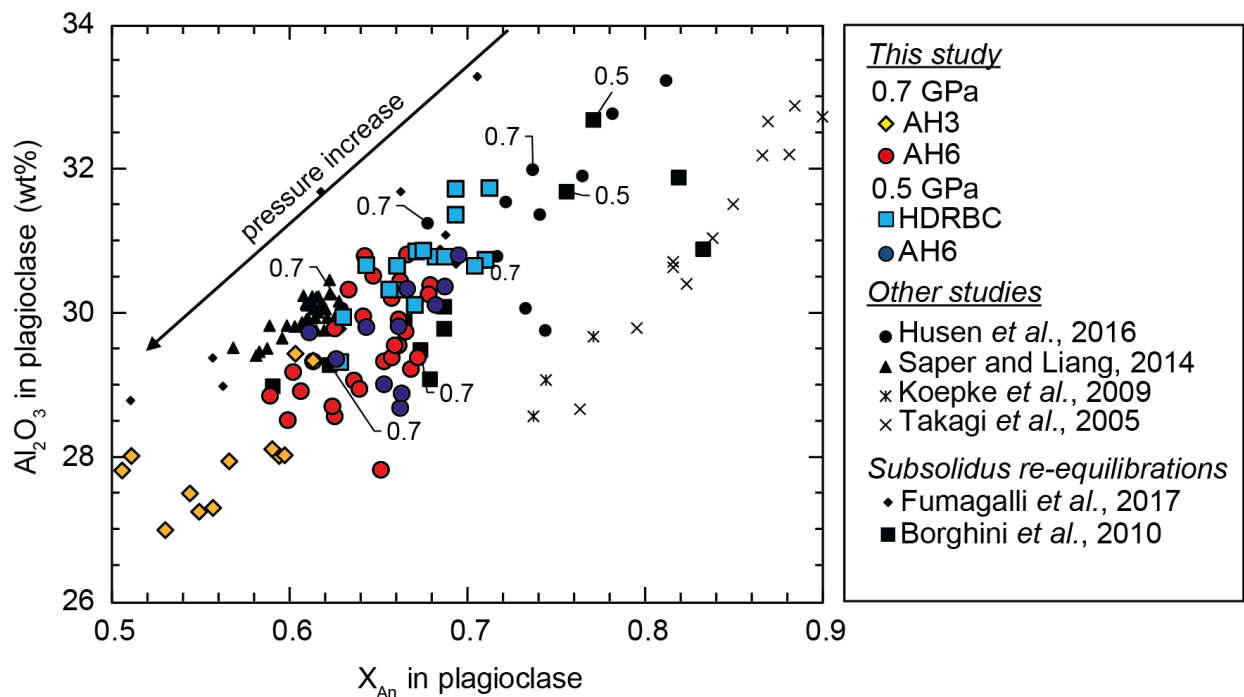


Figure 4-11: Variations of X_{An} vs. Al_2O_3 in plagioclase for each step-cooled experiment at 0.5 and 0.7 GPa in colored symbols. Compositions of plagioclases from other experimental studies at equilibrium (Husen et al., 2016; Koepke et al., 2009 and Tagaki et al., 2005), from reactive dissolution (Saper and Liang, 2014), and subsolidus re-equilibration (Fumagalli et al., 2017 and Borghini et al., 2010). We reported the arrow of pressure increase tendency, Al_2O_3 and X_{An} generally decrease with increasing pressure.

4.4.1.2. The role of pressure on mineral compositions

The effect of pressure on the olivine-rich layers of experimental charges is also visible in the chemistry of plagioclase and clinopyroxene resulting for reactive crystallization process.

Plagioclase composition depends on pressure. As demonstrated by previous experimental studies on plagioclase-melt equilibria, at dry conditions, X_{An} in plagioclase decreases with increasing experimental pressure (e.g. Longhi et al., 1993; Panjasawatwong et al., 1995; Takagi et al., 2005). We reported Al_2O_3 vs X_{An} in plagioclase for the olivine-rich layer of each experiment in Figure 4-12. Comparing data from experiments at 0.7 and 0.5 GPa with melt AH6, we observe plagioclase with a lower X_{An} an Al_2O_3 content crystallized at higher pressure. This follows experimental data on equilibrium crystallization, reactive dissolution and sub-solidus re-equilibrations (e.g. Takagi et al., 2005; Koepke et al., 2009; Boghini et al., 2010; Saper and Liang, 2014; Husen et al., 2016; Fumagalli et al., 2017) represented on Figure 4-12. However, Al_2O_3 and X_{An} content in plagioclase is expected to decrease with increasing temperature (Eq. 26, Putirka, 2005 and Winter, 2014). Step-cooled experiments have been conducted following the same temperature path (see Fig. 2-4e), therefore a large range of

plagioclase composition could be expected from the crystallization of plagioclase during progressive cooling at 1250, 1200 and 1150 °C. In addition, NaSi-Ca₁Al₁ diffusion in plagioclase is known to be very slow (Grove et al., 1984; Liu and Yund, 1992; Costa et al., 2003), resulting in plagioclase zoning. It contributes to enlarging the chemical variations observed in single crystals of plagioclase (Fig. 4-9b and c). Regarding X_{An} and Al behavior with temperature, we could expect plagioclase cores with lower X_{An} and Al₂O₃ content as they crystallized first at higher temperature and a progressive decrease toward the rims, but within the olivine-rich layer the poikilitic nature of the crystals unable us to identify cores or rims in a 2-dimensions observation. Another complementary explanation for the large range in plagioclase compositions could be due mainly to different degrees of fractionation in melt pockets or different buffering phases (clinopyroxene or olivine) adjacent to the melt pocket (Saper and Liang, 2014).

Pressure also influences the clinopyroxene composition. Several geobarometers are based on clinopyroxene composition or clinopyroxene-melt equilibrium, *inter alia*, variations in the clinopyroxene component jadeite (NaAlSi₂O₆; Jd) (Nimis, 1995; Nimis and Ulmer, 1998; Nimis and Taylor, 2000; Putirka et al., 1996, 2003; Masotta et al., 2003). Jd in clinopyroxene increases with increasing pressure (Eq. P1 and P2 in Masotta et al., 2013). In Figure 4-12, two clusters are distinct for both pressures. Clinopyroxene crystallized at 0.5 GPa (OM02) have a lower Jd content [*i.e.* 0.014-0.031] and at 0.7 GPa (OM20) a higher Jd content [*i.e.* 0.028-0.053]. Additionally, Jd in clinopyroxene decreases with increasing temperature, explaining the large variation in clinopyroxene composition resulting from crystallization at decreasing temperature during the step-cooling procedure. The variations in TiO₂ in clinopyroxene follows the Jd trend and can also be attributed to the different temperatures of crystallization. Therefore, the intragranular variations of chemical compositions in clinopyroxene (within single grains) can be the result of the experimental step-cooled temperature path.

We attributed the large intragranular variability of chemical compositions of plagioclase and clinopyroxene to the step-cooling procedure. However, the chemical variability is larger at higher pressure, where porosity is lower (Fig. 4-3) and therefore melt percolation is less intense. We also assumed that early during the experiment, the melt has reached the top of the capsule and melt percolation weak. Therefore, melt is reacting with surrounding olivine and does not circulate easily, involving an evolution as a trapped melt, stronger at the highest pressure. Additionally, we observed a TiO₂ content in clinopyroxene higher at 0.7 GPa than at

0.5 GPa coupled with a rather constant X_{Mg} within the olivine-rich layer of each step-cooled experiment (Fig. 4-12a). The quite constant X_{Mg} composition for olivine and clinopyroxene attests that olivine from the olivine-rich layer is able to buffer the Fe-Mg composition of the percolating melt, but it does not buffer most incompatible elements as Ti and REE which concentrated in the melt (Barnes, 1986; Meyer et al., 1989). Therefore, high TiO_2 content with rather constant X_{Mg} is expected for clinopyroxene crystallizing from trapped melts (Borghini and Rampone, 2007). This trapped melt effect could be at the origin of the intergranular variations of chemical composition. Extremely high TiO_2 contents support the assumption that due to the low porosity, melt circulate less at higher pressure 0.7 GPa, evolving as a trapped melt.

Few effect of pressure are observed in olivine compositions due to the Mg-buffering effect of the reacted melt. Firstly, at lower pressure we observed higher core-rim variations in X_{Mg} and Ni content (Fig. 4-7). Such variations of core-rim variations as a function of pressure can be directly linked to the melt-rock ratio. Indeed, we can assume that lower X_{Mg} and Ni in olivine rim at 0.5 GPa can be obtained by a lower buffering effect. This hypothesis is supported by the fact that interstitial melt proportion is more abundant at 0.5 GPa (see 4.4.1 and Fig. 4-3). Then, at higher pressure olivine is richer in Ni (Fig. 4-7 d).

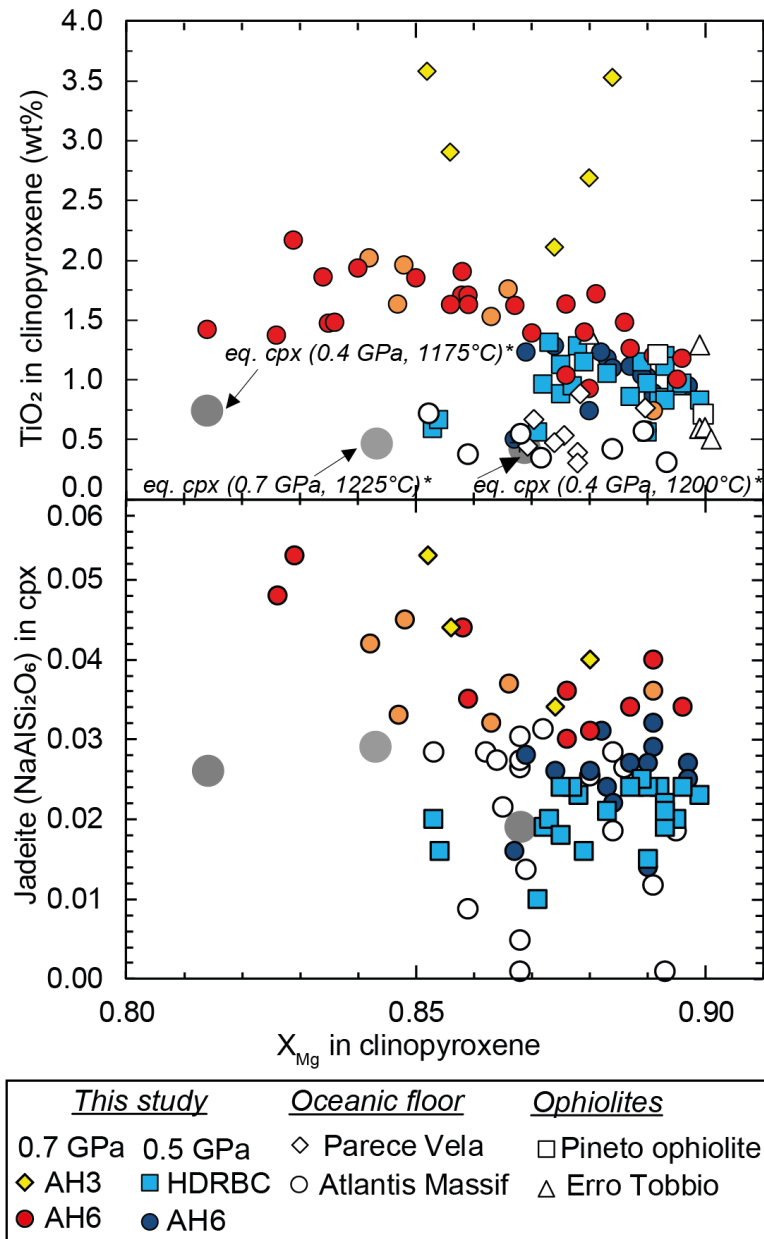


Figure 4-12: Variations of a) TiO_2 and b) Jadeite (Jd) vs X_{Mg} in clinopyroxene from the olivine-rich layer of each step-cooled experiment, and natural olivine-rich troctolite the Godzilla Megamullion (Sanfilippo et al., 2013), the Atlantis Massif (Drouin et al., 2009), the Pineto ophiolite (Sanfilippo and Tribuzio, 2013) and Erro-Tobbio ophiolite (Borghini et al., 2007). We also reported composition of clinopyroxene crystallized at equilibrium at 0.4 and 0.7 GPa from the starting melt AH6 from Husen et al., 2016.

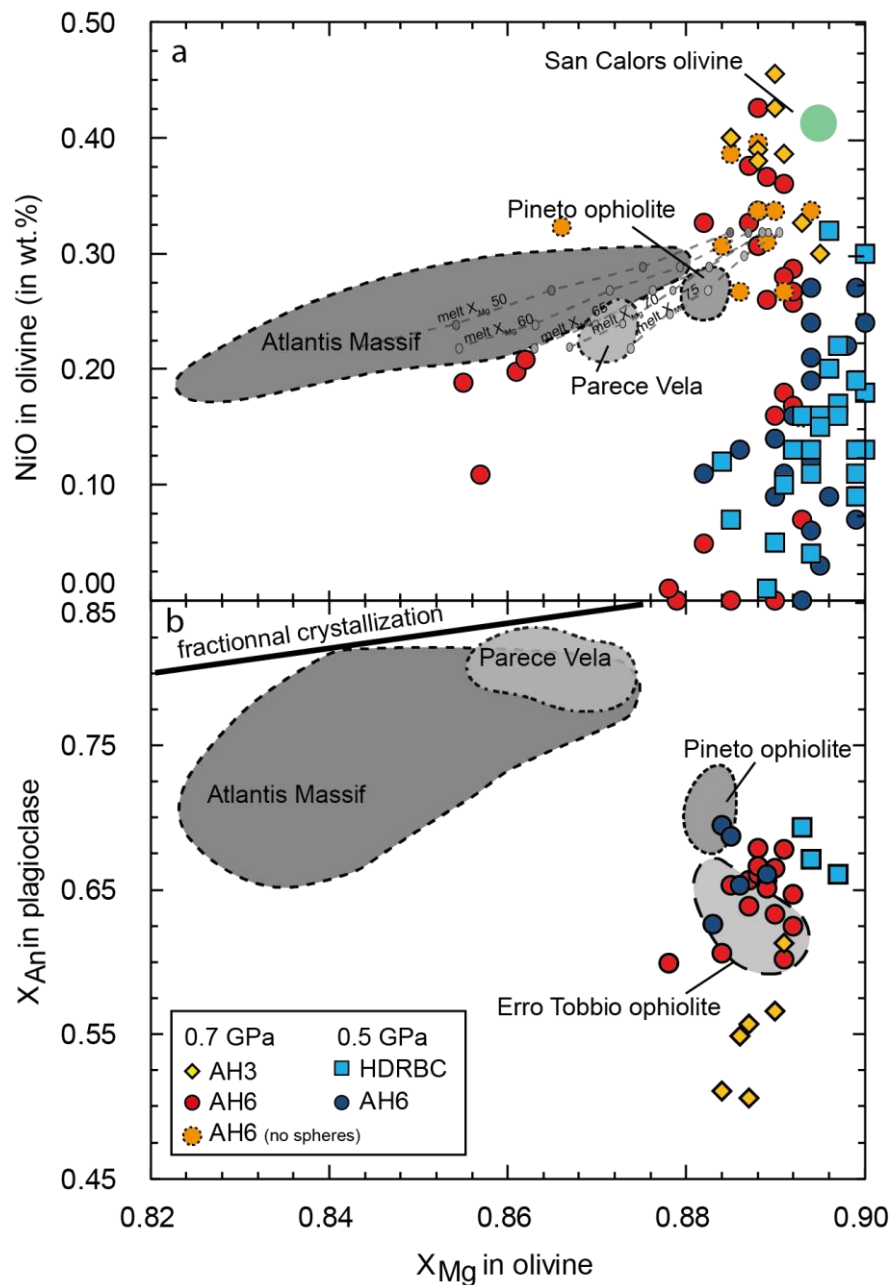


Figure 4-13: Variation of a) X_{Mg} versus NiO content in olivine and b) X_{Mg} in olivine vs anorthite content in plagioclase for rims of couples of mineral from the olivine-rich layer of each step cooled experiment performed for this study. Compositional fields defined by natural olivine-rich troctolites from are shown. The fractional crystallization trend for the melt AH6 is represented by the black bold line, this trend is represented by a linear regression on the complete data from of AH6 crystallization experiments (Husen et al., 2016). In a) dashed lines represent olivine compositions calculated for an AFC model involving 5 different melts at different assimilation percentage (10%) per point from Sanfilippo et al. (2013).

4.4.2. The role of melt composition on textures and mineral chemistry

Melt composition does not significantly affect the texture resulting from reactive dissolution and crystallization and mineral chemistry. At higher pressure (0.7 GPa), we do not observe any difference between phase abundances of the olivine-rich layer of experiments conducted with melt AH6 and AH3 (Fig. 4-4 b). At lower pressure (0.5 GPa), a slight difference have been observed between the experiments OM02 (AH6) and OM03 (HDRBC), indeed, a slight difference in abundance of olivine along the olivine-rich layer of the experiment OM03 have been overserved (Fig. 4-3 c). Olivine content is higher on the upper half of the olivine-rich layer, maintaining the original olivine content of 91% (against 9% of interstitial phases). The interface is diffuse but can be compared to the wehrlite/orthopyroxene-bearing plagioclase peridotite interface observed by Saper and Liang (2014) and assumed to be a lithological marker for the reaction front. Olivine dissolution is more intense in the zone at the contact with the melt reservoir olivine-rich. This reactive boundary layer is assumed to propagate through the olivine-rich layer, until the carbon spheres layer (Saper and Liang, 2014). Indeed, all other experiments where no interface has been observed within the olivine-rich layer, the reactive boundary layer reached the top of the capsule. As the reactive boundary layer did not reach the top of the capsule on the OM03 experiment conducted with the starting melt HDRBC, we can assess that the melt is less reactive and dissolve less olivine than AH6 and AH3 melts. Knowing that melt HDRBC ($X_{\text{Mg}}=0.74$) is rather in equilibrium with San Carlos olivine (Fo_{90}), such a behavior was expected. Image analysis on olivine-rich layer based on X-Ray maps does not able to discriminate accurately clinopyroxene and plagioclase. Therefore, the effect of melt on relative abundances of plagioclase and clinopyroxene cannot be evaluated with this technique. At 0.7 GPa, there is no difference in phase abundance between experiments conducted with melt AH3 and AH6, suggesting that compositional differences between both melts is not enough to induce difference in olivine dissolution.

Starting melt composition has an effect on the chemistry of plagioclase and clinopyroxene, as previously observed in previous studies from Van den Bleeken et al. (2010). On contrary, no melt composition influence on olivine has been observed olivine-rich layer. Plagioclase crystallized from the most primitive melt (HDRBC) has a slightly higher Al_2O_3 content and X_{An} than plagioclase crystallized from AH6. Reversely, plagioclase crystallized from the most evolved melt (AH3) has a lower Al_2O_3 and X_{An} content (Fig. 4-11), as expected.

Indeed, the study performed by Husen et al. (2016) on melt AH3 and AH6 showed that plagioclase crystallized at equilibrium, at 0.7 GPa, ranges between An₅₇~An₆₁ and An₆₄~An₇₃ respectively, consistently with starting melt X_{Ca} (Tab. 2-1).

Finally, clinopyroxene composition (X_{Mg}, Jd and Cr₂O₃) is not dependent of starting melt composition. Only TiO₂ is affected by starting melt composition in the run OM22 (0.7 GPa, AH3), deviating completely from the TiO₂-X_{Mg} trend expected by a fractional crystallization. Such a deviation can be explained by the higher TiO₂ content of the melt AH3 coupled with the trapped melt effect described previously. Indeed, isothermal experiments (see Chapter 3) has been performed with melts AH3 and AH6 and highlighted that reacted melt viscosity depending on the starting melt composition. We analyzed reacted melts from the olivine rich-layer of two isothermal experiment OM14 and OM15, performed at 1250 °C and 0.7 GPa for 24 hours with melts AH3 and AH6 respectively, which can be considered as analogues of step-cooled experiments OM22 and OM20 at the end of the second temperature step, before the crystallization of plagioclase and clinopyroxene. As an indication, we calculated the average dry viscosity (in Log base 10 in Pa.s, Pascal second) from these analysis using McBirney, A.R., 1993 in Hollocher CIPW excel spreadsheet. We obtained an average of 0.24 for OM15 (0.7 GPa, AH6, 24 hrs.) and 0.30 for OM14 (0.7 GPa, AH3, 24 hrs.). As viscosity is expected to be higher in experiments conducted with the melt AH3, we expect a lower melt mobility but also a lower element diffusion in the melt which is preventing from melt chemical homogenization, improving the trapped melt effect, and lowering the extent of olivine-dissolution (Chen and Zhang, 2008; Soulié et al., 2017).

4.4.3. Comparison with natural occurrences

Results of experiments of this work, in terms of textures and phase compositions, can provide constrains on the interpretation of olivine-rich troctolites from natural occurrences, possibly supporting their origin by melt-rock interaction between dunite and percolating basalts at the mantle-crust transition. In this section, we discuss the experimental data by comparing them with data from three well-known case studies from oceanic and ophiolitic settings (Borghini et al., 2007; Drouin et al., 2009; 2010; Sanfilippo et al. 2013; Sanfilippo and Tribuzio 2013; Rampone et al., 2016).

4.4.3.1. Olivine-rich troctolite textures

Olivine-rich troctolites and dunites generated by melt-rock reaction experiments at 0.5 and 0.7 GPa showed textural similarities with olivine-rich troctolite from oceanic lithosphere, as Atlantis Massif (Suhr et al., 2008; Drouin et al., 2009), and ophiolites from Ligurian Alps (Borghini et al., 2007; Rampone et al., 2016) and Corsica (Sanfilippo and Tribuzio, 2013; Sanfilippo et al., 2015), inferred to be originated by melt-rock reactions. Olivine, either euhedral or irregular, show lobate and embayed contacts against plagioclase and clinopyroxene (e.g. Rampone et al., 2016), perfectly matching what observed in this experimental study. Therefore, our reactive dissolution and in-situ recrystallization experiments support the interpretation of a melt-rock reaction origin for those olivine-rich troctolites, troctolites and plagioclase-bearing ultramafics on the basis of this textural evidence.

At 0.5 and 0.7 GPa olivine dissolution occurs along subgrain boundaries regardless of melt composition and leads to the formation of tortuous subhedral olivine. In olivine-rich troctolites from Atlantis Massif, olivine was described as corroded by a reactive melt preferentially along subgrain boundaries and especially dislocations (Suhr et al., 2008; Drouin et al., 2009). Our EBSD and TEM observations are perfectly consistent with these results.

4.4.3.2. Olivine-rich troctolite compositions

A main feature of olivine-rich troctolite inferred to be formed by melt-rock reaction is the occurrence of An content in plagioclase associated to a rather constant Fo in olivine (Figure 4-13b), in contrast to the correlation obtained by fractional crystallization (Figure 4-13b). Olivine-rich troctolites from some Alpine ophiolites (Borghini et al., 2007; Borghini and Rampone, 2007; Sanfilippo and Tribuzio, 2013) have plagioclase with a relatively low An content (0.70-0.61) associated with constant, high X_{Mg} in olivine (0.88-0.89), highlighting a vertical trend in agreement with the experimental olivine-rich troctolites (Fig. 4-13). Experimental samples generated by using melt AH6 at both pressures (0.5 and 0.7 GPa) are chemically similar to Alpine olivine-rich troctolites. This provides pressure constraints on the formation of these troctolites (around 0.5 and 0.7 GPa) and on the possible composition of the melt and the dunite acting in melt-rock reaction. Experiments conducted at 0.5 GPa with melt AH6 have plagioclase and olivine with compositions close to Pineto ophiolite composition.

As previously mentioned, on Figure 4-11 and 13 we can observe that plagioclase

crystallized at lower pressure have a lower An content; this observation is consistent with the assumption that low-anorthite in olivine-rich troctolites from the Alpine Jurassic ophiolites may reflect moderate pressure conditions of crystallization (0.5-0.3 GPa, Borghini et al., 2007). On the contrary, experimental data plot far from the compositions of Godzilla Megamullion Massif (Sanfilippo et al. 2013) and Atlantis Massif (Suhr et al., 2008; Drouin et al., 2009). Indeed, olivine-rich troctolite sampled from oceanic floor referenced present a higher An in plagioclase and lower X_{Mg} in olivine. Assimilation and fractional crystallization models have been calculated assuming olivine Fo_{89.5}, different reacting melt compositions (from $X_{Mg}= 0.75$ to 0.50) and olivine assimilation ratio, from 10 to 50 % (Sanfilippo et al., 2013). Composition of olivine-rich troctolites from Atlantis Massif (Drouin et al., 2009) were reproduced by the interaction between mantle olivine and a melt relatively evolved ($X_{Mg} = 65\sim50$; Sanfilippo et al., 2013)(Fig. 4-13a). This range of melt composition is tested during our melt-rock reaction experiments. But basalt such as AH3 ($X_{Mg} = 0.57$) reacting with San Carlos olivine, induce the crystallization of less anorthitic plagioclases, far from referenced natural olivine-rich troctolites. Lower X_{Mg} in olivine could be obtained by lowering the buffering effect of olivine, by increasing the amount of reacting melt within the impregnated dunite. A melt-rock ratio higher than 9% is required in order to obtain olivine-rich troctolites similar to Atlantis Massif and Godzilla Megamullion Massif ones. As An content of plagioclase is inversely correlated with the pressure of crystallization (Putirka, 2005), higher values of An in plagioclase could be reached for a crystallization at shallower pressure than those experimented.

High nickel concentration in olivine is generally used as an indicator of a mantle origin. High NiO content observed in olivine in our samples is consistent with natural observations from several ophiolite and ocean floor samples. Suhr et al. (2008) described X_{Mg} and Ni content in olivine as controlled by the fraction of olivine dissolution in the reacted melt and the X_{Mg} of the melt. Figure 4-13a shows high-NiO for given X_{Mg} in the olivine from Godzilla Megamullion and Atlantis Massif troctolites. In our experiments, pressure has a significant role in olivine Ni content. Indeed, we managed to obtain olivine compositions consistent with AFC trends modeled by Sanfilippo e al. (2013) and natural data from olivine-rich troctolite only at 0.7 GPa. As the An-Fo covariation shows that pressure of formation of Atlantis Massif and Godzilla Megamullion massif should be shallower 0.5 GPa, we can assume that reacting melt composition affects the final Ni content of olivine after melt-rock reaction. We conducted experiments with a Ni-free starting melts (Tab. 2-1), this has a direct impact on the vertical

trend observed.

Clinopyroxenes of olivine-rich troctolite from the Atlantis Massif have a Jd content close or lower than clinopyroxenes crystallized at 0.5 GPa in our experiments (Fig. 4-12b). This suggests that they could be crystallized at 0.5 GPa and 1250-1150 °C, and at shallower pressures, consistently with An-Fo observations. TiO₂ contents of clinopyroxene obtained at both pressures in our experiments are higher than those documented in all natural olivine-rich troctolites (Fig. 4-12a). Firstly, the composition of the starting melt we used has a direct impact on the composition for the phases crystallizing from the reacted melt. Secondly, we can attribute this high TiO₂ content to a higher trapped melt effect due to the low melt-rock ratio (9%) used in our experiment. High-X_{Mg}, and local Ti-enrichment in clinopyroxene has been ascribed to trapped melt effect (Ross and Elthon, 1997; Drouin et al., 2009; Borghini and Rampone, 2007). By extrapolation, we can assume that most of natural olivine-rich troctolite where formed at pressures under 0.7 GPa, or with a melt-rock ratio greater than 9%, or with melts poorer in TiO₂.

By comparing An-Fo trend, as well as, TiO₂ and Jd vs. X_{Mg} in clinopyroxene, we can argue that Atlantis Massif and Godzilla Megamullion olivine-rich troctolite can be the result of melt-rock reaction pressures shallower than 0.5 GPa, with a melt-rock ratio over 9%. Microstructures and mineral compositions documented in olivine-rich troctolites from Pineto and Erro-Tobbio ophiolites are in good agreement with experiments data performed at 0.5 GPa (Fig. 4-12a and Fig. 4-13b), suggesting that experimental conditions (0.5 GPa, 1300 to 1150 °C, m/r ratio = 9 %) are consistent with the formation of these rocks.

Chapter 5. Future perspectives: Melt infiltration in pre- sintered dunite

A project of melt transport within an olivine matrix has been preliminary initiated. This part represents a future perspective aimed to combine the chemistry of melt-rock interactions to the physics of melt migration by reactive dissolution, exploring at the grain-scale the melt distribution and the wetting behavior at low melt fractions.

We model dunite reactive dissolution by using a sintered dunite-basalt layer dissolution couple Five dunite infiltration experiments were performed at 0.7 GPa, 1150 °C-1250 °C.

5.1. Experimental strategy

As presented in Chapter 2, first rods of dunite are pre-sintered in the piston-cylinder apparatus at 1 GPa or 0.7 GPa and 1200 or 1300 °C (Tab. 5-1) for three to five days. Olivine powder is placed in a molybdenum capsule (6 mm diameter) lined with a graphite inner sleeve (4 mm OD and 2 mm ID) (see Fig. 2-1a). The graphite-lined capsule technique was used to minimize Fe loss with the noble metal capsule (Ulmer and Luth, 1991). After the experiment, the synthesized dunite cylinder was segmented in two or three little rods (Fig. 5-1), which were polished on both the faces under acetone (Fig. 5-1b) and then stored at 110 °C under vacuum. Dunite resulting from the sintering is presented in Figure 5-1 through BSE and EBSD images.

For all experiments, the rods were placed in contact with carbon sphere, and a layer of basalt powder was loaded into a graphite container (4 mm OD, 2 mm ID) that was closed with a graphite lid (Fig. 2-1c). In the last three experiments (see Table 5-1, MDI-03, MDI-04 and MDI-05) we placed a fine graphite thin (~1 mm) ring between dunite and basalt powders, in order to avoid melt migration along dunite rod edges and, therefore, to force melt migration through the dunite. The ring also geometrically indicates the interface between the melt and olivine layers. The graphite container was placed in a molybdenum sleeve sealed by two molybdenum lids. Molybdenum was used in order to prevent from deformations during experiments and keep the geometry preserved. Three experiments have been conducted at temperatures of 1250 °C and 1200 °C at 0.7 (Tab. 5-1), for different run durations (from 48 to 120 hrs.). Only one experiment was conducted following step-cooled procedure described thereafter.

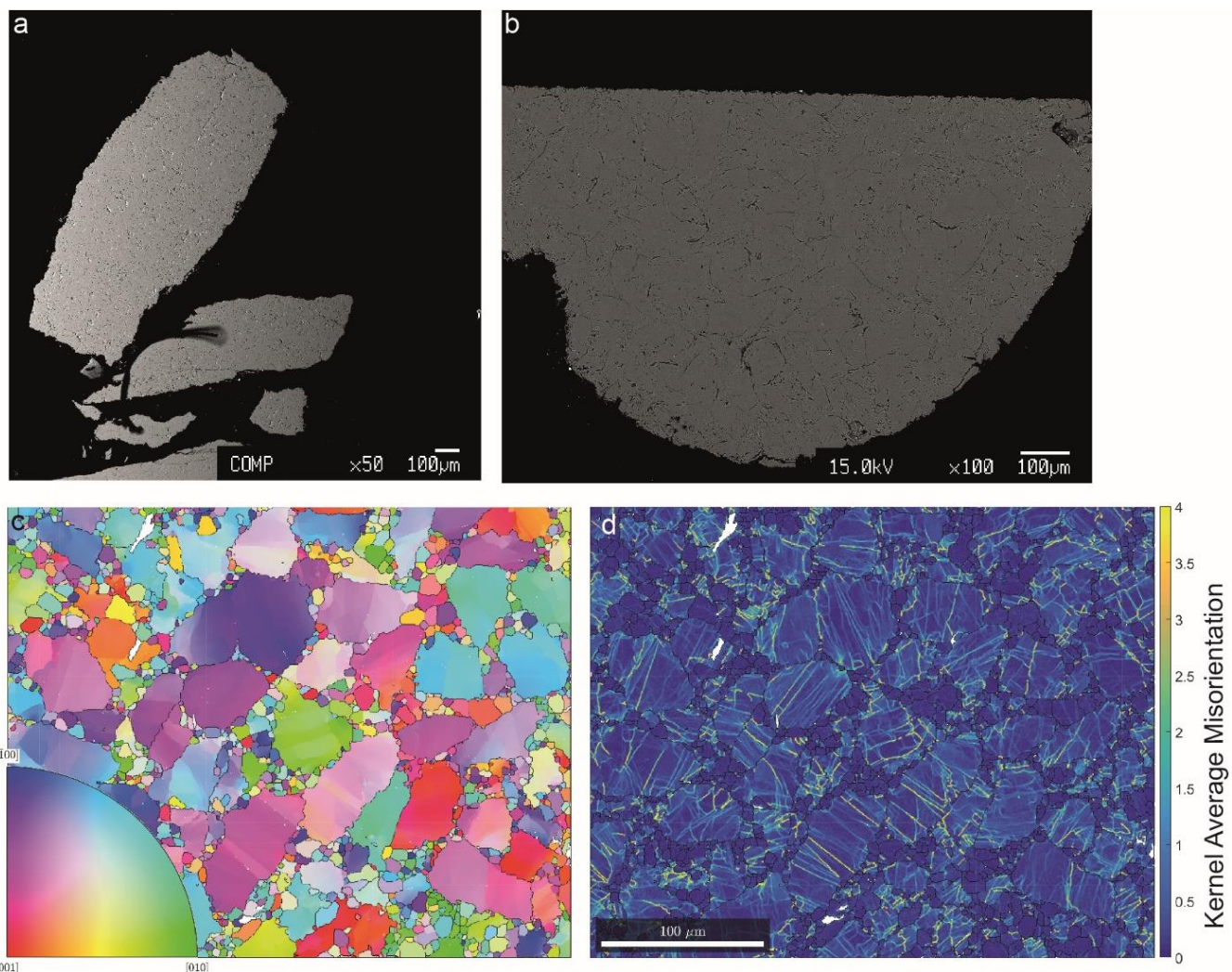


Figure 5-1: EBS and EBSD images of sintered dunite used as starting material for dunite infiltrations experiments: a) BSE image of a longitudinal section of sintered dunite, DS1 b) BSE image of a cross-section from a semi-disk of dunite DS3, c) IPF orientation map of the cross-section and d) KAM map of the same cross-section.

Table 5-1: Experimental run conditions and phase assemblages of dunite reactive dissolution experiments using melt AH6 and AH3

Name	P (GPa)	T (°C)	Cooling rate	Starting Material	Run Time (hrs.)	Run products dunite layer	Run products melt layer
<u>Dunite sintering</u>							
DS1	1	1100	-	SCO*	96	dunite rod	-
DS2	1	1100	-	SCO	120	dunite rod	-
DS3	0.7	1200	-	SCO	120	dunite rod	-
<u>Dunite infiltration</u>							
MDI-01	0.7	1250	None	AH6/DS1	48	ol-gi-cpx	gl - ol- (cpx)
MDI-03	0.7	1250	None	AH6/DS2	48	ol	gl-ol-cpx-plg (symplectite)
MDI-05	0.7	1250	None	AH6/DS3	120	ol	gl - ol
MDI-04	0.7	1200	None	AH3/DS2	48	ol	pl-cpx-ol-(gl)
MDI-02	0.7	1250 to 1150	1°C/min	AH6/ DS1	24 + 24	ol	gl-ol-cpx-plg (symplectite)

SCO*: unsieved San Carlos olivine, SCO; sieved San Carlos olivine; ol: olivine; plg: plagioclase; cpx: clinopyroxene; gl: glass ; AH6 and AH3 basalts from Husen et al., (2016). Generally MDI experiments are 5 to 6 mm long. Only MDI-01 differs with a size smaller than 3 mm.

5.2. Results

5.2.1. Lithologies and textures

A great effort has been done in order to maintain the geometry well constrained during these experiments. It resulted in an unchanged geometry with the presence of a basal glass layer (Tab. 5-1) overlaid by the dunite and finally a layer and carbon spheres (Fig. 5-1a, c, e). The layer of carbon spheres is filled by glass for each experiment even when no infiltration is visible within the dunite. Some experimental charges showed “irregularities”. MDI-01 presents a shift of the carbon spheres on one side of the capsule (Fig. 5-2) and MDI-05 a tilt of the dunite.

Between experiments MDI-01 and MDI-03 conducted with the same starting melt and run duration we intended to observe better melt infiltration with a better constrained geometry. Consequently to the geometry constriction MDI-02 (> 5mm) is significantly longer than MDI-01(<3 mm). MDI-01 resulted in a dunite layer infiltrated by a thin channel of melt partially crystallized in clinopyroxene and the melt-layer crystallized few olivine and clinopyroxene. In MDI-02, we obtained crystallization of a symplectite in the bottom of the experimental charge. This symplectite results from the expected crystallization of clinopyroxene at 1250 °C and plagioclase + olivine between 1225 and 1250 °C at 0.7 GPa for melt AH6 (Husen et al., 2016). Shilling and Wunder (2004) showed that during an experiment with a similar assembly than

ours, temperature gradient are observed. At 1050 °C temperature in the temperature varies of ~10 °C within the 2 mm around the hotspot, explaining the occurrence of clinopyroxene, plagioclase and olivine symplectite at the bottom of the melt layer. Experiment MDI-05 was performed under conditions similar with MDI-01 and MDI-03 (AH6-1250 °C) but for a longer duration in order to observe a possible influence of time on the occurrence of porous melt flow within sintered dunite. Consistently with observations done in Chapter 3 with longer experiments (60 hrs.), an assimilation of San Carlos olivine components and homogenization od melt as a function of time led to the redissolution of plagioclase and clinopyroxene.

One experiment was performed following two steps of temperature (MDI-02 → Tab. 5-1) 1250 and 1250 °C. As a result the melt layer is largely crystallized in a plagioclase-clinopyroxene-olivine symplectite (Fig. 5-2). Crystallization of these phases is consistent with equilibrium crystallization of melt AH6 (Fig 2 in Husen et al., 2016).The dunite-melt layer interface, a layer of 10 to 20 µm of newly crystallized olivine is observed (Fig. 5-3). This reactive boundary layer is observed in several experiments as testified by Figure 5-1 b and c. We observe olivine richer in Fe as shown by the lighter color. Olivine from this reactive boundary layer is subhedral with cusped to euhedral olivine.

MDI-01 (Fig. 5-1a,b) is the unique sample where porous melt flow within dunite by reactive dissolution was observed Figure 5-4. We do not observe significant Mg loss around the infiltration . The vein of melt is no larger than 10 µm, smaller the grain size of the host olivine and can be characterized as porous melt flow. On the bottom of the infiltration we can observe an increase of Mg content, showing that clinopyroxene crystallized from the melt in the vein. Then Figures 5-4b and c which are RGB color combinations of Al-Mg and Si chemical maps, show melt pockets and veins smaller than 10 µm, surrounding rounded olivine at the contact between the dunite and the carbon spheres.

Experiment MDI-04, performed with the starting melt AH3 at 1200 °C, led to the complete crystallization of the melt layer, consistently with equilibrium crystallization experiments of Husen et al. (2016).

5.2.2. Mineral chemistry

Systematic variations of minerals and melt compositions have been observed across the lithological layers and are dependent on the distance (x) from the melt-rock interface. The value of $x=0$ is assigned to the melt-rock interface. Variations of X_{Mg} contents in olivine and melts as a function of distance (x) along the experimental charge and across the melt-olivine interface are reported in Figure 5-6. Large variations are observed at the melt-rock interface where X_{Mg} varies from 0.86 to 0.90 (MDI-01) and 0.74 to 0.90 (MDI-03) in few microns. In the equilibrium crystallization performed on melt composition AH6 (Husen et al., 2016) at 0.7 GPa, 1225 °C olivine crystallization occurs simultaneously with plagioclase and after clinopyroxene. In our experiments no other phases than olivine are present.

As reference we can compare the X_{Mg} values resulted from dissolution experiments with equilibrium data at 0.7 GPa, 1225 °C. In Figure 5-6, we report as references, together with the starting melt composition and San Carlos olivine X_{Mg} values, the equilibrium X_{Mg} of melt and olivine at 1225 °C and 0.7 GPa as recovered in crystallization experiments of melt AH6 reported by Husen et al 2016 . At the melt-dunite interface ($x = 0$ mm), olivine crystallizing in MDI-03 has a composition close to equilibrium olivine ($X_{\text{Mg}} = 0.77$ to 0.82) and suddenly increases to reach San Carlos olivine composition at about 100 μm from the interface ($X_{\text{Mg}}=0.90$). At the interface dunite-carbon spheres layer a slight decrease of X_{Mg} is observed from 0.90 to 0.89.. In MDI-01, only the melt layer-dunite interface has been observed and present an evolution of X_{Mg} from 0.87 to 0.9.

The melt present in MDI-03 melt layer has the exact composition of equilibrium melt at 1225 °C and 0.7GPa ($X_{\text{Mg}} = 0.54$), consistent with the fact that it partially crystallized (Tab. 5-1). Interestingly carbon spheres acted as melt trap. The melt collected within the carbon spheres (at $x=1.5$ mm) is enriched in Mg with value $X_{\text{Mg}} = 0.71$). As a light grey rim can be observed all around the dunite rod, we can assume that melt migrated all around, reacting with the olivine and has been trapped in the carbon spheres. MDI-01 experiment, conducted with a smaller amount of melt (Fig. 5-1) has melt with a X_{Mg} of 0.71; which is also reacted melt. Calculations on Fe-Mg between melt and olivine based on Toplis (2005) show that melt in equilibrium with San Carlos olivine(Fo90) has a XMg of 0.74 (with $Kd_{\text{Mg-Fe}}^{\text{olivine-melt}} = 0.31$). Therefore, we can infer that melt from MDI-01 and the carbon spheres of MDI-03 is close to equilibrium with the olivine of the dunite.

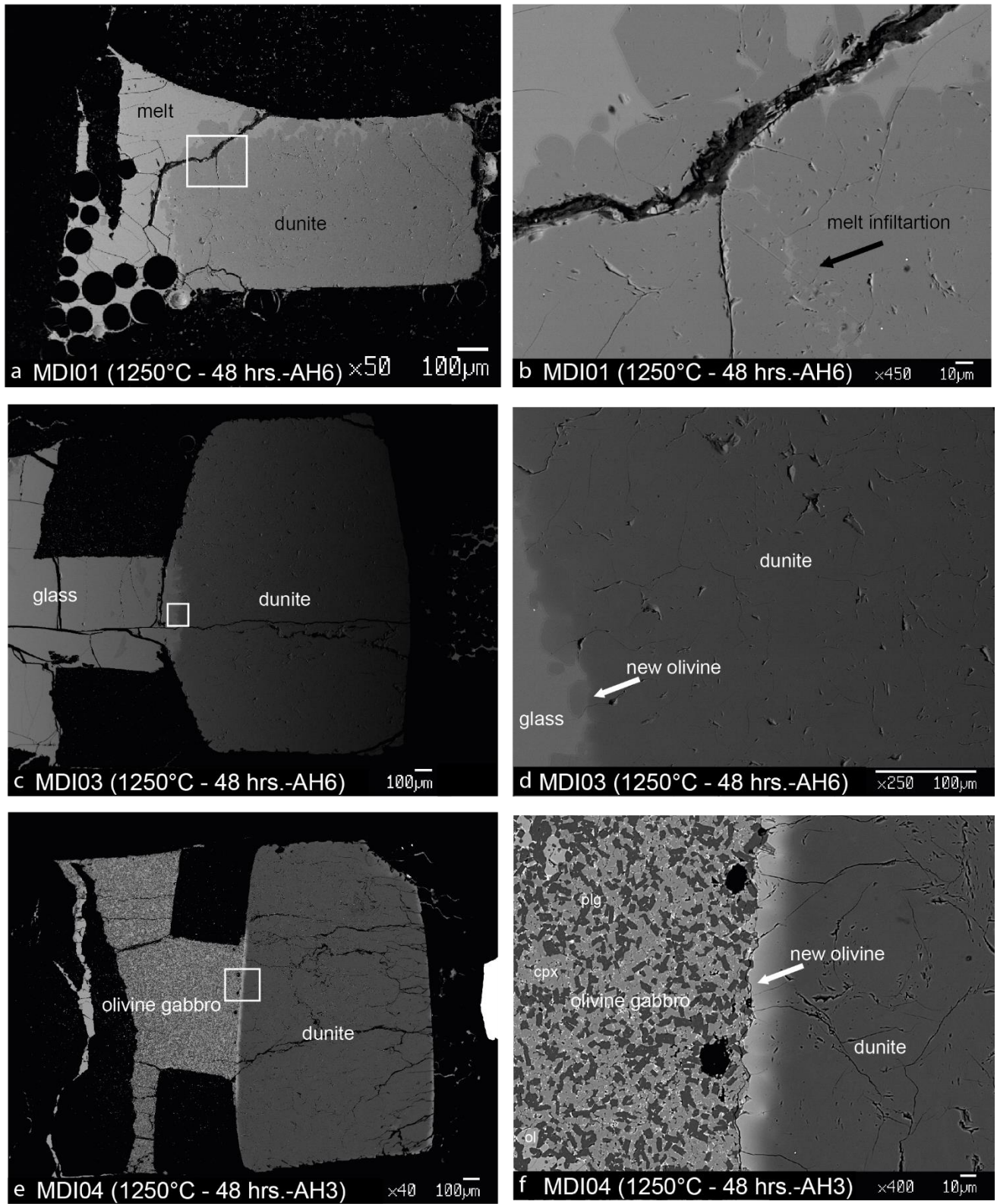


Figure 5-2: Representative BSE images illustrating the geometry and texture of three experiments. a and b represent experiment MDI-01 in global view and zoom on the melt-dunite boundary where infiltration occurs. Melt infiltration is identified by the black arrow. c and d represent MDI-03 in large view and zoomed on the reactive boundary layer. New olivine with lower X_{Mg} is pointed with the white arrow. e and f represent MDI-04. The large view shows that a lighter reactive boundary layer is present almost all around the dunite disk. A zoom on the interface shows that melt crystallized in olivine (ol)+ plagioclase (pl) and clinopyroxene (cpx), low Mg olivine crystalized at the interface and no infiltration occurred in dunite.

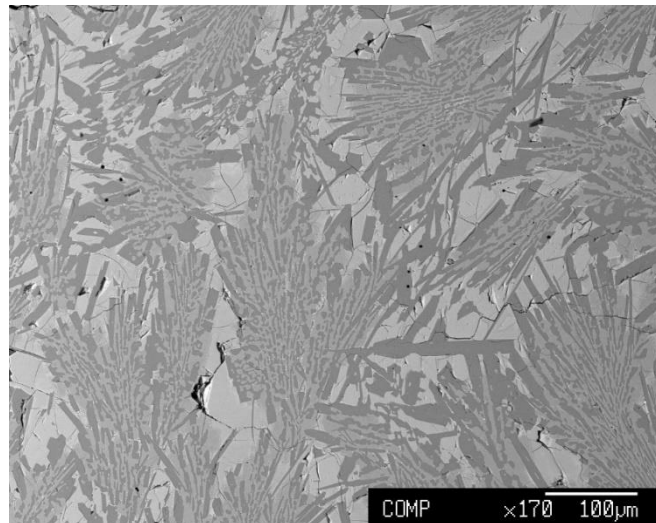


Figure 5-3: Representative BSE image from MDI-02 melt layer. The step cooled procedure down to 1200 °C led to the crystallization of a plagioclase (darkest gray) + olivine (intermediate gray) + clinopyroxene (lightest gray) symplectite.

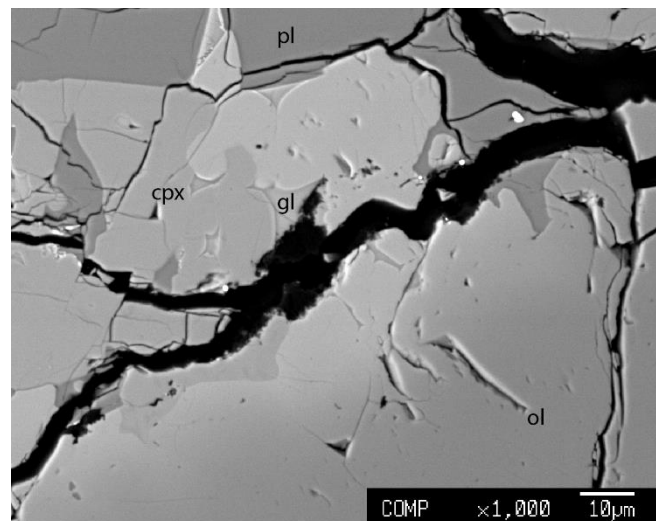


Figure 5-4: Representative BSE image from MDI-02 interface.

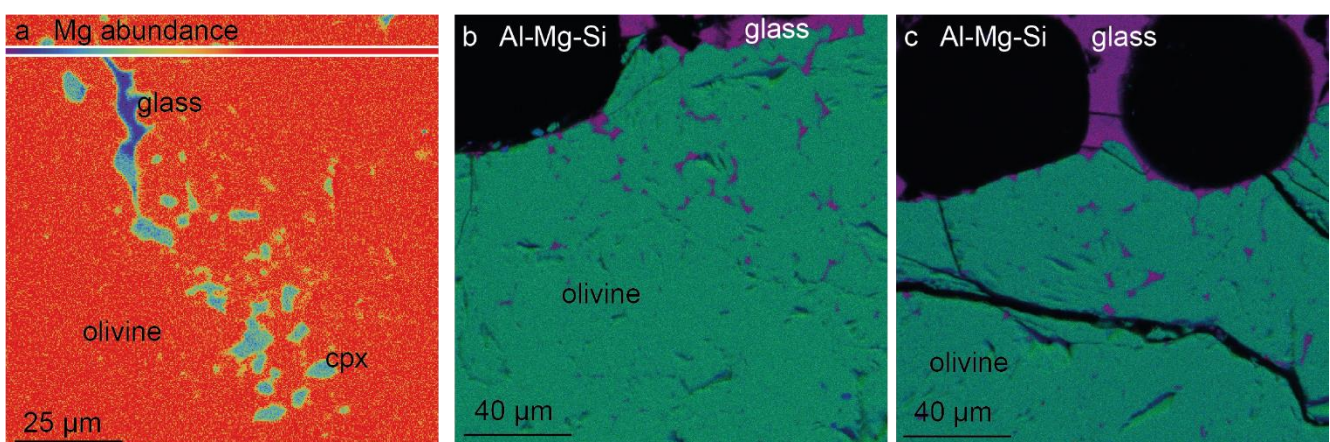


Figure 5-5: Representative X-ray chemical maps of porous melt flow in MDI-01. a is a Mg chemical map of the melt infiltration highlighted before. The color bar on the top of the image indicates Mg relative abundance of the map. The red zone is olivine, the blue is the melt infiltrated and yellow/green is clinopyroxene crystallized from the infiltrating melt. b and c represent Red-Green-Blue (RGB) color combination of Al-Mg and Si chemical maps.

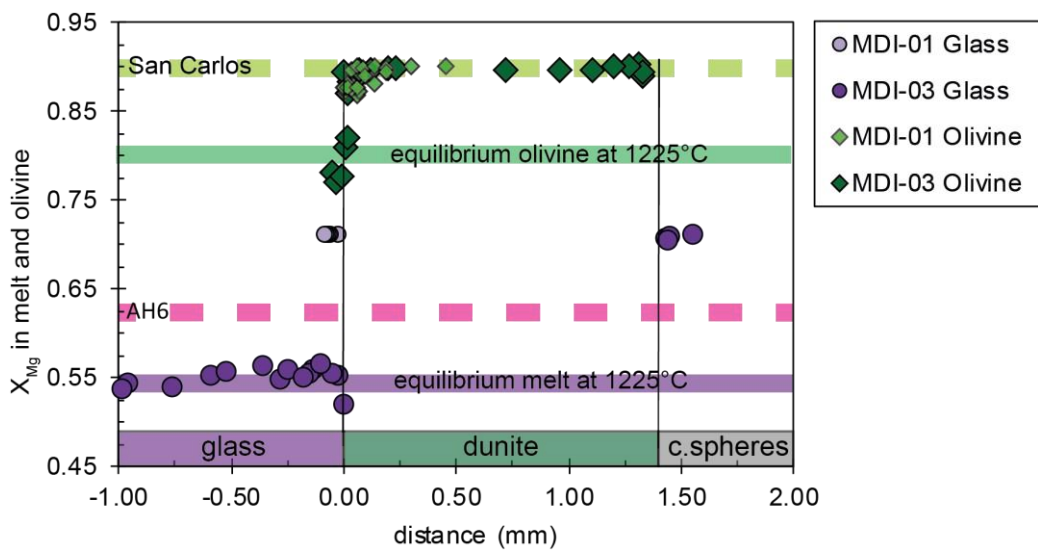


Figure 5-6: Olivine and melt X_{Mg} variation as function of distance within experiments MDI-01 and MDI-03. The distance 0 represents the interface between the melt layer (glass) and the dunite disk. Analysis were performed following a profile perpendicular to the interface. We represented compositions of glass with violet symbols and olivine in green. MDI-01 is represented with lighter colors than MDI-03. Starting material compositions of San Carlos olivine and AH6 melt are represented by the green and pink dashed lines respectively. As well equilibrium olivine and melt from equilibrium crystallization AH6 at 1225 °C and 0.7 GPa (from Husen et al. 2016) is marked by continuous green and violet lines respectively. The largest amount of analysis is done at the interface melt layer-dunite and dunite-carbon spheres layer.

5.2.3. Transmission Electron Microscopy investigations

Transmission Electron Microscopy (TEM) analysis has been performed on sample MDI-01 at the University of Siena (Italy). The sample was prepared following the protocol described in Chapter 2 (2.4.4). The thin section realized with the sample of MDI-01 observed under natural light and cross-polarized light is presented in Figure 5-4. TEM observations and analysis were performed on the thinner zone of MDI-01 thin section circled in red (Fig. 5-4).

Figure 5-7 displays TEM images montages of studied area. Visible phases are olivine, glass and glass with straight sharp to curved contacts between both, evidenced by black arrow heads (Fig. 5-7). Figure 5-7b shows a sharp contact between olivine and glass, whereas Figure 5-7a and c display a cusped olivine/melt contact. Few dislocations are observed in olivine. A well visible dislocation in olivine is present in Figure 5-7b, highlighted by the double white arrow. Cmiral et al (1998) recognized in olivine-basalt aggregates peculiar distribution of melt with 0° dihedral angle that they named “layers” (10-100 nm of size) and “films” (<10 nm). In our experiments we observed the presence of a “layer” separating neighboring olivine crystals (Fig.

5-7c). This straight “layer” occurs at the continuity of a melt infiltration marked by the arrow head. Figure 5-8 displays 12k x magnified and high resolution 800k x magnified TEM images from olivine-glass contact.

Additionally, X-Ray qualitative chemical measurements were performed with the TEM, marked by points on Figure 5-7. There, a local increase of X_{Mg} , at 1 μm to 2 μm from the rim provide more details on data composition profiles obtained by microprobe analysis. A graphic showing Fo in olivine as function of distance in two olivine crystals has been drawn in Figure 5-9. Olivine 1 (from Fig. 5-7c) displays an unsymmetrical Fo content profile with a maximum in the core of the crystal, followed by a sudden decrease. Olivine 2 (from Fig. 5-7a) profile is also unsymmetrical with a maximum value in the middle of the profile. We must highlight that olivine 2 presents a boundary with an olivine and another with glass. The rim at the contact with the melt (at 2 μm) is more evolved than the rim in contact with olivine (at 0.5 μm).

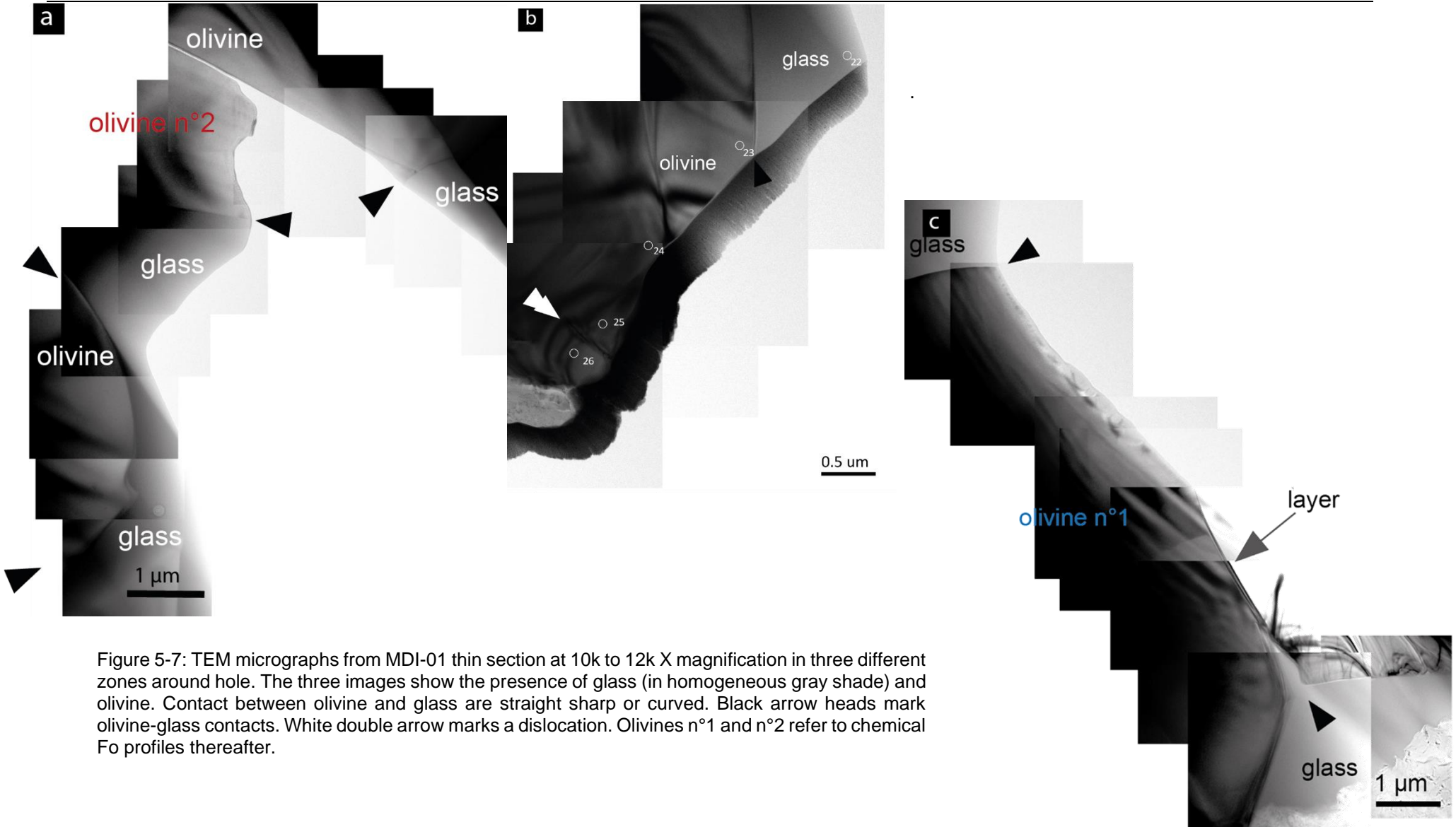


Figure 5-7: TEM micrographs from MDI-01 thin section at 10k to 12k X magnification in three different zones around hole. The three images show the presence of glass (in homogeneous gray shade) and olivine. Contact between olivine and glass are straight sharp or curved. Black arrow heads mark olivine-glass contacts. White double arrow marks a dislocation. Olivines n°1 and n°2 refer to chemical Fo profiles thereafter.

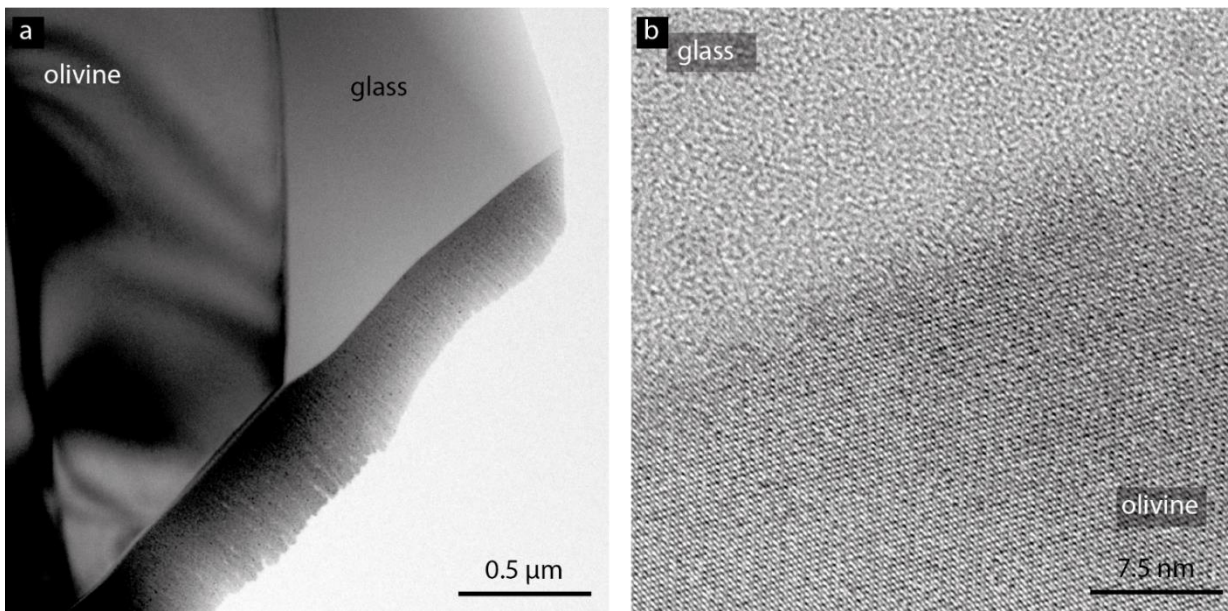


Figure 5-8: TEM micrographs from MDI-01. a: 12k X magnified olivine-glass contact. c: high resolution 800k X magnification on olivine-glass contact.

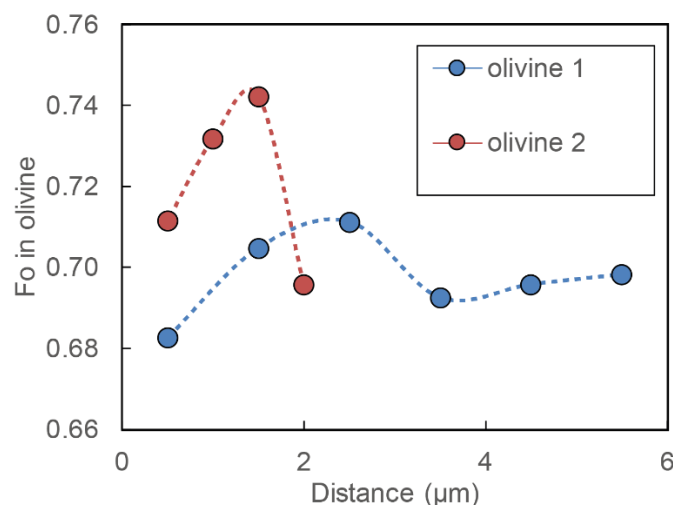


Figure 5-9: Olivine crystals compositional transects. We represented Fo in olivine as function of distance in single olivine grains. Fo values are qualitative; although internally consistent, they do not represent absolute values. Olivine 1 is the large olivine in Figure 5-7c, and olivine 2 is the small olivine on the top-left corner of Figure 5-7a. Both profiles are performed from top to bottom of the crystal.

5.3. Discussion

Dunite dissolution and infiltration by a reactive melt occurred in MDI-01. MDI-03, MDI-04 and MDI-05 led to the formation of a reactive boundary layer all around the dunite. This boundary layer is made of olivine richer in Fe. The main difference between these experiments, beside the geometry, is the nature of starting material. Indeed, MDI-01 was conducted with the sintered dunite DS1, extracted from the first dunite sintering experiment, where starting San Carlos olivine powder was not sieved. On the contrary, San Carlos olivine powder was sieved (36-64 µm) for dunite sintering experiments DS2 and DS3 used for MDI-03, MDI-04 and MDI-05. Therefore, we can assume than DS1 presents more grain size heterogeneity. This heterogeneity able to increase porosity and therefore favors melt infiltration trough the dunite. An evaluation of dunite sintering experiment can be done thanks to EMP imaging and EBSD observation of DS03 (Fig. 5-1). EBSD observation showed that olivine crystals are 10 to 100 µm large. The obtained texture is close to a porphyroclastic texture, with large olivine porphyroblasts surrounded by aggregates of small olivine clasts. Laporte and Provost (2000) describes equilibrium texture by the presence of triple junctions with ~120 ° angles. Such a texture has been observed in DS1 imaged by EMP but not in DS3. Therefore, in DS3 we did not obtain an equilibrated texture. This observation highlights that dunite sintering conditions are critical and have a direct impact on dissolution experiments.

We observed that olivine corrosion produces curved crystal edges with melt penetration along grain boundaries, in agreement with by Boudier (1991). Melt infiltration within the dunite follow grain boundaries (Fig. 5-8). Olivine corrosion create lobate rims as observed in Figure 5-8 a and c, but it can also occur along planar crystalline surfaces with straight contacts such as “layers”. Such a behavior of melt infiltration though a dunite matrix is consistent with some observations of Cmiral et al. (1998). Figures like “layers” separate two grains with a homogeneous thickness ranging from 10 to 100 nm, following both flat or curved surfaces. Their frequency increases as a function grain size, melt/rock ratio and sintering duration (Cmiral et al., 1998) and are only observable with the TEM. The nature of such geometrical features remain still poorly investigated and a careful study on them in experimental charges can contribute in understanding melt geometries more deeply beyond a simple single dihedral angle value.

Chapter 6. Conclusion

In order to investigate the role of reactive dissolution and crystallization in the origin of olivine-rich troctolites at the mantle-crust transition, we performed basalt-dunite reaction experiments, following three experimental strategies.

On a first hand, we performed time-solved dunite reactive dissolution experiments at isothermal conditions using a reaction couple made of a layer of olivine powder (mixed with basalt powder) and a layer of powdered basaltic glass. Experiments were conducted at 0.7 GPa and 0.5 GPa, at temperatures of 1200 °C, 1250 °C and 1300 °C for 20 minutes to 60 hours with three different basalt compositions. The results of this study have provided experimental constraints on kinetics and chemistry resulting from reactive dissolution of olivine:

- Olivine corrosion by reacted melt is fast. After 20 minutes we observed disruption of large crystals that results in the formation of smaller rounded olivines following subgrains boundaries.
- After reaction with starting olivine, residual melt composition is highly heterogeneous in single experiments; as a function of extent of olivine assimilation.
- Run duration favors the extent of melt-rock reaction, leading to:
 - A textural homogenization driven by a more regular repartition of grain size and shape testified by recrystallized “smooth” and large subhedral olivine with curvilinear to euhedral grain boundaries.
 - A chemical homogenization of reacted melts and olivine compositions. Only slow diffuser elements, such as Al and Ti still remain highly heterogeneous in the reacted melt.
- Starting melt composition do not affect final texture.

- MgO, FeO and SiO₂ contents of the reacted melt are buffered by olivine assimilation.

On a second hand, step-cooled experiments performed at 0.7 and 0.5 GPa, 1300-1150 °C, by using three different starting melts provided the following results:

- Reactive dissolution-crystallization of dunite by basaltic melts originates olivine-rich troctolite at 0.5 GPa and plagioclase- and clinopyroxene-bearing dunite at 0.7 GPa.
- At fixed temperature, olivine dissolution by melt is higher at lower pressure 0.5 GPa, and a larger extent of melt percolated within the olivine matrix, thus resulting in higher modal abundance of interstitial phases. Conversely, at higher pressure the early crystallization prevent further melt percolation.
- Starting melt composition influences the chemistry of plagioclases and clinopyroxene.
- A large chemical heterogeneity has been observed in poikilitic and interstitial clinopyroxenes and plagioclases, mostly underlined by local extreme enrichments in TiO₂ in clinopyroxene. This likely evidences a trapped melt effect, as documented in several olivine-rich troctolites from natural occurrences. We found that this process increases with pressure.
- Microstructures and mineral compositions documented in olivine-rich troctolites from Pineto and Erro-Tobbio ophiolites are in good agreement with experiments data performed at 0.5 GPa (Figure 4-12a and Figure 4-13b), suggesting that experimental conditions (0.5 GPa, 1300 to 1150 °C, m/r ratio=9%) are consistent with the formation of these rocks. We inferred that Atlantis Massif and Godzilla Megamullion olivine-rich troctolite can be the result of melt-rock reaction pressures shallower than 0.5 GPa, with a melt-rock ratio over 9%

In a parallel study, we conducted dunite dissolution experiments with a dissolution couple made of sintered dunite rod and basalt powder at 0.7 GPa and 1150 to 1250 °C. Preliminary results indicated that:

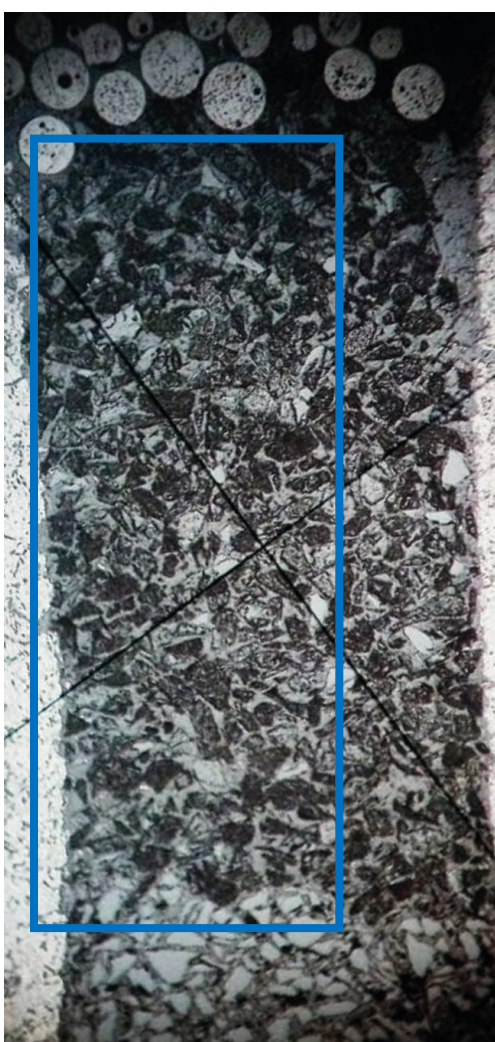
- TEM investigations highlighted that melt percolation occurs by the dissolution of olivine at grain boundaries. Melt percolates along planar crystalline surfaces with straight contacts such as “layers”.
- Olivine corrosion creates lobate rims.

- Olivine dissolution and recrystallization by the reactive melt is localized at the dunite-melt reservoir boundary.
- Dunite sintering conditions are critical and have a direct impact on dissolution experiments.

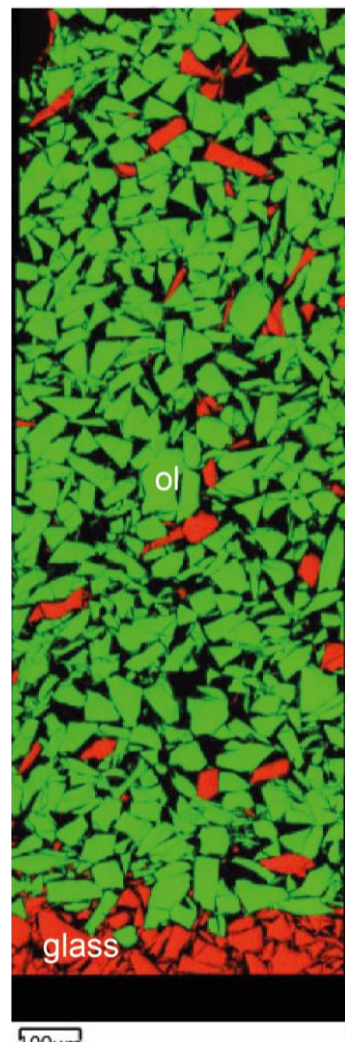
Appendix and References

A1. Appendix

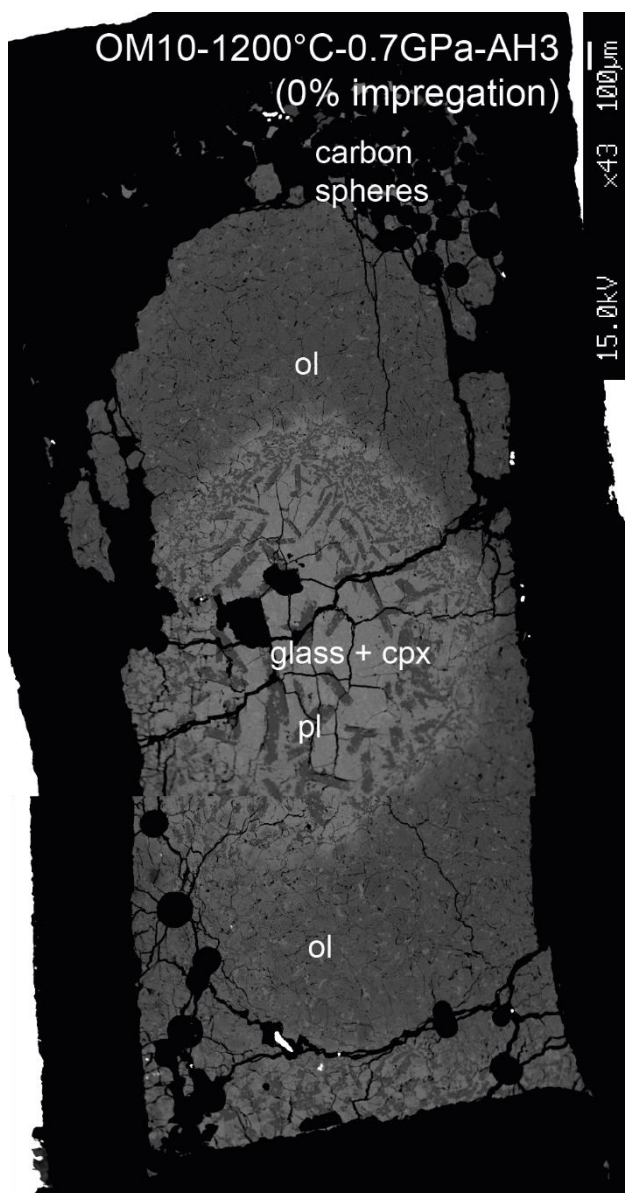
A1.1 Figures



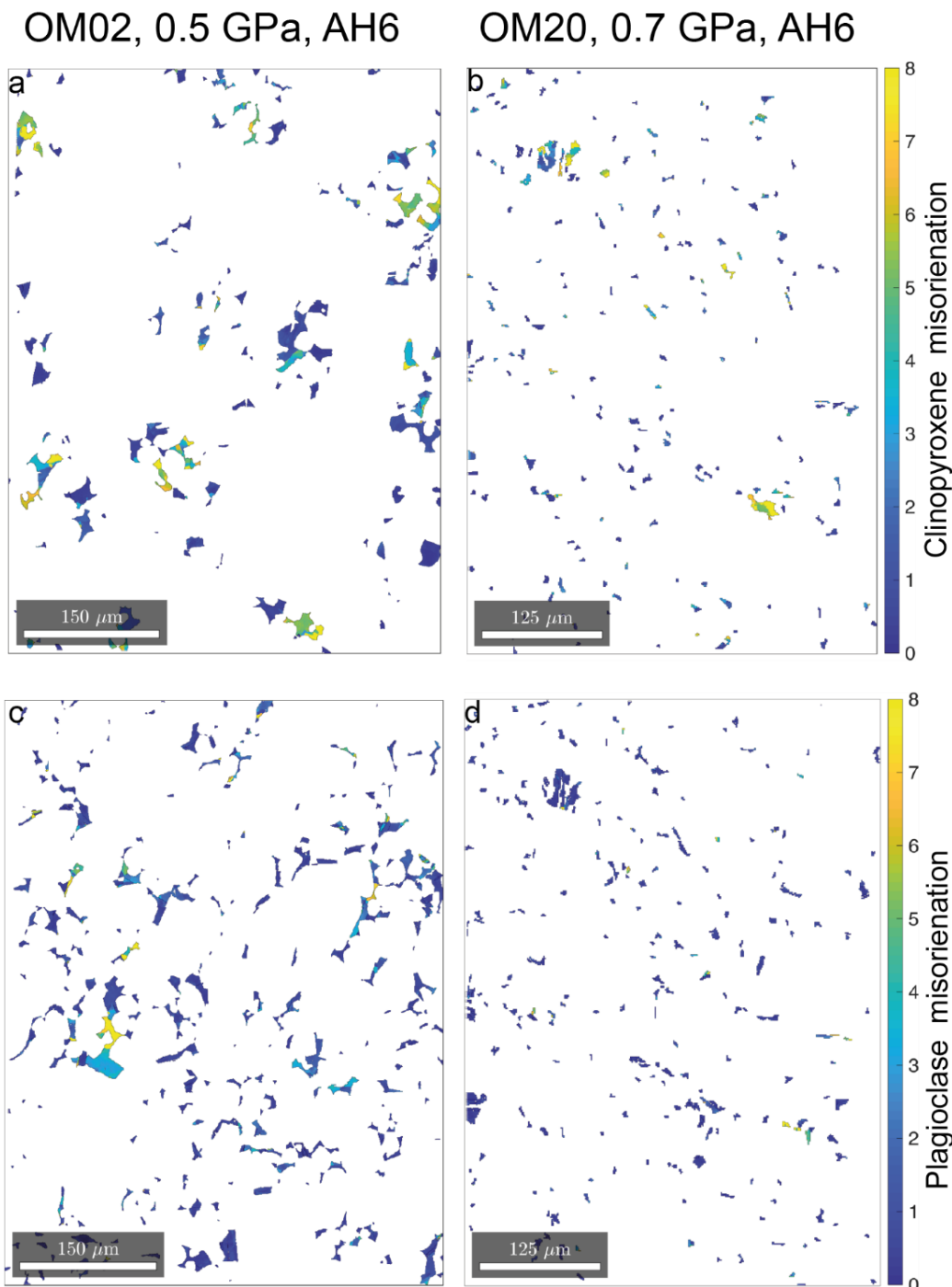
Appendix 3-1: OM26 sample observed at microscope under reflected light. Dark gray fragments correspond to crushed olivine powder whereas light gray fragments correspond to basalt powder.



Appendix 3-2: Color combination chemical map of OM26 sample. We combine Al abundance (red) and Mg abundance (green) maps. Smaller grains of olivine and basalt powder have been lost during sample preparation.



Appendix 3-3: EBS image of OM10. This experiment was conducted with an unimpregnated olivine layer. Starting melt-rock ratio of the olivine layer is 0%. As a result we observe a change in the experimental charge geometry, with a displacement of the “melt layer” within the olivine layer apparently as a “blob”.



Appendix 4-1: Clinopyroxene and plagioclase misorientation maps for OM02 and OM20.

A1.2. Tables

Table 3-2: Representative major element compositions of olivine in isothermal experiments

Table 3-3: Representative major element compositions of glass in isothermal experiments

Table 4.2: Representative major element compositions of olivine from ol-rich layer from step-cooled experiments

Table 4-3: Representative major element compositions of plagioclase from ol-rich layer from step-cooled experiments

Table 4-4: Representative major element compositions of clinopyroxene from ol-rich layer from step-cooled experiments

Table 3-2: Representative major element compositions of olivine in isothermal experiments

Time	12	12	12	12	12	12	12	12	12	12	12	12	12	12	12	12
Sample	OM-11	OM-11	OM-11	OM-11	OM-11	OM-11	OM-11	OM-11	OM-11	OM-11	OM-11	OM-11	OM-11	OM-11	OM-11	OM-11
Melt	AH6	AH6	AH6	AH6	AH6	AH6	AH6	AH6	AH6	AH6	AH6	AH6	AH6	AH6	AH6	AH6
T	1250	1250	1250	1250	1250	1250	1250	1250	1250	1250	1250	1250	1250	1250	1250	1250
P	0.7	0.7	0.7	0.7	0.7	0.7	0.7	0.7	0.7	0.7	0.7	0.7	0.7	0.7	0.7	0.7
Analysis n°	19	18	A-23	24	25	A-25	28c	28	27r	A-31	A-34	59c	59r	58r		
Sample Zone	2	2	2	3	3	3	3	3	3	3	3	3	3	3	3	3
Zone	rim	core	rim	core	rim	core	rim	core	rim	core	rim	core	rim	core	rim	rim
D (mm)	0.02	0.03	0.09	0.19	0.20	0.21	0.30	0.30	0.32	0.32	0.38	0.49	0.63	0.63	0.63	0.63
SiO ₂	40.07	40.60	39.72	41.13	40.81	40.19	40.95	40.89	40.87	40.62	40.41	40.45	40.85	40.98	41.17	
TiO ₂	0.00	0.05	0.05	0.00	0.00	0.04	0.01	0.00	0.00	0.05	0.00	0.00	0.00	0.05	0.00	
Al ₂ O ₃	0.04	0.06	0.10	0.03	0.06	0.04	0.05	0.06	0.05	0.10	0.05	0.05	0.04	0.49	0.01	
Cr ₂ O ₃	0.01	0.00	0.00	0.02	0.02	0.02	0.00	0.01	0.03	0.00	0.03	0.00	0.03	0.01	0.00	
FeO	14.21	12.94	13.95	9.52	10.47	10.69	10.54	10.12	10.55	10.43	10.14	10.28	9.94	10.21	9.95	
MnO	0.27	0.24	0.19	0.17	0.18	0.19	0.17	0.20	0.13	0.11	0.18	0.21	0.21	0.19	0.14	
NiO	0.21	0.27	0.21	0.38	0.38	0.35	0.41	0.30	0.35	0.31	0.24	0.31	0.36	0.28	0.37	
MgO	45.33	46.39	44.21	49.20	48.38	46.96	48.56	48.63	48.26	48.39	47.22	47.19	48.96	48.13	48.94	
CaO	0.31	0.27	0.34	0.08	0.30	0.27	0.27	0.31	0.32	0.35	0.27	0.26	0.28	0.42	0.24	
NaO	0.00	0.02	0.00	0.00	0.00	0.02	0.01	0.00	0.01	0.01	0.00	0.00	0.00	0.08	0.00	
K ₂ O	0.00	0.00	0.00	0.01	0.00	0.00	0.01	0.00	0.00	0.02	0.01	0.00	0.00	0.00	0.01	
Total	100.45	100.84	98.76	100.53	100.60	98.77	100.98	100.52	100.57	100.38	98.54	98.76	100.68	100.83	100.82	
Si	1.00	1.00	1.01	1.00	1.00	1.00	1.00	1.00	1.00	1.00	1.01	1.01	1.00	1.00	1.00	1.00
Ti	0.00	0.00	0.00	0.00	0.00	0.00	0.00	0.00	0.00	0.00	0.00	0.00	0.00	0.00	0.00	0.00
Al	0.00	0.00	0.00	0.00	0.00	0.00	0.00	0.00	0.00	0.00	0.00	0.00	0.00	0.01	0.00	
Cr	0.00	0.00	0.00	0.00	0.00	0.00	0.00	0.00	0.00	0.00	0.00	0.00	0.00	0.00	0.00	
Fe ₂	0.30	0.27	0.30	0.19	0.21	0.22	0.22	0.21	0.22	0.21	0.21	0.21	0.20	0.21	0.20	
Mn	0.01	0.00	0.00	0.00	0.00	0.00	0.00	0.00	0.00	0.00	0.00	0.00	0.00	0.00	0.00	
Ni	0.00	0.01	0.00	0.01	0.01	0.01	0.01	0.01	0.01	0.01	0.00	0.01	0.01	0.01	0.01	
Mg	1.68	1.71	1.67	1.79	1.77	1.75	1.77	1.77	1.76	1.77	1.76	1.76	1.78	1.75	1.78	
Ca	0.01	0.01	0.01	0.00	0.01	0.01	0.01	0.01	0.01	0.01	0.01	0.01	0.01	0.01	0.01	
Na	0.00	0.00	0.00	0.00	0.00	0.00	0.00	0.00	0.00	0.00	0.00	0.00	0.00	0.00	0.00	
K	0.00	0.00	0.00	0.00	0.00	0.00	0.00	0.00	0.00	0.00	0.00	0.00	0.00	0.00	0.00	
XMg	0.84	0.86	0.84	0.90	0.88	0.88	0.88	0.89	0.88	0.88	0.88	0.88	0.89	0.88	0.89	

Zone c or r refers to core or rim analysis

D: Distance is calculated from the x,y coordinates of an olivine from the interface zone (picked up as a 0 mm reference olivine for each sample) and the x,y coordinates of the analysis

Cations are calculated with the Program NORM (version 2013) by Ulmer and Poli

Sample zones : 1: melt layer, 2: Interface, 3: Ol-rich layer bot. half, 4: Ol-rich layer up. Half, 5: carbon spheres

Table 3-2:
Suite 1

Time	12	12	12	12	12	12	12	12	12	12	12	12	12	12	12
Sample	OM-11	OM-11	OM-11	OM-11	OM-11	OM-11	OM-11	OM-12	OM-12	OM-12	OM-12	OM12A	OM12A	OM12A	OM12A
Melt	AH6	AH6	AH6	AH6	AH6	AH6	AH6	AH6	AH6	AH6	AH6	AH6	AH6	AH6	AH6
T	1250	1250	1250	1250	1250	1250	1250	1250	1250	1250	1250	1250	1250	1250	1250
P	0.7	0.7	0.7	0.7	0.7	0.7	0.7	0.7	0.7	0.7	0.7	0.7	0.7	0.7	0.7
Analysis n°	58C	60r	60c	44r	44C	A-46	61R	61C	10	41C	A-10	11	22-11B	22-02OC	22-02OR
Sample Zone	3	4	4	4	4	4	4	2	3	2	2	3	3	3	3
Zone	core	rim	core	rim	core	core	rim	core	rim	core	rim	core	rim	core	rim
D (mm)	0.64	0.82	0.83	0.91	0.92	1.21	1.36	1.37	0.00	0.00	0.00	0.02	0.11	0.20	0.22
SiO ₂	41.01	41.04	41.20	41.35	41.12	40.73	41.00	41.00	40.14	41.25	40.56	40.50	40.69	40.62	40.66
TiO ₂	0.00	0.07	0.00	0.00	0.03	0.01	0.00	0.00	0.03	0.03	0.04	0.04	0.00	0.00	0.01
Al ₂ O ₃	0.02	0.28	0.07	0.19	0.03	0.03	0.06	0.01	0.07	0.05	0.06	0.08	0.03	0.06	0.06
Cr ₂ O ₃	0.02	0.04	0.00	0.00	0.05	0.01	0.00	0.03	0.13	0.01	0.05	0.00	0.00	0.00	0.01
FeO	9.72	9.79	9.89	9.81	9.65	9.98	10.29	9.89	12.90	10.01	12.79	12.88	10.91	10.42	10.59
MnO	0.13	0.11	0.12	0.11	0.17	0.14	0.10	0.14	0.19	0.17	0.23	0.15	0.16	0.19	0.11
NiO	0.38	0.45	0.44	0.32	0.34	0.37	0.14	0.15	0.05	0.32	0.00	0.08	0.38	0.41	0.30
MgO	48.62	48.75	49.36	48.93	49.34	48.18	48.69	48.80	46.93	48.73	46.25	47.05	47.94	48.44	48.06
CaO	0.07	0.41	0.20	0.35	0.11	0.06	0.32	0.09	0.44	0.14	0.46	0.33	0.35	0.33	0.35
NaO	0.00	0.04	0.00	0.05	0.03	0.01	0.00	0.03	0.02	0.01	0.00	0.02	0.01	0.01	0.00
K2O	0.01	0.00	0.01	0.01	0.01	0.01	0.01	0.00	0.01	0.00	0.00	0.01	0.01	0.00	0.00
Total	100.00	100.99	101.30	101.13	100.88	99.52	100.61	100.14	100.90	100.71	100.44	101.14	100.50	100.48	100.15
Si	1.01	1.00	1.00	1.00	1.00	1.01	1.00	1.00	0.99	1.01	1.01	0.99	1.00	1.00	1.00
Ti	0.00	0.00	0.00	0.00	0.00	0.00	0.00	0.00	0.00	0.00	0.00	0.00	0.00	0.00	0.00
Al	0.00	0.01	0.00	0.01	0.00	0.00	0.00	0.00	0.00	0.00	0.00	0.00	0.00	0.00	0.00
Cr	0.00	0.00	0.00	0.00	0.00	0.00	0.00	0.00	0.00	0.00	0.00	0.00	0.00	0.00	0.00
Fe2	0.20	0.20	0.20	0.20	0.20	0.21	0.21	0.20	0.27	0.20	0.27	0.26	0.22	0.21	0.22
Mn	0.00	0.00	0.00	0.00	0.00	0.00	0.00	0.00	0.00	0.00	0.00	0.00	0.00	0.00	0.00
Ni	0.01	0.01	0.01	0.01	0.01	0.01	0.00	0.00	0.00	0.01	0.00	0.00	0.01	0.01	0.01
Mg	1.78	1.77	1.78	1.77	1.79	1.77	1.77	1.78	1.72	1.77	1.71	1.72	1.75	1.77	1.76
Ca	0.00	0.01	0.01	0.01	0.00	0.00	0.01	0.00	0.01	0.00	0.01	0.01	0.01	0.01	0.01
Na	0.00	0.00	0.00	0.00	0.00	0.00	0.00	0.00	0.00	0.00	0.00	0.00	0.00	0.00	0.00
K	0.00	0.00	0.00	0.00	0.00	0.00	0.00	0.00	0.00	0.00	0.00	0.00	0.00	0.00	0.00
XMg	0.89	0.88	0.89	0.89	0.89	0.89	0.89	0.89	0.86	0.89	0.86	0.86	0.88	0.88	0.88

Table 3-2:
Suite 2

Time	12	12	12	12	12	12	12	12	12	12	12	12	12	12	12
Sample	OM-12	OM12A	OM12A	OM12A	OM12A	OM-12	OM-12	OM-12	OM-12	OM-12	OM-12	OM-12	OM-12	OM-12	OM-12
Melt	AH6	AH6	AH6	AH6	AH6	AH3	AH6	AH6	AH6	AH6	AH6	AH6	AH6	AH6	AH6
T	1250	1250	1250	1250	1250	1250	1250	1250	1250	1250	1250	1250	1250	1250	1250
P	0.7	0.7	0.7	0.7	0.7	0.7	0.7	0.7	0.7	0.7	0.7	0.7	0.7	0.7	0.7
						22-01B									
Analysis n°	A-14	22-01OC	22-01E	22-01OR	R	40R	40C	42R	42C	22-05OC	41R	04Res	22-04OC	22-06C	22-06E
Sample Zone	3	3	3	3	3	3	3	3	3	3	3	3	3	3	3
Zone	core	core	core	rim	rim	core	rim	core	core	rim	rim	core	core	core	rim
D (mm)	0.22	0.23	0.23	0.24	0.24	0.45	0.45	0.56	0.56	0.58	0.65	0.72	0.73	0.74	0.74
SiO ₂	40.99	40.71	40.87	40.96	40.99	40.81	41.05	40.32	40.34	40.53	40.78	40.89	40.63	40.83	40.67
TiO ₂	0.00	0.00	0.01	0.00	0.01	0.04	0.00	0.00	0.00	0.01	0.00	0.00	0.00	0.00	0.00
Al ₂ O ₃	0.02	0.03	0.09	0.09	0.14	0.05	0.03	0.05	0.02	0.10	0.08	0.04	0.04	0.10	0.09
Cr ₂ O ₃	0.04	0.00	0.00	0.00	0.00	0.02	0.08	0.00	0.08	0.00	0.01	0.00	0.00	0.00	0.00
FeO	10.22	10.49	10.30	10.33	10.00	10.03	10.12	9.83	9.76	10.12	10.23	9.75	9.83	10.10	9.71
MnO	0.11	0.15	0.11	0.21	0.16	0.16	0.09	0.17	0.13	0.15	0.13	0.08	0.14	0.19	0.10
NiO	0.41	0.45	0.36	0.36	0.34	0.32	0.45	0.31	0.43	0.29	0.36	0.40	0.34	0.34	0.39
MgO	48.24	48.44	48.46	48.20	48.11	48.20	48.47	48.02	48.83	48.93	48.72	48.85	49.04	48.47	48.26
CaO	0.18	0.28	0.37	0.37	0.34	0.31	0.20	0.27	0.09	0.34	0.35	0.26	0.11	0.29	0.30
NaO	0.02	0.02	0.00	0.02	0.00	0.00	0.02	0.00	0.03	0.02	0.03	0.01	0.00	0.03	0.01
K ₂ O	0.00	0.01	0.01	0.00	0.01	0.00	0.00	0.00	0.00	0.01	0.00	0.00	0.00	0.00	0.00
Total	100.22	100.59	100.58	100.56	100.10	99.95	100.52	98.98	99.71	100.49	100.70	100.27	100.13	100.35	99.52
Si	1.01	1.00	1.00	1.00	1.01	1.00	1.00	0.99	0.99	1.00	1.00	1.00	1.00	1.00	1.00
Ti	0.00	0.00	0.00	0.00	0.00	0.00	0.00	0.00	0.00	0.00	0.00	0.00	0.00	0.00	0.00
Al	0.00	0.00	0.00	0.00	0.00	0.00	0.00	0.00	0.00	0.00	0.00	0.00	0.00	0.00	0.00
Cr	0.00	0.00	0.00	0.00	0.00	0.00	0.00	0.00	0.00	0.00	0.00	0.00	0.00	0.00	0.00
Fe ₂	0.21	0.21	0.21	0.21	0.21	0.21	0.21	0.20	0.20	0.21	0.21	0.20	0.20	0.21	0.20
Mn	0.00	0.00	0.00	0.00	0.00	0.00	0.00	0.00	0.00	0.00	0.00	0.00	0.00	0.00	0.00
Ni	0.01	0.01	0.01	0.01	0.01	0.01	0.01	0.01	0.01	0.01	0.01	0.01	0.01	0.01	0.01
Mg	1.77	1.77	1.77	1.76	1.76	1.77	1.77	1.78	1.79	1.78	1.77	1.78	1.79	1.77	1.78
Ca	0.00	0.01	0.01	0.01	0.01	0.01	0.01	0.01	0.00	0.01	0.01	0.01	0.00	0.01	0.01
Na	0.00	0.00	0.00	0.00	0.00	0.00	0.00	0.00	0.00	0.00	0.00	0.00	0.00	0.00	0.00
K	0.00	0.00	0.00	0.00	0.00	0.00	0.00	0.00	0.00	0.00	0.00	0.00	0.00	0.00	0.00
XMg	0.89	0.88	0.88	0.88	0.89	0.89	0.89	0.89	0.89	0.89	0.88	0.89	0.89	0.89	0.89

Table 3-2:
Suite 3

Table 3-2:
Suite 4

Time	12	12	13	13	13	13	13	13	13	13	13	13	13	13	13
Sample	OM-12	OM12A	OM-13	OM-13	OM-13	OM-13	OM-13	OM-13	OM-13	OM-13	OM-13	OM-13	OM-13	OM-13	OM-13
Melt	AH6	AH6	HDRBC	HDRBC	HDRBC	HDRBC	HDRBC	HDRBC	HDRBC	HDRBC	HDRBC	HDRBC	HDRBC	HDRBC	HDRBC
T	1250	1250	1250	1250	1250	1250	1250	1250	1250	1250	1250	1250	1250	1250	1250
P	0.7	0.7	0.7	0.7	0.7	0.7	0.7	0.7	0.7	0.7	0.7	0.7	0.7	0.7	0.7
Analysis n°	43R	22-10B	A-07	A-08	A-10	A-13	A-15	A-12	A-17	A-18	A-19	A-20	A-22	A-23	A-24
Sample Zone	3	3	2	2	2	3	3	3	3	3	3	3	3	3	3
Zone	rim	core	core	rim	core	rim	core	core	rim	core	rim	core	rim	core	core
D (mm)	0.95	0.96	0.00	0.02	0.05	0.26	0.26	0.47	0.48	0.62	0.64	0.67	0.67	0.70	0.70
SiO ₂	40.64	40.77	41.45	40.77	41.60	41.13	40.98	41.14	41.27	41.66	41.44	41.19	41.56	41.77	41.58
TiO ₂	0.02	0.00	0.00	0.08	0.05	0.00	0.00	0.00	0.03	0.00	0.00	0.01	0.00	0.03	0.02
Al ₂ O ₃	0.07	0.08	0.01	0.10	0.01	0.03	0.04	0.06	0.06	0.07	0.03	0.04	0.04	0.07	0.05
Cr ₂ O ₃	0.01	0.00	0.03	0.00	0.00	0.01	0.05	0.00	0.00	0.07	0.02	0.01	0.00	0.08	0.00
FeO	10.00	9.90	10.78	14.17	12.83	10.43	10.55	10.03	9.94	10.20	9.69	9.90	9.96	10.13	9.59
MnO	0.10	0.17	0.18	0.23	0.18	0.16	0.16	0.16	0.15	0.12	0.09	0.16	0.14	0.10	0.18
NiO	0.43	0.08	0.23	0.25	0.35	0.35	0.29	0.34	0.37	0.33	0.36	0.32	0.35	0.39	0.40
MgO	48.61	49.03	48.22	45.72	46.85	46.12	46.05	46.40	47.44	47.47	47.30	47.90	47.85	47.63	48.56
CaO	0.29	0.34	0.13	0.33	0.27	0.31	0.36	0.15	0.26	0.30	0.11	0.29	0.24	0.31	0.09
NaO	0.03	0.00	0.02	0.00	0.00	0.00	0.00	0.02	0.01	0.02	0.00	0.00	0.00	0.00	0.01
K ₂ O	0.00	0.00	0.00	0.01	0.00	0.00	0.00	0.00	0.00	0.01	0.00	0.00	0.02	0.00	0.00
Total	100.20	100.36	101.04	101.64	102.14	98.54	98.48	98.29	99.53	100.25	99.05	99.83	100.15	100.52	100.48
Si	1.00	1.00	1.01	1.01	1.02	1.03	1.03	1.02	1.03	1.03	1.02	1.02	1.03	1.02	1.02
Ti	0.00	0.00	0.00	0.00	0.00	0.00	0.00	0.00	0.00	0.00	0.00	0.00	0.00	0.00	0.00
Al	0.00	0.00	0.00	0.00	0.00	0.00	0.00	0.00	0.00	0.00	0.00	0.00	0.00	0.00	0.00
Cr	0.00	0.00	0.00	0.00	0.00	0.00	0.00	0.00	0.00	0.00	0.00	0.00	0.00	0.00	0.00
Fe ₂	0.21	0.20	0.22	0.29	0.26	0.22	0.22	0.21	0.21	0.21	0.20	0.20	0.20	0.21	0.20
Mn	0.00	0.00	0.00	0.00	0.00	0.00	0.00	0.00	0.00	0.00	0.00	0.00	0.00	0.00	0.00
Ni	0.01	0.00	0.00	0.00	0.01	0.01	0.01	0.01	0.01	0.01	0.01	0.01	0.01	0.01	0.01
Mg	1.78	1.79	1.75	1.68	1.70	1.73	1.73	1.74	1.75	1.74	1.75	1.76	1.75	1.74	1.77
Ca	0.01	0.01	0.00	0.01	0.01	0.01	0.01	0.00	0.01	0.01	0.00	0.01	0.01	0.01	0.00
Na	0.00	0.00	0.00	0.00	0.00	0.00	0.00	0.00	0.00	0.00	0.00	0.00	0.00	0.00	0.00
K	0.00	0.00	0.00	0.00	0.00	0.00	0.00	0.00	0.00	0.00	0.00	0.00	0.00	0.00	0.00
XMg	0.89	0.89	0.88	0.84	0.86	0.88	0.88	0.88	0.89	0.88	0.89	0.89	0.89	0.88	0.89

Table 3-2:
Suite 5

Time	13	13	13	13	13	13	13	13	13	13	24	24	24	24
Sample	OM-13	OM-13	OM-13	OM-13	OM-13	OM-13	OM-13	OM-13	OM-13	OM-13	OM-15	OM-15	OM-15	OM-15
Melt	HDRBC	HDRBC	HDRBC	HDRBC	HDRBC	HDRBC	HDRBC	HDRBC	HDRBC	HDRBC	AH6	AH6	AH6	AH6
T	1250	1250	1250	1250	1250	1250	1250	1250	1250	1250	1250	1250	1250	1250
P	0.7	0.7	0.7	0.7	0.7	0.7	0.7	0.7	0.7	0.7	0.7	0.7	0.7	0.7
Analysis n°	A-25	A-27	A-28	A-29	A-30	A-33	A-34	A-35	A-39	A-37	A-38	01EC	01ER	65
Sample Zone	3	4	4	4	4	4	4	4	4	4	1	1	2	2
Zone	rim	rim	core	core	rim	core	rim	core	core	core	rim	rim	rim	core
D (mm)	0.73	0.93	0.95	1.06	1.06	1.17	1.29	1.30	1.32	1.32	-0.55	-0.46	-0.07	-0.05
SiO ₂	41.36	41.06	40.65	41.50	41.10	41.61	41.70	41.77	41.05	40.40	41.18	40.13	40.69	40.08
TiO ₂	0.00	0.07	0.03	0.01	0.05	0.00	0.00	0.00	0.03	0.00	0.00	0.02	0.00	0.01
Al ₂ O ₃	0.12	0.16	0.01	0.05	0.06	0.01	0.07	0.08	0.02	0.04	0.03	0.06	0.06	0.04
Cr ₂ O ₃	0.05	0.01	0.00	0.00	0.00	0.09	0.03	0.01	0.00	0.04	0.04	0.05	0.07	0.04
FeO	10.00	10.03	10.03	9.84	10.19	9.88	10.07	10.08	9.95	9.77	10.02	13.48	12.78	12.28
MnO	0.19	0.17	0.16	0.16	0.16	0.15	0.11	0.22	0.17	0.13	0.12	0.18	0.17	0.19
NiO	0.36	0.45	0.37	0.40	0.23	0.33	0.30	0.15	0.18	0.25	0.27	0.07	d.l.	0.12
MgO	47.90	46.87	47.38	47.69	47.37	47.86	47.87	47.82	46.64	46.11	46.94	46.65	46.94	46.91
CaO	0.29	0.30	0.09	0.25	0.29	0.16	0.29	0.32	0.18	0.09	0.11	0.44	0.40	0.27
NaO	0.00	0.01	0.05	0.00	0.01	0.00	0.01	0.02	0.00	0.00	0.00	0.00	0.00	0.01
K2O	0.00	0.00	0.02	0.00	0.00	0.01	0.00	0.00	0.00	0.01	0.00	0.00	0.01	0.00
Total	100.27	99.13	98.78	99.90	99.47	100.09	100.45	100.47	98.23	96.83	98.72	101.08	101.12	99.95
Si	1.02	1.02	1.01	1.02	1.02	1.02	1.02	1.03	1.03	1.03	0.99	1.00	0.99	0.99
Ti	0.00	0.00	0.00	0.00	0.00	0.00	0.00	0.00	0.00	0.00	0.00	0.00	0.00	0.00
Al	0.00	0.00	0.00	0.00	0.00	0.00	0.00	0.00	0.00	0.00	0.00	0.00	0.00	0.00
Cr	0.00	0.00	0.00	0.00	0.00	0.00	0.00	0.00	0.00	0.00	0.00	0.00	0.00	0.00
Fe2	0.21	0.21	0.21	0.20	0.21	0.20	0.21	0.21	0.21	0.21	0.21	0.28	0.26	0.25
Mn	0.00	0.00	0.00	0.00	0.00	0.00	0.00	0.00	0.00	0.00	0.00	0.00	0.00	0.00
Ni	0.01	0.01	0.01	0.01	0.00	0.01	0.01	0.00	0.00	0.01	0.01	0.00	0.00	0.00
Mg	1.75	1.74	1.76	1.75	1.75	1.76	1.75	1.75	1.75	1.75	1.75	1.71	1.72	1.73
Ca	0.01	0.01	0.00	0.01	0.01	0.00	0.01	0.01	0.01	0.00	0.00	0.01	0.01	0.01
Na	0.00	0.00	0.00	0.00	0.00	0.00	0.00	0.00	0.00	0.00	0.00	0.00	0.00	0.00
K	0.00	0.00	0.00	0.00	0.00	0.00	0.00	0.00	0.00	0.00	0.00	0.00	0.00	0.00
XMg	0.89	0.88	0.89	0.89	0.88	0.89	0.89	0.89	0.89	0.89	0.89	0.85	0.86	0.86

Table 3-2:
Suite 6

Table 3-2:
Suite 7

Table 3-2:
Suite 8

Table 3-2:
Suite 9

Time	60	60	60	60	60	60	60	60	60	60	60	60	60	60	60
Sample	OM-17	OM-18	OM-18	OM-18	OM-18	OM-18	OM-18	OM-18	OM-18						
Melt	AH3	AH6	AH6	AH6	AH6	AH6	AH6	AH6	AH6						
T	1250	1250	1250	1250	1250	1250	1250	1250	1250	1250	1250	1250	1250	1250	1250
P	0.7	0.7	0.7	0.7	0.7	0.7	0.7	0.7	0.7	0.7	0.7	0.7	0.7	0.7	0.7
Analysis n°	10	12	14	16	11	13	15	17	02R	02C	04C	08C	48-01BR	48-01EC	48-01ER
Sample Zone	3	3	3	3	3	3	3	2	2	2	3	2	2	2	2
Zone	core	core	core	core	rim	rim	rim	rim	core	core	core	rim	core	core	rim
D (mm)	0.31	0.50	0.87	0.85	0.29	0.52	0.84	0.86	0.00	0.00	0.23	1.73	0.07	0.03	0.00
SiO ₂	40.89	40.10	40.45	40.33	40.79	40.39	40.54	40.21	40.31	40.58	41.07	41.25	40.49	40.52	40.83
TiO ₂	0.00	0.01	0.00	0.00	0.00	0.02	0.00	0.00	0.02	0.00	0.00	0.01	0.00	0.02	0.01
Al ₂ O ₃	0.06	0.04	0.06	0.04	0.04	0.03	0.07	0.04	0.07	0.07	0.09	0.04	0.08	0.06	0.07
Cr ₂ O ₃	0.01	0.00	0.06	0.00	0.01	0.01	0.00	0.00	0.12	0.03	0.08	0.03	0.06	0.05	
FeO	10.56	10.38	10.36	10.23	10.47	10.36	10.15	10.21	10.29	10.34	9.96	9.58	9.76	9.89	10.16
MnO	0.15	0.12	0.11	0.15	0.14	0.17	0.20	0.15	0.17	0.17	0.17	0.20	0.15	0.12	0.13
NiO	0.17	0.18	0.18	0.17	0.08	0.22	0.14	0.16	0.04	0.06	0.07	0.07	d.l.	d.l.	0.02
MgO	47.73	47.60	47.88	48.06	48.00	47.67	47.98	48.18	47.82	47.82	48.45	48.99	48.63	48.67	49.18
CaO	0.29	0.27	0.29	0.29	0.30	0.32	0.30	0.30	0.40	0.39	0.39	0.30	0.34	0.34	0.37
NaO	0.02	0.03	0.00	0.02	0.05	0.03	0.00	0.03	0.00	0.01	0.01	0.02	0.02	0.02	0.03
K2O	0.00	0.00	0.00	0.01	0.01	0.00	0.00	0.01	0.01	0.00	0.01	0.00	0.00	0.00	0.00
Total	99.88	98.72	99.40	99.30	99.90	99.21	99.38	99.27	99.27	99.47	100.29	100.49	99.50	99.72	100.86
Si	1.01	1.00	1.00	1.00	1.00	1.00	1.00	1.00	1.00	1.01	1.01	1.00	1.00	1.00	0.99
Ti	0.00	0.00	0.00	0.00	0.00	0.00	0.00	0.00	0.00	0.00	0.00	0.00	0.00	0.00	0.00
Al	0.00	0.00	0.00	0.00	0.00	0.00	0.00	0.00	0.00	0.00	0.00	0.00	0.00	0.00	0.00
Cr	0.00	0.00	0.00	0.00	0.00	0.00	0.00	0.00	0.00	0.00	0.00	0.00	0.00	0.00	0.00
Fe2	0.22	0.22	0.21	0.21	0.22	0.22	0.21	0.21	0.21	0.21	0.20	0.20	0.20	0.20	0.21
Mn	0.00	0.00	0.00	0.00	0.00	0.00	0.00	0.00	0.00	0.00	0.00	0.00	0.00	0.00	0.00
Ni	0.00	0.00	0.00	0.00	0.00	0.00	0.00	0.00	0.00	0.00	0.00	0.00	0.00	0.00	0.00
Mg	1.76	1.77	1.77	1.77	1.76	1.76	1.77	1.78	1.77	1.76	1.77	1.78	1.79	1.78	1.78
Ca	0.01	0.01	0.01	0.01	0.01	0.01	0.01	0.01	0.01	0.01	0.01	0.01	0.01	0.01	0.01
Na	0.00	0.00	0.00	0.00	0.00	0.00	0.00	0.00	0.00	0.00	0.00	0.00	0.00	0.00	0.00
K	0.00	0.00	0.00	0.00	0.00	0.00	0.00	0.00	0.00	0.00	0.00	0.00	0.00	0.00	0.00
XMg	0.88	0.88	0.88	0.89	0.88	0.88	0.89	0.89	0.88	0.88	0.89	0.89	0.89	0.89	0.89

Table 3-2:
Suite 10

Time	60	60	60	60	60	60	60	60	60	60	60	60	60	60	60
Sample	OM-18	OM-18	OM-18	OM-18	OM-18	OM-18	OM-18	OM-18	OM-18	OM-18	OM-18	OM-18	OM-18	OM-18	OM-18
Melt	AH6	AH6	AH6	AH6	AH6	AH6	AH6	AH6	AH6	AH6	AH6	AH6	AH6	AH6	AH6
T	1250	1250	1250	1250	1250	1250	1250	1250	1250	1250	1250	1250	1250	1250	1250
P	0.7	0.7	0.7	0.7	0.7	0.7	0.7	0.7	0.7	0.7	0.7	0.7	0.7	0.7	0.7
Analysis n°	48-02BC	48-02BR	05Res	06BR	06BC	48-07BC	48-07BR	05EC	48-08BS	05ER	03R	03C	48-09BR	48-09BC	48-09EC
Sample Zone	2	2	3	3	3	3	3	3	3	2	3	3	3	3	3
Zone	core	rim	rim	rim	core	core	rim	core	core	rim	rim	core	rim	core	core
D (mm)	0.09	0.10	0.22	0.24	0.25	0.25	0.27	0.28	0.31	0.32	0.37	0.41	0.60	0.60	0.64
SiO ₂	40.49	40.98	40.87	40.91	40.38	40.75	41.06	40.40	40.93	40.92	40.94	40.29	40.73	40.67	40.88
TiO ₂	0.04	0.00	0.01	0.03	0.00	0.00	0.03	0.00	0.03	0.02	0.01	0.00	0.04	0.01	0.02
Al ₂ O ₃	0.08	0.08	0.10	0.13	0.06	0.04	0.06	0.06	0.49	0.08	0.09	0.08	0.06	0.04	0.06
Cr ₂ O ₃	0.08	0.07	0.00	0.05	0.04	0.06	0.00	0.04	0.03	0.04	0.03	0.02	0.05	0.07	0.05
FeO	10.01	9.98	10.07	10.23	9.98	10.03	10.22	10.34	10.01	10.44	10.33	10.22	9.81	10.13	10.06
MnO	0.16	0.11	0.12	0.09	0.19	0.16	0.15	0.16	0.18	0.13	0.10	0.10	0.17	0.19	0.12
NiO	0.07	d.l.	d.l.	d.l.	d.l.	d.l.	0.04	0.05	0.06	0.01	0.08	0.20	0.05	0.06	0.10
MgO	49.09	48.98	49.23	49.36	49.59	49.05	49.32	49.04	48.30	49.20	48.34	47.99	49.10	49.46	49.30
CaO	0.37	0.39	0.40	0.41	0.39	0.37	0.39	0.37	0.78	0.35	0.36	0.32	0.37	0.34	0.34
NaO	0.00	0.02	0.01	0.00	0.02	0.02	0.04	0.02	0.03	0.03	0.02	0.01	0.01	0.01	0.00
K2O	0.00	0.00	0.00	0.00	0.01	0.00	0.00	0.00	0.01	0.00	0.00	0.00	0.01	0.01	0.00
Total	100.39	100.61	100.80	101.21	100.66	100.48	101.31	100.48	100.83	101.22	100.31	99.24	100.40	100.99	100.93
Si	0.99	1.00	0.99	0.99	0.98	0.99	0.99	0.99	1.00	0.99	1.00	1.00	0.99	0.99	0.99
Ti	0.00	0.00	0.00	0.00	0.00	0.00	0.00	0.00	0.00	0.00	0.00	0.00	0.00	0.00	0.00
Al	0.00	0.00	0.00	0.00	0.00	0.00	0.00	0.00	0.01	0.00	0.00	0.00	0.00	0.00	0.00
Cr	0.00	0.00	0.00	0.00	0.00	0.00	0.00	0.00	0.00	0.00	0.00	0.00	0.00	0.00	0.00
Fe2	0.20	0.20	0.20	0.21	0.20	0.20	0.21	0.21	0.20	0.21	0.21	0.21	0.20	0.21	0.20
Mn	0.00	0.00	0.00	0.00	0.00	0.00	0.00	0.00	0.00	0.00	0.00	0.00	0.00	0.00	0.00
Ni	0.00	0.00	0.00	0.00	0.00	0.00	0.00	0.00	0.00	0.00	0.00	0.00	0.00	0.00	0.00
Mg	1.79	1.78	1.78	1.78	1.80	1.78	1.78	1.78	1.76	1.78	1.77	1.77	1.79	1.79	1.79
Ca	0.01	0.01	0.01	0.01	0.01	0.01	0.01	0.01	0.02	0.01	0.01	0.01	0.01	0.01	0.01
Na	0.00	0.00	0.00	0.00	0.00	0.00	0.00	0.00	0.00	0.00	0.00	0.00	0.00	0.00	0.00
K	0.00	0.00	0.00	0.00	0.00	0.00	0.00	0.00	0.00	0.00	0.00	0.00	0.00	0.00	0.00
XMg	0.89	0.89	0.89	0.89	0.89	0.89	0.89	0.89	0.88	0.89	0.89	0.89	0.89	0.89	0.89

Table 3-2:
Suite 11

Table 3-2:
Suite 12

Time	60	60	60	60	60	60	60	60	60	60	60	60	60	60	60
Sample	OM-18	OM-18	OM-18	OM-18	OM-18	OM-18	OM-18	OM-18	OM-18	OM-18	OM-18	OM-18	OM-18	OM-18	OM-18
Melt	AH6	AH6	AH6	AH6	AH6	AH6	AH6	AH6	AH6	AH6	AH6	AH6	AH6	AH6	AH6
T	1250	1250	1250	1250	1250	1250	1250	1250	1250	1250	1250	1250	1250	1250	1250
P	0.7	0.7	0.7	0.7	0.7	0.7	0.7	0.7	0.7	0.7	0.7	0.7	0.7	0.7	0.7
Analysis n°	48-13BS	48-14BC	48-14BR	48-14ER	48-14EC	07R	48-18ER	07C	48-18EC	48-17EC	48-17BC	48-17BR	48-16BC	48-16BR	48-16BS
Sample Zone	4	4	4	4	4	4	4	4	4	4	4	4	4	4	4
Zone	core	core	rim	rim	core	rim	core	core	core	core	rim	core	core	rim	core
D (mm)	1.14	1.19	1.20	1.21	1.23	1.38	1.40	1.42	1.43	1.46	1.48	1.49	1.61	1.62	1.62
SiO ₂	40.88	40.65	40.34	40.63	40.71	41.00	40.71	41.11	40.90	41.21	40.76	40.48	40.76	41.09	40.75
TiO ₂	0.04	0.02	0.01	0.01	0.01	0.02	0.00	0.03	0.02	0.01	0.00	0.00	0.00	0.06	0.01
Al ₂ O ₃	0.06	0.07	0.11	0.09	0.08	0.06	0.07	0.11	0.07	0.07	0.06	0.10	0.06	0.12	0.10
Cr ₂ O ₃	0.08	0.02	0.04	0.04	0.00	0.06	0.04	0.02	0.00	0.04	0.01	0.00	0.05	0.01	0.01
FeO	9.66	9.72	9.66	9.35	9.71	9.69	9.42	9.46	9.39	9.51	9.52	9.35	9.36	9.20	9.29
MnO	0.10	0.18	0.13	0.13	0.17	0.09	0.12	0.17	0.13	0.14	0.13	0.16	0.08	0.10	0.12
NiO	0.12	0.12	0.11	0.08	0.27	0.15	d.l.	0.27	0.13	0.15	0.10	0.10	0.09	0.09	d.l.
MgO	49.53	49.63	49.24	49.13	49.36	48.62	48.58	48.70	48.49	48.73	48.75	48.49	49.58	49.18	48.89
CaO	0.35	0.32	0.36	0.34	0.29	0.32	0.33	0.27	0.30	0.29	0.29	0.35	0.36	0.40	0.34
NaO	0.00	0.01	0.02	0.02	0.01	0.02	0.00	0.00	0.01	0.01	0.03	0.01	0.01	0.00	0.02
K ₂ O	0.00	0.01	0.00	0.01	0.01	0.01	0.00	0.00	0.00	0.01	0.00	0.00	0.00	0.00	0.00
Total	100.82	100.75	100.02	99.83	100.62	100.03	99.27	100.15	99.45	100.16	99.65	99.03	100.36	100.25	99.53
Si	0.99	0.99	0.99	1.00	0.99	1.01	1.00	1.01	1.01	1.01	1.00	1.00	0.99	1.00	1.00
Ti	0.00	0.00	0.00	0.00	0.00	0.00	0.00	0.00	0.00	0.00	0.00	0.00	0.00	0.00	0.00
Al	0.00	0.00	0.00	0.00	0.00	0.00	0.00	0.00	0.00	0.00	0.00	0.00	0.00	0.00	0.00
Cr	0.00	0.00	0.00	0.00	0.00	0.00	0.00	0.00	0.00	0.00	0.00	0.00	0.00	0.00	0.00
Fe ₂	0.20	0.20	0.20	0.19	0.20	0.20	0.19	0.19	0.19	0.19	0.20	0.19	0.19	0.19	0.19
Mn	0.00	0.00	0.00	0.00	0.00	0.00	0.00	0.00	0.00	0.00	0.00	0.00	0.00	0.00	0.00
Ni	0.00	0.00	0.00	0.00	0.01	0.00	0.00	0.01	0.00	0.00	0.00	0.00	0.00	0.00	0.00
Mg	1.79	1.80	1.80	1.79	1.79	1.78	1.79	1.78	1.78	1.78	1.79	1.79	1.80	1.79	1.79
Ca	0.01	0.01	0.01	0.01	0.01	0.01	0.01	0.01	0.01	0.01	0.01	0.01	0.01	0.01	0.01
Na	0.00	0.00	0.00	0.00	0.00	0.00	0.00	0.00	0.00	0.00	0.00	0.00	0.00	0.00	0.00
K	0.00	0.00	0.00	0.00	0.00	0.00	0.00	0.00	0.00	0.00	0.00	0.00	0.00	0.00	0.00
XMg	0.89	0.89	0.89	0.90	0.89	0.89	0.90	0.89	0.90	0.89	0.89	0.89	0.90	0.90	0.90

Table 3-2:
Suite 13

Time	60	60	60	60	60	60	60	60	60	60	60	60	60	60	60	60
Sample	OM-18	OM-18	OM-18	OM-18	OM-18	OM-18	OM-18	OM-18	OM-19	OM-19	OM-19	OM-19	OM-19	OM-19	OM-19	OM-19
Melt	AH6	AH6	AH6	AH6	AH6	AH6	AH6	AH6	AH6	AH6	AH6	AH6	AH6	AH6	AH6	AH6
T	1250	1250	1250	1250	1250	1250	1250	1250	1250	1250	1250	1250	1250	1250	1250	1250
P	0.7	0.7	0.7	0.7	0.7	0.7	0.7	0.7	0.7	0.7	0.7	0.7	0.7	0.7	0.7	0.7
Analysis n°	48-16ER	48-16EC	08R	48-15ER	48-15EC	15Res	48-15BC	48-15BR	98-01ER	98-01EC	98-01Res	98-03BS	98-02ER	98-02EC	98-02Res	
Sample Zone	4	4	4	4	4	4	4	4	1	1	1	2	2	2	2	
Zone	rim	core	rim	rim	core	rim	core	rim	rim	core	rim	core	rim	core	rim	
D (mm)	1.64	1.66	1.74	1.79	1.82	1.84	1.85	1.86	-0.72	-0.70	-0.68	-0.06	-0.05	-0.04	-0.03	
SiO ₂	40.71	40.80	40.85	40.78	40.67	40.88	40.98	40.89	40.53	40.23	40.38	41.12	41.05	40.96	41.01	
TiO ₂	0.00	0.01	0.00	0.00	0.02	0.00	0.00	0.00	0.01	0.00	0.03	0.04	0.03	0.00	0.00	
Al ₂ O ₃	0.14	0.06	0.08	0.07	0.07	0.06	0.04	0.07	0.08	0.08	0.10	0.08	0.07	0.04	0.03	
Cr ₂ O ₃	0.09	0.00	0.06	0.05	0.00	0.03	0.01	0.02	0.04	0.05	0.06	0.06	0.09	0.01	0.06	
FeO	9.33	9.38	9.36	9.25	9.38	9.32	9.16	9.23	9.51	11.82	10.63	8.96	9.46	9.67	9.05	
MnO	0.14	0.14	0.13	0.16	0.11	0.14	0.13	0.15	0.17	0.16	0.15	0.16	0.17	0.13	0.19	
NiO	0.05	0.04	0.05	d.l.	0.07	d.l.	0.01	d.l.	0.04	d.l.	d.l.	0.05	0.06	0.07	d.l.	
MgO	48.85	48.86	49.15	48.94	48.67	49.31	49.11	49.37	49.06	46.98	48.15	50.05	49.56	49.10	49.74	
CaO	0.31	0.29	0.36	0.32	0.29	0.33	0.34	0.34	0.41	0.40	0.42	0.40	0.39	0.38	0.40	
NaO	0.00	0.01	0.02	0.02	0.00	0.05	0.00	0.03	0.03	0.02	0.00	0.01	0.04	0.00	0.03	
K ₂ O	0.00	0.00	0.00	0.00	0.00	0.00	0.00	0.00	0.00	0.00	0.00	0.01	0.00	0.00	0.00	
Total	99.62	99.59	100.05	99.59	99.26	100.12	99.79	100.10	99.89	99.73	99.92	100.93	100.93	100.36	100.51	
Si	1.00	1.00	1.00	1.00	1.00	1.00	1.00	1.00	0.99	1.00	0.99	0.99	1.00	1.00	1.00	
Ti	0.00	0.00	0.00	0.00	0.00	0.00	0.00	0.00	0.00	0.00	0.00	0.00	0.00	0.00	0.00	
Al	0.00	0.00	0.00	0.00	0.00	0.00	0.00	0.00	0.00	0.00	0.00	0.00	0.00	0.00	0.00	
Cr	0.00	0.00	0.00	0.00	0.00	0.00	0.00	0.00	0.00	0.00	0.00	0.00	0.00	0.00	0.00	
Fe ₂	0.19	0.19	0.19	0.19	0.19	0.19	0.19	0.19	0.19	0.25	0.22	0.18	0.19	0.20	0.18	
Mn	0.00	0.00	0.00	0.00	0.00	0.00	0.00	0.00	0.00	0.00	0.00	0.00	0.00	0.00	0.00	
Ni	0.00	0.00	0.00	0.00	0.00	0.00	0.00	0.00	0.00	0.00	0.00	0.00	0.00	0.00	0.00	
Mg	1.79	1.79	1.79	1.79	1.79	1.80	1.79	1.80	1.79	1.74	1.77	1.80	1.79	1.79	1.80	
Ca	0.01	0.01	0.01	0.01	0.01	0.01	0.01	0.01	0.01	0.01	0.01	0.01	0.01	0.01	0.01	
Na	0.00	0.00	0.00	0.00	0.00	0.00	0.00	0.00	0.00	0.00	0.00	0.00	0.00	0.00	0.00	
K	0.00	0.00	0.00	0.00	0.00	0.00	0.00	0.00	0.00	0.00	0.00	0.00	0.00	0.00	0.00	
XMg	0.90	0.90	0.90	0.90	0.90	0.90	0.90	0.90	0.89	0.87	0.88	0.90	0.89	0.89	0.90	

Table 3-2:
Suite 14

Time	60	60	60	60	60	60	60	60	60	60	60	60	60	60	60	60
Sample	OM-19	OM-19	OM-19	OM-19	OM-19	OM-19	OM-19	OM-19	OM-19	OM-19	OM-19	OM-19	OM-19	OM-19	OM-19	OM-19
Melt	AH6	AH6	AH6	AH6	AH6	AH6	AH6	AH6	AH6	AH6	AH6	AH6	AH6	AH6	AH6	AH6
T	1250	1250	1250	1250	1250	1250	1250	1250	1250	1250	1250	1250	1250	1250	1250	1250
P	0.7	0.7	0.7	0.7	0.7	0.7	0.7	0.7	0.7	0.7	0.7	0.7	0.7	0.7	0.7	0.7
Analysis n°	03r	03c	2	1	98-05BS	98-04BS	04r	04c	98-07Res	98-07EC	98-06BS	05c	05r	06r	06c	
Sample Zone	2	2	2	2	3	3	3	3	3	3	3	3	3	3	3	3
Zone	rim	core	rim	core	core	core	rim	core	rim	core	core	core	rim	rim	rim	core
D (mm)	-0.02	-0.01	0.00	0.01	0.15	0.20	0.31	0.32	0.55	0.56	0.62	0.66	0.68	0.77	0.78	
SiO ₂	40.53	40.35	41.04	40.69	40.80	41.10	40.71	40.40	40.72	40.50	41.09	40.73	40.14	40.85	40.60	
TiO ₂	0.00	0.00	0.00	0.04	0.00	0.01	0.01	0.00	0.02	0.00	0.02	0.04	0.03	0.03	0.04	
Al ₂ O ₃	0.11	0.07	0.07	0.07	0.09	0.04	0.06	0.04	0.05	0.06	0.07	0.05	0.05	0.08	0.05	
Cr ₂ O ₃	0.01	0.04	0.00	0.11	0.05	0.03	0.05	0.03	0.05	0.06	0.10	0.06	0.03	0.02	0.06	
FeO	9.55	10.07	9.17	9.23	9.08	9.27	9.47	10.36	9.56	9.63	9.80	10.07	9.48	9.81	9.93	
MnO	0.18	0.18	0.16	0.14	0.13	0.12	0.18	0.11	0.16	0.17	0.16	0.15	0.20	0.10	0.10	
NiO	0.11	0.05	0.08	d.l.	0.09	0.11	d.l.	0.26	0.06	d.l.	0.04	0.16	0.01	0.07	0.18	
MgO	48.56	47.78	48.74	48.62	50.26	48.99	48.32	47.43	49.75	49.61	49.51	48.33	48.06	48.58	48.46	
CaO	0.39	0.36	0.43	0.38	0.39	0.36	0.38	0.34	0.35	0.32	0.32	0.30	0.33	0.33	0.23	
NaO	0.01	0.00	0.00	0.00	0.00	0.00	0.03	0.00	0.02	0.02	0.01	0.00	0.00	0.01	0.01	
K ₂ O	0.00	0.01	0.01	0.00	0.00	0.01	0.00	0.00	0.00	0.01	0.01	0.00	0.01	0.00	0.00	
Total	99.46	98.91	99.70	99.30	100.88	100.04	99.21	98.97	100.74	100.38	101.12	99.90	98.35	99.89	99.66	
Si	1.00	1.00	1.01	1.00	0.99	1.01	1.01	1.01	0.99	0.99	1.00	1.00	1.00	1.00	1.00	
Ti	0.00	0.00	0.00	0.00	0.00	0.00	0.00	0.00	0.00	0.00	0.00	0.00	0.00	0.00	0.00	
Al	0.00	0.00	0.00	0.00	0.00	0.00	0.00	0.00	0.00	0.00	0.00	0.00	0.00	0.00	0.00	
Cr	0.00	0.00	0.00	0.00	0.00	0.00	0.00	0.00	0.00	0.00	0.00	0.00	0.00	0.00	0.00	
Fe ₂	0.20	0.21	0.19	0.19	0.18	0.19	0.20	0.22	0.19	0.20	0.20	0.21	0.20	0.20	0.20	
Mn	0.00	0.00	0.00	0.00	0.00	0.00	0.00	0.00	0.00	0.00	0.00	0.00	0.00	0.00	0.00	
Ni	0.00	0.00	0.00	0.00	0.00	0.00	0.00	0.01	0.00	0.00	0.00	0.00	0.00	0.00	0.00	
Mg	1.78	1.77	1.78	1.79	1.81	1.79	1.78	1.76	1.80	1.80	1.79	1.77	1.79	1.78	1.78	
Ca	0.01	0.01	0.01	0.01	0.01	0.01	0.01	0.01	0.01	0.01	0.01	0.01	0.01	0.01	0.01	
Na	0.00	0.00	0.00	0.00	0.00	0.00	0.00	0.00	0.00	0.00	0.00	0.00	0.00	0.00	0.00	
K	0.00	0.00	0.00	0.00	0.00	0.00	0.00	0.00	0.00	0.00	0.00	0.00	0.00	0.00	0.00	
XMg	0.89	0.89	0.90	0.90	0.90	0.90	0.89	0.88	0.90	0.90	0.89	0.89	0.89	0.89	0.89	

Table 3-2:
Suite 15

Time	60	60	60	60	60	60	60	60	0.5	0.5	0.5	0.5	0.5	0.5
Sample	OM-19	OM-19	OM-19	OM-19	OM-19	OM-19	OM-19	OM-19	OM-23	OM-23	OM-23	OM-23	OM-23	OM-23
Melt	AH6	AH6	AH6	AH6	AH6	AH6	AH6	AH6	AH6	AH6	AH6	AH6	AH6	AH6
T	1250	1250	1250	1250	1250	1250	1250	1250	1300	1300	1300	1300	1300	1300
P	0.7	0.7	0.7	0.7	0.7	0.7	0.7	0.7	0.5	0.5	0.5	0.5	0.5	0.5
Analysis n°	08r	08c	07r	07c	98-09ER	98-09EC	09r	98-08BS	09c	01OC	01OR	02O1	02O3	02OC
Sample Zone	4	4	4	4	5	5	4	5	4	1	1	2	2	2
Zone	rim	core	rim	core	rim	core	rim	core	core	rim	rim	rim	core	rim
D (mm)	0.99	0.99	1.01	1.02	1.12	1.12	1.18	1.19	1.19	-0.10	-0.10	0.00	0.01	0.00
SiO ₂	40.77	40.37	41.16	40.75	40.95	40.77	40.67	40.83	40.64	41.15	40.67	40.85	40.42	40.85
TiO ₂	0.01	0.04	0.01	0.01	0.00	0.00	0.00	0.01	0.00	0.05	0.03	0.00	0.02	0.00
Al ₂ O ₃	0.18	0.09	0.04	0.05	0.06	0.07	0.10	0.08	0.08	0.02	0.09	0.05	0.05	0.03
Cr ₂ O ₃	0.00	0.00	0.05	0.03	0.00	0.01	0.09	0.00	0.03	0.01	0.04	0.02	0.09	0.00
FeO	9.24	9.10	9.55	9.40	9.13	9.38	9.18	8.76	9.15	9.60	10.80	9.97	10.61	9.72
MnO	0.14	0.20	0.18	0.18	0.12	0.16	0.11	0.16	0.15	0.13	0.15	0.18	0.17	0.14
NiO	0.11	d.l.	0.09	0.02	0.06	0.03	0.03	0.06	0.02	0.32	0.22	0.28	0.34	0.35
MgO	48.74	48.82	49.10	48.64	49.95	49.84	49.18	49.87	48.70	48.77	48.07	48.29	47.93	48.83
CaO	0.38	0.32	0.33	0.30	0.35	0.32	0.33	0.37	0.32	0.09	0.42	0.28	0.41	0.11
NaO	0.03	0.00	0.00	0.00	0.01	0.00	0.00	0.00	0.03	0.00	0.03	0.01	0.00	0.05
K ₂ O	0.00	0.00	0.00	0.00	0.00	0.00	0.00	0.02	0.00	0.00	0.01	0.01	0.01	0.00
Total	99.59	98.95	100.52	99.37	100.63	100.59	99.69	100.16	99.11	100.14	100.53	99.94	100.04	100.09
Si	1.00	1.00	1.00	1.00	0.99	0.99	1.00	0.99	1.00	1.01	1.00	1.00	1.00	1.00
Ti	0.00	0.00	0.00	0.00	0.00	0.00	0.00	0.00	0.00	0.00	0.00	0.00	0.00	0.00
Al	0.01	0.00	0.00	0.00	0.00	0.00	0.00	0.00	0.00	0.00	0.00	0.00	0.00	0.00
Cr	0.00	0.00	0.00	0.00	0.00	0.00	0.00	0.00	0.00	0.00	0.00	0.00	0.00	0.00
Fe ₂	0.19	0.19	0.19	0.19	0.19	0.19	0.19	0.18	0.19	0.20	0.22	0.21	0.22	0.20
Mn	0.00	0.00	0.00	0.00	0.00	0.00	0.00	0.00	0.00	0.00	0.00	0.00	0.00	0.00
Ni	0.00	0.00	0.00	0.00	0.00	0.00	0.00	0.00	0.00	0.01	0.00	0.01	0.01	0.00
Mg	1.79	1.80	1.78	1.79	1.81	1.80	1.80	1.81	1.79	1.78	1.76	1.77	1.76	1.78
Ca	0.01	0.01	0.01	0.01	0.01	0.01	0.01	0.01	0.01	0.00	0.01	0.01	0.01	0.01
Na	0.00	0.00	0.00	0.00	0.00	0.00	0.00	0.00	0.00	0.00	0.00	0.00	0.00	0.00
K	0.00	0.00	0.00	0.00	0.00	0.00	0.00	0.00	0.00	0.00	0.00	0.00	0.00	0.00
XMg	0.89	0.90	0.89	0.90	0.90	0.90	0.90	0.90	0.90	0.90	0.88	0.89	0.89	0.89

Table 3-2:
Suite 16

Time	0.5	0.5	0.5	0.5	0.5	0.5	0.5	0.5	0.5	0.5	0.5	0.5	0.33	0.33	
Sample	OM-23	OM-23	OM-23	OM-23	OM-23	OM-23	OM-23	OM-23	OM-23	OM-23	OM-23	OM-23	OM-24	OM-24	
Melt	AH6	AH6	AH6	AH6	AH6	AH6	AH6	AH6	AH6	AH6	AH6	AH6	AH6	AH7	
T	1300	1300	1300	1300	1300	1300	1300	1300	1300	1300	1300	1300	1300	1300	
P	0.5	0.5	0.5	0.5	0.5	0.5	0.5	0.5	0.5	0.5	0.5	0.5	0.5	0.5	
Analysis n°	03O2	04OC	04OR	05OC	06OC	10OC	11OC	13OC	13OR	16O1	17O1	17O3	04OC	04OR	
Sample Zone	3	3	3	3	3	3	3	3	3	3	3	3	3	3	
Zone	rim	core	rim	core	core	core	rim	core	core	rim	rim	rim	core	rim	
D (mm)	0.24	0.33	0.33	0.43	0.85	1.11	1.10	1.08	1.33	1.43	0.89	0.94	0.94	1.48	1.47
SiO ₂	40.63	40.75	40.96	40.51	40.84	41.26	40.86	40.80	40.82	40.70	40.64	40.98	40.65	40.96	41.39
TiO ₂	0.01	0.00	0.00	0.00	0.00	0.00	0.01	0.02	0.07	0.00	0.03	0.00	0.04	0.02	0.00
Al ₂ O ₃	0.07	0.03	0.04	0.02	0.02	0.01	0.05	0.00	0.01	0.03	0.08	0.12	0.00	0.02	0.02
Cr ₂ O ₃	0.00	0.00	0.01	0.00	0.00	0.06	0.00	0.02	0.00	0.01	0.00	0.00	0.05	0.00	0.00
FeO	10.48	9.70	10.09	9.17	9.59	9.13	9.44	9.64	9.31	8.80	9.99	9.86	9.58	9.23	9.77
MnO	0.09	0.14	0.15	0.15	0.13	0.14	0.15	0.18	0.14	0.15	0.13	0.13	0.12	0.19	0.14
NiO	0.41	0.36	0.30	0.38	0.34	0.38	0.36	0.44	0.37	0.10	0.38	0.41	0.30	0.31	0.36
MgO	48.29	48.88	48.71	49.36	49.25	49.11	48.80	49.17	49.33	49.77	48.38	48.68	48.69	49.72	49.65
CaO	0.35	0.08	0.16	0.08	0.09	0.10	0.18	0.08	0.08	0.35	0.37	0.36	0.19	0.11	0.15
NaO	0.00	0.01	0.01	0.00	0.03	0.01	0.00	0.01	0.00	0.02	0.04	0.01	0.00	0.00	0.01
K2O	0.00	0.00	0.00	0.00	0.02	0.01	0.01	0.00	0.01	0.00	0.01	0.00	0.01	0.01	0.00
Total	100.33	99.95	100.43	99.67	100.31	100.21	99.86	100.36	100.14	99.93	100.05	100.55	99.62	100.57	101.49
Si	1.00	1.00	1.00	0.99	1.00	1.01	1.00	1.00	0.99	1.00	1.00	1.00	1.00	1.00	1.00
Ti	0.00	0.00	0.00	0.00	0.00	0.00	0.00	0.00	0.00	0.00	0.00	0.00	0.00	0.00	0.00
Al	0.00	0.00	0.00	0.00	0.00	0.00	0.00	0.00	0.00	0.00	0.00	0.00	0.00	0.00	0.00
Cr	0.00	0.00	0.00	0.00	0.00	0.00	0.00	0.00	0.00	0.00	0.00	0.00	0.00	0.00	0.00
Fe2	0.22	0.20	0.21	0.19	0.20	0.19	0.19	0.20	0.19	0.18	0.21	0.20	0.20	0.19	0.20
Mn	0.00	0.00	0.00	0.00	0.00	0.00	0.00	0.00	0.00	0.00	0.00	0.00	0.00	0.00	0.00
Ni	0.01	0.01	0.01	0.01	0.01	0.01	0.01	0.01	0.01	0.00	0.01	0.01	0.01	0.01	0.01
Mg	1.77	1.79	1.78	1.80	1.79	1.79	1.79	1.79	1.80	1.81	1.77	1.77	1.79	1.80	1.79
Ca	0.01	0.00	0.00	0.00	0.00	0.00	0.00	0.00	0.00	0.01	0.01	0.01	0.01	0.00	0.00
Na	0.00	0.00	0.00	0.00	0.00	0.00	0.00	0.00	0.00	0.00	0.00	0.00	0.00	0.00	0.00
K	0.00	0.00	0.00	0.00	0.00	0.00	0.00	0.00	0.00	0.00	0.00	0.00	0.00	0.00	0.00
XMg	0.88	0.89	0.89	0.90	0.90	0.90	0.89	0.89	0.90	0.90	0.89	0.89	0.89	0.90	0.89

Table 3-2:
Suite 17

Time	0.33	0.33	0.33
Sample	OM-24	OM-24	OM-24
Melt	AH8	AH9	AH10
T	1300	1300	1300
P	0.5	0.5	0.5
Analysis n°	05O2	06O3	06O4
Sample Zone	3	3	3
Zone	rim	rim	rim
D (mm)	1.51	1.28	1.27
SiO ₂	41.13	41.46	41.22
TiO ₂	0.04	0.02	0.00
Al ₂ O ₃	0.06	0.03	0.02
Cr ₂ O ₃	0.04	0.04	0.05
FeO	9.67	9.75	9.79
MnO	0.16	0.18	0.12
NiO	0.30	0.39	0.39
MgO	49.67	49.81	49.79
CaO	0.35	0.12	0.14
NaO	0.00	0.03	0.00
K2O	0.00	0.00	0.00
Total	101.42	101.83	101.52
Si	0.99	1.00	1.00
Ti	0.00	0.00	0.00
Al	0.00	0.00	0.00
Cr	0.00	0.00	0.00
Fe2	0.20	0.20	0.20
Mn	0.00	0.00	0.00
Ni	0.01	0.01	0.01
Mg	1.79	1.79	1.79
Ca	0.01	0.00	0.00
Na	0.00	0.00	0.00
K	0.00	0.00	0.00
XMg	0.89	0.89	0.89

Table 3-3
Representative major element compositions of glass in isothermal experiments

Time	12	12	12	12	12	12	12	12	12	12	12	12	12
Sample	OM-11												
Melt	AH6												
T	1250	1250	1250	1250	1250	1250	1250	1250	1250	1250	1250	1250	1250
P	0.7	0.7	0.7	0.7	0.7	0.7	0.7	0.7	0.7	0.7	0.7	0.7	0.7
Analysis n°	2	1	3	4	5	6	7	8	9	10	20M	19M	25M
Sample Zone	1	1	1	1	1	1	1	1	1	1	2	2	3
D (mm)	-0.61	-0.59	-0.53	-0.51	-0.47	-0.40	-0.36	-0.27	-0.14	-0.02	0	0.018	0.2094
SiO ₂	49.76	49.42	50.02	49.92	49.72	50.19	50.24	50.14	50.24	50.12	49.39	49.77	51.85
TiO ₂	1.54	1.52	1.41	1.44	1.38	1.43	1.36	1.39	1.43	1.38	1.38	1.40	1.50
Al ₂ O ₃	16.24	16.21	16.10	16.00	16.08	15.80	15.60	15.55	15.57	15.66	16.07	16.12	19.26
Cr ₂ O ₃	0.00	0.02	0.01	0.01	0.00	0.00	0.02	0.00	0.05	0.00	0.01	0.00	0.00
FeO	10.45	10.39	10.36	10.33	10.30	10.29	10.49	10.41	10.20	10.27	10.34	10.46	6.04
MnO	0.16	0.17	0.21	0.16	0.22	0.19	0.25	0.31	0.17	0.19	0.20	0.18	0.15
NiO	0.02	0.00	0.00	0.00	0.02	0.05	0.00	0.00	0.00	0.06	0.00	0.05	0.02
MgO	7.68	8.03	7.69	7.66	7.79	7.68	7.61	7.82	7.97	8.01	8.25	7.38	5.71
CaO	11.20	11.33	11.20	11.36	11.39	11.35	11.36	11.23	11.33	11.22	11.10	11.47	11.83
NaO	2.74	2.74	2.82	2.91	2.88	2.82	2.85	2.95	2.86	2.87	3.08	3.00	3.42
K ₂ O	0.22	0.17	0.19	0.21	0.21	0.20	0.21	0.20	0.18	0.21	0.18	0.17	0.22
Total	100.00	100.00	100.00	100.00	100.00	100.00	100.00	100.00	100.00	100.00	100.00	100.00	100.00
Si	0.83	0.82	0.83	0.83	0.83	0.84	0.84	0.83	0.84	0.83	0.82	0.83	0.86
Ti	0.02	0.02	0.02	0.02	0.02	0.02	0.02	0.02	0.02	0.02	0.02	0.02	0.02
Al	0.32	0.32	0.32	0.31	0.32	0.31	0.31	0.30	0.31	0.31	0.32	0.32	0.38
Cr	0.00	0.00	0.00	0.00	0.00	0.00	0.00	0.00	0.00	0.00	0.00	0.00	0.00
Fe ₂	0.15	0.14	0.14	0.14	0.14	0.14	0.15	0.14	0.14	0.14	0.14	0.15	0.08
Mn	0.00	0.00	0.00	0.00	0.00	0.00	0.00	0.00	0.00	0.00	0.00	0.00	0.00
Ni	0.00	0.00	0.00	0.00	0.00	0.00	0.00	0.00	0.00	0.00	0.00	0.00	0.00
Mg	0.19	0.20	0.19	0.19	0.19	0.19	0.19	0.19	0.20	0.20	0.20	0.18	0.14
Ca	0.20	0.20	0.20	0.20	0.20	0.20	0.20	0.20	0.20	0.20	0.20	0.20	0.21
Na	0.09	0.09	0.09	0.09	0.09	0.09	0.09	0.10	0.09	0.09	0.10	0.10	0.11
K	0.00	0.00	0.00	0.00	0.00	0.00	0.00	0.00	0.00	0.00	0.00	0.00	0.00
XCa	0.69	0.70	0.69	0.68	0.69	0.69	0.69	0.68	0.69	0.68	0.67	0.68	0.66
XMg	0.57	0.58	0.57	0.57	0.57	0.57	0.56	0.57	0.58	0.58	0.59	0.56	0.63

D: Distance is calculated from the x,y coordinates of an olivine from the interface zone (picked up as a 0 mm reference olivine for each sample) and the x,y coordinates of the analysis

Oxyde wt% are recalculated at 100%, Cations are calculated by dividing oxyde wt% by the molar mass for each oxyde

Sample zones : 1: melt layer, 2: Interface, 3: Ol-rich layer bot. half, 4: Ol-rich layer up. Half, 5: carbon spheres

Table 3-3
Suite 1

Time	12	12	12	12	12	12	12	12	12	12	12	12	12	
Sample	OM-11	OM-12	OM-12	OM-12	OM-12	OM-12								
Melt	AH6	AH3	AH3	AH3	AH3	AH3	AH3							
T	1250	1250	1250	1250	1250	1250	1250	1250	1250	1250	1250	1250	1250	
P	0.7	0.7	0.7	0.7	0.7	0.7	0.7	0.7	0.7	0.7	0.7	0.7	0.7	
Analysis n°	27	29	33	58m	60m	41	44m	61M	59	A-01	A-02	54	A-03	A-04
Sample Zone	3	3	3	3	3	4	3	4	5	1	1	1	1	
D (mm)	0.30	0.37	0.49	0.6294	0.8238	0.89	0.9048	1.3542	3.3084	-0.956	-0.836	-0.761	-0.726	-0.61
SiO ₂	51.89	52.72	53.11	53.29	52.48	52.82	52.51	51.95	50.15	48.60	48.77	48.58	48.68	48.70
TiO ₂	1.59	1.58	1.62	1.64	1.55	1.48	1.52	1.50	1.43	0.90	0.86	0.87	0.88	0.84
Al ₂ O ₃	17.54	18.23	18.27	18.81	18.28	16.73	18.02	16.81	15.80	16.43	16.39	16.38	16.38	16.35
Cr ₂ O ₃	0.05	0.04	0.01	0.00	0.02	0.01	0.01	0.05	0.03	0.06	0.09	0.05	0.07	0.06
FeO	6.28	5.78	5.73	5.40	6.00	6.24	5.98	6.83	10.05	8.75	8.69	8.74	8.68	8.70
MnO	0.07	0.11	0.11	0.12	0.20	0.10	0.14	0.19	0.26	0.20	0.19	0.16	0.18	0.16
NiO	0.01	0.08	0.08	0.00	0.01	0.12	0.08	0.06	0.00	0.00	0.01	0.07	0.06	0.00
MgO	7.84	5.93	5.46	4.63	5.85	8.02	6.76	7.40	8.07	9.50	9.17	9.69	9.18	9.19
CaO	11.21	11.89	11.92	12.67	12.25	11.31	11.64	12.53	11.10	13.29	13.43	13.11	13.45	13.54
NaO	3.26	3.39	3.43	3.21	3.14	2.92	3.10	2.49	2.92	2.19	2.30	2.26	2.35	2.36
K ₂ O	0.26	0.24	0.27	0.24	0.24	0.24	0.23	0.19	0.19	0.08	0.11	0.10	0.09	0.11
Total	100.00	100.00	100.00	100.00	100.00	100.00	100.00	100.00	100.00	100.00	100.00	100.00	100.00	
Si	0.86	0.88	0.88	0.89	0.87	0.88	0.87	0.86	0.83	0.81	0.81	0.81	0.81	0.81
Ti	0.02	0.02	0.02	0.02	0.02	0.02	0.02	0.02	0.02	0.01	0.01	0.01	0.01	0.01
Al	0.34	0.36	0.36	0.37	0.36	0.33	0.35	0.33	0.31	0.32	0.32	0.32	0.32	0.32
Cr	0.00	0.00	0.00	0.00	0.00	0.00	0.00	0.00	0.00	0.00	0.00	0.00	0.00	0.00
Fe ₂	0.09	0.08	0.08	0.08	0.08	0.09	0.08	0.10	0.14	0.12	0.12	0.12	0.12	0.12
Mn	0.00	0.00	0.00	0.00	0.00	0.00	0.00	0.00	0.00	0.00	0.00	0.00	0.00	0.00
Ni	0.00	0.00	0.00	0.00	0.00	0.00	0.00	0.00	0.00	0.00	0.00	0.00	0.00	0.00
Mg	0.19	0.15	0.14	0.11	0.15	0.20	0.17	0.18	0.20	0.24	0.23	0.24	0.23	0.23
Ca	0.20	0.21	0.21	0.23	0.22	0.20	0.21	0.22	0.20	0.24	0.24	0.23	0.24	0.24
Na	0.11	0.11	0.11	0.10	0.10	0.09	0.10	0.08	0.09	0.07	0.07	0.07	0.08	0.08
K	0.01	0.01	0.01	0.01	0.01	0.01	0.00	0.00	0.00	0.00	0.00	0.00	0.00	0.00
XCa	0.66	0.66	0.66	0.69	0.68	0.68	0.68	0.74	0.68	0.77	0.76	0.76	0.76	0.76
XMg	0.69	0.65	0.63	0.60	0.63	0.70	0.67	0.66	0.59	0.66	0.65	0.66	0.65	0.65

Table 3-3
Suite 2

Time	12	12	12	12	12	12	12	12	12	12	
Sample	OM-12										
Melt	AH3										
T	1250	1250	1250	1250	1250	1250	1250	1250	1250	1250	
P	0.7	0.7	0.7	0.7	0.7	0.7	0.7	0.7	0.7	0.7	
Analysis n°	53	A-05	A-06	52	A-07	51	A-08	9.00	A-09	50	A-12
Sample Zone	1	1	1	1	1	1	1	2	2	3	
D (mm)	-0.56	-0.51	-0.31	-0.30	-0.23	-0.17	-0.03	-0.02	0.01	0.09	0.18
SiO ₂	48.80	48.99	48.85	48.73	49.05	48.62	48.97	48.60	48.77	49.09	49.43
TiO ₂	0.72	0.82	0.87	0.89	0.80	0.87	0.86	0.84	0.90	0.88	0.87
Al ₂ O ₃	16.46	16.40	16.35	16.26	16.24	16.75	16.59	16.68	16.74	16.84	17.00
Cr ₂ O ₃	0.04	0.06	0.07	0.13	0.09	0.02	0.09	0.05	0.09	0.05	0.07
FeO	8.61	8.61	8.68	8.48	8.80	8.61	8.56	8.57	8.77	8.40	7.69
MnO	0.17	0.11	0.17	0.17	0.21	0.12	0.20	0.16	0.14	0.17	0.17
NiO	0.00	0.00	0.00	0.00	0.03	0.00	0.00	0.01	0.00	0.04	0.03
MgO	9.55	9.19	9.19	9.52	9.13	9.56	9.27	9.47	8.86	8.56	8.74
CaO	13.24	13.39	13.51	13.35	13.15	13.11	13.18	13.22	13.34	13.72	13.60
NaO	2.31	2.32	2.23	2.38	2.23	2.23	2.20	2.30	2.28	2.17	2.29
K ₂ O	0.10	0.09	0.08	0.10	0.11	0.11	0.09	0.09	0.11	0.07	0.11
Total	100.00	100.00	100.00	100.00	100.00	100.00	100.00	100.00	100.00	100.00	100.00
Si	0.81	0.82	0.81	0.81	0.82	0.81	0.81	0.81	0.81	0.82	0.82
Ti	0.01	0.01	0.01	0.01	0.01	0.01	0.01	0.01	0.01	0.01	0.01
Al	0.32	0.32	0.32	0.32	0.32	0.33	0.33	0.33	0.33	0.33	0.33
Cr	0.00	0.00	0.00	0.00	0.00	0.00	0.00	0.00	0.00	0.00	0.00
Fe ₂	0.12	0.12	0.12	0.12	0.12	0.12	0.12	0.12	0.12	0.12	0.11
Mn	0.00	0.00	0.00	0.00	0.00	0.00	0.00	0.00	0.00	0.00	0.00
Ni	0.00	0.00	0.00	0.00	0.00	0.00	0.00	0.00	0.00	0.00	0.00
Mg	0.24	0.23	0.23	0.24	0.23	0.24	0.23	0.24	0.22	0.21	0.22
Ca	0.24	0.24	0.24	0.24	0.23	0.23	0.23	0.24	0.24	0.24	0.24
Na	0.07	0.07	0.07	0.08	0.08	0.07	0.07	0.07	0.07	0.07	0.07
K	0.00	0.00	0.00	0.00	0.00	0.00	0.00	0.00	0.00	0.00	0.00
XCa	0.76	0.76	0.77	0.76	0.75	0.76	0.77	0.76	0.76	0.78	0.77
XMg	0.66	0.66	0.65	0.67	0.65	0.66	0.66	0.66	0.64	0.64	0.67

Table 3-3
Suite 3

Time	12	12	12	12	13	13	13	13
Sample	OM-12	OM-12	OM-12	OM-12	OM-13	OM-13	OM-13	OM-13
Melt	AH3	AH3	AH3	AH3	HDRBC	HDRBC	HDRBC	HDRBC
T	1250	1250	1250	1250	1250	1250	1250	1250
P	0.7	0.7	0.7	0.7	0.7	0.7	0.7	0.7
Analysis n°	A-15	A-18	A-21	A-24	A-01	A-02	A-03	A-04
Sample Zone	3	3	3	3	1	1	1	1
D (mm)	0.25	0.33	0.44	0.65	-0.94	-0.81	-0.50	-0.21
SiO ₂	50.44	50.78	51.18	50.91	48.32	48.17	48.75	48.80
TiO ₂	0.85	0.94	0.94	0.93	0.94	0.99	0.92	0.92
Al ₂ O ₃	18.05	18.85	19.09	18.82	17.24	17.09	17.17	17.09
Cr ₂ O ₃	0.05	0.03	0.00	0.01	0.00	0.00	0.00	0.01
FeO	7.04	6.57	6.34	6.53	10.50	10.43	10.17	10.12
MnO	0.16	0.14	0.07	0.11	0.15	0.22	0.18	0.15
NiO	0.02	0.03	0.04	0.02	0.05	0.00	0.00	0.01
MgO	6.87	5.75	5.02	6.16	7.96	8.17	8.01	8.27
CaO	14.06	14.38	14.69	13.86	12.13	12.08	12.21	11.91
NaO	2.35	2.38	2.49	2.51	2.59	2.75	2.47	2.60
K2O	0.11	0.15	0.14	0.13	0.13	0.11	0.12	0.12
Total	100.00	100.00	100.00	100.00	100.00	100.00	100.00	100.00
Si	0.84	0.85	0.85	0.85	0.80	0.80	0.81	0.81
Ti	0.01	0.01	0.01	0.01	0.01	0.01	0.01	0.01
Al	0.35	0.37	0.37	0.37	0.34	0.34	0.34	0.34
Cr	0.00	0.00	0.00	0.00	0.00	0.00	0.00	0.00
Fe2	0.10	0.09	0.09	0.09	0.15	0.15	0.14	0.14
Mn	0.00	0.00	0.00	0.00	0.00	0.00	0.00	0.00
Ni	0.00	0.00	0.00	0.00	0.00	0.00	0.00	0.00
Mg	0.17	0.14	0.12	0.15	0.20	0.20	0.20	0.21
Ca	0.25	0.26	0.26	0.25	0.22	0.22	0.22	0.21
Na	0.08	0.08	0.08	0.08	0.08	0.09	0.08	0.08
K	0.00	0.00	0.00	0.00	0.00	0.00	0.00	0.00
XCa	0.77	0.77	0.77	0.75	0.72	0.71	0.73	0.72
XMg	0.64	0.61	0.59	0.63	0.57	0.58	0.58	0.59

Table 3-3
Suite 4

Time	13	13	13	13	13	13	13	13	13	24	24	24	24	
Sample	OM-13	OM-15	OM-15	OM-15	OM-15									
Melt	HDRBC	AH6	AH6	AH6	AH6									
T	1250	1250	1250	1250	1250	1250	1250	1250	1250	1250	1250	1250	1250	
P	0.7	0.7	0.7	0.7	0.7	0.7	0.7	0.7	0.7	0.7	0.7	0.7	0.7	
Analysis n°	A-05	A-09	A-09	A-21	A-16	A-21	A-26	A-31	A-32	A-36	59	48-01M	48-01M2	A-06
Sample Zone	1	2	2	3	3	3	4	4	4	1	1	1	1	
D (mm)	-0.09	0.03	0.03	0.65	0.25	0.65	0.93	1.07	1.16	1.29	-0.62	-0.46	-0.43	-0.18
SiO ₂	48.59	49.12	49.12	50.61	50.06	50.61	50.28	51.08	50.58	50.99	48.33	48.14	47.93	49.36
TiO ₂	0.98	1.00	1.00	0.86	1.05	0.86	1.08	1.04	1.17	1.16	0.89	0.88	0.87	0.89
Al ₂ O ₃	17.14	18.83	18.83	19.30	20.03	19.30	18.79	19.53	19.02	19.75	16.18	16.60	16.77	15.56
Cr ₂ O ₃	0.00	0.05	0.05	0.03	0.01	0.03	0.00	0.00	0.00	0.00	0.08	0.07	0.06	0.01
FeO	9.79	8.99	8.99	6.04	6.67	6.04	6.41	6.14	6.39	5.97	8.91	8.71	8.73	9.17
MnO	0.25	0.22	0.22	0.06	0.13	0.06	0.16	0.18	0.14	0.11	0.18	0.19	0.21	0.15
NiO	0.00	0.05	0.05	0.06	0.00	0.06	0.05	0.07	0.05	0.00	0.04	0.00	0.00	0.00
MgO	8.36	5.84	5.84	7.83	5.72	7.83	7.44	5.92	6.68	5.69	10.16	9.83	9.85	9.46
CaO	12.07	13.00	13.00	12.03	13.22	12.03	12.66	12.95	13.02	13.13	12.89	13.20	13.05	12.97
NaO	2.71	2.78	2.78	3.03	2.95	3.03	2.98	2.92	2.81	3.04	2.24	2.28	2.43	2.33
K ₂ O	0.11	0.12	0.12	0.16	0.16	0.16	0.15	0.18	0.15	0.17	0.10	0.10	0.10	0.11
Total	100.00	100.00	100.00	100.00	100.00	100.00	100.00	100.00	100.00	100.00	100.00	100.00	100.00	100.00
Si	0.81	0.82	0.82	0.84	0.83	0.84	0.84	0.85	0.84	0.85	0.80	0.80	0.80	0.82
Ti	0.01	0.01	0.01	0.01	0.01	0.01	0.01	0.01	0.01	0.01	0.01	0.01	0.01	0.01
Al	0.34	0.37	0.37	0.38	0.39	0.38	0.37	0.38	0.37	0.39	0.32	0.33	0.33	0.31
Cr	0.00	0.00	0.00	0.00	0.00	0.00	0.00	0.00	0.00	0.00	0.00	0.00	0.00	0.00
Fe ₂	0.14	0.13	0.13	0.08	0.09	0.08	0.09	0.09	0.09	0.08	0.12	0.12	0.12	0.13
Mn	0.00	0.00	0.00	0.00	0.00	0.00	0.00	0.00	0.00	0.00	0.00	0.00	0.00	0.00
Ni	0.00	0.00	0.00	0.00	0.00	0.00	0.00	0.00	0.00	0.00	0.00	0.00	0.00	0.00
Mg	0.21	0.14	0.14	0.19	0.14	0.19	0.18	0.15	0.17	0.14	0.25	0.24	0.24	0.23
Ca	0.22	0.23	0.23	0.21	0.24	0.21	0.23	0.23	0.23	0.23	0.23	0.24	0.23	0.23
Na	0.09	0.09	0.09	0.10	0.10	0.10	0.10	0.09	0.09	0.10	0.07	0.07	0.08	0.08
K	0.00	0.00	0.00	0.00	0.00	0.00	0.00	0.00	0.00	0.00	0.00	0.00	0.00	0.00
XCa	0.71	0.72	0.72	0.69	0.71	0.69	0.70	0.71	0.72	0.71	0.76	0.76	0.75	0.75
XMg	0.60	0.54	0.54	0.70	0.60	0.70	0.67	0.63	0.65	0.63	0.67	0.67	0.67	0.65

Table 3-3
Suite 5

Time	24	24	24	24	24	24	24	24	24	24	24	24	24	24
Sample	OM-15													
Melt	AH6													
T	1250	1250	1250	1250	1250	1250	1250	1250	1250	1250	1250	1250	1250	1250
P	0.7	0.7	0.7	0.7	0.7	0.7	0.7	0.7	0.7	0.7	0.7	0.7	0.7	0.7
Analysis n°	59	59	A-07	58	A-08	48-19M	54	A-54	A-26	A-50	48-24M	57	48-05M	A-57
Sample Zone	2	2	2	2	2	2	2	3	3	3	3	3	3	3
D (mm)	-0.06	-0.06	-0.06	-0.05	-0.05	0.03	0.04	0.13	0.35	0.38	0.40	0.41	0.43	0.48
SiO ₂	48.33	48.33	49.06	48.62	49.34	48.06	49.41	50.73	50.20	50.40	49.39	48.93	49.94	49.72
TiO ₂	0.89	0.89	0.83	0.80	0.83	0.85	1.02	0.93	0.91	0.87	0.90	0.82	0.99	0.82
Al ₂ O ₃	16.18	16.18	15.50	16.29	15.66	16.14	18.21	17.60	16.60	17.87	17.02	17.06	18.41	16.34
Cr ₂ O ₃	0.08	0.08	0.10	0.03	0.05	0.01	0.05	0.00	0.01	0.04	0.04	0.00	0.09	0.09
FeO	8.91	8.91	9.11	8.87	9.07	9.00	8.29	8.10	8.25	7.61	8.03	7.57	7.29	7.86
MnO	0.18	0.18	0.15	0.15	0.19	0.21	0.14	0.19	0.13	0.13	0.18	0.15	0.15	0.21
NiO	0.04	0.04	0.00	0.02	0.02	0.04	0.02	0.02	0.07	0.05	0.04	0.00	0.02	0.00
MgO	10.16	10.16	9.63	9.96	9.47	10.27	5.41	5.01	7.42	5.52	7.81	10.42	6.25	9.62
CaO	12.89	12.89	13.16	12.94	12.99	13.06	14.93	14.89	14.05	14.91	14.19	12.64	14.20	12.83
NaO	2.24	2.24	2.35	2.21	2.29	2.26	2.41	2.44	2.26	2.48	2.30	2.29	2.54	2.41
K ₂ O	0.10	0.10	0.11	0.10	0.11	0.10	0.11	0.09	0.09	0.12	0.09	0.11	0.11	0.10
Total	100.00	100.00	100.00	100.00	100.00	100.00	100.00	100.00	100.00	100.00	100.00	100.00	100.00	100.00
Si	0.80	0.80	0.82	0.81	0.82	0.80	0.82	0.84	0.84	0.84	0.82	0.81	0.83	0.83
Ti	0.01	0.01	0.01	0.01	0.01	0.01	0.01	0.01	0.01	0.01	0.01	0.01	0.01	0.01
Al	0.32	0.32	0.30	0.32	0.31	0.32	0.36	0.35	0.33	0.35	0.33	0.33	0.36	0.32
Cr	0.00	0.00	0.00	0.00	0.00	0.00	0.00	0.00	0.00	0.00	0.00	0.00	0.00	0.00
Fe ₂	0.12	0.12	0.13	0.12	0.13	0.13	0.12	0.11	0.11	0.11	0.11	0.11	0.10	0.11
Mn	0.00	0.00	0.00	0.00	0.00	0.00	0.00	0.00	0.00	0.00	0.00	0.00	0.00	0.00
Ni	0.00	0.00	0.00	0.00	0.00	0.00	0.00	0.00	0.00	0.00	0.00	0.00	0.00	0.00
Mg	0.25	0.25	0.24	0.25	0.23	0.25	0.13	0.12	0.18	0.14	0.19	0.26	0.16	0.24
Ca	0.23	0.23	0.23	0.23	0.23	0.23	0.27	0.27	0.25	0.27	0.25	0.23	0.25	0.23
Na	0.07	0.07	0.08	0.07	0.07	0.07	0.08	0.08	0.07	0.08	0.07	0.07	0.08	0.08
K	0.00	0.00	0.00	0.00	0.00	0.00	0.00	0.00	0.00	0.00	0.00	0.00	0.00	0.00
XCa	0.76	0.76	0.76	0.76	0.76	0.76	0.77	0.77	0.77	0.77	0.77	0.75	0.76	0.75
XMg	0.67	0.67	0.65	0.67	0.65	0.67	0.54	0.52	0.62	0.56	0.63	0.71	0.60	0.69

Table 3-3

Suite 6

Time	24	24	24	24	24	24	24	24	24	24	24	24	24	24
Sample	OM-15	OM-15	OM-15	OM-15	OM-15	OM-15	OM-15	OM-15						
Melt	AH6	AH6	AH6	AH6	AH6	AH6	AH6	AH6						
T	1250	1250	1250	1250	1250	1250	1250	1250	1250	1250	1250	1250	1250	1250
P	0.7	0.7	0.7	0.7	0.7	0.7	0.7	0.7	0.7	0.7	0.7	0.7	0.7	0.7
Analysis n°	A-28	48-06M	32	A-29	48-07M	A-34	48-09M2	48-09M	48-10M	38	A-38	60	A-44	A-09
Sample Zone	3	3	3	3	4	4	4	4	4	4	4	4	4	5
D (mm)	0.53	0.53	0.54	0.58	0.64	0.75	0.81	0.82	0.95	0.97	1.06	1.06	1.09	1.25
SiO ₂	50.45	48.09	50.10	50.93	49.47	51.24	49.60	50.31	50.65	49.78	50.33	49.41	50.65	51.01
TiO ₂	0.86	0.73	0.94	0.95	0.87	0.98	0.95	0.98	0.97	0.83	0.90	0.89	0.83	0.85
Al ₂ O ₃	16.80	15.58	18.20	17.65	17.65	18.13	18.04	18.70	17.82	16.40	15.94	16.52	15.90	15.74
Cr ₂ O ₃	0.03	0.00	0.01	0.05	0.04	0.03	0.00	0.01	0.02	0.02	0.05	0.06	0.00	0.00
FeO	7.64	7.52	7.21	7.25	6.88	6.87	7.18	6.57	6.95	7.21	7.51	6.96	7.47	7.08
MnO	0.16	0.16	0.16	0.12	0.16	0.16	0.15	0.16	0.13	0.14	0.11	0.16	0.10	0.15
NiO	0.00	0.08	0.02	0.01	0.00	0.00	0.10	0.10	0.08	0.02	0.03	0.00	0.00	0.00
MgO	8.10	14.64	6.55	6.34	9.60	6.10	7.66	5.97	6.04	10.42	10.09	11.18	9.80	10.26
CaO	13.70	10.72	14.30	14.24	12.66	13.66	13.82	14.21	14.75	12.74	12.67	12.25	12.78	12.32
NaO	2.17	2.38	2.40	2.37	2.54	2.72	2.40	2.88	2.52	2.33	2.22	2.43	2.37	2.48
K ₂ O	0.09	0.09	0.11	0.10	0.11	0.13	0.11	0.12	0.07	0.09	0.12	0.13	0.11	0.11
Total	100.00	100.00	100.00	100.00	100.00	100.00	100.00	100.00	100.00	100.00	100.00	100.00	100.00	100.00
Si	0.84	0.80	0.83	0.85	0.82	0.85	0.83	0.84	0.84	0.83	0.84	0.82	0.84	0.85
Ti	0.01	0.01	0.01	0.01	0.01	0.01	0.01	0.01	0.01	0.01	0.01	0.01	0.01	0.01
Al	0.33	0.31	0.36	0.35	0.35	0.36	0.35	0.37	0.35	0.32	0.31	0.32	0.31	0.31
Cr	0.00	0.00	0.00	0.00	0.00	0.00	0.00	0.00	0.00	0.00	0.00	0.00	0.00	0.00
Fe ₂	0.11	0.10	0.10	0.10	0.10	0.10	0.10	0.09	0.10	0.10	0.10	0.10	0.10	0.10
Mn	0.00	0.00	0.00	0.00	0.00	0.00	0.00	0.00	0.00	0.00	0.00	0.00	0.00	0.00
Ni	0.00	0.00	0.00	0.00	0.00	0.00	0.00	0.00	0.00	0.00	0.00	0.00	0.00	0.00
Mg	0.20	0.36	0.16	0.16	0.24	0.15	0.19	0.15	0.15	0.26	0.25	0.28	0.24	0.25
Ca	0.24	0.19	0.25	0.25	0.23	0.24	0.25	0.25	0.26	0.23	0.23	0.22	0.23	0.22
Na	0.07	0.08	0.08	0.08	0.08	0.09	0.08	0.09	0.08	0.08	0.07	0.08	0.08	0.08
K	0.00	0.00	0.00	0.00	0.00	0.00	0.00	0.00	0.00	0.00	0.00	0.00	0.00	0.00
XCa	0.78	0.71	0.77	0.77	0.73	0.74	0.76	0.73	0.76	0.75	0.76	0.74	0.75	0.73
XMg	0.65	0.78	0.62	0.61	0.71	0.61	0.66	0.62	0.61	0.72	0.71	0.74	0.70	0.72

Table 3-3
Suite 7

Time	24	24	24	24	24	24	24	24	24	24	60	60	60	
Sample	OM-15	OM-17	OM-17	OM-17										
Melt	AH6	AH3	AH3	AH3										
T	1250	1250	1250	1250	1250	1250	1250	1250	1250	1250	1250	1250	1250	
P	0.7	0.7	0.7	0.7	0.7	0.7	0.7	0.7	0.7	0.7	0.7	0.7	0.7	
Analysis n°	A-10	A-11	69	A-12	70	A-13	A-14	A-15	A-18	A-17	A-16	M1	M2	
Sample Zone	5	5	5	5	5	5	5	5	5	5	1	1	2	
D (mm)	1.30	1.33	1.37	1.42	1.45	1.46	1.58	1.66	1.67	1.71	1.83	-1.54	-0.86	-0.02
SiO ₂	50.67	50.59	49.88	50.87	49.99	50.95	50.60	50.52	50.84	51.44	51.18	49.56	49.91	51.76
TiO ₂	0.85	0.86	0.93	0.86	0.88	0.89	0.92	0.91	0.93	0.85	0.87	1.28	1.31	1.53
Al ₂ O ₃	15.75	15.77	16.39	15.80	16.37	15.71	16.04	16.02	15.92	16.02	15.91	14.20	14.10	15.90
Cr ₂ O ₃	0.03	0.05	0.03	0.00	0.01	0.05	0.03	0.00	0.07	0.00	0.02	0.03	0.00	0.04
FeO	7.14	7.07	6.82	7.02	6.84	7.02	6.81	6.78	6.67	6.49	6.63	8.52	8.48	8.16
MnO	0.14	0.19	0.13	0.11	0.09	0.17	0.15	0.17	0.18	0.08	0.14	0.19	0.22	0.17
NiO	0.11	0.00	0.00	0.00	0.00	0.00	0.00	0.00	0.00	0.06	0.05	0.05	0.09	0.02
MgO	10.40	10.61	11.20	10.57	11.15	10.61	10.88	10.99	10.50	10.37	10.42	12.43	12.26	6.27
CaO	12.25	12.10	12.08	12.11	12.11	12.04	12.01	12.09	12.14	12.09	12.13	11.11	10.88	13.10
NaO	2.54	2.65	2.42	2.52	2.44	2.46	2.47	2.41	2.62	2.47	2.54	2.46	2.57	2.90
K ₂ O	0.12	0.10	0.12	0.13	0.12	0.11	0.10	0.11	0.13	0.13	0.10	0.16	0.17	0.16
Total	100.00	100.00	100.00	100.00	100.00	100.00	100.00	100.00	100.00	100.00	100.00	100.00	100.00	100.00
Si	0.84	0.84	0.83	0.85	0.83	0.85	0.84	0.84	0.85	0.86	0.85	0.82	0.83	0.86
Ti	0.01	0.01	0.01	0.01	0.01	0.01	0.01	0.01	0.01	0.01	0.01	0.02	0.02	0.02
Al	0.31	0.31	0.32	0.31	0.32	0.31	0.31	0.31	0.31	0.31	0.31	0.28	0.28	0.31
Cr	0.00	0.00	0.00	0.00	0.00	0.00	0.00	0.00	0.00	0.00	0.00	0.00	0.00	0.00
Fe ₂	0.10	0.10	0.09	0.10	0.10	0.10	0.09	0.09	0.09	0.09	0.09	0.12	0.12	0.11
Mn	0.00	0.00	0.00	0.00	0.00	0.00	0.00	0.00	0.00	0.00	0.00	0.00	0.00	0.00
Ni	0.00	0.00	0.00	0.00	0.00	0.00	0.00	0.00	0.00	0.00	0.00	0.00	0.00	0.00
Mg	0.26	0.26	0.28	0.26	0.28	0.26	0.27	0.27	0.26	0.26	0.26	0.31	0.30	0.16
Ca	0.22	0.22	0.22	0.22	0.21	0.21	0.22	0.22	0.22	0.22	0.22	0.20	0.19	0.23
Na	0.08	0.09	0.08	0.08	0.08	0.08	0.08	0.08	0.08	0.08	0.08	0.08	0.08	0.09
K	0.00	0.00	0.00	0.00	0.00	0.00	0.00	0.00	0.00	0.00	0.00	0.00	0.00	0.00
XCa	0.73	0.72	0.73	0.73	0.73	0.73	0.73	0.74	0.72	0.73	0.73	0.71	0.70	0.71
XMg	0.72	0.73	0.75	0.73	0.74	0.73	0.74	0.74	0.74	0.74	0.72	0.72	0.72	0.58

Table 3-3
Suite 8

Time	60	60	60	60	60	60	60	60	60	60	60	60	60	
Sample	OM-17	OM-17	OM-17	OM-17	OM-18									
Melt	AH3	AH3	AH3	AH3	AH6									
T	1250	1250	1250	1250	1250	1250	1250	1250	1250	1250	1250	1250	1250	
P	0.7	0.7	0.7	0.7	0.7	0.7	0.7	0.7	0.7	0.7	0.7	0.7	0.7	
Analysis n°	22	22	23	24	01M	02M	02M	01M5μ	02M5μ	07M2	48-09M	05M	48-09M2	06M
Sample Zone	3	3	3	5	2	2	2	2	3	3	3	3	3	3
D (mm)	0.55	0.55	1.33	1.73	-0.06	-0.04	-0.04	-0.01	0.11	0.27	0.59	0.60	0.65	0.80
SiO ₂	50.89	50.89	52.09	51.03	49.46	48.75	48.75	48.60	49.53	49.50	49.35	50.11	49.75	50.15
TiO ₂	1.35	1.35	1.50	1.30	0.95	0.80	0.80	0.83	0.91	0.92	0.93	0.98	0.90	0.89
Al ₂ O ₃	15.28	15.28	15.77	13.60	17.09	15.18	15.18	16.05	17.19	17.63	17.62	17.40	18.20	16.78
Cr ₂ O ₃	0.01	0.01	0.04	0.00	0.08	0.05	0.05	0.00	0.03	0.01	0.01	0.00	0.05	0.01
FeO	8.66	8.66	7.69	7.85	8.12	8.54	8.54	8.08	7.86	7.83	7.87	7.90	7.57	7.99
MnO	0.19	0.19	0.15	0.12	0.20	0.21	0.21	0.16	0.17	0.11	0.15	0.17	0.11	0.19
NiO	0.00	0.00	0.00	0.06	0.00	0.06	0.06	0.05	0.00	0.05	0.01	0.00	0.01	0.00
MgO	8.49	8.49	6.89	12.56	6.96	11.35	11.35	10.87	7.28	7.16	7.54	6.34	6.56	7.82
CaO	12.51	12.51	12.91	10.65	14.79	12.83	12.83	13.12	14.62	14.45	14.11	14.72	14.32	13.75
NaO	2.47	2.47	2.77	2.65	2.23	2.13	2.13	2.31	2.31	2.25	2.28	2.29	2.41	2.31
K ₂ O	0.18	0.18	0.20	0.18	0.11	0.09	0.09	0.10	0.10	0.09	0.13	0.10	0.11	0.11
Total	100.00	100.00	100.00	100.00	100.00	100.00	100.00	100.00	100.00	100.00	100.00	100.00	100.00	100.00
Si	0.85	0.85	0.87	0.85	0.82	0.81	0.81	0.82	0.82	0.82	0.83	0.83	0.83	0.83
Ti	0.02	0.02	0.02	0.02	0.01	0.01	0.01	0.01	0.01	0.01	0.01	0.01	0.01	0.01
Al	0.30	0.30	0.31	0.27	0.34	0.30	0.30	0.31	0.34	0.35	0.35	0.34	0.36	0.33
Cr	0.00	0.00	0.00	0.00	0.00	0.00	0.00	0.00	0.00	0.00	0.00	0.00	0.00	0.00
Fe ₂	0.12	0.12	0.11	0.11	0.11	0.12	0.12	0.11	0.11	0.11	0.11	0.11	0.11	0.11
Mn	0.00	0.00	0.00	0.00	0.00	0.00	0.00	0.00	0.00	0.00	0.00	0.00	0.00	0.00
Ni	0.00	0.00	0.00	0.00	0.00	0.00	0.00	0.00	0.00	0.00	0.00	0.00	0.00	0.00
Mg	0.21	0.21	0.17	0.31	0.17	0.28	0.28	0.27	0.18	0.18	0.19	0.16	0.16	0.19
Ca	0.22	0.22	0.23	0.19	0.26	0.23	0.23	0.23	0.26	0.26	0.25	0.26	0.26	0.25
Na	0.08	0.08	0.09	0.09	0.07	0.07	0.07	0.07	0.07	0.07	0.07	0.07	0.08	0.07
K	0.00	0.00	0.00	0.00	0.00	0.00	0.00	0.00	0.00	0.00	0.00	0.00	0.00	0.00
XCa	0.74	0.74	0.72	0.69	0.79	0.77	0.77	0.77	0.78	0.78	0.77	0.78	0.77	0.77
XMg	0.64	0.64	0.61	0.74	0.60	0.70	0.70	0.71	0.62	0.62	0.63	0.59	0.61	0.64

Table 3-3
Suite 9

Time	60	60	60	60	60	60	60	60	60	60	60	60	60
Sample	OM-18	OM-18	OM-18										
Melt	AH6	AH6	AH6										
T	1250	1250	1250	1250	1250	1250	1250	1250	1250	1250	1250	1250	1250
P	0.7	0.7	0.7	0.7	0.7	0.7	0.7	0.7	0.7	0.7	0.7	0.7	0.7
Analysis n°	48-10M	48-12M	48-13M	48-14M	9	07M	10	48-18M	48-17M	48-16M	48-15M2	48-15M	9
Sample Zone	3	3	4	4	4	5	5	5	5	5	5	5	5
D (mm)	0.82	0.92	1.15	1.20	1.30	1.34	1.37	1.39	1.50	1.63	1.77	1.87	1.91
SiO ₂	48.76	49.95	49.44	50.08	50.11	50.90	50.25	50.63	50.64	51.03	50.29	50.05	50.11
TiO ₂	0.93	0.99	0.96	1.04	0.85	0.94	0.83	0.95	0.97	0.94	0.97	0.87	0.85
Al ₂ O ₃	16.86	18.00	17.49	18.40	15.27	17.43	15.25	16.90	17.52	17.94	16.18	15.92	15.27
Cr ₂ O ₃	0.05	0.00	0.06	0.01	0.00	0.10	0.03	0.04	0.05	0.05	0.00	0.02	0.00
FeO	8.10	7.22	7.72	7.34	7.28	7.58	7.28	7.35	7.13	6.84	7.78	7.35	7.28
MnO	0.17	0.17	0.15	0.15	0.12	0.08	0.15	0.19	0.20	0.13	0.13	0.13	0.12
NiO	0.00	0.00	0.00	0.00	0.00	0.02	0.00	0.00	0.02	0.04	0.00	0.06	0.00
MgO	9.01	7.70	7.62	6.30	12.05	6.74	12.05	7.38	6.59	6.45	8.57	10.32	12.05
CaO	13.79	13.22	14.08	14.16	11.60	13.65	11.50	13.87	14.15	13.70	13.62	12.72	11.60
NaO	2.22	2.61	2.37	2.40	2.58	2.43	2.53	2.55	2.59	2.73	2.35	2.43	2.58
K ₂ O	0.10	0.13	0.10	0.12	0.13	0.13	0.13	0.13	0.15	0.15	0.12	0.13	0.13
Total	100.00	100.00	100.00	100.00	100.00	100.00	100.00	100.00	100.00	100.00	100.00	100.00	100.00
Si	0.81	0.83	0.82	0.83	0.83	0.85	0.84	0.84	0.84	0.85	0.84	0.83	0.83
Ti	0.01	0.01	0.01	0.01	0.01	0.01	0.01	0.01	0.01	0.01	0.01	0.01	0.01
Al	0.33	0.35	0.34	0.36	0.30	0.34	0.30	0.33	0.34	0.35	0.35	0.32	0.31
Cr	0.00	0.00	0.00	0.00	0.00	0.00	0.00	0.00	0.00	0.00	0.00	0.00	0.00
Fe ₂	0.11	0.10	0.11	0.10	0.10	0.11	0.10	0.10	0.10	0.10	0.11	0.10	0.10
Mn	0.00	0.00	0.00	0.00	0.00	0.00	0.00	0.00	0.00	0.00	0.00	0.00	0.00
Ni	0.00	0.00	0.00	0.00	0.00	0.00	0.00	0.00	0.00	0.00	0.00	0.00	0.00
Mg	0.22	0.19	0.19	0.16	0.30	0.17	0.30	0.18	0.16	0.16	0.21	0.26	0.30
Ca	0.25	0.24	0.25	0.25	0.21	0.24	0.21	0.25	0.25	0.24	0.24	0.23	0.21
Na	0.07	0.08	0.08	0.08	0.08	0.08	0.08	0.08	0.08	0.09	0.08	0.08	0.08
K	0.00	0.00	0.00	0.00	0.00	0.00	0.00	0.00	0.00	0.00	0.00	0.00	0.00
XCa	0.77	0.74	0.77	0.77	0.71	0.76	0.72	0.75	0.75	0.73	0.76	0.74	0.71
XMg	0.66	0.66	0.64	0.60	0.75	0.61	0.75	0.64	0.62	0.63	0.66	0.71	0.75

Table 3-3
Suite 10

Table 3-3
Suite 11

Time	60	60	60	60	60	60	60	60	60	60	60	60	60
Sample	OM-19	OM-19	OM-19	OM-19	OM-19	OM-19	OM-19						
Melt	AH6	AH6	AH6	AH6	AH6	AH6	AH6						
T	1250	1250	1250	1250	1250	1250	1250	1250	1250	1250	1250	1250	1250
P	0.7	0.7	0.7	0.7	0.7	0.7	0.7	0.7	0.7	0.7	0.7	0.7	0.7
Analysis n°	Profil1	Profil1	Profil1	Profil1	Profil1	Profil1	98-02M2	98-03M	03m	98-02M1	98-05M	98-04M	04m
Sample Zone	1	1	1	1	1	1	2	2	2	3	3	3	3
D (mm)	-0.31	-0.31	-0.25	-0.25	-0.19	-0.19	-0.06	-0.06	-0.01	0.00	0.15	0.21	0.33
SiO ₂	49.27	49.27	49.36	49.36	49.36	49.32	50.42	49.85	49.21	50.14	50.15	49.83	50.26
TiO ₂	0.84	0.84	0.77	0.77	0.76	0.76	0.73	0.93	0.93	0.86	0.87	0.96	1.00
Al ₂ O ₃	15.63	15.63	15.63	15.63	15.68	15.68	15.59	16.05	16.51	15.88	15.94	17.19	16.58
Cr ₂ O ₃	0.02	0.02	0.10	0.10	0.01	0.01	0.08	0.00	0.00	0.07	0.00	0.00	0.00
FeO	7.19	7.19	7.03	7.03	7.05	7.05	7.06	7.30	7.21	7.19	7.43	7.16	7.46
MnO	0.07	0.07	0.14	0.14	0.13	0.13	0.14	0.13	0.19	0.18	0.17	0.12	0.16
NiO	0.01	0.01	0.00	0.00	0.00	0.00	0.00	0.00	0.09	0.00	0.00	0.05	0.03
MgO	11.98	11.98	11.85	11.85	11.94	11.94	11.99	7.75	7.99	11.03	8.68	6.88	8.16
CaO	12.64	12.64	12.76	12.76	12.72	12.72	12.73	15.22	14.83	13.34	14.53	15.28	14.44
NaO	2.26	2.26	2.27	2.27	2.25	2.25	2.27	2.12	2.31	2.14	2.15	2.19	2.22
K2O	0.09	0.09	0.09	0.09	0.10	0.10	0.08	0.07	0.09	0.09	0.08	0.09	0.09
Total	100.00	100.00	100.00	100.00	100.00	100.00	100.00	100.00	100.00	100.00	100.00	100.00	100.00
Si	0.82	0.82	0.82	0.82	0.82	0.82	0.84	0.83	0.82	0.83	0.83	0.83	0.84
Ti	0.01	0.01	0.01	0.01	0.01	0.01	0.01	0.01	0.01	0.01	0.01	0.01	0.01
Al	0.31	0.31	0.31	0.31	0.31	0.31	0.31	0.32	0.31	0.31	0.34	0.33	0.33
Cr	0.00	0.00	0.00	0.00	0.00	0.00	0.00	0.00	0.00	0.00	0.00	0.00	0.00
Fe2	0.10	0.10	0.10	0.10	0.10	0.10	0.10	0.10	0.10	0.10	0.10	0.10	0.10
Mn	0.00	0.00	0.00	0.00	0.00	0.00	0.00	0.00	0.00	0.00	0.00	0.00	0.00
Ni	0.00	0.00	0.00	0.00	0.00	0.00	0.00	0.00	0.00	0.00	0.00	0.00	0.00
Mg	0.30	0.30	0.29	0.29	0.30	0.30	0.30	0.19	0.20	0.27	0.22	0.17	0.20
Ca	0.23	0.23	0.23	0.23	0.23	0.23	0.23	0.27	0.26	0.24	0.26	0.27	0.26
Na	0.07	0.07	0.07	0.07	0.07	0.07	0.07	0.07	0.07	0.07	0.07	0.07	0.07
K	0.00	0.00	0.00	0.00	0.00	0.00	0.00	0.00	0.00	0.00	0.00	0.00	0.00
XCa	0.76	0.76	0.76	0.76	0.76	0.76	0.76	0.80	0.78	0.77	0.79	0.79	0.78
XMg	0.75	0.75	0.75	0.75	0.75	0.75	0.75	0.65	0.66	0.73	0.68	0.63	0.64

Table 3-3
Suite 12

Time	60	60	60	60	60	60	60	60	60	60	60	60	0.5
Sample	OM-19	OM-19	OM-19	OM-19	OM-19	OM19	OM19	OM-19	OM19	OM-19	OM-19	OM-19	OM-23
Melt	AH6												
T	1250	1250	1250	1250	1250	1250	1250	1250	1250	1250	1250	1250	1300
P	0.7	0.7	0.7	0.7	0.7	0.7	0.7	0.7	0.7	0.7	0.7	0.7	0.5
Analysis n°	98-07M	98-06M	05m	06m	07m	98-09M	98-09M	09m	98-08M	10m	11m	12m	01M
Sample Zone	3	3	3	3	4	5	5	5	5	5	5	5	2
D (mm)	0.54	0.63	0.71	0.79	1.01	1.12	1.12	1.19	1.20	1.63	1.75	2.10	-0.07
SiO ₂	50.30	50.71	50.83	50.79	51.51	51.39	51.39	51.59	51.16	51.47	51.07	51.51	51.49
TiO ₂	0.95	1.01	0.97	0.89	0.94	0.99	0.99	0.91	0.89	0.81	0.79	0.76	0.80
Al ₂ O ₃	17.67	17.61	17.21	17.29	17.33	17.41	17.41	16.88	15.80	15.02	15.05	15.03	15.08
Cr ₂ O ₃	0.00	0.00	0.05	0.00	0.03	0.00	0.00	0.04	0.00	0.00	0.00	0.00	0.11
FeO	7.17	7.04	7.13	7.42	6.93	6.82	6.82	6.84	7.11	6.90	6.65	6.37	6.63
MnO	0.17	0.16	0.19	0.18	0.15	0.16	0.16	0.12	0.13	0.09	0.12	0.16	0.12
NiO	0.03	0.00	0.07	0.02	0.00	0.02	0.02	0.00	0.05	0.00	0.03	0.00	0.02
MgO	6.36	6.03	6.66	6.49	6.61	6.26	6.26	7.55	8.81	11.47	12.09	12.10	11.82
CaO	14.84	14.70	14.24	14.37	14.05	14.34	14.34	13.54	13.51	11.67	11.46	11.38	11.33
NaO	2.37	2.61	2.53	2.43	2.33	2.50	2.50	2.44	2.42	2.43	2.60	2.58	2.49
K ₂ O	0.13	0.11	0.12	0.11	0.13	0.11	0.11	0.09	0.11	0.14	0.13	0.11	0.05
Total	100.00	100.00	100.00	100.00	100.00	100.00	100.00	100.00	100.00	100.00	100.00	100.00	100.00
Si	0.84	0.84	0.85	0.85	0.86	0.86	0.86	0.85	0.86	0.85	0.86	0.86	0.81
Ti	0.01	0.01	0.01	0.01	0.01	0.01	0.01	0.01	0.01	0.01	0.01	0.01	0.01
Al	0.35	0.35	0.34	0.34	0.34	0.34	0.34	0.33	0.31	0.29	0.30	0.29	0.30
Cr	0.00	0.00	0.00	0.00	0.00	0.00	0.00	0.00	0.00	0.00	0.00	0.00	0.00
Fe ₂	0.10	0.10	0.10	0.10	0.09	0.09	0.09	0.10	0.10	0.10	0.09	0.09	0.12
Mn	0.00	0.00	0.00	0.00	0.00	0.00	0.00	0.00	0.00	0.00	0.00	0.00	0.00
Ni	0.00	0.00	0.00	0.00	0.00	0.00	0.00	0.00	0.00	0.00	0.00	0.00	0.00
Mg	0.16	0.15	0.17	0.16	0.16	0.16	0.16	0.19	0.22	0.28	0.30	0.30	0.29
Ca	0.26	0.26	0.25	0.26	0.25	0.26	0.26	0.24	0.24	0.21	0.20	0.20	0.27
Na	0.08	0.08	0.08	0.08	0.08	0.08	0.08	0.08	0.08	0.08	0.08	0.08	0.07
K	0.00	0.00	0.00	0.00	0.00	0.00	0.00	0.00	0.00	0.00	0.00	0.00	0.00
XCa	0.78	0.76	0.76	0.77	0.77	0.76	0.76	0.75	0.75	0.73	0.71	0.71	0.72
XMg	0.61	0.60	0.62	0.61	0.63	0.62	0.62	0.66	0.69	0.75	0.76	0.77	0.59

Table 3-3
Suite 13

Time	0.5	0.5	0.5	0.5	0.5	0.5	0.5	0.5	0.5	0.5	0.5	0.5	0.5	0.5
Sample	OM-23													
Melt	AH6													
T	1300	1300	1300	1300	1300	1300	1300	1300	1300	1300	1300	1300	1300	1300
P	0.5	0.5	0.5	0.5	0.5	0.5	0.5	0.5	0.5	0.5	0.5	0.5	0.5	0.5
Analysis n°	02M	03M	04M	06M	07M	08M	08M1	09M	10M	11M	12M	12M2	13M	14M
Sample Zone	2	3	3	3	3	3	3	4	4	4	4	4	4	4
D (mm)	0.01	0.25	0.37	0.85	0.80	0.74	0.73	0.80	1.07	1.13	1.33	1.33	1.51	1.75
SiO ₂	48.23	49.22	49.60	49.61	49.69	49.59	49.43	49.54	50.10	50.32	49.78	49.40	48.60	48.96
TiO ₂	0.62	0.93	1.06	1.06	1.19	1.18	1.07	1.27	1.27	1.40	1.18	1.29	0.94	1.13
Al ₂ O ₃	18.15	18.38	18.08	17.22	17.50	16.54	16.90	17.41	17.84	18.66	17.00	16.37	14.50	15.57
Cr ₂ O ₃	0.02	0.10	0.08	0.07	0.04	0.00	0.00	0.04	0.11	0.00	0.04	0.09	0.06	0.03
FeO	8.48	7.74	7.67	8.03	7.98	8.20	8.26	8.19	7.65	7.14	7.71	8.38	8.58	7.90
MnO	0.15	0.12	0.16	0.16	0.08	0.20	0.14	0.21	0.11	0.14	0.17	0.11	0.19	0.10
NiO	0.02	0.00	0.00	0.01	0.00	0.00	0.02	0.00	0.00	0.00	0.03	0.00	0.00	0.01
MgO	6.95	6.12	5.51	7.20	6.19	7.90	7.68	6.55	5.56	4.41	7.10	7.96	12.27	11.65
CaO	15.14	15.04	15.28	13.82	14.42	13.62	13.68	14.07	14.33	14.87	13.99	13.73	12.40	11.72
NaO	2.16	2.28	2.48	2.67	2.79	2.64	2.64	2.58	2.89	2.89	2.86	2.53	2.34	2.77
K ₂ O	0.07	0.07	0.09	0.15	0.13	0.13	0.17	0.15	0.15	0.16	0.15	0.15	0.13	0.14
Total	100.00	100.00	100.00	100.00	100.00	100.00	100.00	100.00	100.00	100.00	100.00	100.00	100.00	100.00
Si	0.80	0.82	0.83	0.83	0.83	0.82	0.82	0.83	0.84	0.83	0.82	0.81	0.81	0.81
Ti	0.01	0.01	0.01	0.01	0.01	0.01	0.01	0.02	0.02	0.02	0.01	0.02	0.01	0.01
Al	0.36	0.36	0.35	0.34	0.34	0.32	0.33	0.34	0.35	0.37	0.33	0.32	0.28	0.31
Cr	0.00	0.00	0.00	0.00	0.00	0.00	0.00	0.00	0.00	0.00	0.00	0.00	0.00	0.00
Fe ₂	0.12	0.11	0.11	0.11	0.11	0.11	0.12	0.11	0.11	0.10	0.11	0.12	0.12	0.11
Mn	0.00	0.00	0.00	0.00	0.00	0.00	0.00	0.00	0.00	0.00	0.00	0.00	0.00	0.00
Ni	0.00	0.00	0.00	0.00	0.00	0.00	0.00	0.00	0.00	0.00	0.00	0.00	0.00	0.00
Mg	0.17	0.15	0.14	0.18	0.15	0.20	0.19	0.16	0.14	0.11	0.18	0.20	0.30	0.29
Ca	0.27	0.27	0.27	0.25	0.26	0.24	0.24	0.25	0.26	0.27	0.25	0.24	0.22	0.21
Na	0.07	0.07	0.08	0.09	0.09	0.09	0.09	0.08	0.09	0.09	0.09	0.08	0.08	0.09
K	0.00	0.00	0.00	0.00	0.00	0.00	0.00	0.00	0.00	0.00	0.00	0.00	0.00	0.00
XCa	0.79	0.78	0.77	0.74	0.74	0.74	0.74	0.75	0.73	0.74	0.73	0.75	0.75	0.70
XMg	0.59	0.59	0.56	0.61	0.58	0.63	0.62	0.59	0.56	0.52	0.62	0.63	0.72	0.72

Table 3-3
Suite 14

Time	0.5	0.3	0.3	0.3	0.3	0.3	0.3
Sample	OM-23	OM-24	OM-24	OM-24	OM-24	OM-24	OM-24
Melt	AH6	AH6	AH6	AH6	AH6	AH6	AH6
T	1300	1300	1300	1300	1300	1300	1300
P	0.5	0.5	0.5	0.5	0.5	0.5	0.5
Analysis n°	15M	04M	05M	01M2 5μ	01M3	02M1	03M1
Sample Zone	4	4	4	5	5	5	5
D (mm)	1.78	1.49	1.51	1.83	1.84	1.59	1.86
SiO ₂	48.94	50.85	50.30	48.30	48.44	49.84	47.96
TiO ₂	1.20	1.38	1.30	1.16	1.27	1.26	1.27
Al ₂ O ₃	15.63	17.72	16.97	14.93	15.90	16.36	14.74
Cr ₂ O ₃	0.00	0.01	0.06	0.00	0.00	0.04	0.04
FeO	7.67	7.75	8.08	8.74	8.40	8.24	8.79
MnO	0.13	0.15	0.19	0.14	0.15	0.18	0.17
NiO	0.00	0.00	0.06	0.09	0.00	0.07	0.02
MgO	11.81	4.89	6.78	13.04	12.95	8.28	13.38
CaO	11.79	14.25	13.34	10.89	10.50	12.67	10.89
NaO	2.66	2.84	2.74	2.54	2.24	2.87	2.57
K2O	0.16	0.17	0.18	0.17	0.14	0.20	0.17
Total	100.00	100.00	100.00	100.00	100.00	100.00	100.00
Si	0.81	0.85	0.84	0.80	0.81	0.83	0.80
Ti	0.02	0.02	0.02	0.01	0.02	0.02	0.02
Al	0.31	0.35	0.33	0.29	0.31	0.32	0.29
Cr	0.00	0.00	0.00	0.00	0.00	0.00	0.00
Fe2	0.11	0.11	0.11	0.12	0.12	0.11	0.12
Mn	0.00	0.00	0.00	0.00	0.00	0.00	0.00
Ni	0.00	0.00	0.00	0.00	0.00	0.00	0.00
Mg	0.29	0.12	0.17	0.32	0.32	0.21	0.33
Ca	0.21	0.25	0.24	0.19	0.19	0.23	0.19
Na	0.09	0.09	0.09	0.08	0.07	0.09	0.08
K	0.00	0.00	0.00	0.00	0.00	0.00	0.00
XCa	0.71	0.74	0.73	0.70	0.72	0.71	0.70
XMg	0.73	0.53	0.60	0.73	0.73	0.64	0.73

Table 4-2

Representative major element compositions of olivine from ol-rich layer from step-cooled and isothermal experiments

Sample	OM02	OM02	OM02	OM02	OM02	OM02	OM02	OM02	OM02	OM02	OM02	OM02	OM02	OM02								
Analysis n°	OM02-101	OM02-102	OM02-104	OM02-106	OM02-107	OM02-109	OM02-110	OM02-119	OM02-120	OM02-16	OM02-17	OM02-18	OM02-19	OM02-21	OM02-22	OM02-24	OM02-30	OM02-31	OM02-37			
Sample zone	3	3	3	3	3	3	3	3	3	3	3	3	3	3	3	3	3	3	3	3	3	3
Zone	r	c	r	c	c	r	r	c	r	c	r	c	r	c	r	c	r	c	r	c	c	c
Distance (mm)	0.31	0.31	0.37	0.05	0.09	0.06	0.03	0.16	0.16	0.80	0.80	0.85	0.85	0.75	0.74	0.74	0.68	0.69	0.38			
SiO ₂	40.77	40.40	40.70	41.05	40.49	40.92	40.51	40.98	40.60	40.79	40.70	40.69	40.92	40.51	40.76	40.58	40.48	40.54	40.84			
TiO ₂	0.04	0.06	0.01	0.04	0.00	0.00	0.07	0.04	0.04	0.00	0.04	0.03	0.04	0.03	0.02	0.02	0.03	0.00	0.00			
Al ₂ O ₃	0.05	0.05	0.05	0.04	0.05	0.06	0.04	0.07	0.08	0.05	0.04	0.05	0.08	0.07	0.02	0.07	0.06	0.03	0.02			
Cr ₂ O ₃	0.04	0.02	0.00	0.02	0.03	0.10	0.00	0.00	0.09	0.07	0.02	0.04	0.00	0.08	0.03	0.07	0.01	0.00	0.02			
FeO	10.26	10.18	10.12	9.88	9.51	10.41	11.76	10.59	10.62	8.95	9.64	9.68	10.35	9.46	9.99	9.74	10.15	10.07	9.22			
MnO	0.16	0.16	0.13	0.12	0.11	0.16	0.15	0.18	0.13	0.13	0.13	0.13	0.14	0.08	0.14	0.11	0.12	0.11	0.13			
NiO	0.08	0.13	0.04	0.11	0.21	0.06	0.06	0.11	0.05	0.27	0.10	0.00	0.03	0.12	0.06	0.16	0.04	0.09	0.22			
MgO	48.27	48.51	48.38	48.88	49.11	48.92	47.62	48.35	48.75	49.31	49.13	48.87	48.64	49.05	48.50	49.31	49.08	49.02	49.20			
CaO	0.33	0.37	0.31	0.29	0.33	0.36	0.36	0.39	0.42	0.25	0.33	0.31	0.35	0.35	0.33	0.36	0.32	0.24				
NaO	0.03	0.00	0.01	0.00	0.00	0.04	0.03	0.03	0.02	0.01	0.00	0.02	0.00	0.05	0.00	0.00	0.02	0.01	0.00			
K ₂ O	0.00	0.00	0.01	0.01	0.00	0.00	0.00	0.00	0.00	0.00	0.00	0.00	0.02	0.00	0.00	0.00	0.00	0.02	0.00			
Total	100.03	99.88	99.75	100.44	99.85	101.04	100.61	100.73	100.80	99.83	100.12	99.83	100.57	99.79	99.85	100.38	100.35	100.20	99.89			
Si	1.002	0.994	1.002	1.003	0.993	0.995	0.996	1.002	0.990	0.999	0.996	0.999	1.000	0.994	1.002	0.990	0.989	0.992	1.000			
Ti	0.001	0.001	0.000	0.001	0.000	0.000	0.001	0.001	0.001	0.000	0.001	0.001	0.001	0.001	0.001	0.000	0.000	0.001	0.000			
Al	0.001	0.002	0.001	0.001	0.001	0.002	0.001	0.002	0.002	0.002	0.001	0.001	0.002	0.002	0.002	0.000	0.002	0.002	0.001			
Cr	0.001	0.000	0.000	0.000	0.001	0.002	0.000	0.000	0.002	0.001	0.000	0.001	0.000	0.002	0.001	0.001	0.000	0.000	0.000			
Fe ₂	0.211	0.209	0.208	0.202	0.195	0.212	0.242	0.217	0.217	0.183	0.197	0.199	0.212	0.194	0.206	0.199	0.207	0.206	0.189			
Mn	0.003	0.003	0.003	0.003	0.002	0.003	0.003	0.004	0.003	0.003	0.003	0.003	0.003	0.002	0.003	0.002	0.003	0.002	0.003			
Ni	0.002	0.003	0.001	0.002	0.004	0.001	0.001	0.002	0.001	0.005	0.002	0.000	0.001	0.002	0.001	0.003	0.001	0.002	0.004			
Mg	1.769	1.778	1.776	1.780	1.795	1.773	1.745	1.762	1.773	1.800	1.792	1.788	1.772	1.793	1.778	1.794	1.788	1.788	1.796			
Ca	0.009	0.010	0.008	0.008	0.009	0.010	0.010	0.010	0.011	0.007	0.009	0.008	0.009	0.009	0.009	0.009	0.009	0.009	0.008	0.006		
Na	0.001	0.000	0.000	0.000	0.000	0.002	0.001	0.001	0.001	0.000	0.001	0.001	0.000	0.003	0.000	0.001	0.001	0.001	0.000			
Forsterite	0.885	0.886	0.889	0.891	0.894	0.885	0.871	0.882	0.882	0.899	0.894	0.893	0.886	0.894	0.890	0.892	0.889	0.890	0.898			

Zone c or r refers to core or rim analysis. Analysis names like ORes or OS refers to Resorbed olivines, ORn to rounded olivines and OE to Euhedral olivines.

Distance is calculated from the x,y coordinates of an olivine from the interface zone (picked up as a 0 mm reference olivine for each sample) and the x,y coordinates of the analysis Cations are calculated with the Program NORM (version 2013) by Ulmer and Poli

Sample zones : 2: Interface, 3: Ol-rich layer bot. half, 4: Ol-rich layer up. half + spheres.

Table 4-2

Suite 1

Sample	OM02																		
Analysis n°	OM02-38	OM02-40	OM02-41	OM02-43	OM02-46	OM02-47	OM02-48	OM02-52	OM02-53	OM02-56	OM02-57	OM02-59	OM02-80	OM02-81	OM02-83	OM02-84	OM02-85	OM02-88	OM02-89
Sample zone	3	3	3	3	3	3	3	3	3	3	2	2	3	4	3	3	3	3	4
Zone	r	r	c	r	r	c	r	c	r	r	c	r	c	r	c	c	r	c	r
Distance (mm)	0.36	0.35	0.35	0.36	0.22	0.22	0.25	0.15	0.16	0.06	0.05	0.00	0.94	0.95	0.88	0.82	0.83	0.78	0.76
SiO ₂	40.53	40.56	40.54	40.31	40.58	40.59	40.36	41.08	41.07	40.93	41.06	40.60	40.95	40.65	40.94	41.24	40.24	40.87	40.74
TiO ₂	0.00	0.00	0.00	0.00	0.09	0.00	0.00	0.02	0.00	0.01	0.02	0.03	0.00	0.04	0.03	0.00	0.02	0.00	0.00
Al ₂ O ₃	0.05	0.07	0.03	0.10	0.09	0.03	0.05	0.07	0.04	0.05	0.06	0.05	0.06	0.05	0.06	0.04	0.03	0.01	0.05
Cr ₂ O ₃	0.03	0.05	0.00	0.00	0.04	0.11	0.00	0.05	0.07	0.03	0.04	0.06	0.00	0.06	0.03	0.01	0.06	0.02	0.04
FeO	10.01	9.75	9.96	10.37	10.46	9.47	10.73	9.25	10.32	10.98	10.31	12.01	9.08	9.90	9.57	9.58	10.07	9.12	10.17
MnO	0.17	0.15	0.12	0.16	0.15	0.16	0.17	0.15	0.12	0.13	0.10	0.19	0.17	0.16	0.16	0.16	0.16	0.14	0.18
NiO	0.05	0.09	0.14	0.09	0.07	0.19	0.03	0.09	0.08	0.01	0.03	0.05	0.07	0.01	0.06	0.03	0.00	0.24	0.08
MgO	48.72	48.63	49.12	48.29	48.51	49.23	48.37	49.25	48.85	48.33	49.30	47.49	49.40	48.86	48.96	48.79	48.42	49.44	48.88
CaO	0.32	0.33	0.39	0.30	0.33	0.30	0.36	0.36	0.35	0.35	0.33	0.36	0.36	0.31	0.32	0.28	0.33	0.20	0.32
NaO	0.01	0.02	0.00	0.01	0.00	0.02	0.03	0.01	0.00	0.03	0.01	0.00	0.00	0.00	0.00	0.01	0.00	0.03	0.01
K ₂ O	0.01	0.00	0.01	0.00	0.00	0.00	0.02	0.00	0.00	0.00	0.00	0.01	0.00	0.01	0.02	0.00	0.00	0.00	0.00
Total	99.90	99.65	100.31	99.63	100.32	100.09	100.12	100.34	100.90	100.85	101.25	100.85	100.10	100.05	100.15	100.13	99.34	100.06	100.46
Si	0.995	0.998	0.991	0.994	0.995	0.993	0.992	1.002	1.000	1.000	0.995	0.997	1.000	0.997	1.002	1.010	0.994	0.999	0.996
Ti	0.000	0.000	0.000	0.000	0.002	0.000	0.000	0.000	0.000	0.000	0.000	0.001	0.000	0.001	0.001	0.000	0.001	0.000	0.000
Al	0.001	0.002	0.001	0.003	0.003	0.001	0.002	0.002	0.001	0.002	0.002	0.002	0.002	0.002	0.002	0.001	0.001	0.000	0.001
Cr	0.001	0.001	0.000	0.000	0.001	0.002	0.000	0.001	0.001	0.001	0.001	0.001	0.000	0.001	0.001	0.000	0.001	0.000	0.001
Fe ₂	0.206	0.201	0.204	0.214	0.214	0.194	0.220	0.189	0.210	0.224	0.209	0.247	0.186	0.203	0.196	0.196	0.208	0.186	0.208
Mn	0.004	0.003	0.003	0.003	0.003	0.003	0.004	0.003	0.003	0.003	0.002	0.004	0.004	0.003	0.003	0.003	0.004	0.003	0.004
Ni	0.001	0.002	0.003	0.002	0.001	0.004	0.001	0.002	0.002	0.000	0.001	0.001	0.001	0.000	0.001	0.001	0.000	0.005	0.002
Mg	1.783	1.784	1.789	1.775	1.773	1.795	1.771	1.791	1.774	1.760	1.781	1.738	1.798	1.785	1.786	1.781	1.783	1.800	1.781
Ca	0.009	0.009	0.010	0.008	0.009	0.008	0.009	0.009	0.009	0.009	0.009	0.010	0.009	0.008	0.009	0.007	0.009	0.005	0.008
Na	0.001	0.001	0.000	0.000	0.000	0.001	0.001	0.001	0.000	0.001	0.001	0.000	0.000	0.000	0.001	0.001	0.000	0.001	0.000
Forsterite	0.890	0.891	0.890	0.885	0.884	0.894	0.882	0.896	0.887	0.880	0.889	0.868	0.899	0.891	0.894	0.895	0.889	0.900	0.888

Table4-1

Suite 2

Sample	OM02	OM02	OM02	OM02	OM02b	OM02b	OM02b	OM02b	OM02b	OM03	OM03	OM03	OM03	OM03	OM03	OM03	OM03	OM03	
Analysis n°	OM02-91	OM02-92	OM02-98	OM02-99	OM02b-1	OM02b-10	OM02b-2	OM02b-5	OM02b-8	OM03-9	OM03-111	OM03-14	OM03-15	OM03-16	OM03-17	OM03-2	OM03-20	OM03-22	OM03-23
Sample zone	3	3	3	3	4	4	4	4	4	2	4	4	4	3	3	4	3	3	
Zone	c	r	r	c	c	r	r	r	c	r	c	r	c	c	r	r	c		
Distance (mm)	0.38	0.39	0.45	0.43	0.83	0.84	0.83	0.84	0.84	0.06	1.35	1.35	1.17	1.21	1.43	1.21	1.27	1.28	
SiO ₂	40.87	40.54	41.07	40.90	41.13	40.74	40.54	40.55	40.69	40.61	41.04	40.58	41.20	41.39	40.97	40.95	40.93	40.79	40.92
TiO ₂	0.02	0.03	0.01	0.00	0.01	0.04	0.00	0.01	0.00	0.00	0.04	0.02	0.04	0.00	0.02	0.00	0.05	0.04	0.03
Al ₂ O ₃	0.02	0.04	0.09	0.02	0.03	0.04	0.08	0.05	0.01	0.05	0.02	0.02	0.04	0.05	0.03	0.02	0.05	0.11	0.00
Cr ₂ O ₃	0.04	0.01	0.00	0.04	0.05	0.00	0.00	0.00	0.01	0.03	0.00	0.06	0.00	0.02	0.05	0.01	0.00	0.00	0.00
FeO	9.47	10.42	9.84	9.35	8.94	9.65	9.90	9.92	9.63	9.63	10.07	9.97	10.03	9.17	9.69	11.76	9.67	10.25	10.25
MnO	0.14	0.23	0.19	0.15	0.13	0.14	0.17	0.14	0.11	0.18	0.13	0.10	0.16	0.12	0.10	0.19	0.10	0.17	0.16
NiO	0.24	0.14	0.18	0.27	0.29	0.11	0.06	0.04	0.01	0.04	0.06	0.02	0.05	0.13	0.16	0.00	0.03	0.05	0.01
MgO	48.92	48.06	48.63	48.79	49.90	49.27	49.10	49.28	49.67	49.31	48.66	49.23	48.74	49.55	49.50	48.12	49.44	48.63	48.29
CaO	0.30	0.34	0.37	0.28	0.19	0.25	0.33	0.35	0.32	0.36	0.32	0.31	0.28	0.28	0.29	0.28	0.28	0.23	0.23
NaO	0.02	0.00	0.00	0.04	0.03	0.02	0.00	0.01	0.00	0.00	0.00	0.05	0.02	0.02	0.00	0.03	0.00	0.00	0.00
K ₂ O	0.00	0.00	0.00	0.00	0.02	0.02	0.02	0.01	0.00	0.00	0.02	0.01	0.00	0.00	0.01	0.00	0.00	0.00	0.00
Total	100.03	99.81	100.37	99.84	100.72	100.28	100.21	100.35	100.46	100.21	100.34	100.32	100.59	100.74	100.84	101.35	100.57	100.28	99.89
Si	1.001	1.000	1.005	1.004	0.998	0.995	0.991	0.990	0.990	0.992	1.005	0.991	1.006	1.005	0.995	0.999	0.996	0.999	1.007
Ti	0.000	0.001	0.000	0.000	0.000	0.001	0.000	0.000	0.000	0.000	0.001	0.000	0.001	0.000	0.000	0.000	0.001	0.001	0.001
Al	0.001	0.001	0.003	0.001	0.001	0.001	0.002	0.002	0.000	0.002	0.001	0.001	0.001	0.002	0.001	0.001	0.003	0.000	0.000
Cr	0.001	0.000	0.000	0.001	0.001	0.000	0.000	0.000	0.001	0.000	0.001	0.000	0.000	0.001	0.000	0.000	0.000	0.000	0.000
Fe ₂	0.194	0.215	0.201	0.192	0.181	0.197	0.203	0.203	0.196	0.197	0.206	0.204	0.205	0.186	0.197	0.240	0.197	0.210	0.211
Mn	0.003	0.005	0.004	0.003	0.003	0.003	0.004	0.003	0.002	0.004	0.003	0.002	0.003	0.002	0.004	0.002	0.003	0.003	0.003
Ni	0.005	0.003	0.004	0.005	0.006	0.002	0.001	0.001	0.000	0.001	0.001	0.000	0.001	0.003	0.003	0.000	0.001	0.001	0.000
Mg	1.787	1.767	1.774	1.785	1.804	1.793	1.790	1.793	1.802	1.795	1.776	1.792	1.774	1.793	1.792	1.749	1.794	1.776	1.772
Ca	0.008	0.009	0.010	0.007	0.005	0.007	0.009	0.009	0.008	0.009	0.008	0.008	0.007	0.007	0.008	0.007	0.007	0.006	0.006
Na	0.001	0.000	0.000	0.002	0.001	0.001	0.000	0.001	0.000	0.000	0.000	0.000	0.003	0.001	0.001	0.001	0.000	0.000	0.000
Forsterite	0.894	0.883	0.889	0.894	0.901	0.894	0.891	0.892	0.897	0.894	0.890	0.893	0.891	0.900	0.895	0.874	0.897	0.889	0.889

Table 4-2
Suite 3

Sample	OM03	OM03	OM03	OM03	OM03	OM03	OM03	OM03	OM03	OM03	OM03	OM03							
Analysis n°	OM03-24	OM03-27	OM03-30	OM03-31	OM03-34	OM03-35	OM03-37	OM03-38	OM03-4	OM03-41	OM03-42	OM03-45	OM03-46	OM03-49	OM03-50	OM03-53	OM03-54	OM03-56	OM03-57
Sample zone	3	3	3	3	3	3	3	3	3	3	3	3	3	3	3	3	3	3	3
Zone	c	r	r	c	r	c	r	c	c	r	c	r	c	r	c	r	c	r	c
Distance (mm)	1.19	1.20	1.16	1.15	1.05	1.05	1.06	1.05	1.32	0.90	0.89	0.65	0.67	0.77	0.74	0.84	0.82	0.83	0.82
SiO ₂	41.17	41.11	41.06	41.01	40.82	40.88	40.84	40.87	40.45	40.75	41.16	40.80	40.98	41.03	40.92	40.67	40.93	40.89	40.98
TiO ₂	0.04	0.00	0.01	0.01	0.04	0.00	0.06	0.06	0.07	0.00	0.01	0.03	0.02	0.00	0.00	0.01	0.01	0.00	0.00
Al ₂ O ₃	0.04	0.06	0.04	0.03	0.07	0.04	0.03	0.03	0.01	0.08	0.04	0.03	0.06	0.05	0.03	0.05	0.06	0.04	0.04
Cr ₂ O ₃	0.05	0.01	0.00	0.06	0.06	0.00	0.07	0.01	0.01	0.08	0.00	0.02	0.06	0.00	0.04	0.01	0.00	0.01	0.04
FeO	9.36	9.65	9.87	9.72	9.95	9.44	9.45	9.51	10.52	10.04	9.91	10.05	9.45	9.55	9.05	9.87	9.63	9.65	9.65
MnO	0.09	0.17	0.17	0.19	0.19	0.13	0.12	0.11	0.16	0.15	0.21	0.11	0.20	0.19	0.14	0.19	0.13	0.17	0.08
NiO	0.13	0.08	0.04	0.04	0.12	0.17	0.06	0.16	0.07	0.21	0.16	0.17	0.32	0.18	0.30	0.14	0.20	0.14	0.15
MgO	49.42	48.99	48.86	49.09	48.64	49.33	49.34	49.26	47.82	48.93	49.26	49.20	49.72	48.88	49.32	49.15	49.53	48.95	49.28
CaO	0.27	0.26	0.29	0.30	0.34	0.27	0.28	0.24	0.26	0.29	0.20	0.26	0.25	0.29	0.19	0.28	0.27	0.27	0.32
NaO	0.00	0.01	0.00	0.01	0.01	0.00	0.01	0.02	0.00	0.02	0.02	0.02	0.02	0.00	0.00	0.04	0.02	0.02	0.00
K ₂ O	0.00	0.00	0.01	0.00	0.01	0.02	0.00	0.01	0.00	0.00	0.00	0.01	0.00	0.01	0.00	0.02	0.00	0.00	0.00
Total	100.57	100.34	100.35	100.47	100.25	100.29	100.26	100.27	99.38	100.55	100.98	100.69	101.08	100.16	100.00	100.40	100.79	100.15	100.54
Si	1.002	1.005	1.004	1.001	1.000	0.998	0.997	0.998	1.002	0.995	1.000	0.994	0.993	1.005	1.001	0.993	0.994	1.001	0.999
Ti	0.001	0.000	0.000	0.000	0.001	0.000	0.001	0.001	0.001	0.000	0.000	0.001	0.000	0.000	0.000	0.000	0.000	0.000	0.000
Al	0.001	0.002	0.001	0.001	0.002	0.001	0.001	0.001	0.000	0.002	0.001	0.001	0.002	0.001	0.001	0.002	0.002	0.001	0.001
Cr	0.001	0.000	0.000	0.001	0.001	0.000	0.001	0.000	0.000	0.002	0.000	0.000	0.001	0.000	0.001	0.000	0.000	0.000	0.001
Fe ₂	0.191	0.197	0.202	0.198	0.204	0.193	0.193	0.194	0.218	0.205	0.201	0.205	0.191	0.196	0.185	0.202	0.196	0.198	0.197
Mn	0.002	0.003	0.004	0.004	0.004	0.003	0.002	0.002	0.003	0.003	0.004	0.002	0.004	0.004	0.003	0.004	0.003	0.004	0.002
Ni	0.003	0.002	0.001	0.001	0.002	0.003	0.001	0.003	0.002	0.004	0.003	0.003	0.006	0.004	0.006	0.003	0.004	0.003	0.003
Mg	1.793	1.784	1.781	1.785	1.776	1.795	1.795	1.793	1.766	1.781	1.784	1.786	1.795	1.784	1.798	1.788	1.793	1.786	1.790
Ca	0.007	0.007	0.008	0.008	0.009	0.007	0.007	0.006	0.007	0.008	0.005	0.007	0.006	0.008	0.005	0.007	0.007	0.007	0.008
Na	0.000	0.001	0.000	0.001	0.000	0.000	0.000	0.001	0.000	0.001	0.001	0.001	0.001	0.000	0.000	0.002	0.001	0.001	0.000
Forsterite	0.899	0.895	0.893	0.894	0.890	0.897	0.898	0.897	0.885	0.890	0.893	0.892	0.896	0.894	0.900	0.893	0.896	0.894	0.895

Table 4-2
Suite 4

Sample	OM03	OM03	OM03	OM03	OM03	OM03	OM03	OM03	OM03	OM03	OM03	OM03	OM03	OM03	OM03	OM03	OM03	OM03	OM03	OM03
Analysis n°	OM03-60	OM03-61	OM03-62	OM03-65	OM03-7	OM03-73	OM03-74	OM03-76	OM03-77	OM03-78	OM03-79	OM03-8	OM03-83	OM03-84	OM03-87	OM03-88	OM03-89	OM03-9	OM03-93	
Sample zone	3	3	3	3	3	3	3	3	3	3	3	3	3	3	3	3	3	3	2	
Zone	r	c	r	c	c	r	c	r	c	c	r	r	r	c	r	c	r	c	r	
Distance (mm)	0.69	0.68	0.68	0.37	1.22	0.24	0.26	0.49	0.49	0.39	0.38	1.22	0.21	0.22	0.18	0.18	0.18	0.90	0.10	
SiO ₂	40.82	40.88	40.82	40.98	41.46	40.87	41.13	41.22	41.03	41.25	40.54	41.07	40.88	40.92	40.97	40.41	40.71	41.23	40.49	
TiO ₂	0.05	0.03	0.00	0.07	0.03	0.03	0.05	0.05	0.06	0.02	0.12	0.02	0.01	0.00	0.00	0.07	0.00	0.00	0.03	
Al ₂ O ₃	0.05	0.04	0.04	0.04	0.03	0.03	0.06	0.07	0.05	0.08	0.04	0.03	0.04	0.07	0.05	0.01	0.05	0.04	0.05	
Cr ₂ O ₃	0.00	0.01	0.00	0.01	0.00	0.00	0.00	0.05	0.04	0.07	0.00	0.04	0.01	0.04	0.00	0.02	0.00	0.00	0.00	
FeO	10.18	9.74	10.12	9.26	9.50	10.59	10.04	10.03	9.41	10.03	10.58	10.14	10.58	9.82	11.16	10.66	10.85	9.46	10.32	
MnO	0.15	0.14	0.17	0.08	0.13	0.21	0.21	0.14	0.11	0.15	0.17	0.13	0.14	0.10	0.19	0.14	0.19	0.12	0.17	
NiO	0.13	0.11	0.08	0.18	0.11	0.05	0.10	0.20	0.22	0.13	0.16	0.07	0.06	0.13	0.06	0.12	0.09	0.19	0.00	
MgO	47.82	48.72	48.31	49.58	50.29	48.29	48.78	48.63	49.02	48.92	48.78	49.71	48.58	48.89	48.66	48.34	48.74	50.26	48.95	
CaO	0.27	0.27	0.24	0.28	0.25	0.28	0.24	0.28	0.24	0.23	0.28	0.22	0.27	0.26	0.28	0.28	0.28	0.25	0.31	
NaO	0.00	0.00	0.01	0.00	0.03	0.00	0.01	0.00	0.02	0.00	0.00	0.00	0.02	0.00	0.00	0.01	0.00	0.00	0.00	
K2O	0.00	0.00	0.00	0.00	0.00	0.02	0.01	0.00	0.01	0.00	0.02	0.00	0.01	0.00	0.01	0.02	0.00	0.01	0.01	
Total	99.46	99.95	99.79	100.48	101.83	100.36	100.63	100.67	100.21	100.90	100.66	101.45	100.59	100.24	101.38	100.08	100.92	101.55	100.33	
Si	1.010	1.003	1.005	0.998	0.995	1.003	1.004	1.007	1.003	1.004	0.990	0.992	1.000	1.001	0.996	0.994	0.993	0.993	0.990	
Ti	0.001	0.001	0.000	0.001	0.001	0.001	0.001	0.001	0.001	0.000	0.002	0.000	0.000	0.000	0.000	0.001	0.000	0.000	0.001	
Al	0.001	0.001	0.001	0.001	0.001	0.001	0.002	0.002	0.001	0.002	0.001	0.001	0.001	0.002	0.001	0.000	0.001	0.001	0.002	
Cr	0.000	0.000	0.000	0.000	0.000	0.000	0.000	0.001	0.001	0.001	0.000	0.001	0.000	0.001	0.000	0.000	0.000	0.000	0.000	
Fe ₂	0.211	0.200	0.208	0.189	0.191	0.217	0.205	0.205	0.192	0.204	0.216	0.205	0.216	0.201	0.227	0.219	0.221	0.190	0.211	
Mn	0.003	0.003	0.004	0.002	0.003	0.004	0.004	0.003	0.002	0.003	0.004	0.003	0.003	0.002	0.004	0.003	0.004	0.002	0.004	
Ni	0.003	0.002	0.002	0.004	0.002	0.001	0.002	0.004	0.004	0.003	0.003	0.001	0.001	0.003	0.001	0.002	0.002	0.004	0.000	
Mg	1.764	1.782	1.773	1.799	1.800	1.766	1.775	1.770	1.787	1.775	1.776	1.790	1.771	1.783	1.763	1.772	1.771	1.803	1.785	
Ca	0.007	0.007	0.006	0.007	0.006	0.007	0.006	0.007	0.006	0.006	0.007	0.006	0.007	0.007	0.007	0.008	0.007	0.006	0.008	
Na	0.000	0.000	0.000	0.000	0.002	0.000	0.001	0.000	0.001	0.000	0.000	0.000	0.001	0.000	0.000	0.000	0.000	0.000	0.000	
Forsterite	0.888	0.894	0.890	0.900	0.899	0.885	0.891	0.890	0.897	0.892	0.885	0.893	0.886	0.894	0.880	0.884	0.883	0.899	0.889	

Table 4-2

Suite 5

Sample	OM03 OM03- 94	OM03 OM03- 97	OM03b OM03b- 13	OM03b OM03b- 14	OM03b OM03b- 18	OM03b OM03b- 20	OM03b OM03b- 22	OM03b OM03b- 6	OM03b OM03b- 7	OM20 OM20- 02OEC	OM20 OM20- 03OC	OM20 OM20- 03OR1	OM20 OM20- 03OR2	OM20 OM20- 04OC	OM20 OM20- 04OEC	OM20 OM20- 04ORes	OM20 OM20- 04OR1	OM20 OM20- 04OR2	OM20 OM20- 04ORn
Analysis n°																			
Sample																			
zone	2	2	3	3	3	3	3	3	3	2	2	2	2	2	2	2	2	2	
Zone	c	c	c	r	r	r	r	c	r	c	c	r	r	c	c	r	r	r	
Distance																			
(mm)	0.10	0.00	0.97	0.96	0.74	0.31	0.17	1.04	1.04	0.01	0.02	0.02	0.00	0.12	0.08	0.08	0.13	0.13	0.14
SiO ₂	40.89	40.38	40.97	40.79	40.60	40.97	40.43	40.76	40.99	39.59	36.85	36.76	36.73	39.92	40.24	39.78	39.58	39.90	39.99
TiO ₂	0.00	0.01	0.02	0.01	0.04	0.02	0.06	0.05	0.06	0.00	0.00	0.08	0.05	0.01	0.02	0.04	0.00	0.03	0.03
Al ₂ O ₃	0.05	0.06	0.07	0.03	0.02	0.06	0.03	0.03	0.00	0.04	0.06	0.09	0.08	0.08	0.05	0.06	0.08	0.03	0.05
Cr ₂ O ₃	0.04	0.00	0.06	0.06	0.01	0.01	0.00	0.00	0.01	0.00	0.00	0.00	0.00	0.00	0.00	0.00	0.00	0.00	0.00
FeO	10.08	11.11	9.28	9.58	9.79	10.40	10.30	10.07	10.53	15.36	28.37	29.22	31.97	13.25	13.77	15.99	14.16	13.87	14.11
MnO	0.11	0.21	0.09	0.13	0.13	0.15	0.21	0.19	0.15	0.26	0.41	0.43	0.51	0.21	0.18	0.25	0.14	0.23	0.20
NiO	0.02	0.07	0.09	0.04	0.02	0.06	0.05	0.05	0.04	0.12	0.01	0.00	0.00	0.12	0.19	0.13	0.15	0.09	0.12
MgO	48.66	48.27	49.12	49.39	48.76	48.59	48.62	48.33	48.06	44.35	33.92	33.04	30.99	45.97	45.92	43.97	45.52	45.83	45.43
CaO	0.31	0.26	0.28	0.28	0.31	0.30	0.34	0.30	0.24	0.37	0.37	0.37	0.46	0.38	0.33	0.31	0.36	0.36	0.28
NaO	0.03	0.01	0.01	0.02	0.00	0.00	0.00	0.00	0.00	0.00	0.03	0.00	0.01	0.02	0.01	0.04	0.03	0.02	0.02
K ₂ O	0.00	0.01	0.01	0.01	0.01	0.00	0.00	0.00	0.00	0.00	0.00	0.00	0.02	0.01	0.00	0.01	0.00	0.00	0.00
Total	100.20	100.39	99.99	100.35	99.69	100.56	100.03	99.77	100.09	100.08	100.00	100.02	100.81	99.95	100.72	100.54	100.03	100.37	100.22
Si	1.002	0.991	1.003	0.995	0.998	1.002	0.993	1.004	1.009	0.995	0.988	0.990	0.995	0.995	0.998	0.999	0.989	0.993	0.998
Ti	0.000	0.000	0.000	0.000	0.001	0.000	0.001	0.001	0.001	0.000	0.000	0.002	0.001	0.000	0.000	0.001	0.000	0.001	0.001
Al	0.002	0.002	0.002	0.001	0.001	0.002	0.001	0.001	0.000	0.001	0.002	0.003	0.003	0.002	0.001	0.002	0.002	0.001	0.002
Cr	0.001	0.000	0.001	0.001	0.000	0.000	0.000	0.000	0.000	0.001	0.000	0.000	0.001	0.001	0.001	0.001	0.001	0.001	0.000
Fe ₂	0.207	0.228	0.190	0.195	0.201	0.213	0.212	0.207	0.217	0.323	0.636	0.658	0.724	0.276	0.286	0.336	0.296	0.289	0.295
Mn	0.002	0.004	0.002	0.003	0.003	0.003	0.004	0.004	0.003	0.005	0.009	0.010	0.012	0.005	0.004	0.005	0.003	0.005	0.004
Ni	0.000	0.001	0.002	0.001	0.000	0.001	0.001	0.001	0.002	0.000	0.000	0.000	0.002	0.004	0.003	0.003	0.002	0.002	0.002
Mg	1.777	1.766	1.792	1.795	1.787	1.771	1.780	1.774	1.763	1.662	1.355	1.326	1.251	1.708	1.697	1.646	1.695	1.699	1.690
Ca	0.008	0.007	0.007	0.007	0.008	0.008	0.009	0.008	0.006	0.010	0.011	0.011	0.013	0.010	0.009	0.008	0.009	0.010	0.008
Na	0.001	0.000	0.001	0.001	0.000	0.000	0.000	0.000	0.000	0.000	0.000	0.002	0.000	0.001	0.001	0.000	0.002	0.001	0.001
Forsterite	0.891	0.880	0.899	0.897	0.894	0.887	0.887	0.890	0.886	0.830	0.674	0.662	0.625	0.854	0.849	0.824	0.845	0.848	0.846

Table 4-2

Suite 6

Sample	OM20	OM20	OM20	OM20	OM20	OM20	OM20	OM20	OM20	OM20	OM20	OM20	OM20	OM20	OM20	OM20	OM20	OM20	
Analysis n°	OM20-05OC	OM20-05OC	OM20-05OC2	OM20-05OR2	OM20-06OC	OM20-06OR	OM20-07OC	OM20-07OR	OM20-08OC	OM20-08OR	OM20-09OC	OM20-09OR	OM20-11OC	OM20-11OR	OM20-11ORn	OM20-11ORn	OM20-12OR	OM20-13OC	
Sample zone	3	3	3	3	3	3	3	3	3	3	3	3	3	3	3	3	3	3	
Zone	c	c	c	r	c	r	c	r	c	r	c	r	c	r	r	r	r	c	
Distance (mm)	0.30	0.30	0.29	0.30	0.19	0.19	0.72	0.72	0.76	0.74	1.10	1.10	1.28	1.27	1.14	1.26	1.12	1.27	1.55
SiO ₂	40.15	39.30	39.93	39.60	39.92	39.72	40.70	40.49	40.18	40.43	40.24	40.30	40.40	40.20	40.66	40.70	40.34	40.45	40.44
TiO ₂	0.00	0.00	0.03	0.00	0.05	0.01	0.08	0.07	0.00	0.00	0.03	0.06	0.01	0.02	0.04	0.00	0.01	0.05	0.00
Al ₂ O ₃	0.03	0.04	0.07	0.04	0.04	0.06	0.06	0.09	0.07	0.11	0.06	0.08	0.08	0.06	0.06	0.16	0.06	0.22	0.07
Cr ₂ O ₃	0.00	0.00	0.00	0.00	0.00	0.00	0.00	0.00	0.00	0.00	0.00	0.00	0.00	0.00	0.00	0.00	0.00	0.00	0.00
FeO	13.08	13.01	12.44	12.82	12.61	13.41	10.61	10.37	10.11	10.45	9.95	10.11	10.03	10.13	10.27	10.26	10.40	10.15	9.73
MnO	0.18	0.18	0.25	0.19	0.17	0.16	0.20	0.19	0.16	0.16	0.15	0.15	0.20	0.16	0.19	0.14	0.19	0.11	0.17
NiO	0.19	0.11	0.20	0.22	0.21	0.19	0.33	0.40	0.38	0.40	0.43	0.31	0.33	0.31	0.31	0.31	0.32	0.31	0.29
MgO	45.87	46.26	46.18	46.41	46.44	46.11	48.37	48.59	48.49	48.47	48.42	48.45	48.19	48.29	48.89	48.27	48.25	48.37	48.75
CaO	0.34	0.33	0.35	0.31	0.22	0.31	0.31	0.26	0.33	0.29	0.34	0.31	0.29	0.23	0.26	0.24	0.29	0.26	0.29
NaO	0.03	0.00	0.02	0.03	0.00	0.00	0.03	0.00	0.02	0.00	0.01	0.01	0.01	0.00	0.02	0.00	0.00	0.00	0.00
K ₂ O	0.00	0.00	0.01	0.00	0.00	0.00	0.00	0.00	0.00	0.00	0.02	0.00	0.00	0.02	0.00	0.00	0.00	0.00	0.00
Total	99.86	99.23	99.47	99.62	99.66	99.96	100.65	100.47	99.71	100.31	99.61	99.79	99.53	99.40	100.69	100.09	99.84	99.90	99.74
Si	1.002	0.984	0.998	0.988	0.995	0.990	0.996	0.991	0.990	0.992	0.992	0.992	0.998	0.993	0.992	1.000	0.994	0.995	0.995
Ti	0.000	0.000	0.001	0.000	0.001	0.000	0.001	0.001	0.000	0.000	0.001	0.001	0.000	0.000	0.001	0.000	0.000	0.001	0.000
Al	0.001	0.001	0.002	0.001	0.001	0.002	0.002	0.003	0.002	0.003	0.002	0.002	0.002	0.002	0.002	0.005	0.002	0.006	0.002
Cr	0.000	0.000	0.001	0.000	0.000	0.000	0.001	0.001	0.000	0.000	0.001	0.001	0.000	0.002	0.000	0.000	0.001	0.000	0.000
Fe ₂	0.273	0.273	0.260	0.267	0.263	0.280	0.217	0.212	0.208	0.214	0.205	0.208	0.207	0.209	0.209	0.211	0.214	0.209	0.200
Mn	0.004	0.004	0.005	0.004	0.004	0.003	0.004	0.004	0.003	0.003	0.003	0.003	0.004	0.003	0.004	0.003	0.004	0.002	0.003
Ni	0.004	0.002	0.004	0.004	0.004	0.004	0.006	0.008	0.008	0.008	0.008	0.006	0.007	0.006	0.006	0.006	0.006	0.006	0.006
Mg	1.706	1.727	1.720	1.725	1.726	1.713	1.765	1.772	1.780	1.772	1.780	1.777	1.773	1.779	1.778	1.768	1.772	1.773	1.787
Ca	0.009	0.009	0.009	0.008	0.006	0.008	0.008	0.007	0.009	0.007	0.009	0.008	0.008	0.006	0.007	0.006	0.008	0.007	0.008
Na	0.002	0.000	0.001	0.001	0.000	0.000	0.000	0.001	0.000	0.001	0.000	0.001	0.001	0.001	0.001	0.001	0.000	0.000	0.000
Forsterite	0.855	0.857	0.861	0.859	0.862	0.853	0.882	0.885	0.887	0.884	0.888	0.887	0.887	0.888	0.887	0.887	0.884	0.888	0.892

Table 4-2
Suite 7

Sample	OM20-13OR	OM20-14OR	OM20-15OC	OM20-16OC	OM20-16OR	OM20-18OC	OM20-18OR	OM20-18ORn	OM20-19OC	OM20-19OR	OM20-20OC	OM20-20OR	OM20-21OC	OM20-21OR	OM20-23OC	OM20-23OR	OM20-25OC	OM20-25OR	OM20-27OC
Analysis n°	Sample zone	3r	3r	3c	3c	3r	3c	3r	3c	3r	3c	3r	3c	3r	3c	3r	3c	3r	3c
Zone																			
Distance (mm)	1.56	1.56	1.85	1.83	1.85	2.01	2.01	1.99	2.01	2.01	2.06	2.05	2.06	2.05	2.18	2.18	2.26	2.26	2.32
SiO ₂	40.48	40.53	40.85	40.95	40.73	40.70	40.97	40.60	40.73	40.54	40.30	40.33	40.71	40.70	40.72	40.60	40.78	40.86	40.00
TiO ₂	0.06	0.00	0.03	0.00	0.03	0.02	0.00	0.00	0.09	0.05	0.08	0.07	0.00	0.00	0.01	0.00	0.02	0.00	0.06
Al ₂ O ₃	0.07	0.05	0.03	0.05	0.03	0.07	0.08	0.04	0.07	0.08	0.02	0.05	0.04	0.13	0.13	0.02	0.05	0.06	0.01
Cr ₂ O ₃	0.00	0.00	0.00	0.00	0.00	0.00	0.00	0.00	0.00	0.00	0.00	0.00	0.00	0.00	0.00	0.00	0.00	0.00	0.00
FeO	9.97	9.98	9.83	9.82	9.96	9.74	9.82	9.94	10.01	9.99	9.90	9.98	10.07	10.22	9.86	10.11	10.27	10.33	11.39
MnO	0.16	0.14	0.17	0.12	0.13	0.16	0.16	0.10	0.11	0.15	0.14	0.12	0.14	0.13	0.15	0.17	0.15	0.12	0.18
NiO	0.29	0.43	0.36	0.28	0.25	0.26	0.21	0.21	0.18	0.16	0.17	0.14	0.16	0.14	0.07	0.00	0.00	0.05	0.00
MgO	48.62	48.56	49.01	48.68	48.65	48.50	48.61	48.61	48.65	48.38	48.78	49.04	48.81	48.61	48.80	48.62	48.72	48.59	48.12
CaO	0.27	0.26	0.30	0.31	0.26	0.27	0.26	0.24	0.25	0.21	0.24	0.23	0.30	0.23	0.28	0.27	0.28	0.25	0.23
NaO	0.00	0.03	0.01	0.00	0.00	0.00	0.00	0.01	0.00	0.00	0.00	0.00	0.01	0.00	0.01	0.02	0.00	0.00	0.00
K ₂ O	0.01	0.02	0.01	0.02	0.00	0.00	0.00	0.00	0.00	0.00	0.01	0.00	0.00	0.00	0.00	0.00	0.00	0.00	0.00
Total	99.93	100.00	100.60	100.23	100.04	99.72	100.11	99.75	100.09	99.56	99.63	99.96	100.24	100.16	100.03	99.81	100.27	100.26	99.98
Si	0.995	0.996	0.996	1.003	1.000	1.001	1.005	0.999	0.999	1.000	0.991	0.989	0.997	0.998	0.998	0.998	0.999	1.001	0.986
Ti	0.001	0.000	0.001	0.000	0.001	0.000	0.000	0.000	0.002	0.001	0.002	0.001	0.000	0.000	0.000	0.000	0.000	0.000	0.001
Al	0.002	0.001	0.001	0.001	0.001	0.002	0.002	0.001	0.002	0.002	0.001	0.002	0.001	0.004	0.004	0.001	0.002	0.002	0.000
Cr	0.000	0.000	0.001	0.000	0.000	0.002	0.001	0.000	0.000	0.001	0.002	0.000	0.000	0.001	0.000	0.001	0.000	0.000	0.000
Fe ₂	0.205	0.205	0.201	0.201	0.204	0.200	0.201	0.205	0.205	0.206	0.204	0.205	0.206	0.210	0.202	0.208	0.210	0.212	0.235
Mn	0.003	0.003	0.004	0.003	0.003	0.003	0.003	0.002	0.002	0.003	0.003	0.003	0.003	0.003	0.003	0.004	0.003	0.003	0.004
Ni	0.006	0.008	0.007	0.006	0.005	0.005	0.004	0.004	0.004	0.003	0.003	0.003	0.003	0.003	0.003	0.001	0.000	0.001	0.000
Mg	1.781	1.778	1.782	1.777	1.780	1.778	1.777	1.782	1.779	1.778	1.788	1.792	1.781	1.777	1.783	1.782	1.779	1.775	1.768
Ca	0.007	0.007	0.008	0.008	0.007	0.007	0.007	0.006	0.007	0.006	0.006	0.006	0.008	0.006	0.007	0.007	0.007	0.007	0.006
Na	0.000	0.001	0.000	0.000	0.000	0.000	0.000	0.000	0.000	0.000	0.000	0.000	0.000	0.000	0.001	0.001	0.000	0.000	0.000
Forsterite	0.890	0.889	0.891	0.891	0.890	0.892	0.892	0.891	0.891	0.891	0.892	0.893	0.890	0.889	0.893	0.891	0.890	0.889	0.879

Table 4-2
Suite 8

Sample	OM20	OM20	OM20	OM20	OM20	OM20	OM20	OM20	OM20	OM20	OM20	OM20	OM20	OM20	OM20	OM20	OM20	OM21	
Analysis n°	OM20-27OC	OM20-27OC2	OM20-27OR	OM20-27OR	OM20-31OR	OM20-40OC	OM20-40OR	OM20-40ORn	OM20-41OC3	OM20-41OCC1	OM20-41OCC2	OM20-41OR1	OM20-41OR2	OM20-41OR3	OM20-42OC	OM20-42OR	OM20-43OC	OM20-43OR	OM21-03OEC
Sample zone	3	3	3	3	4	3	3	3	3	3	3	3	3	3	3	3	3	2	
Zone	c	c	r	r	r	c	r	r	c	c	c	r	r	c	c	r	c	c	
Distance (mm)	2.43	2.41	2.33	2.43	2.91	1.48	1.48	1.49	1.69	1.69	1.71	1.69	1.71	1.69	2.43	2.42	2.17	2.15	0.03
SiO ₂	40.29	40.63	40.04	40.33	37.93	40.59	40.37	40.35	40.81	40.46	40.55	40.68	40.60	40.46	40.60	40.40	40.76	40.69	39.72
TiO ₂	0.03	0.01	0.03	0.00	0.08	0.04	0.04	0.00	0.06	0.03	0.00	0.02	0.03	0.04	0.04	0.07	0.01	0.02	0.02
Al ₂ O ₃	0.06	0.03	0.06	0.05	0.07	0.04	0.06	0.06	0.07	0.06	0.03	0.09	0.14	0.06	0.05	0.14	0.02	0.04	0.05
Cr ₂ O ₃	0.00	0.00	0.00	0.00	0.00	0.00	0.00	0.00	0.00	0.00	0.00	0.00	0.00	0.00	0.00	0.00	0.00	0.00	0.00
FeO	11.38	10.69	11.35	11.45	25.56	10.16	10.25	10.07	10.02	9.86	10.04	9.92	9.97	10.14	10.81	10.61	9.64	9.69	13.83
MnO	0.19	0.18	0.12	0.17	0.37	0.13	0.15	0.11	0.16	0.15	0.15	0.11	0.14	0.15	0.17	0.14	0.15	0.14	0.24
NiO	0.01	0.00	0.07	0.02	0.04	0.26	0.26	0.27	0.31	0.37	0.34	0.30	0.22	0.31	0.05	0.03	0.27	0.29	0.09
MgO	47.81	48.28	47.69	47.76	36.20	48.90	48.53	48.35	48.61	48.12	48.75	48.67	48.40	48.55	47.87	48.47	48.49	48.47	45.63
CaO	0.23	0.25	0.24	0.22	0.29	0.27	0.23	0.25	0.34	0.28	0.32	0.24	0.27	0.28	0.26	0.19	0.30	0.28	0.34
NaO	0.04	0.03	0.00	0.00	0.04	0.03	0.00	0.03	0.02	0.02	0.03	0.02	0.00	0.00	0.00	0.03	0.00	0.03	0.01
K ₂ O	0.02	0.00	0.00	0.00	0.02	0.00	0.00	0.00	0.00	0.00	0.01	0.01	0.00	0.00	0.00	0.00	0.00	0.00	0.00
Total	100.05	100.10	99.59	99.99	100.59	100.42	99.88	99.49	100.39	99.34	100.21	100.06	99.76	99.98	99.85	100.07	99.64	99.65	99.92
Si	0.993	0.999	0.992	0.996	0.997	0.992	0.993	0.996	0.999	1.001	0.993	0.998	0.999	0.994	1.002	0.992	1.004	1.002	0.992
Ti	0.001	0.000	0.001	0.000	0.002	0.001	0.001	0.000	0.001	0.001	0.000	0.000	0.001	0.001	0.001	0.001	0.000	0.000	0.000
Al	0.002	0.001	0.002	0.001	0.002	0.001	0.002	0.002	0.002	0.002	0.001	0.003	0.004	0.002	0.001	0.004	0.001	0.001	0.002
Cr	0.001	0.000	0.000	0.000	0.000	0.000	0.000	0.001	0.000	0.001	0.000	0.001	0.001	0.000	0.001	0.000	0.000	0.000	0.001
Fe ₂	0.235	0.220	0.235	0.236	0.562	0.208	0.211	0.208	0.205	0.204	0.206	0.204	0.205	0.208	0.223	0.218	0.199	0.200	0.289
Mn	0.004	0.004	0.003	0.003	0.008	0.003	0.003	0.002	0.003	0.003	0.003	0.002	0.003	0.003	0.004	0.003	0.003	0.003	0.005
Ni	0.000	0.000	0.001	0.000	0.001	0.005	0.005	0.005	0.006	0.007	0.007	0.006	0.004	0.006	0.001	0.001	0.005	0.006	0.002
Mg	1.757	1.769	1.761	1.757	1.418	1.782	1.780	1.778	1.773	1.774	1.780	1.779	1.776	1.779	1.761	1.774	1.780	1.779	1.699
Ca	0.006	0.007	0.006	0.006	0.008	0.007	0.006	0.007	0.009	0.007	0.008	0.006	0.007	0.007	0.007	0.005	0.008	0.007	0.009
Na	0.002	0.002	0.000	0.000	0.002	0.002	0.000	0.001	0.001	0.001	0.001	0.001	0.001	0.000	0.000	0.002	0.000	0.002	0.001
Forsterite	0.878	0.885	0.878	0.877	0.710	0.889	0.888	0.889	0.888	0.889	0.888	0.891	0.890	0.888	0.882	0.887	0.892	0.892	0.848

Table 4-2

Suite 9

Sample	OM21 OM21- 03Res	OM21 OM21- 04OE	OM21 OM21- 04OER	OM21 OM21- 05OER	OM21 OM21- 05OR	OM21 OM21- 07OE	OM21 OM21- 07OE	OM21 OM21- 07Res	OM21 OM21- 08OEC	OM21 OM21- 08OER	OM21 OM21- 10OEC	OM21 OM21- 10OER	OM21 OM21- 11Res	OM21 OM21- 12OR	OM21 OM21- 13OEC	OM21 OM21- 13OER	OM21 OM21- 13OS	OM21 OM21- 14OS	OM21 OM21- 15OS
Analysis n°																			
Sample																			
zone	2	3	3	3	3	3	3	3	3	3	3	3	3	3	3	3	3	3	
Zone	r	c	r	r	r	c	r	r	c	r	c	r	r	r	c	r	r	r	
Distance (mm)	0.01	0.12	0.14	0.12	0.14	0.42	0.40	0.43	0.59	0.60	0.74	0.75	0.75	0.84	1.05	1.05	1.04	1.06	1.16
SiO ₂	36.47	40.01	40.00	40.15	39.85	39.95	39.88	40.71	40.81	40.49	40.66	40.89	41.02	40.78	40.73	40.57	40.75	40.59	40.42
TiO ₂	0.06	0.03	0.03	0.00	0.00	0.00	0.00	0.00	0.00	0.04	0.03	0.04	0.00	0.06	0.01	0.04	0.01	0.03	0.01
Al ₂ O ₃	0.06	0.06	0.07	0.04	0.02	0.03	0.04	0.05	0.05	0.04	0.04	0.04	0.03	0.03	0.06	0.07	0.05	0.06	0.06
Cr ₂ O ₃	0.00	0.00	0.00	0.00	0.00	0.00	0.00	0.00	0.00	0.00	0.00	0.00	0.00	0.00	0.00	0.00	0.00	0.00	0.00
FeO	32.30	12.04	12.74	12.92	13.30	10.70	11.07	10.91	10.32	10.62	10.10	10.22	10.21	10.36	9.53	10.21	10.44	10.47	10.19
MnO	0.59	0.15	0.17	0.14	0.24	0.09	0.15	0.17	0.17	0.20	0.18	0.18	0.15	0.14	0.11	0.16	0.24	0.16	0.15
NiO	0.09	0.32	0.20	0.10	0.22	0.31	0.24	0.33	0.39	0.25	0.31	0.29	0.45	0.41	0.34	0.36	0.32	0.33	0.36
MgO	30.45	46.82	46.57	46.73	46.52	48.50	47.72	48.38	48.50	48.38	48.86	48.51	48.36	48.44	49.16	48.58	48.29	48.38	48.78
CaO	0.40	0.30	0.32	0.36	0.29	0.21	0.25	0.22	0.28	0.31	0.26	0.33	0.25	0.25	0.32	0.30	0.32	0.27	0.30
NaO	0.02	0.00	0.02	0.00	0.01	0.03	0.00	0.02	0.00	0.00	0.00	0.00	0.03	0.00	0.01	0.00	0.00	0.02	0.02
K ₂ O	0.03	0.00	0.00	0.01	0.01	0.00	0.00	0.00	0.00	0.00	0.00	0.00	0.00	0.01	0.01	0.00	0.01	0.01	0.01
Total	100.47	99.73	100.11	100.44	100.46	99.82	99.34	100.79	100.51	100.32	100.44	100.50	100.50	100.46	100.28	100.41	100.30	100.29	
Si	0.994	0.995	0.993	0.993	0.987	0.983	0.990	0.995	0.999	0.993	0.994	1.001	1.004	0.999	0.995	0.994	0.999	0.996	0.990
Ti	0.001	0.001	0.001	0.000	0.000	0.000	0.000	0.000	0.000	0.001	0.001	0.001	0.000	0.001	0.000	0.001	0.000	0.001	0.000
Al	0.002	0.002	0.002	0.001	0.001	0.001	0.001	0.001	0.001	0.001	0.001	0.001	0.001	0.001	0.002	0.002	0.002	0.002	0.002
Cr	0.001	0.000	0.001	0.001	0.001	0.002	0.000	0.001	0.001	0.000	0.001	0.001	0.001	0.001	0.001	0.001	0.001	0.000	0.001
Fe ₂	0.736	0.250	0.265	0.267	0.276	0.220	0.230	0.223	0.211	0.218	0.207	0.209	0.209	0.212	0.195	0.209	0.214	0.215	0.209
Mn	0.014	0.003	0.003	0.003	0.005	0.002	0.003	0.004	0.004	0.004	0.004	0.004	0.003	0.003	0.002	0.003	0.005	0.003	0.003
Ni	0.002	0.006	0.004	0.002	0.004	0.006	0.005	0.007	0.008	0.005	0.006	0.006	0.009	0.008	0.007	0.007	0.006	0.007	0.007
Mg	1.237	1.735	1.723	1.723	1.718	1.779	1.765	1.763	1.770	1.769	1.780	1.770	1.765	1.769	1.790	1.775	1.765	1.769	1.780
Ca	0.012	0.008	0.009	0.009	0.008	0.005	0.007	0.006	0.007	0.008	0.007	0.009	0.007	0.007	0.008	0.008	0.008	0.007	0.008
Na	0.001	0.000	0.001	0.000	0.000	0.001	0.000	0.001	0.000	0.000	0.000	0.000	0.002	0.000	0.000	0.000	0.000	0.001	0.001
Forsterite	0.618	0.866	0.860	0.859	0.854	0.884	0.878	0.881	0.885	0.883	0.889	0.886	0.885	0.894	0.886	0.883	0.884	0.887	

Table 4-2
Suite 10

Sample	OM21	OM21	OM21	OM21	OM21	OM21	OM21	OM21	OM21	OM21	OM21	OM21	OM21	OM21	OM21	OM21	OM21	OM21	OM22
Analysis n°	OM21-16OEC	OM21-16Res	OM21-16Res2	OM21-17OEC	OM21-17OER	OM21-18OC	OM21-18OEC	OM21-18OE	OM21-180	OM21-19OE	OM21-19OE	OM21-20OE	OM21-21OBS	OM21-22OE	OM21-23Res	OM21-24OEC	OM21-24OE	OM21-24OE2	OM21-21OR
Sample zone	3	3	3	3	3	3	3	3	3	3	3	3	3	3	3	3	3	3	0
Zone	c	r	r	c	r	c	c	r	r	c	r	c	r	r	r	c	r	r	r
Distance (mm)	1.51	1.50	1.52	1.36	1.38	1.72	1.70	1.71	1.72	1.78	1.78	1.90	2.07	2.17	2.17	2.19	2.21	2.21	0.00
SiO ₂	40.49	40.43	40.63	40.89	40.92	40.86	40.99	40.51	40.28	40.70	40.64	40.75	40.52	40.60	40.58	41.03	40.74	40.53	35.77
TiO ₂	0.00	0.00	0.05	0.04	0.01	0.04	0.00	0.03	0.04	0.00	0.01	0.00	0.05	0.02	0.05	0.00	0.04	0.04	0.15
Al ₂ O ₃	0.04	0.03	0.03	0.01	0.06	0.06	0.03	0.07	0.03	0.06	0.08	0.07	0.03	0.05	0.05	0.04	0.05	0.03	0.07
Cr ₂ O ₃	0.00	0.00	0.00	0.00	0.00	0.00	0.00	0.00	0.00	0.00	0.00	0.00	0.00	0.00	0.00	0.00	0.00	0.00	0.00
FeO	10.08	10.00	10.24	9.99	10.33	10.33	9.85	10.09	10.29	9.89	10.31	9.80	10.36	10.15	10.22	9.95	10.05	10.45	35.02
MnO	0.17	0.17	0.17	0.16	0.12	0.16	0.16	0.17	0.18	0.12	0.09	0.14	0.15	0.12	0.16	0.11	0.20	0.17	0.55
NiO	0.34	0.45	0.29	0.40	0.41	0.27	0.34	0.27	0.28	0.27	0.33	0.31	0.21	0.04	0.02	0.16	0.14	0.12	0.11
MgO	48.63	48.55	48.63	48.46	48.53	48.41	48.60	48.47	48.38	48.64	48.89	48.54	48.49	48.60	48.81	49.06	48.51	48.48	28.62
CaO	0.27	0.24	0.23	0.25	0.28	0.28	0.31	0.30	0.28	0.30	0.27	0.31	0.19	0.25	0.25	0.18	0.24	0.21	0.31
NaO	0.00	0.00	0.02	0.01	0.00	0.01	0.01	0.00	0.01	0.00	0.00	0.03	0.00	0.01	0.03	0.01	0.02	0.05	0.00
K ₂ O	0.01	0.01	0.00	0.00	0.00	0.00	0.00	0.00	0.01	0.00	0.01	0.01	0.01	0.00	0.00	0.00	0.00	0.00	0.02
Total	100.02	99.87	100.27	100.20	100.65	100.41	100.28	99.91	99.76	99.98	100.62	99.93	100.03	99.83	100.15	100.56	99.98	100.04	100.96
Si	0.994	0.994	0.996	1.004	1.001	1.002	1.004	0.996	0.992	0.999	0.992	1.001	0.996	0.998	0.995	1.001	1.001	0.996	0.985
Ti	0.000	0.000	0.001	0.001	0.000	0.001	0.000	0.001	0.001	0.000	0.000	0.000	0.001	0.000	0.001	0.000	0.001	0.001	0.003
Al	0.001	0.001	0.001	0.000	0.002	0.002	0.001	0.002	0.001	0.002	0.002	0.002	0.001	0.002	0.002	0.001	0.001	0.001	0.002
Cr	0.000	0.000	0.001	0.000	0.000	0.000	0.000	0.000	0.000	0.001	0.000	0.000	0.000	0.000	0.000	0.001	0.000	0.000	0.000
Fe ₂	0.207	0.206	0.210	0.205	0.211	0.212	0.202	0.208	0.212	0.203	0.210	0.201	0.213	0.209	0.209	0.203	0.207	0.215	0.807
Mn	0.004	0.004	0.003	0.003	0.003	0.003	0.003	0.004	0.004	0.003	0.002	0.003	0.003	0.003	0.003	0.002	0.004	0.004	0.013
Ni	0.007	0.009	0.006	0.008	0.008	0.005	0.007	0.005	0.006	0.005	0.006	0.006	0.004	0.001	0.001	0.003	0.003	0.002	0.002
Mg	1.780	1.780	1.776	1.772	1.769	1.768	1.774	1.777	1.777	1.780	1.779	1.778	1.776	1.781	1.783	1.784	1.776	1.776	1.175
Ca	0.007	0.006	0.006	0.007	0.007	0.007	0.008	0.008	0.007	0.008	0.007	0.008	0.005	0.007	0.006	0.005	0.006	0.005	0.009
Na	0.000	0.000	0.001	0.000	0.000	0.000	0.001	0.000	0.000	0.000	0.000	0.002	0.000	0.001	0.001	0.001	0.001	0.003	0.000
Forsterite	0.888	0.888	0.888	0.888	0.885	0.886	0.890	0.888	0.886	0.891	0.887	0.891	0.888	0.891	0.890	0.893	0.890	0.887	0.586

Table 4-2
Suite 11

Sample	OM22	OM22	OM22	OM22	OM22	OM22	OM22												
Analysis n°	OM22-27OC	OM22-27OR	OM22-28OC	OM22-28OR	OM22-29OC	OM22-29OR	OM22-31OC	OM22-32OC	OM22-32OR	OM22-33OC	OM22-33OR	OM22-33ORn	OM22-34OR	OM22-35OC	OM22-35OR	OM22-36OC	OM22-36OR	OM22-37OC	OM22-37OR
Sample zone	2	2	2	2	2	2	3	3	3	3	3	3	3	3	3	3	3	3	
Zone	c	r	c	r	c	r	c	c	r	c	r	r	r	c	r	c	r	c	
Distance (mm)	0.23	0.25	0.23	0.22	0.26	0.26	0.66	0.65	0.66	0.98	0.99	0.96	0.96	1.04	1.03	1.52	1.52	2.26	2.26
SiO ₂	40.55	41.03	40.64	40.83	40.81	40.77	40.79	41.03	40.71	40.70	40.79	40.37	40.85	40.76	41.04	40.58	40.46	40.69	40.83
TiO ₂	0.00	0.02	0.02	0.05	0.05	0.03	0.00	0.00	0.02	0.01	0.05	0.03	0.00	0.00	0.03	0.01	0.00	0.07	0.03
Al ₂ O ₃	0.04	0.03	0.02	0.06	0.01	0.07	0.01	0.02	0.06	0.04	0.10	0.07	0.03	0.03	0.03	0.03	0.08	0.04	0.06
Cr ₂ O ₃	0.00	0.00	0.00	0.00	0.00	0.00	0.00	0.00	0.00	0.00	0.00	0.00	0.00	0.00	0.00	0.00	0.00	0.00	0.00
FeO	10.41	10.86	10.96	11.09	10.91	10.93	10.34	10.41	10.40	10.15	10.34	10.15	10.40	9.95	10.19	9.63	9.98	9.91	10.06
MnO	0.12	0.17	0.13	0.16	0.13	0.18	0.19	0.15	0.16	0.12	0.16	0.13	0.18	0.15	0.13	0.09	0.23	0.16	0.12
NiO	0.35	0.30	0.40	0.41	0.31	0.38	0.40	0.40	0.33	0.39	0.38	0.39	0.37	0.46	0.36	0.30	0.33	0.43	0.47
MgO	48.75	48.27	47.78	47.99	48.28	47.78	48.60	48.48	48.96	48.68	48.75	48.73	48.09	48.47	48.84	49.50	49.16	48.64	49.18
CaO	0.11	0.17	0.21	0.27	0.23	0.25	0.24	0.19	0.21	0.20	0.20	0.16	0.23	0.14	0.17	0.24	0.19	0.15	0.17
NaO	0.00	0.04	0.01	0.01	0.01	0.01	0.03	0.03	0.02	0.00	0.00	0.02	0.01	0.03	0.00	0.00	0.00	0.03	0.02
K ₂ O	0.00	0.00	0.00	0.00	0.00	0.01	0.00	0.00	0.00	0.02	0.00	0.00	0.01	0.00	0.00	0.00	0.00	0.00	0.01
Total	100.44	101.06	100.38	101.14	100.97	100.65	100.84	100.90	101.08	100.49	100.97	100.20	100.38	100.12	100.96	100.62	100.27	101.11	
Si	0.993	1.003	1.002	1.000	0.999	1.002	0.997	1.003	0.992	0.997	0.995	0.991	1.005	1.001	1.001	0.990	0.988	0.998	0.993
Ti	0.000	0.000	0.000	0.001	0.001	0.001	0.000	0.000	0.000	0.000	0.000	0.001	0.001	0.000	0.000	0.001	0.000	0.001	0.001
Al	0.001	0.001	0.001	0.002	0.000	0.002	0.000	0.001	0.002	0.001	0.003	0.002	0.001	0.001	0.001	0.001	0.002	0.001	0.002
Cr	0.000	0.000	0.000	0.000	0.001	0.001	0.001	0.001	0.000	0.001	0.000	0.000	0.001	0.001	0.001	0.000	0.000	0.001	0.000
Fe ₂	0.213	0.222	0.226	0.227	0.223	0.225	0.211	0.213	0.212	0.208	0.211	0.208	0.214	0.204	0.208	0.196	0.204	0.203	0.205
Mn	0.003	0.004	0.003	0.003	0.003	0.004	0.004	0.003	0.003	0.003	0.003	0.003	0.004	0.003	0.003	0.002	0.005	0.003	0.002
Ni	0.007	0.006	0.008	0.008	0.006	0.008	0.008	0.008	0.006	0.008	0.008	0.008	0.007	0.009	0.007	0.006	0.007	0.008	0.009
Mg	1.780	1.759	1.755	1.752	1.761	1.751	1.771	1.766	1.778	1.777	1.773	1.783	1.763	1.775	1.776	1.799	1.790	1.779	1.783
Ca	0.003	0.005	0.006	0.007	0.006	0.007	0.006	0.005	0.006	0.005	0.005	0.004	0.006	0.004	0.004	0.006	0.005	0.004	0.004
Na	0.000	0.002	0.000	0.000	0.001	0.002	0.002	0.001	0.001	0.000	0.000	0.001	0.000	0.001	0.000	0.000	0.002	0.001	0.001
Forsterite	0.888	0.882	0.879	0.877	0.881	0.878	0.885	0.885	0.887	0.888	0.886	0.889	0.884	0.890	0.889	0.895	0.890	0.890	0.890

Table 4-2
Suite 12

Sample	OM22 OM22- 38OC	OM22 OM22- 38OR	OM22 OM22- 38ORES	OM22 OM22- 39OC	OM22 OM22- 39OR	OM22 OM22- 40OR	OM22 OM22-41O
Analysis n°	3	3	3	3	3	3	4
Sample zone	c	r	r	c	r	r	
Zone							
Distance (mm)	2.07	2.07	2.07	2.07	2.07	2.71	2.91
SiO ₂	40.57	41.00	41.02	40.55	40.05	40.84	40.53
TiO ₂	0.02	0.05	0.05	0.04	0.00	0.03	0.03
Al ₂ O ₃	0.01	0.12	0.03	0.04	0.33	0.10	0.02
Cr ₂ O ₃	0.00	0.00	0.00	0.00	0.00	0.00	0.00
FeO	9.65	9.72	10.24	9.98	9.83	10.52	13.29
MnO	0.16	0.14	0.16	0.13	0.16	0.08	0.24
NiO	0.33	0.39	0.36	0.39	0.40	0.13	0.00
MgO	49.07	49.05	48.60	49.16	49.51	48.44	46.46
CaO	0.26	0.17	0.16	0.15	0.20	0.21	0.21
NaO	0.01	0.04	0.03	0.00	0.05	0.06	0.01
K ₂ O	0.00	0.01	0.00	0.00	0.02	0.02	0.01
Total	100.34	100.85	100.80	100.58	100.73	100.59	101.00
Si	0.993	0.999	1.003	0.990	0.975	1.000	1.002
Ti	0.000	0.001	0.001	0.001	0.000	0.001	0.001
Al	0.000	0.004	0.001	0.001	0.010	0.003	0.001
Cr	0.001	0.000	0.000	0.000	0.000	0.001	0.000
Fe ₂	0.198	0.198	0.209	0.204	0.200	0.216	0.275
Mn	0.003	0.003	0.003	0.003	0.003	0.002	0.005
Ni	0.006	0.008	0.007	0.008	0.008	0.003	0.000
Mg	1.790	1.782	1.771	1.789	1.796	1.768	1.711
Ca	0.007	0.004	0.004	0.004	0.005	0.006	0.006
Na	0.001	0.002	0.001	0.000	0.002	0.002	0.000
Forsterite	0.893	0.893	0.888	0.891	0.892	0.887	0.857

Table 4-3

Representative major element compositions of plagioclase from ol-rich layer from step-cooled experiments

Melt	AH6 0.5	AH6 0.5	AH6 0.5	AH6 0.5	AH6 0.5	AH6 0.5	AH6 0.5	AH6 0.5	AH6 0.5	AH6 0.5	AH6 0.5	HDRBC 0.5	HDRBC 0.5	HDRBC 0.5		
P (Gpa)	Analysis n°	OM02- 111	OM02- 51	OM02- 116	OM02- 45	OM02- 100	OM02- 44	OM02- 103	OM02- 94	OM02- 27	OM02b- 35	OM02b- 6	OM02b- 11	OM02- 20	OM02- 32	OM02- 33
D (mm)	0.04	0.09	0.15	0.21	0.31	0.37	0.38	0.39	0.74	0.81	0.84	0.84	0.84	0.84	0.84	0.87
SiO ₂	50.69	50.43	51.24	51.14	51.10	51.38	52.28	52.80	51.70	52.91	53.47	52.04	51.94	51.62	51.35	
TiO ₂	0.05	0.01	0.01	0.03	0.04	0.09	0.09	0.08	0.05	0.06	0.06	0.04	0.06	0.02	0.10	
Al ₂ O ₃	30.88	30.99	30.45	30.81	30.37	30.34	29.81	29.36	28.67	29.73	28.99	29.80	29.00	28.88	30.11	
Fe ₂ O ₃	0.68	0.00	0.32	0.59	0.42	0.65	0.00	0.13	0.00	0.17	0.41	0.55	0.00	0.08	0.08	
FeO	0.00	0.47	0.29	0.00	0.16	0.00	0.60	0.42	0.62	0.38	0.00	0.02	0.51	0.46	0.41	
NiO	0.00	0.00	0.00	0.03	0.00	0.02	0.00	0.02	0.04	0.04	0.03	0.01	0.00	0.00	0.02	
MgO	0.38	0.33	0.27	0.34	0.31	0.26	0.30	0.21	0.37	0.22	0.22	0.22	0.18	0.36	0.36	
CaO	14.69	14.39	13.74	14.12	13.91	13.49	13.35	12.73	13.27	12.27	11.89	13.08	13.07	13.36	13.75	
Na ₂ O	3.17	3.11	3.56	3.43	3.50	3.74	3.79	4.21	3.74	4.32	4.67	4.01	3.83	3.76	3.55	
K ₂ O	0.06	0.06	0.05	0.06	0.04	0.08	0.06	0.07	0.05	0.11	0.10	0.06	0.09	0.06	0.05	
Total	100.60	99.85	100.01	100.59	99.92	100.08	100.33	100.08	98.50	100.24	99.89	99.89	98.69	98.61	99.78	
Si	2.301	2.305	2.334	2.317	2.331	2.337	2.372	2.396	2.390	2.395	2.424	2.368	2.396	2.382	2.344	
Ti	0.002	0.001	0.001	0.001	0.002	0.003	0.003	0.003	0.002	0.002	0.002	0.002	0.002	0.001	0.003	
Al	1.652	1.669	1.635	1.646	1.632	1.626	1.594	1.570	1.562	1.586	1.549	1.598	1.576	1.571	1.620	
Fe ₃	0.023	0.000	0.011	0.020	0.014	0.022	0.000	0.005	0.000	0.006	0.014	0.019	0.000	0.003	0.003	
Fe ₂	0.000	0.018	0.011	0.000	0.006	0.000	0.023	0.016	0.024	0.014	0.000	0.001	0.020	0.018	0.016	
Ni	0.000	0.000	0.000	0.001	0.000	0.001	0.000	0.001	0.001	0.002	0.001	0.001	0.000	0.000	0.001	
Mg	0.000	0.000	0.000	0.000	0.000	0.000	0.000	0.000	0.000	0.000	0.000	0.000	0.000	0.000	0.000	
Ca	0.026	0.022	0.019	0.023	0.021	0.018	0.021	0.014	0.025	0.015	0.015	0.015	0.013	0.025	0.025	
Na	0.714	0.705	0.671	0.686	0.680	0.657	0.649	0.619	0.657	0.595	0.578	0.638	0.646	0.661	0.672	
K	0.279	0.276	0.314	0.301	0.310	0.330	0.333	0.370	0.335	0.379	0.410	0.354	0.343	0.336	0.314	
XAn	0.717	0.716	0.679	0.692	0.685	0.663	0.658	0.623	0.660	0.607	0.581	0.641	0.650	0.660	0.680	

D: Distance is calculated from the x,y coordinates of an olivine from the interface zone (picked up as a 0 mm reference olivine for each sample) and the x,y coordinates of the analysis

Cations are calculated with the Program NORM (version 2013) by Ulmer and

Poli

Table 4-3

Suite 1

Melt P (Gpa) Analysis n°	HDRBC 0.5 OM02- 15	HDRBC 0.5 OM03b- 31	HDRBC 0.5 OM03- 101	HDRBC 0.5 OM03- 91	HDRBC 0.5 OM03- 90	HDRBC 0.5 OM03- 102	HDRBC 0.5 OM03- 71	HDRBC 0.5 OM03b- 8	HDRBC 0.5 OM03- 67	HDRBC 0.5 OM03- 69	HDRBC 0.5 OM03- 63	HDRBC 0.5 OM03- 48	HDRBC 0.5 OM03- 52	HDRBC 0.5 OM03- 39	HDRBC 0.5 OM03- 43
D (mm)	1.09	-0.80	0.01	0.10	0.11	0.17	0.21	0.39	0.39	0.41	0.64	0.77	0.85	0.90	0.91
SiO ₂	52.71	50.76	50.44	49.67	50.51	50.71	52.53	52.60	50.84	51.46	51.48	51.39	50.90	51.37	52.78
TiO ₂	0.06	0.09	0.09	0.03	0.07	0.07	0.06	0.08	0.10	0.05	0.04	0.05	0.03	0.03	0.10
Al ₂ O ₃	28.45	31.08	31.46	31.60	31.74	31.73	30.67	29.31	30.66	30.74	30.78	30.86	31.37	30.78	29.94
Fe ₂ O ₃	0.00	0.41	0.76	0.65	0.67	0.61	0.08	0.51	0.59	0.00	0.42	0.62	0.62	0.14	0.34
FeO	0.19	0.00	0.00	0.00	0.00	0.00	0.42	0.00	0.02	0.60	0.25	0.00	0.00	0.40	0.27
NiO	0.00	0.00	0.08	0.03	0.00	0.03	0.00	0.00	0.05	0.00	0.00	0.00	0.01	0.00	0.04
MgO	0.21	0.44	0.36	0.39	0.34	0.33	0.26	0.27	0.36	0.43	0.38	0.30	0.34	0.31	0.40
CaO	12.58	14.72	14.36	14.21	14.44	14.02	12.98	12.85	14.30	14.26	13.92	13.56	13.90	13.68	12.68
Na ₂ O	4.20	3.18	3.18	3.22	3.23	3.44	3.98	4.21	3.32	3.22	3.50	3.68	3.41	3.53	4.11
K ₂ O	0.04	0.04	0.06	0.04	0.06	0.05	0.08	0.10	0.05	0.07	0.05	0.08	0.09	0.08	0.11
Total	98.50	100.80	100.79	99.87	101.05	101.06	101.10	99.97	100.31	100.89	100.84	100.55	100.69	100.34	100.78
Si	2.429	2.297	2.285	2.267	2.280	2.285	2.360	2.389	2.313	2.328	2.326	2.326	2.303	2.331	2.379
Ti	0.002	0.003	0.003	0.001	0.002	0.002	0.002	0.003	0.003	0.002	0.001	0.002	0.001	0.001	0.003
Al	1.545	1.658	1.680	1.699	1.688	1.685	1.624	1.569	1.644	1.639	1.639	1.646	1.673	1.646	1.590
Fe ₃	0.000	0.014	0.026	0.022	0.023	0.021	0.003	0.017	0.020	0.000	0.014	0.021	0.021	0.005	0.012
Fe ₂	0.007	0.000	0.000	0.000	0.000	0.000	0.016	0.000	0.001	0.023	0.010	0.000	0.000	0.015	0.010
Ni	0.000	0.000	0.003	0.001	0.000	0.001	0.000	0.000	0.002	0.000	0.000	0.000	0.000	0.000	0.001
Mg	0.000	0.030	0.025	0.026	0.023	0.022	0.017	0.018	0.025	0.029	0.026	0.020	0.023	0.021	0.027
Ca	0.015	0.714	0.697	0.695	0.698	0.677	0.625	0.625	0.697	0.691	0.674	0.658	0.674	0.665	0.612
Na	0.621	0.279	0.279	0.285	0.283	0.301	0.347	0.371	0.293	0.282	0.307	0.323	0.299	0.311	0.359
K	0.375	0.003	0.003	0.002	0.003	0.003	0.005	0.006	0.003	0.004	0.003	0.004	0.005	0.005	0.006
XAn	0.622	0.717	0.712	0.708	0.709	0.690	0.640	0.624	0.702	0.707	0.685	0.668	0.689	0.678	0.626

Table 4-3
Suite 2

Melt P (Gpa)	HDRBC 0.5 OM03- 29	HDRBC 0.5 OM03- 19	HDRBC 0.5 OM03- 127	HDRBC 0.5 OM03b- 2	HDRBC 0.5 OM03- 11	AH6 0.7 OM20- 03PR2	AH6 0.7 OM20- 03PC	AH6 0.7 OM20- 03PR1	AH6 0.7 OM20- 05-01	AH6 0.7 OM20- 05-02	AH6 0.7 OM20- 05PR	AH6 0.7 OM20- 04PR	AH6 0.7 OM20- 03PR	AH6 0.7 OM20- 04PC	
D (mm)	1.16	1.22	1.22	1.22	1.36	0.00	0.00	0.00	0.01	0.01	0.01	0.02	0.03	0.03	0.05
SiO ₂	51.97	51.49	51.33	52.04	51.91	52.77	53.57	52.37	55.30	55.44	54.42	52.53	53.09	52.34	52.78
TiO ₂	0.06	0.10	0.06	0.11	0.07	0.05	0.05	0.05	0.07	0.05	0.05	0.07	0.07	0.07	0.06
Al ₂ O ₃	30.66	30.33	30.87	30.33	30.11	29.61	28.73	29.24	28.33	27.94	28.59	28.01	28.40	28.53	29.11
Fe ₂ O ₃	0.28	0.57	0.66	0.00	0.55	0.93	0.52	0.79	0.00	0.00	1.06	0.87	0.42	0.42	0.29
FeO	0.22	0.01	0.00	0.20	0.02	0.00	0.14	0.29	0.95	0.94	0.00	0.29	0.46	0.44	0.47
NiO	0.05	0.02	0.02	0.00	0.04	0.04	0.06	0.02	0.00	0.03	0.05	0.00	0.00	0.03	0.01
MgO	0.31	0.40	0.39	0.20	0.44	0.11	0.09	0.13	0.10	0.08	0.10	0.14	0.22	0.31	0.34
CaO	13.33	13.21	13.73	13.21	13.58	12.84	12.27	12.92	11.02	10.81	10.92	12.30	12.59	13.20	12.88
Na ₂ O	3.80	3.74	3.65	3.82	3.70	4.26	4.60	4.11	5.03	5.23	5.34	4.40	4.32	3.95	4.08
K ₂ O	0.06	0.11	0.09	0.09	0.09	0.09	0.09	0.08	0.12	0.12	0.13	0.08	0.10	0.09	0.10
Total	100.75	100.00	100.83	100.02	100.58	100.70	100.12	99.99	100.92	100.64	100.68	98.69	99.67	99.35	100.12
Si	2.346	2.342	2.317	2.365	2.350	2.383	2.426	2.384	2.482	2.492	2.443	2.421	2.421	2.399	2.396
Ti	0.002	0.003	0.002	0.004	0.003	0.002	0.002	0.002	0.002	0.002	0.003	0.003	0.002	0.002	0.002
Al	1.631	1.626	1.642	1.625	1.606	1.576	1.534	1.569	1.499	1.480	1.513	1.521	1.526	1.541	1.558
Fe ₃	0.010	0.019	0.022	0.000	0.019	0.032	0.018	0.027	0.000	0.000	0.036	0.030	0.015	0.014	0.010
Fe ₂	0.009	0.000	0.000	0.008	0.001	0.000	0.005	0.011	0.036	0.035	0.000	0.011	0.018	0.017	0.018
Ni	0.002	0.001	0.001	0.000	0.002	0.002	0.002	0.001	0.000	0.001	0.002	0.000	0.000	0.001	0.000
Mg	0.021	0.027	0.027	0.013	0.030	0.000	0.000	0.000	0.000	0.000	0.007	0.000	0.000	0.000	0.000
Ca	0.645	0.644	0.664	0.643	0.659	0.007	0.006	0.009	0.007	0.005	0.525	0.010	0.015	0.021	0.023
Na	0.333	0.330	0.319	0.337	0.325	0.621	0.595	0.630	0.530	0.521	0.465	0.607	0.615	0.648	0.627
K	0.004	0.006	0.005	0.005	0.005	0.373	0.404	0.363	0.438	0.456	0.007	0.393	0.382	0.351	0.359
XAn	0.657	0.657	0.672	0.653	0.666	0.621	0.592	0.632	0.544	0.530	0.527	0.604	0.613	0.645	0.632

Table 4-3
Suite 3

Melt P (Gpa)	AH6 0.7 OM20- 04PR1	AH6 0.7 OM20- 06P	AH6 0.7 OM20- 05PC1	AH6 0.7 OM20- 05PC2	AH6 0.7 OM20- 07PC	AH6 0.7 OM20- 07PR	AH6 0.7 OM20- 08PR	AH6 0.7 OM20- 09P	AH6 0.7 OM20- 10P	AH6 0.7 OM20- 12P	AH6 0.7 OM20- 11P	AH6 0.7 OM20- 40P	AH6 0.7 OM20- 14P	AH6 0.7 OM20- 13PR	
D (mm)	0.05	0.08	0.12	0.12	0.29	0.29	0.29	0.44	0.45	0.51	0.51	0.60	0.60	0.63	0.63
SiO ₂	52.76	52.39	53.07	52.37	51.68	51.81	53.11	52.11	51.88	51.77	51.11	52.14	52.14	52.20	51.33
TiO ₂	0.10	0.04	0.08	0.08	0.04	0.07	0.02	0.00	0.08	0.01	0.08	0.05	0.05	0.04	0.05
Al ₂ O ₃	28.90	28.83	29.32	29.06	29.22	29.32	28.91	29.38	29.38	29.55	30.39	30.82	30.82	30.21	29.74
Fe ₂ O ₃	0.00	0.00	0.72	0.91	0.63	0.71	0.16	0.59	0.31	0.86	0.78	0.82	0.82	0.14	0.85
FeO	0.79	0.69	0.00	0.00	0.07	0.00	0.42	0.11	0.51	0.00	0.00	0.01	0.01	0.54	0.00
NiO	0.02	0.03	0.06	0.00	0.03	0.00	0.04	0.00	0.07	0.00	0.01	0.03	0.03	0.00	0.00
MgO	0.35	0.31	0.26	0.33	0.30	0.26	0.15	0.27	0.44	0.57	0.32	0.45	0.45	0.31	0.89
CaO	12.89	12.77	12.46	12.99	13.61	13.37	12.26	13.45	13.52	13.48	13.79	13.45	13.45	13.22	13.40
Na ₂ O	4.01	3.87	4.34	4.10	3.73	3.92	4.40	3.88	3.65	3.82	3.61	3.73	3.73	3.81	3.73
K ₂ O	0.11	0.12	0.16	0.14	0.12	0.11	0.15	0.08	0.09	0.10	0.09	0.11	0.11	0.11	0.09
Total	99.93	99.05	100.47	99.98	99.43	99.57	99.62	99.87	99.93	100.16	100.18	101.61	101.61	100.58	100.08
Si	2.402	2.407	2.398	2.382	2.368	2.368	2.419	2.375	2.366	2.351	2.324	2.335	2.335	2.361	2.331
Ti	0.004	0.001	0.003	0.003	0.002	0.002	0.001	0.000	0.003	0.000	0.003	0.002	0.002	0.002	0.002
Al	1.550	1.561	1.561	1.558	1.578	1.579	1.552	1.578	1.579	1.582	1.629	1.627	1.627	1.610	1.592
Fe ₃	0.000	0.000	0.025	0.031	0.022	0.024	0.006	0.020	0.011	0.030	0.027	0.028	0.028	0.005	0.029
Fe ₂	0.030	0.026	0.000	0.000	0.003	0.000	0.016	0.004	0.020	0.000	0.000	0.001	0.001	0.021	0.000
Ni	0.001	0.001	0.002	0.000	0.001	0.000	0.001	0.000	0.003	0.000	0.000	0.001	0.001	0.000	0.000
Mg	0.000	0.000	0.000	0.000	0.000	0.000	0.000	0.000	0.000	0.000	0.000	0.000	0.000	0.000	0.000
Ca	0.024	0.021	0.018	0.022	0.021	0.018	0.010	0.018	0.030	0.039	0.022	0.030	0.030	0.021	0.060
Na	0.629	0.629	0.603	0.633	0.668	0.655	0.598	0.657	0.661	0.656	0.672	0.645	0.645	0.641	0.652
K	0.354	0.345	0.380	0.362	0.331	0.347	0.389	0.343	0.323	0.336	0.318	0.324	0.324	0.334	0.328
XAn	0.636	0.641	0.608	0.631	0.664	0.649	0.601	0.654	0.668	0.657	0.675	0.662	0.662	0.653	0.661

Table 4-3
Suite 4

Melt P (Gpa)	AH6 0.7 OM20- 13P	AH6 0.7 OM20- 41P2	AH6 0.7 OM20- 41P	AH6 0.7 OM20- 15P1	AH6 0.7 OM20- 15P2	AH6 0.7 OM20- 15P3	AH6 0.7 OM20- 16P	AH6 0.7 OM20- 15P4	AH6 0.7 OM20- 18P3	AH6 0.7 OM20- 18P1	AH6 0.7 OM20- 19PL	AH6 0.7 OM20- 19P2	AH6 0.7 OM20- 18P	AH6 0.7 OM20- 19P3	AH6 0.7 OM20- 20P1
D (mm)	0.63	0.67	0.68	0.73	0.73	0.74	0.74	0.75	0.80	0.81	0.81	0.81	0.81	0.82	0.82
SiO ₂	52.03	52.16	52.02	52.15	52.81	52.29	52.39	51.44	51.66	52.06	51.59	51.00	52.54	52.56	52.49
TiO ₂	0.08	0.07	0.06	0.04	0.09	0.04	0.04	0.01	0.05	0.02	0.04	0.00	0.09	0.08	0.03
Al ₂ O ₃	29.91	30.80	30.44	29.95	29.65	30.03	30.33	30.01	29.88	30.42	30.26	30.97	29.78	30.31	30.32
Fe ₂ O ₃	0.74	0.68	0.76	0.73	0.72	0.62	0.60	0.85	0.78	0.20	0.13	0.74	0.66	0.48	0.61
FeO	0.07	0.00	0.00	0.00	0.00	0.00	0.00	0.00	0.00	0.39	0.52	0.00	0.00	0.08	0.00
NiO	0.07	0.00	0.05	0.00	0.05	0.05	0.01	0.03	0.01	0.02	0.04	0.00	0.00	0.00	0.05
MgO	0.34	0.33	0.31	0.31	0.38	0.31	0.36	0.44	0.99	0.29	0.41	0.37	0.40	0.21	0.29
CaO	13.43	13.16	13.51	13.05	12.20	12.48	12.79	13.18	13.01	13.51	13.50	14.03	12.80	12.80	12.75
Na ₂ O	3.80	4.05	3.81	4.04	4.36	4.28	4.10	3.90	3.87	3.73	3.55	3.52	4.24	4.13	4.26
K ₂ O	0.10	0.11	0.11	0.11	0.15	0.13	0.12	0.12	0.10	0.09	0.11	0.12	0.11	0.11	0.12
Total	100.57	101.36	101.07	100.38	100.41	100.22	100.74	99.98	100.35	100.73	100.15	100.75	100.62	100.76	100.92
Si	2.356	2.337	2.343	2.360	2.385	2.365	2.360	2.338	2.336	2.351	2.345	2.305	2.369	2.368	2.358
Ti	0.003	0.002	0.002	0.001	0.003	0.001	0.001	0.000	0.002	0.001	0.001	0.000	0.003	0.003	0.001
Al	1.596	1.626	1.616	1.597	1.578	1.601	1.610	1.608	1.593	1.619	1.621	1.649	1.583	1.609	1.606
Fe ₃	0.025	0.023	0.026	0.025	0.025	0.021	0.020	0.029	0.026	0.007	0.005	0.025	0.022	0.016	0.021
Fe ₂	0.003	0.000	0.000	0.000	0.000	0.000	0.000	0.000	0.000	0.015	0.020	0.000	0.000	0.003	0.000
Ni	0.003	0.000	0.002	0.000	0.002	0.002	0.000	0.001	0.000	0.001	0.001	0.000	0.000	0.000	0.002
Mg	0.000	0.000	0.000	0.000	0.000	0.000	0.000	0.000	0.000	0.000	0.000	0.000	0.000	0.000	0.000
Ca	0.023	0.022	0.021	0.021	0.025	0.021	0.024	0.030	0.067	0.020	0.028	0.025	0.027	0.014	0.019
Na	0.652	0.632	0.652	0.633	0.590	0.605	0.617	0.642	0.630	0.654	0.658	0.679	0.618	0.618	0.614
K	0.334	0.352	0.333	0.354	0.381	0.375	0.358	0.344	0.339	0.327	0.313	0.308	0.371	0.361	0.371
XAn	0.658	0.638	0.658	0.637	0.602	0.613	0.628	0.646	0.646	0.663	0.673	0.683	0.621	0.627	0.619

Table 4-3
Suite 5

Melt P (Gpa)	AH6 0.7 OM20- 43P	AH6 0.7 OM20- 24P	AH6 0.7 OM20- 23P	AH6 0.7 OM20- 26P	AH6 0.7 OM20- 27M	AH6 0.7 OM20- 29PC	AH6 0.7 OM20- 29PR	AH6 0.7 OM20- 28PC	AH6 0.7 OM20- 28PR	AH6 0.7 OM20- 32P2	AH6 0.7 OM20- 32P1	AH6 0.7 OM20- 30PR	AH6 0.7 OM20- 30PC	AH6 0.7 OM20- 30PC1	AH6 0.7 OM21- 06PR
D (mm)	0.85	0.86	0.87	0.92	0.93	1.11	1.12	1.12	1.13	1.17	1.17	1.19	1.19	1.21	0.05
SiO ₂	52.69	53.11	53.32	51.83	52.99	53.90	53.71	53.74	53.48	55.44	54.53	53.93	54.46	54.75	54.71
TiO ₂	0.05	0.15	0.11	0.00	0.04	0.08	0.12	0.09	0.09	0.08	0.06	0.11	0.03	0.02	0.08
Al ₂ O ₃	30.52	28.84	29.18	28.94	28.50	28.32	27.95	28.75	28.30	27.97	27.98	27.76	27.90	27.55	27.36
Fe ₂ O ₃	0.38	0.76	0.00	0.65	0.59	0.00	0.00	0.00	0.18	0.00	0.00	0.00	0.00	0.00	0.49
FeO	0.33	0.00	0.56	0.00	0.00	0.33	0.32	0.25	0.13	0.31	0.28	0.50	0.51	0.27	0.23
NiO	0.01	0.00	0.05	0.00	0.00	0.03	0.05	0.06	0.00	0.00	0.00	0.00	0.00	0.00	0.00
MgO	0.32	0.28	0.22	0.85	0.49	0.16	0.14	0.10	0.18	0.17	0.15	0.25	0.23	0.13	0.39
CaO	13.12	12.02	12.06	12.99	12.01	11.78	11.86	11.99	11.82	9.81	11.28	11.77	11.90	11.63	10.87
Na ₂ O	3.96	4.64	4.40	4.06	4.45	4.72	4.62	4.63	4.73	5.19	5.07	4.68	4.41	4.76	5.10
K ₂ O	0.09	0.17	0.17	0.09	0.11	0.13	0.13	0.10	0.11	0.17	0.13	0.13	0.15	0.13	0.23
Total	101.47	99.97	100.07	99.41	99.18	99.45	98.90	99.71	99.02	99.14	99.48	99.13	99.59	99.24	99.46
Si	2.360	2.408	2.416	2.364	2.421	2.454	2.460	2.442	2.444	2.526	2.476	2.464	2.483	2.499	2.487
Ti	0.002	0.005	0.004	0.000	0.001	0.003	0.004	0.003	0.003	0.003	0.002	0.004	0.001	0.001	0.003
Al	1.611	1.541	1.558	1.556	1.535	1.520	1.509	1.539	1.525	1.502	1.497	1.495	1.499	1.482	1.466
Fe ₃	0.013	0.026	0.000	0.022	0.020	0.000	0.000	0.000	0.006	0.000	0.000	0.000	0.000	0.000	0.017
Fe ₂	0.012	0.000	0.021	0.000	0.000	0.013	0.012	0.009	0.005	0.012	0.011	0.019	0.019	0.010	0.009
Ni	0.001	0.000	0.002	0.000	0.000	0.001	0.002	0.002	0.000	0.000	0.000	0.000	0.000	0.000	0.000
Mg	0.000	0.000	0.000	0.000	0.000	0.000	0.000	0.000	0.000	0.000	0.000	0.000	0.000	0.000	0.026
Ca	0.021	0.019	0.015	0.058	0.033	0.011	0.010	0.007	0.012	0.012	0.010	0.017	0.016	0.009	0.530
Na	0.630	0.584	0.585	0.635	0.588	0.575	0.582	0.584	0.579	0.479	0.549	0.576	0.581	0.569	0.450
K	0.344	0.408	0.387	0.359	0.394	0.417	0.410	0.408	0.419	0.458	0.446	0.415	0.390	0.421	0.013
XAn	0.643	0.583	0.596	0.635	0.595	0.575	0.582	0.585	0.576	0.506	0.547	0.577	0.593	0.570	0.534

Table 4-3
Suite 6

Melt P (Gpa)	AH6 0.7 OM21- 05PR	AH6 0.7 OM21- 08PR	AH6 0.7 OM21- 10PR	AH6 0.7 OM21- 11PR	AH6 0.7 OM21- 12OPC	AH6 0.7 OM21- 13PR	AH6 0.7 OM21- 15PR	AH6 0.7 OM21- 16PR	AH6 0.7 OM21- 19PR	AH6 0.7 OM21- 23PR	AH6 0.7 OM21- 22PR	AH6 0.7 OM21- 24PR	AH3 0.7 OM22- 26P	AH3 0.7 OM22- 30P2	AH3 0.7 OM22- 30P
D (mm)	0.05	0.25	0.30	0.30	0.33	0.42	0.47	0.61	0.71	0.86	0.87	0.89	0.06	0.09	0.09
SiO ₂	52.49	53.41	53.15	52.96	52.73	51.97	51.87	54.08	52.64	52.49	53.15	52.88	54.45	54.15	54.52
TiO ₂	0.11	0.07	0.07	0.07	0.08	0.08	0.09	0.12	0.07	0.07	0.04	0.11	0.14	0.17	0.14
Al ₂ O ₃	27.99	28.58	28.02	27.65	28.34	29.03	28.52	28.61	28.46	28.76	28.65	28.86	26.89	27.48	26.97
Fe ₂ O ₃	0.95	0.41	0.30	0.01	0.78	0.83	0.29	0.38	0.77	0.68	0.00	0.23	0.93	0.73	0.77
FeO	0.00	0.39	0.41	0.86	0.00	0.00	0.42	0.30	0.00	0.00	0.64	0.45	0.00	0.00	0.00
NiO	0.03	0.00	0.02	0.00	0.00	0.03	0.02	0.06	0.03	0.04	0.00	0.00	0.04	0.03	0.00
MgO	0.66	0.22	0.25	0.32	0.34	0.41	0.41	0.21	0.37	0.24	0.32	0.30	0.85	0.21	0.49
CaO	12.88	12.38	12.63	12.99	12.84	13.31	13.74	12.16	12.89	12.92	12.93	12.99	11.18	11.02	10.83
Na ₂ O	4.08	4.38	4.29	4.05	4.42	3.93	3.65	4.59	4.17	4.23	4.06	4.07	5.12	5.11	5.30
K ₂ O	0.16	0.19	0.16	0.15	0.19	0.14	0.13	0.19	0.18	0.17	0.13	0.17	0.23	0.22	0.25
Total	99.34	100.07	99.35	99.13	99.74	99.75	99.14	100.79	99.57	99.63	99.95	100.08	99.84	99.12	99.28
Si	2.404	2.424	2.432	2.433	2.400	2.371	2.386	2.435	2.404	2.394	2.419	2.403	2.464	2.471	2.480
Ti	0.004	0.003	0.003	0.002	0.003	0.003	0.003	0.004	0.002	0.003	0.001	0.004	0.005	0.006	0.005
Al	1.511	1.529	1.511	1.497	1.520	1.561	1.546	1.518	1.532	1.546	1.537	1.546	1.434	1.478	1.446
Fe ₃	0.033	0.014	0.010	0.000	0.027	0.028	0.010	0.013	0.026	0.023	0.000	0.008	0.032	0.025	0.026
Fe ₂	0.000	0.015	0.016	0.033	0.000	0.000	0.016	0.011	0.000	0.000	0.025	0.017	0.000	0.000	0.000
Ni	0.001	0.000	0.001	0.000	0.000	0.001	0.001	0.002	0.001	0.002	0.000	0.000	0.001	0.001	0.000
Mg	0.045	0.015	0.017	0.022	0.023	0.028	0.028	0.014	0.025	0.017	0.022	0.020	0.057	0.014	0.034
Ca	0.632	0.602	0.619	0.639	0.626	0.651	0.677	0.587	0.631	0.631	0.630	0.633	0.542	0.539	0.528
Na	0.362	0.386	0.381	0.361	0.390	0.348	0.326	0.401	0.369	0.374	0.358	0.359	0.450	0.452	0.468
K	0.009	0.011	0.009	0.009	0.011	0.008	0.008	0.011	0.010	0.010	0.007	0.010	0.013	0.013	0.015
XAn	0.630	0.603	0.614	0.634	0.610	0.646	0.670	0.588	0.624	0.622	0.633	0.632	0.539	0.537	0.522

Table 4-3
Suite 7

Melt P (Gpa)	AH3 0.7 OM22- 27P	AH3 0.7 OM22- 29PR	AH3 0.7 OM22- 29PC	AH3 0.7 OM22- 32P	AH3 0.7 OM22- 31PR	AH3 0.7 OM22- 31PC	AH3 0.7 OM22- 33P	AH3 0.7 OM22- 36PC	AH3 0.7 OM22- 36PR	AH3 0.7 OM22- 37P2	AH3 0.7 OM22- 38P	AH3 0.7 OM22- 39P	AH3 0.7 OM22- 40P	AH3 0.7 OM22- 41P
D (mm)	0.10	0.11	0.11	0.27	0.27	0.27	0.40	0.60	0.61	0.91	0.95	1.07	1.09	1.15
SiO ₂	56.91	54.41	54.84	54.13	53.14	53.43	54.50	53.45	53.71	52.72	53.47	55.71	56.28	54.21
TiO ₂	0.24	0.12	0.09	0.13	0.05	0.09	0.07	0.05	0.04	0.15	0.07	0.16	0.18	0.16
Al ₂ O ₃	25.87	27.32	27.40	27.28	28.00	28.01	27.22	28.10	27.93	29.43	29.34	28.00	27.80	29.04
Fe ₂ O ₃	0.66	0.61	0.60	1.00	0.72	0.82	0.78	0.02	0.64	0.78	0.00	0.44	0.00	0.00
FeO	0.00	0.10	0.10	0.00	0.00	0.00	0.00	0.66	0.00	0.00	0.73	0.24	0.59	0.28
NiO	0.01	0.00	0.01	0.00	0.00	0.04	0.02	0.04	0.00	0.06	0.13	0.03	0.00	0.00
MgO	0.21	0.23	0.32	0.42	0.29	0.25	0.31	0.25	0.29	0.53	0.45	0.66	0.29	0.20
CaO	9.08	10.94	10.70	11.33	12.18	12.19	11.17	11.80	11.46	11.97	12.12	10.08	9.84	11.31
Na ₂ O	6.18	5.13	5.23	4.98	4.60	4.55	5.08	4.53	4.85	4.35	4.23	5.32	5.30	4.74
K ₂ O	0.38	0.22	0.22	0.21	0.17	0.18	0.24	0.19	0.19	0.18	0.19	0.32	0.32	0.16
Total	99.55	99.08	99.51	99.48	99.15	99.56	99.39	99.09	99.11	100.17	100.73	100.96	100.60	100.09
Si	2.572	2.484	2.490	2.463	2.429	2.436	2.481	2.446	2.452	2.387	2.410	2.490	2.528	2.451
Ti	0.008	0.004	0.003	0.004	0.002	0.003	0.003	0.002	0.001	0.005	0.003	0.005	0.006	0.006
Al	1.378	1.470	1.466	1.463	1.509	1.505	1.460	1.516	1.503	1.570	1.559	1.475	1.472	1.548
Fe ₃	0.023	0.021	0.020	0.034	0.025	0.028	0.027	0.001	0.022	0.027	0.000	0.015	0.000	0.000
Fe ₂	0.000	0.004	0.004	0.000	0.000	0.000	0.000	0.025	0.000	0.000	0.028	0.009	0.022	0.011
Ni	0.000	0.000	0.000	0.000	0.000	0.001	0.001	0.002	0.000	0.002	0.005	0.001	0.000	0.000
Mg	0.014	0.016	0.022	0.029	0.020	0.017	0.021	0.017	0.020	0.036	0.030	0.044	0.019	0.013
Ca	0.440	0.535	0.521	0.552	0.597	0.596	0.545	0.579	0.560	0.581	0.585	0.483	0.474	0.548
Na	0.542	0.454	0.460	0.439	0.407	0.402	0.448	0.402	0.429	0.382	0.370	0.461	0.462	0.416
K	0.022	0.013	0.013	0.012	0.010	0.011	0.014	0.011	0.011	0.010	0.011	0.018	0.018	0.009
XAn	0.438	0.534	0.524	0.550	0.588	0.591	0.541	0.584	0.560	0.597	0.606	0.502	0.497	0.563

Table 4-4

Representative major element compositions of clinopyroxene from ol-rich layer from step-cooled experiments

Starting melt P (Gpa)	AH6 0.5 OM02-39	AH6 0.5 OM02-90	AH6 0.5 OM02-23	AH6 0.5 OM02-112	AH6 0.5 OM02-26	AH6 0.5 OM02-118	AH6 0.5 OM02-55	AH6 0.5 OM02-96	AH6 0.5 OM02-49	AH6 0.5 OM02-50	AH6 0.5 OM02-10	AH6 0.5 OM02-117	AH6 0.5 OM02-82	HDRBC 0.5 OM03-92	HDRBC 0.5 OM03b-21
D (mm)	0.34	0.76	0.74	0.10	0.75	0.16	0.07	0.45	0.25	0.22	1.13	0.15	0.95	0.10	0.17
SiO ₂	52.42	51.59	51.42	51.45	50.87	51.12	51.15	50.50	50.36	50.73	49.88	49.73	49.89	50.23	52.17
TiO ₂	0.58	0.95	0.95	1.04	1.11	1.10	1.07	1.02	1.18	1.23	0.74	1.28	1.23	1.31	0.86
Al ₂ O ₃	4.77	5.42	5.50	5.69	6.03	6.16	6.27	6.88	7.24	7.31	7.45	7.50	7.72	7.38	4.87
Cr ₂ O ₃	0.23	0.25	0.29	0.35	0.21	0.34	0.33	0.22	0.31	0.26	0.13	0.19	0.29	0.11	0.09
FeO	4.21	3.56	3.54	3.80	3.96	3.89	4.09	3.52	3.87	4.35	3.95	4.12	3.72	4.44	4.20
MnO	0.08	0.11	0.10	0.10	0.15	0.06	0.13	0.07	0.10	0.13	0.11	0.09	0.09	0.13	0.13
NiO	0.05	0.11	0.01	0.00	0.00	0.05	0.01	0.00	0.05	0.06	0.08	0.02	0.02	0.05	0.01
MgO	19.02	17.31	17.38	17.07	17.39	16.71	16.68	16.03	16.45	16.14	16.21	16.03	15.59	17.15	18.54
CaO	18.23	19.87	19.64	20.18	19.65	20.26	20.35	21.03	19.86	19.73	20.02	20.16	20.41	18.91	18.48
Na ₂ O	0.19	0.35	0.38	0.34	0.39	0.31	0.42	0.37	0.33	0.40	0.35	0.36	0.43	0.28	0.34
K ₂ O	0.01	0.02	0.00	0.00	0.00	0.00	0.00	0.01	0.00	0.00	0.01	0.02	0.00	0.02	0.00
Total	99.79	99.54	99.21	100.02	99.75	100.00	100.51	99.65	99.75	100.33	98.94	99.50	99.39	100.00	99.68
Si	1.89	1.88	1.87	1.86	1.85	1.85	1.85	1.84	1.83	1.83	1.83	1.82	1.82	1.82	1.89
Ti	0.02	0.03	0.03	0.03	0.03	0.03	0.03	0.03	0.03	0.03	0.02	0.04	0.03	0.04	0.02
Al	0.20	0.23	0.24	0.24	0.26	0.26	0.27	0.30	0.31	0.31	0.32	0.32	0.33	0.32	0.21
Cr	0.01	0.01	0.01	0.01	0.01	0.01	0.01	0.01	0.01	0.01	0.00	0.01	0.01	0.00	0.00
Fe ₂	0.13	0.11	0.11	0.12	0.12	0.12	0.12	0.11	0.12	0.13	0.12	0.13	0.11	0.13	0.13
Mn	0.00	0.00	0.00	0.00	0.00	0.00	0.00	0.00	0.00	0.00	0.00	0.00	0.00	0.00	0.00
Ni	0.00	0.00	0.00	0.00	0.00	0.00	0.00	0.00	0.00	0.00	0.00	0.00	0.00	0.00	0.00
Mg	1.02	0.94	0.94	0.92	0.94	0.90	0.90	0.87	0.89	0.87	0.89	0.87	0.85	0.93	1.00
Ca	0.71	0.77	0.77	0.78	0.77	0.79	0.79	0.82	0.77	0.76	0.79	0.79	0.80	0.73	0.72
Na	0.01	0.02	0.03	0.02	0.03	0.02	0.03	0.03	0.02	0.03	0.03	0.03	0.02	0.02	0.02
K.	0.00	0.00	0.00	0.00	0.00	0.00	0.00	0.00	0.00	0.00	0.00	0.00	0.00	0.00	0.00
XMg	0.89	0.90	0.90	0.89	0.89	0.88	0.88	0.89	0.88	0.87	0.88	0.87	0.88	0.87	0.89

D: Distance is calculated from the x,y coordinates of an olivine from the interface zone (picked up as a 0 mm reference olivine for each sample) and the x,y coordinates of the analysis

Cations and XMg are calculated with the Program NORM (version 2013) by Ulmer and Poli

Table 4-4
Suite 1

Melt P (Gpa)	HDRBC 0.5 OM03-85	HDRBC 0.5 OM03-103	HDRBC 0.5 OM03-70	HDRBC 0.5 OM03b-19	HDRBC 0.5 OM03b-68	HDRBC 0.5 OM03b-17	HDRBC 0.5 OM03-55	HDRBC 0.5 OM03-64	HDRBC 0.5 OM03-40	HDRBC 0.5 OM03b-15	HDRBC 0.5 OM03b-16	HDRBC 0.5 OM03-36	HDRBC 0.5 OM03b-9	HDRBC 0.5 OM03-131	HDRBC 0.5 OM03-18
Analysis n°															
D (mm)	0.18	0.19	0.22	0.32	0.39	0.73	0.83	0.89	0.90	0.99	1.06	1.06	1.17	1.18	1.20
SiO ₂	53.99	51.60	53.78	50.54	50.55	51.65	51.19	50.99	52.75	52.52	53.83	51.21	52.61	49.92	51.88
TiO ₂	0.56	1.05	1.15	1.13	1.28	0.83	0.95	0.97	0.83	0.95	0.56	0.97	0.88	1.15	0.96
Al ₂ O ₃	2.36	5.58	3.26	7.74	7.47	5.97	5.93	7.13	4.38	5.30	3.28	6.41	4.64	7.68	5.60
Cr ₂ O ₃	0.07	0.13	0.08	0.05	0.03	0.03	0.11	0.10	0.13	0.01	0.06	0.09	0.10	0.03	0.02
FeO	4.99	4.46	5.43	4.15	4.26	3.94	3.83	3.47	3.82	5.03	5.90	3.99	5.43	3.84	5.01
MnO	0.19	0.14	0.14	0.14	0.12	0.16	0.13	0.14	0.14	0.20	0.16	0.12	0.25	0.09	0.21
NiO	0.00	0.06	0.02	0.00	0.05	0.01	0.02	0.00	0.00	0.04	0.00	0.00	0.08	0.04	0.02
MgO	22.60	18.81	22.16	16.32	17.24	18.37	18.23	16.85	19.09	20.09	22.42	18.08	21.30	17.33	19.10
CaO	14.48	17.90	13.70	19.41	18.36	18.66	18.93	19.88	17.86	15.45	13.54	18.17	14.62	18.80	16.94
Na ₂ O	0.21	0.30	0.22	0.33	0.33	0.30	0.28	0.32	0.31	0.32	0.15	0.33	0.24	0.35	0.27
K ₂ O	0.01	0.00	0.02	0.00	0.00	0.01	0.01	0.02	0.01	0.03	0.00	0.01	0.02	0.02	0.00
Total	99.47	100.02	99.95	99.81	99.69	99.93	99.61	99.87	99.32	99.94	99.90	99.38	100.17	99.24	100.01
Si	1.94	1.86	1.92	1.83	1.83	1.86	1.86	1.84	1.91	1.89	1.93	1.86	1.89	1.82	1.87
Ti	0.02	0.03	0.03	0.03	0.03	0.02	0.03	0.03	0.02	0.03	0.02	0.03	0.02	0.03	0.03
Al	0.10	0.24	0.14	0.33	0.32	0.25	0.25	0.30	0.19	0.22	0.14	0.27	0.20	0.33	0.24
Cr	0.00	0.00	0.00	0.00	0.00	0.00	0.00	0.00	0.00	0.00	0.00	0.00	0.00	0.00	0.00
Fe ₂	0.15	0.13	0.16	0.13	0.13	0.12	0.12	0.10	0.12	0.15	0.18	0.12	0.16	0.12	0.15
Mn	0.01	0.00	0.00	0.00	0.00	0.00	0.00	0.00	0.00	0.01	0.00	0.00	0.01	0.00	0.01
Ni	0.00	0.00	0.00	0.00	0.00	0.00	0.00	0.00	0.00	0.00	0.00	0.00	0.00	0.00	0.00
Mg	1.21	1.01	1.18	0.88	0.93	0.99	0.99	0.91	1.03	1.08	1.20	0.98	1.14	0.94	1.03
Ca	0.56	0.69	0.53	0.75	0.71	0.72	0.74	0.77	0.69	0.59	0.52	0.71	0.56	0.73	0.65
Na	0.01	0.02	0.02	0.02	0.02	0.02	0.02	0.02	0.02	0.02	0.01	0.02	0.02	0.02	0.02
K.	0.00	0.00	0.00	0.00	0.00	0.00	0.00	0.00	0.00	0.00	0.00	0.00	0.00	0.00	0.00
XMg	0.89	0.88	0.88	0.88	0.88	0.89	0.90	0.90	0.90	0.88	0.87	0.89	0.88	0.89	0.87

Table 4-4
Suite 2

Melt P (Gpa)	HDRBC 0.5 OM03-6	HDRBC 0.5 OM03b-	HDRBC 0.5 OM03b-	HDRBC 0.5 OM03-	AH6 0.7 OM20-										
Analysis n°		11	4	13	05C1	05C2	11C	13C	14C	17C	16C	18C	43C	23C	29CR
D (mm)	1.25	1.27	1.28	1.37	0.30	0.31	1.27	1.56	1.57	1.81	1.86	2.02	2.12	2.18	2.82
SiO ₂	52.93	53.77	51.78	51.28	49.59	48.41	49.90	49.01	49.72	49.85	50.65	51.25	50.89	51.12	50.79
TiO ₂	1.20	0.67	0.59	1.11	1.37	2.17	1.71	1.71	1.63	1.20	0.93	1.18	1.04	1.26	0.95
Al ₂ O ₃	4.94	3.66	5.28	7.01	7.60	8.83	7.76	8.76	8.22	7.92	7.61	6.47	7.91	7.12	5.51
Cr ₂ O ₃	0.07	0.05	0.05	0.04	0.11	0.06	0.01	0.05	0.08	0.06	0.09	0.07	0.05	0.17	0.02
FeO	4.15	6.46	5.59	4.64	5.77	5.06	4.88	4.54	4.01	4.01	4.16	3.61	4.34	4.02	11.09
MnO	0.12	0.22	0.15	0.20	0.18	0.19	0.19	0.10	0.04	0.19	0.13	0.10	0.03	0.12	0.27
NiO	0.03	0.01	0.00	0.00	0.05	0.04	0.07	0.06	0.12	0.12	0.18	0.02	0.06	0.00	0.00
MgO	19.50	21.21	18.26	17.61	15.40	13.79	16.58	15.54	15.88	18.30	17.16	17.54	17.18	17.77	18.54
CaO	17.85	13.87	16.63	18.25	19.35	20.41	18.77	19.87	19.94	17.92	18.44	18.95	18.18	18.35	12.40
Na ₂ O	0.27	0.23	0.27	0.28	0.69	0.74	0.63	0.48	0.51	0.58	0.43	0.48	0.43	0.48	0.35
K ₂ O	0.00	0.00	0.00	0.00	0.00	0.01	0.00	0.02	0.01	0.01	0.00	0.00	0.00	0.00	0.00
Total	101.07	100.16	98.60	100.42	100.11	99.71	100.50	100.14	100.16	100.16	99.78	99.67	100.11	100.41	99.92
Si	1.88	1.93	1.90	1.84	1.81	1.78	1.81	1.78	1.80	1.80	1.83	1.85	1.83	1.84	1.86
Ti	0.03	0.02	0.02	0.03	0.04	0.06	0.05	0.05	0.04	0.03	0.03	0.03	0.03	0.03	0.03
Al	0.21	0.15	0.23	0.30	0.33	0.38	0.33	0.38	0.35	0.34	0.32	0.28	0.34	0.30	0.24
Cr	0.00	0.00	0.00	0.00	0.00	0.00	0.00	0.00	0.00	0.00	0.00	0.00	0.00	0.00	0.00
Fe ₂	0.12	0.19	0.17	0.14	0.18	0.16	0.15	0.14	0.12	0.12	0.13	0.11	0.13	0.12	0.34
Mn	0.00	0.01	0.00	0.01	0.01	0.01	0.01	0.00	0.00	0.01	0.00	0.00	0.00	0.00	0.01
Ni	0.00	0.00	0.00	0.00	0.00	0.00	0.00	0.00	0.00	0.00	0.01	0.00	0.00	0.00	0.00
Mg	1.03	1.13	1.00	0.94	0.84	0.76	0.89	0.84	0.86	0.98	0.93	0.95	0.92	0.95	1.01
Ca	0.68	0.53	0.65	0.70	0.76	0.80	0.73	0.77	0.77	0.69	0.72	0.73	0.70	0.71	0.49
Na	0.02	0.02	0.02	0.02	0.05	0.05	0.04	0.03	0.04	0.04	0.03	0.03	0.03	0.03	0.02
K.	0.00	0.00	0.00	0.00	0.00	0.00	0.00	0.00	0.00	0.00	0.00	0.00	0.00	0.00	0.00
XMg	0.89	0.85	0.85	0.87	0.83	0.83	0.86	0.86	0.88	0.89	0.88	0.90	0.88	0.89	0.75

Table 4-4
Suite 3

Melt P (Gpa)	AH6 0.7 cpx56	AH6 0.7 cpx57	AH6 0.7 cpx52	AH6 0.7 cpx53	AH6 0.7 cpx54	AH6 0.7 cpx183	AH6 0.7 cpx184	AH6 0.7 cpx185	AH6 0.7 cpx186	AH6 0.7 cpx301	AH6 0.7 cpx302	AH6 0.7 cpx303	AH6 0.7 cpx305	AH6 0.7 cpx311	AH6 0.7 cpx312
<i>Analysis n°</i>															
D (mm)	48.66	48.34	48.79	48.41	48.25	49.22	50.99	49.18	50.24	48.14	48.00	48.39	49.46	48.37	49.26
SiO ₂	1.92	1.46	1.41	1.85	1.47	1.39	0.99	1.71	1.47	1.62	1.62	1.89	1.84	1.61	1.38
TiO ₂	9.42	10.32	10.03	9.49	9.02	9.02	6.89	8.69	7.35	9.80	10.69	9.38	8.46	9.29	8.89
Al ₂ O ₃	0.07	0.08	0.10	0.10	0.13	0.14	0.23	0.16	0.12	0.02	0.04	0.06	0.10	0.09	0.10
Cr ₂ O ₃	5.03	4.95	5.96	5.03	5.59	4.02	3.61	3.80	3.80	4.15	4.43	4.34	5.12	4.35	4.03
FeO	0.15	0.14	0.19	0.13	0.12	0.11	0.15	0.17	0.12	0.10	0.12	0.16	0.12	0.05	0.12
MnO	0.03	0.03	0.04	0.00	0.02	0.07	0.10	0.00	0.02	0.13	0.09	0.05	0.14	0.11	0.07
NiO	14.78	14.06	14.61	14.16	15.93	16.37	17.24	15.75	16.63	13.89	15.20	14.76	16.24	15.86	15.14
MgO	19.65	19.74	18.58	19.95	18.99	18.98	19.79	20.13	19.61	21.26	19.43	20.00	18.16	19.72	20.56
CaO	0.70	0.64	0.55	0.67	0.62	0.39	0.52	0.52	0.48	0.57	0.46	0.53	0.56	0.56	0.56
Na ₂ O	0.00	0.01	0.00	0.02	0.00	0.00	0.00	0.00	0.00	0.01	0.00	0.01	0.00	0.00	0.01
K ₂ O	0.00	0.00	0.00	0.00	0.00	0.00	0.00	0.00	0.00	0.00	0.00	0.00	0.00	0.00	0.00
Total	100.41	99.77	100.26	99.81	100.14	99.71	100.51	100.11	99.84	99.69	100.08	99.57	100.20	100.01	100.12
Si	1.77	1.77	1.77	1.77	1.76	1.79	1.84	1.78	1.82	1.76	1.74	1.77	1.79	1.76	1.79
Ti	0.05	0.04	0.04	0.05	0.04	0.04	0.03	0.05	0.04	0.04	0.04	0.05	0.05	0.04	0.04
Al	0.40	0.44	0.43	0.41	0.39	0.39	0.29	0.37	0.31	0.42	0.46	0.40	0.36	0.40	0.38
Cr	0.00	0.00	0.00	0.00	0.00	0.00	0.01	0.00	0.00	0.00	0.00	0.00	0.00	0.00	0.00
Fe ₂	0.15	0.15	0.18	0.15	0.17	0.12	0.11	0.12	0.12	0.13	0.13	0.13	0.16	0.13	0.12
Mn	0.00	0.00	0.01	0.00	0.00	0.00	0.00	0.01	0.00	0.00	0.00	0.01	0.00	0.00	0.00
Ni	0.00	0.00	0.00	0.00	0.00	0.00	0.00	0.00	0.00	0.00	0.00	0.00	0.00	0.00	0.00
Mg	0.80	0.77	0.79	0.77	0.87	0.89	0.93	0.85	0.90	0.76	0.82	0.80	0.88	0.86	0.82
Ca	0.77	0.77	0.72	0.78	0.74	0.74	0.76	0.78	0.76	0.83	0.76	0.78	0.71	0.77	0.80
Na	0.05	0.05	0.04	0.05	0.04	0.03	0.04	0.04	0.03	0.04	0.03	0.04	0.04	0.04	0.04
K.	0.00	0.00	0.00	0.00	0.00	0.00	0.00	0.00	0.00	0.00	0.00	0.00	0.00	0.00	0.00
XMg	0.84	0.84	0.81	0.83	0.84	0.88	0.90	0.88	0.89	0.86	0.86	0.85	0.87	0.87	0.87

Table 4-4
Suite 4

Melt P (Gpa)	AH6 0.7 OM21- 10CR	AH6 0.7 OM21- 11CR	AH6 0.7 OM21- 14CR	AH6 0.7 OM21- 16CR	AH6 0.7 OM21- 21CR	AH6 0.7 OM21- 24CR	AH3 0.7 OM22- 29p1	AH3 0.7 OM22- 29c	AH3 0.7 OM22- 32c	AH3 0.7 OM22- 33c	AH3 0.7 OM22- 36c	AH3 0.7 OM22- 38C	AH3 0.7 OM22- 39C	AH3 0.7 OM22- 41C
Analysis n°														
D (mm)	0.74	0.75	1.06	1.50	2.06	2.22	0.25	0.28	0.66	0.99	1.51	2.35	2.68	2.88
SiO ₂	49.55	49.18	49.26	49.84	50.14	53.97	48.88	49.16	48.83	49.83	48.10	50.08	50.64	51.65
TiO ₂	1.96	2.02	1.63	1.74	1.53	0.74	2.31	2.25	3.58	2.90	2.69	2.11	3.53	1.71
Al ₂ O ₃	8.02	8.68	9.21	7.91	7.81	3.57	8.04	6.24	6.76	6.63	7.38	7.88	7.04	5.55
Cr ₂ O ₃	0.04	0.07	0.09	0.17	0.10	0.19	0.08	0.05	0.05	0.04	0.04	0.06	0.18	0.07
FeO	4.73	4.82	4.92	4.33	4.62	4.39	5.01	4.38	4.70	5.27	4.26	4.42	4.02	4.53
MnO	0.14	0.13	0.09	0.09	0.12	0.14	0.14	0.15	0.14	0.10	0.07	0.11	0.11	0.18
NiO	0.05	0.07	0.00	0.12	0.00	0.00	0.09	0.09	0.11	0.10	0.11	0.06	0.02	0.00
MgO	14.76	14.45	15.23	15.71	16.37	20.22	16.14	18.47	15.18	17.64	17.45	17.23	17.23	19.65
CaO	20.83	20.57	19.57	19.72	18.81	16.52	18.30	17.59	19.95	17.46	18.82	17.86	17.40	15.86
Na ₂ O	0.61	0.59	0.47	0.52	0.45	0.52	0.63	0.74	0.75	0.62	0.58	0.48	1.10	0.44
K ₂ O	0.03	0.01	0.00	0.00	0.00	0.00	0.01	0.00	0.00	0.00	0.00	0.00	0.01	0.00
Total	100.72	100.59	100.47	100.16	99.95	100.26	99.63	99.13	100.05	100.60	99.50	100.29	101.28	99.64
Si	1.80	1.79	1.78	1.81	1.82	1.93	1.79	1.80	1.79	1.80	1.76	1.81	1.81	1.86
Ti	0.05	0.06	0.04	0.05	0.04	0.02	0.06	0.06	0.10	0.08	0.07	0.06	0.09	0.05
Al	0.34	0.37	0.39	0.34	0.33	0.15	0.35	0.27	0.29	0.28	0.32	0.33	0.30	0.24
Cr	0.00	0.00	0.00	0.00	0.00	0.01	0.00	0.00	0.00	0.00	0.00	0.00	0.01	0.00
Fe ₂	0.14	0.15	0.15	0.13	0.14	0.13	0.15	0.13	0.14	0.16	0.13	0.13	0.12	0.14
Mn	0.00	0.00	0.00	0.00	0.00	0.00	0.00	0.00	0.00	0.00	0.00	0.00	0.00	0.01
Ni	0.00	0.00	0.00	0.00	0.00	0.00	0.00	0.00	0.00	0.00	0.00	0.00	0.00	0.00
Mg	0.80	0.78	0.82	0.85	0.88	1.08	0.88	1.01	0.83	0.95	0.95	0.93	0.92	1.06
Ca	0.81	0.80	0.76	0.77	0.73	0.63	0.72	0.69	0.78	0.68	0.74	0.69	0.67	0.61
Na	0.04	0.04	0.03	0.04	0.03	0.04	0.04	0.05	0.05	0.04	0.04	0.03	0.08	0.03
K.	0.00	0.00	0.00	0.00	0.00	0.00	0.00	0.00	0.00	0.00	0.00	0.00	0.00	0.00
XMg	0.85	0.84	0.85	0.87	0.86	0.89	0.85	0.88	0.85	0.86	0.88	0.87	0.88	0.89

A3. References

- Barnes, S.J. (1986) The effect of trapped liquid crystallization on cumulus mineral compositions in layered intrusions. *Contrib Mineral and Petrol*, 93:524. doi:10.1007/BF00371722
- Bedard J.H. (1994) A procedure for calculating the equilibrium distribution of trace elements among the minerals of cumulate rocks, and the concentration of trace elements in coexisting liquids. *Chem Geol* 118:143–153
- Bernstein S. (2006) In situ fractional crystallization of a mafic pluton: microanalytical study of a Paleogene gabbronorite plug in East Greenland. *Lithos* 92:222–237
- Borghini G., Rampone E. (2007) Postcumulus processes in oceanic-type olivine-rich cumulates: the role of trapped melt crystallization versus melt/rock interaction. *Contrib Mineral Petrol* 154:619–633
- Borghini G., Fumagalli P., Rampone E. (2010) The Stability of Plagioclase in the Upper Mantle: Subsolidus Experiments on Fertile and Depleted Lherzolite. *J Petrol*, 51:229–254. doi:10.1093/petrology/egp079
- Boudier F. (1991) Olivine xenocrysts in picritic magmas. *Contrib Mineral Petrol*, 109:114–123.
- Bowen N. L., Schairer J. F. (1932) The system FeO-SiO₂. *American Journal of Science*, 24:141
- Cawthorn R.G. (1996) Models for incompatible trace element abundances in cumulus minerals and their application to plagioclase and pyroxenes in the Bushveld Complex. *Contrib Mineral Petrol* 123:109–115
- Chalokwu C.I., Grant N.K. (1990) Petrology of the partrige river intrusion, Duluth complex, Minnesota: 1. Relationships between mineral compositions, density and trapped liquid abundance. *J Petrol* 31:265–293
- Charlier B., Auwera J.V., Duchesne J.C. (2005) Geochemistry of cumulates from the

Bjerkreim-Sokndal layered intrusion (S. Norway) Part II. REE and the trapped liquid fraction. *Lithos* 83:255–276

Chen Y., Zhang Y. (2008) Olivine dissolution in basaltic melt. *Geochimica et Cosmochimica Acta*, 72:4756-4777

Costa F., Chakraborty S., Dohmen R. (2003) Diffusion coupling between trace and major elements and a model for calculation of magma residence times using plagioclase. *Geochimica et Cosmochimica Acta*, 67:2189-2200. doi:10.1016/S0016-7037(02)01345-5

Coleman R. G., Opholites. Berlin: Springer-Verlag, 229pp ISBN: 978-3-642-66673-5

Cmiral M., Fitz Gerald J.D., Faul H., Green D. (1998) A close look at dihedral angles and melt geometry in olivine-basalt aggregates : A TEM study, *Contrib Mineral Petrol*, 130: 335-435.

Daines M, Kohlstedt D (1994) The transition from porous to channelized flow due to melt/rock reaction during melt migration. *Geophysical Reshearch Letters*, 21:145-148. doi: 10.1029/93GL03052

Dick H.J.B. (1977) Evidence of partial melting in the Josephine Peridotite. In: H.J.B. Dick (Ed.), *Magma Genesis*. Portland, OR: Oregon Dept. Geol. Mineral Industries, 59-62.

Dohmen R., Becker H.W. and Chakraborty (2007) Fe–Mg diffusion in olivine I: experimental determination between 700 and 1200°C as a function of composition, crystal orientation and oxygen fugacity. *Phys Chem Miner* 34:389–407

Drouin M, Godard M, Ildefonse B, Brugier O, Garrido CJ (2009) Geochemical and petrographic evidence for magmatic impregnation in the oceanic lithosphere at Atlantis Massif, Mid-Atlantic Ridge (IODP Hole U1309D, 30°N). *Chem Geol* 264:71–88

Drouin M., Ildefonse B. and Godard M. (2010) A microstructural imprint of melt impregnation in slow-spread lithosphere: olivine-rich troctolites from the Atlantis Massif (Mid-Atlantic Ridge 30°N, IODP Hole U1309D). *Geochem Geophys Geosyst* 11:Q06003. doi:10.1029/2009GC002995

Dygert N, Liang Y and Kelemen P.B. (2016) Formation of plagioclase Iherzolite and associated dunite–harzburgite–Iherzolite sequences by multiple episodes of melt percolation and melt-rock reaction: an example from the trinity ophiolite, California, USA. *Journal of Petrology*, 2016, 1–23. doi: 10.1093/petrology/egw018

Erdmann S., Scaillet B., Martel C. and Cadoux A. (2014) Characteristic Textures of Recrystallized, Peritectic, and Primary Magmatic Olivine in Experimental Samples and Natural Volcanic Rocks. *Journal of Petrology*, 55:2377-2402. doi:10.1093/petrology/egu060

Fumagalli P., Borghini G., Rampone E. and Poli S. (2017) Experimental calibration of Forsterite–Anorthite–Ca-Tschermark–Enstatite (FACE) geobarometer for mantle peridotites. *Contrib Mineral Petrol* 172: 38. doi:10.1007/s00410-017-1352-2

Gillis K.M., Meyer P.S. (2001) Metasomatism of oceanic gabbros by late stage melts and hydrothermal fluids: evidence from the rare earth element composition of amphiboles. *Geophys Geochem Geosys* 2, paper number 2000GC000087

Gillis, K., et al. (2014) Primitive layered gabbros from fast-spreading lower oceanic crust: *Nature*, 505:204–207. doi:10.1038/nature12778

Godard M., Awaji S., Hansen H.-E., Hellebrand E., Brunelli D., Johnson K.T.M., Yamasaki T., Maeda J., Abratis M., Christie D., Kato Y., Mariet C., Rosner M. (2009). Geochemistry of a long in-situ section of intrusive slow-spread lithosphere: Results from IODP Site U1309 (Atlantis Massif, 30°N Mid-Atlantic-Ridge). *Earth and Planetary Science Letters* 279, 110–122. doi:10.1016/j.epsl.2008.12.034.

Grove T., Baker M., Kinzler R. (1984) Coupled CaAl-NaSi diffusion in plagioclase feldspar: Experiments and applications to cooling rate speedometry. *Geochimica et Cosmochimica Acta*, 48 :2113-2121. doi:10.1016/0016-7037(84)90391-0

Hammouda T., Laporte D. (2000) Ultrafast mantle impregnation by carbonatite melts. *Geology*; March 2000; v. 28; no. 3; p. 283–285

Hersum T., Hilpert M., Marsh B. (2005) Permeability and melt flow in simulated and natural partially molten basaltic magmas. *Earth and Planetary Science Letters*, 237:798-814. doi: 10.1016/j.epsl.2005.07.008

Husen A., Almeev R., Holtz F. (2016) The Effect of H₂O and Pressure on Multiple Saturation and Liquid Lines of Descent in Basalt from the Shatsky Rise. *Journal of Petrology*, 57:309-344

Kelemen P.B., Joyce D.B., Webster J.D. and Holloway J.R. (1990) Reaction between ultramafic rock and fractionating basaltic magma. II. Experimental investigations of reaction between olivine tholeiite and harzburgite at 1150-1050 °C and 5 kbar. *J. Petrol.*, 31: 99-134.

Kelemen P.B., Shimizu N. and Salters V.J.M. (1995) Extraction of mid-ocean-ridge basalt from the upwelling mantle by focused flow of melt in dunite channels. *Nature*, 375: 747-753.

Kinzler R., Grove T. and Recca S. (1990) An experimental study on the effect of temperature and melt composition on the partitioning of nickel between olivine and silicate melt. *Geochimica et Cosmochimica Acta*, 54 :1255-1265. doi:10.1016/0016-7037(90)90151-A

Koepke J., Schoenborn S., Oelze M., Wittmann H., Feig S.T., Hellebrand E., Boudier F., Schoenberg R. (2009) Petrogenesis of crustal wehrellites in the Oman ophiolite: Experiments and natural rocks. *Geochemistry, Geophysics, Geosystems*, 10:1525-2027. doi: 10.1029/2009GC002488

Kohlstedt D.L., Goetze C. (1974) Low-stress high-temperature creep in olivine single crystals. *Journal of Geophysical Research*, Vol.79, No14: 2045-2051

Lambart S., Laporte D., Schiano P. (2008) Partial Melting Experiments of Three Pyroxenites at 1 and 1.5 GPa: Implications for Basalt Genesis and Host Mantle Composition. *American Geophysical Union, Fall Meeting 2008*

Laporte D., Provost A. (2000) The Grain-Scale Distribution of Silicate, Carbonate and Metallosulfide Partial Melts: a Review of Theory and Experiments. *Physics and Chemistry of Partially Molten Rocks. Petrology and Structural Geology*, 11:93-140. doi:10.1007/978-94-011-4016-4_4

Levine J.S.F. ,Mosher S. and Rahl J.M. (2016) The role of subgrain boundaries in partial melting. *Journal of Structural Geology* 89: 181-196,

doi.org/10.1016/j.jsg.2016.06.006

Liang Y. (2003) Kinetics of crystal-melt reaction in partially molten silicates: 1. Grain scale processes. *Geochemistry, Geophysics, Geosystems*, 4:1045. doi:10.1029/2002GC000375

Liang Y., Price J.D., Wark D.A., Watson E.B. (2001) Nonlinear pressure diffusion in a porous medium: approximate solutions with applications to permeability measurements using transient pulse decay method, *J. Geophys. Res.* 106 (2001) 529–535.

Lissenberg, C. J. & Dick, H. J. B. (2008). Melt–rock reaction in the lower oceanic crust and its implications for the genesis of mid-ocean ridge basalt. *Earth and Planetary Science Letters* 271, 311–25

Longhi J., Fram M., Vander Auwera J., Montieth J. (1994) Pressure effects, kinetics, and rheology of anorthositic and related magmas. *American Mineralogist*, 78:1016-1030.

Lui M., Yund R. (1992) NaSi-CaAl interdiffusion in plagioclase. *American Mineralogist*, 77 :275-283.

Mainprice D., Bachmann F., Hielscher R. and Schaeben H. (2004) Descriptive tools for the analysis of texture projects with large datasets using MTEX: strength, symmetry and components. Geological Society, London, Special Publications, doi 10.1144/SP409.8

Maitland T. and Sitzman S. (2007) Electron Backscatter Diffraction ‘EBDS) Technique and Materials Characterization Examples “Scanning Macroscopy for Nanotechnology Techniques and Applications”, Zhou W. and Wang Z.L. (Eds), 2:41-75. ISBN: 978-0-387-33325-0

Masotta M., Mollo S., Freda C., Gaeta M., Moore G. (2003) Clinopyroxene–liquid thermometers and barometers specific to alkaline differentiated magmas. *Contrib Mineral Petrol* (2013) 166:1545–1561. doi 10.1007/s00410-013-0927-9

Matzen A., Baker M., Beckett J., Wood B., Stolper E. (2017) The effect of liquid

composition on the partitioning of Ni between olivine and silicate melt. *Contrib Mineral Petrol* 172:3. doi: 10.1007/s00410-016-1319-8

McBirney A.R., (1993) Igneous Petrology, Second Edition. Appendix B, in, Jones and Bartlett Publishers, Boston, 508 p.

Meyer P.S., Dick H.J.B., Thompson G. (1989). Cumulate gabbros from the southwest Indian Ridge, 54°S–7°16'E: implications for magmatic processes at slow spreading ridge. *Contributions to Mineralogy and Petrology* 103, 44–63.

Morgan Z., Liang Y. (2003) An experimental and numerical study of the kinetics of harzburgite reactive dissolution with applications to dunite dike formation. *Earth and Planetary Science Letters*, 214:59-74 doi:10.1016/S0012-821X(03)00375-3

Morgan Z., Liang Y. (2005) An experimental study of the kinetics of lherzolite reactive dissolution with applications to melt channel formation. *Contributions to Mineralogy and Petrology*, 150:369-385

Nimis P. (1995) A clinopyroxene geobarometer for basaltic systems based on crystal-structure modeling. *Contrib Mineral Petrol*, 121:115. doi:10.1007/s004100050093

Nimis P. and Ulmer P. (1998) Clinopyroxene geobarometry of magmatic rocks Part 1: An expanded structural geobarometer for anhydrous and hydrous, basic and ultrabasic systems. *Contrib Mineral Petrol*, 133:122. doi:10.1007/s004100050442

Nimis, P. & Taylor, W (2000) Single clinopyroxene thermobarometry for garnet peridotites. Part I. Calibration and testing of a Cr-in-Cpx barometer and an enstatite-in-Cpx thermometer. *Contrib Mineral Petrol*, 139:541. doi:10.1007/s004100000156

Panjasawatwong Y., Danyushevsky L.V., Crawford A.J. et al. (1995) An experimental study of the effects of melt composition on plagioclase-melt equilibria at 5 and 10 kbar: implications for the origin of magmatic high-An plagioclase. *Contrib Mineral and Petrol*, 118: 420. doi:10.1007/s004100050024

Putirka K. (2008) Thermometers and barometers for volcanic systems. In: Putirka K, Tepley F (eds) Minerals, inclusions and volcanic processes, vol 69, Reviews in

mineralogy and geochemistry. Mineralogical Society of America, pp 61–120. doi: 10.2138/rmg.2008.69.3

Putirka K., Johnson M., Kinzler R., Walker D. (1996) Thermobarometry of mafic igneous rocks based on clinopyroxene-liquid equilibria, 0–30 kbar. *Contrib Mineral Petrol* 123:92–108

Putirka K., Ryerson F.J., Mikaelian H. (2003) New igneous thermobarometers for mafic and evolved lava compositions, based on clinopyroxene + liquid equilibria. *American Mineralogist* 88:1542–1554

Quick J.E. (1981) The origin and significance of large, tabular dunite bodies in the Trinity Peridotite, Northern California. *Contrib Mineral Petrol*, 78: 413-422.

Rampone E., Borghini G., Godard M., Idlefonse B., Crispini L., Fumagalli P. (2016) Melt/rock reaction at oceanic peridotite/gabbro transition as revealed by trace element chemistry of olivine. *Geochimica et Cosmochimica Acta*

Rampone E., Piccardo G.B. and Hofmann A.W. (2008) Multi-stage melt–rock interaction in the Mt. Maggiore (Corsica, France) ophiolitic peridotites: microstructural and geochemical evidence. *Contrib Mineral Petrol*, 156:453. doi:10.1007

Ross K., Elthon D. (1997) Cumulus and postcumulus crystallization in the ocean crust : Major and trace element geochemistry of Leg 153 gabbroic rocks. *Proceedings of the Ocean Drilling Program, Scientific Results*, 153:333-349.

Sanfilippo A., Dick H. J. B., Ohara Y. (2013) Melt-rock reaction in the mantle: mantle troctolites from the Parece Vela ancient back-arc spreading center. *J Petrol* 54:861–885

Sanfilippo A., Tribuzio R. (2013a) Origin of olivine-rich troctolites from the oceanic lithosphere: a comparison between the Alpine Jurassic ophiolites and modern slow spreading ridges. *Ofioliti* 38:89–99

Sanfilippo A., Tribuzio R. (2013b) Building of the deepest crust at a fossil slow-spreading center (Pineto gabbroic sequence, Alpine Jurassic ophiolites). *Contrib Mineral Petrol* 165:705–721

- Sanfilippo A., Tribuzio R., Tiepolo M., Berno D. (2015) Reactive flow as dominant evolution process in the lowermost oceanic crust: evidence from olivine of the Pineto ophiolite (Corsica). *Contrib Mineral Petrol*, 170:38-50. doi:10.1007/s00410-015-1194-8
- Saper L., Liang Y. (2014) Formation of plagioclase-bearing peridotite and plagioclase-bearing wehrlite and gabbro suite through reactive crystallization: an experimental study. *Contributions to Mineralogy and Petrology*, 167:985. doi:10.1007/s00410-014-0985-7
- Schilling F., Wunder B. (2004) Temperature distribution in piston-cylinder assemblies. *European Journal of Mineralogy* 29. doi:10.1127/0935-1221/2004/0016-0007
- Soulié C., Libourel G. and Tissandier L. (2017) Olivine dissolution in molten silicates: An experimental study with application to chondrule formation. *Meteoritics and Planetary Science* 52, 225–250.
- Spandler C., O'Neill H. S. (2010) Diffusion and partition coefficients of minor and trace elements in San Carlos olivine at 1,300°C with some geochemical implications. *Contrib Mineral Petrol* (2010) 159:791-818. doi:10.1007/s00410-009-0456-8
- Suhr G., Kelemen P., Paulick H. (2008) Microstructures in Hole 1274A peridotites, ODP Leg 209, Mid-Atlantic Ridge: Tracking the fate of melts percolating in peridotite as the lithosphere is intercepted. *Geochemistry, Geophysics, Geosystems*, 9. doi:10.1029/2007GC001726
- Suhr G. (1999) Melt migration under oceanic ridges: inferences from reactive transport modelling of upper mantle hosted dunites. *J. Petrol.*, 40: 575-599.
- Takagi D., Sato H. & Nakagawa M. (2005) Experimental study of a low-alkali tholeiite at 1–5 kbar: optimal condition for the crystallization of high-An plagioclase in hydrous arc tholeiite. *Contrib Mineral Petrol* 149: 527. doi:10.1007/s00410-005-0666-7
- Toplis M. J. (2005) The thermodynamics of iron and magnesium partitioning between olivine and liquid: criteria for assessing and predicting equilibrium in natural and experimental systems. *Contrib Mineral Petrol* (2005) 149: 22–39

- Tursack E., Liang Y. (2011) A comparative study of melt-rock reactions in the mantle: laboratory dissolution experiments and geological field observations. Contributions to Mineralogy and Petrology, 163:861-876
- Tribuzio R., Tiepolo M., Vannucci R., Bottazzi P. (1999) Trace element distribution within the olivine-bearing gabbros from the Northern Apennine ophiolites (Italy): evidence for post-cumulus crystallization in MOR-type gabbroic rocks. Contrib Mineral Petrol 134:123–133
- Tribuzio R., Tiepolo M., Thirlwall M.F. (2000) Origin of titanian pargasite in gabbroic rocks from the Northern Apennine ophiolites (Italy): insights into the late-magmatic evolution of a MOR-type intrusive sequence. Earth Planet Sci Lett 176:281–293
- Ulmer P., Luth R. (1991). The graphite–COH fluid equilibrium in P, T, fO₂ space. Contributions to Mineralogy and Petrology, 106:265–272
- Van Den Bleeken G., Müntener O, Ulmer P (2010) Reaction Processes between Tholeiitic Melt and Residual Peridotite in the Uppermost Mantle: an Experimental Study at 0.8 GPa. Journal of Petrology, 51:153-183
- Van Den Bleeken G., Müntener O, Ulmer P (2011) Melt variability in percolated peridotite: an experimental study applied to reactive migration of tholeiitic basalt in the upper mantle. Contributions to Mineralogy and Petrology, 161:921-945
- Winter J.D. (2014) Principles of Igneous and Metamorphic Petrology, Second Edition, Pearson Education Limited 2014, 738p
- Zhang Y., Walker D., and Lesher C. E. (1989) Diffusive crystal dissolution. Contributions to Mineralogy and Petrology 102:492–513.